CONDUCTIVE POLYMER BASED NANOCOMPOSITES AND THEIR APPLICATIONS FOR RENEWABLE ENERGY

Thesis Submitted for the Award of the Degree of

DOCTOR OF PHILOSOPHY

in

Physics

By

Yugesh Singh Thakur

Registration Number: 11916772

Supervised By
Dr. Aman Deep Acharya (19358)
Department of Physics (Associate Professor)
Lovely Professional University

LOVELY PROFESSIONAL UNIVERSITY, PUNJAB
2025

DECLARATION

I, hereby declared that the presented work in the thesis entitled "**Conductive polymer based nanocomposites and their applications for renewable energy**" in fulfilment of degree of **Doctor of Philosophy (Ph. D.)** is outcome of research work carried out by me under the supervision Dr. Aman Deep Acharya, working as Associate Professor in the "Department of Physics" of Lovely Professional University, Punjab, India. In keeping with general practice of reporting scientific observations, due acknowledgements have been made whenever work described here has been based on findings of other investigator. This work has not been submitted in part or full to any other University or Institute for the award of any degree.

Yugesh Singh Thakur
Registration No. 11916772
Department of Physics
School of Chemical Engineering
and Physical Sciences
Lovely Professional University,
Jalandhar-Delhi, G.T. Road (NH-1), Phagwara
Punjab (INDIA)

CERTIFICATE

This is to certify that the work reported in the Ph. D. thesis entitled "**Conductive polymer based nanocomposites and their applications for renewable energy**" submitted in fulfillment of the requirement for the reward of degree of **Doctor of Philosophy (Ph.D.)** in the **Department of Physics, School of Physical Sciences, Lovely Professional University**, is a research work carried out by **Mr. Yugesh Singh Thakur (11916772)**, is bonafide record of his original work carried out under my supervision and that no part of thesis has been submitted for any other degree, diploma or equivalent course.

Dr. Aman Deep Acharya
Associate Professor Department of Physics
Lovely Professional University
Jalandhar-Delhi, G.T. Road (NH-1), Phagwara
Punjab (INDIA)-144411

Acknowledgements

My journey of doctorate had been very fascinating and exciting and, I take this opportunity to thanks people who have helped me throughout this journey in different ways:

To commence with, I would like to pay gratitude to GOD for blessing me with this opportunity to pursue Doctorate, to have bestowed upon me good health, and giving me strength and motivation to stay strong and hopeful.

Words can hardly express my deep sense of gratitude for my research supervisor, advisor, and mentor **Dr. Aman Deep Acharya**, Associate Professor, Department of Physics, Lovely Professional University, Jalandhar, India, for his guidance and constant encouragement. I have learnt how to solve a complicated problem by proper planning and execution. I will ever remain indebted for the way he has groomed me.

I whole heartedly thank **Dr. Kailash Chandra Juglan**, Professor and Head of School of Chemical Engineering and Physical Sciences, Lovely Professional University for his suggestions and support. My sincere thanks to **Dr. Rajesh Kumar**, Head of lab for providing the necessary facilities to carry out the research work at Lab. I acknowledge Assistant Superintendent **Mr. Nitin Kumar**, Assistant Superintendent **Mr. Ramesh** and Deputy Superintendent **Mr. Omkar**, for helping me with all the equipment in the lab. I would also like to express my gratitude to the ETP panel members for their valuable suggestions and corrections to my research work.

I am grateful to the committee and staff members of the Central Instrumentation Facility (CIF), Division of Research Development, Lovely Professional University, for providing contemporary analytical instrument facilities to expedite basic and advanced research.

I am thankful to **Mr. Dharmender Singh Rana** Assistant Professor, Department of Physics, Maharaja Lakshman Sen Memorial College Sundernagar (H.P) and **Dr. Dilbag Singh Rana** Assistant Professor Department of Environmental Sciences, Central University of Himachal Pradesh for allowing me to visit and utilize Electrochemical workstation.

I would like to take the opportunity to thank **Prof. B.C. Chauhan**, Campus Director of the Central University Himachal Pradesh, for his valuable suggestions and support at all times.

I feel incredibly blessed to have the wonderful company of friends and lab mates. I want to extend my heartfelt thanks to my friend, **Divya Bisen**, for her unwavering moral and emotional support. I am also deeply grateful to my close friends, **Rahul, Dr. Vidushi Karol and Dr. Hamnesh Mahajan**, for their constant encouragement and support throughout my research journey. Additionally, I wish to express my sincere gratitude to my senior and dear labmate, **Dr. Sakshi Sharma**, for her gracious and supportive companionship throughout our research endeavors. I am deeply indebted to my research groupmate **Amisha**, for their support and encouragement.

Finally, and most importantly, I want to express my heartfelt gratitude to my loving father, Shri **Hem Raj Thakur**, my mother, Smt**. Uma Vati**, my sister, **Hem Lata Thakur**, my brothers, **Krishan Thakur** and **Anil Thakur**, and my wonderful partner, **Nisha Thakur**. Their unconditional love and unwavering support have been my anchor throughout this journey. The dream of earning a doctorate degree became a reality thanks to the steadfast encouragement and care of my family.

Yugesh Singh Thakur
(Reg. No.: 11916772)

Abstract

Sustainable and renewable energy sources have the potential to diminish the dependence on fossil fuels and decline the destructive impacts on the ecosystem, including climate change and CO_2 emissions. These sources of energy are abundant and can be replenished naturally, unlike non-renewable sources. The rising use of renewable energy can also reduce air and water pollution and can help preserve natural resources for future generations. To efficiently utilize renewable energy supplies, it is pointed to have reliable energy storage approaches that can preserve the energy generated when it is abundant, and release it when it is needed. Supercapacitors, along with other energy storage equipment such as rechargeable batteries and fuel cells, can play a vital role in this regard. Supercapacitors are considered a capable energy storage technology because they can deliver high power density, store more energy than conventional dielectric capacitors, and have advantages such as rapid charge/discharge rates, extended cycle life, high coulombic efficiency, minimal maintenance costs, and safe operation. These characteristics make them suitable for a broad span of applications, including memory backup systems, electric vehicles, and smart grids. This thesis investigates the usage of conducting polymer-based nanocomposites as electrode materials to expand the efficiency of supercapacitors. To gain insights into the supercapacitive behavior of these nanocomposites and the variables controlling them, the study examines the structural, morphological, and detailed electrochemical characteristics of conducting polymers-based nanocomposites. Additionally, it investigates how various parameters—such as shape, size, quantity, and type of metal oxide—affect the supercapacitive performance of the nanocomposites. The present research involves the preparation of two distinct series of conducting polymer nanocomposites using in situ and physical blending methods, detailed as follows:

- V_2O_5-PANI nanocomposites with 10, 20, and 30 wt.% of V_2O_5 were prepared via in situ polymerization method.
- PPy-BiOCl nanocomposites with 5, 7, and 9 wt.% of PPy were prepared by physical blending technique.

Before assessing the supercapacitive characteristics of the electrodes, diverse characterization systems were employed to examine their fundamental structural and morphological attributes. The electrochemical performance and energy storage mechanism of the prepared conducting polymers-based nanocomposite electrodes were thoroughly evaluated using KOH electrolytes. In addition, this thesis includes the fabrication of a supercapacitor device to evaluate the practical application of the electrodes. The successful illumination of an LED by the fabricated supercapacitor demonstrates that these electrodes hold substantial ability for next-generation energy storage applications. Beyond the capable electrochemical properties of V_2O_5-PANI for supercapacitors, the present thesis also explores the optical applications of V_2O_5-PANI nanocomposites. These materials demonstrate unique optical characteristics resulting from the synergistic effects of vanadium pentoxide (V_2O_5) and polyaniline (PANI), which enhance light absorption and modulation capabilities. The study investigates how incorporating V_2O_5 into PANI matrices can improve optical properties, including tunable band gaps and enhanced UV shielding efficiency.

Overall, this thesis underscores the promise of various conducting polymer-based nanocomposites as electrode materials for improving supercapacitor performance. Additionally, V_2O_5-PANI optical studies provide valuable insights for developing optical devices for future applications.

Table of Contents

Contents

LIST OF SYMBOLS

Symbol	Description
Ω	Angular frequency
Θ	Bragg's angle
C	Capacitance
ΔE	Change in energy
Rct	Charge transfer resistance
I	Current
ºC	Degree Celsius
2θ	Diffraction angle
Ro	Series resistance
δ	Dislocation density
Z	Impedance
%	Percentage
χ	Susceptibility
Å	Angstrom
D	Crystallite size
TWh	Terawatt hours
MW	Mega Watt
Q	Charge

Wh	Watt-Hour
~	Approximately
ε	Permittivity
Kg	Kilogram
F	Farad
g	Gram
σ_{opti}	Optical Conductivity
mV	Milli Volt
eV	Electron Volt
A	Absorption Coefficient
Π	pi (3.14)
E_g^{opti}	Optical energy band gap
n	Refractive index
$\chi^{(1)}$	First-order susceptibility
$\chi^{(3)}$	Third-order susceptibility
$n^{(2)}$	Nonlinear refractive index
S_1	Average oscillator strength
F	Parameter is oscillator strength
k	Extinction coefficient
R	Reflectance
E_o	Single-oscillator energy
E_d	Dispersion energy
ε_r	Real components
ε_i	Imaginary components

ε_1	Dielectric constant of lattice
a.u	Arbitrary unit
D	Average crystallite size
K	Scherrer constant
β	FWHM of the diffraction
$\log(\nu)$	Logarithm of scan rate
$\log(i)$	Logarithm of current
Δt	Discharging time
m	Mass
Ω	Ohm

LIST OF ACRONYMS AND ABBREVIATIONS

Acronym and Abbreviations	**Description**
BET	Brunauer-Emmett-Teller
CNT	Carbon Nano Tube
CV	Cyclic Voltammetry
CDC	Carbon-derived Carbon
DEG	Diethylene Glycol
ESR	Equivalent Series Resistance
ED	Energy Density

EG	Ethylene Glycol
EDLC	Electric double-layer capacitor
EIS	Electrochemical impedance spectroscopy
ESCs	Electrochemical supercapacitors
EDX	Energy-dispersive X-ray analysis
Eq.	Equation
etc.	Et cetera
FESEM	Field emission scanning electron microscopy
TEM	Transmission electron microscope
Fig.	Figure
FTIR	Fourier transform infrared spectroscopy
GCD	Galvanostatic charge-discharge
GO	Graphene oxide
IR	Infrared
JCPDS	Joint Committee Powder Diffraction Standards
LED	Light-emitting diode
NMP	n-methyl-2-pyrrolidone
PD	Power Density
PMMA	Polymethyl methacrylate
PANI	Polyaniline
PPy	Polypyrrole
PVDF	Polyvinylidene fluoride

RES	Renewable Energy Sources
SEM	Scanning electron microscopy
SC	Supercapacitor
SELF	Surface Energy Loss Function
TEM	Transmission electron microscopy
TEG	Triethylene Glycol
TGA	Thermogravimetric Analysis
UV-VIS	Ultraviolet-visible
VELF	Volume Energy Loss Function
Wt.	Weight
XRD	X-ray diffraction
XPS	X-ray photoelectron spectroscopy
CD	Current density

LIST OF FIGURES

LIST OF TABLES

Chapter 1

Introduction

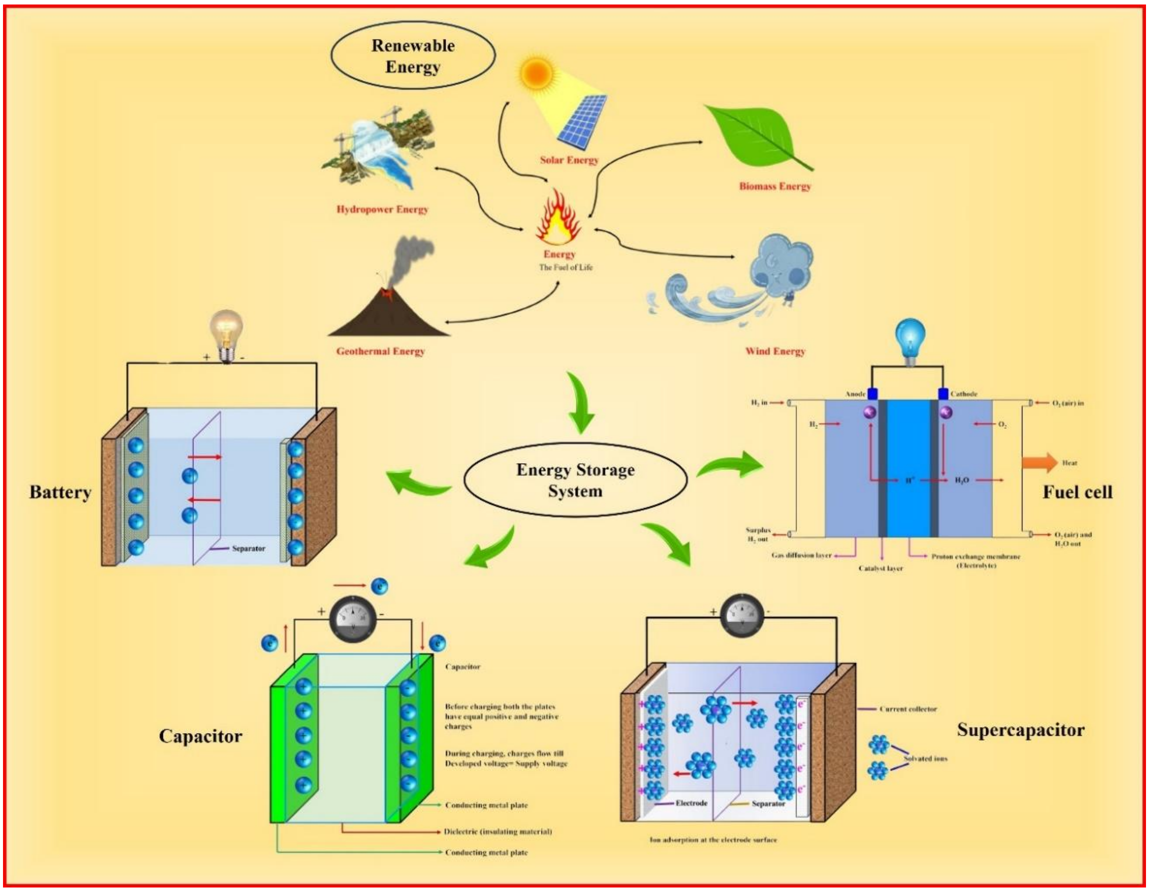

This chapter gives a comprehensive overview of renewable energy, need for renewable energy storage systems, various types of supercapacitors, and an extensive range of supercapacitors applications.

1.1. Preamble

Recent scientific advancements and innovations in the field of renewable energy sources have been increasing to bring a solution for the negative environmental effects triggered by the use of non-sustainable power sources such as fossil fuels and nuclear power materials.

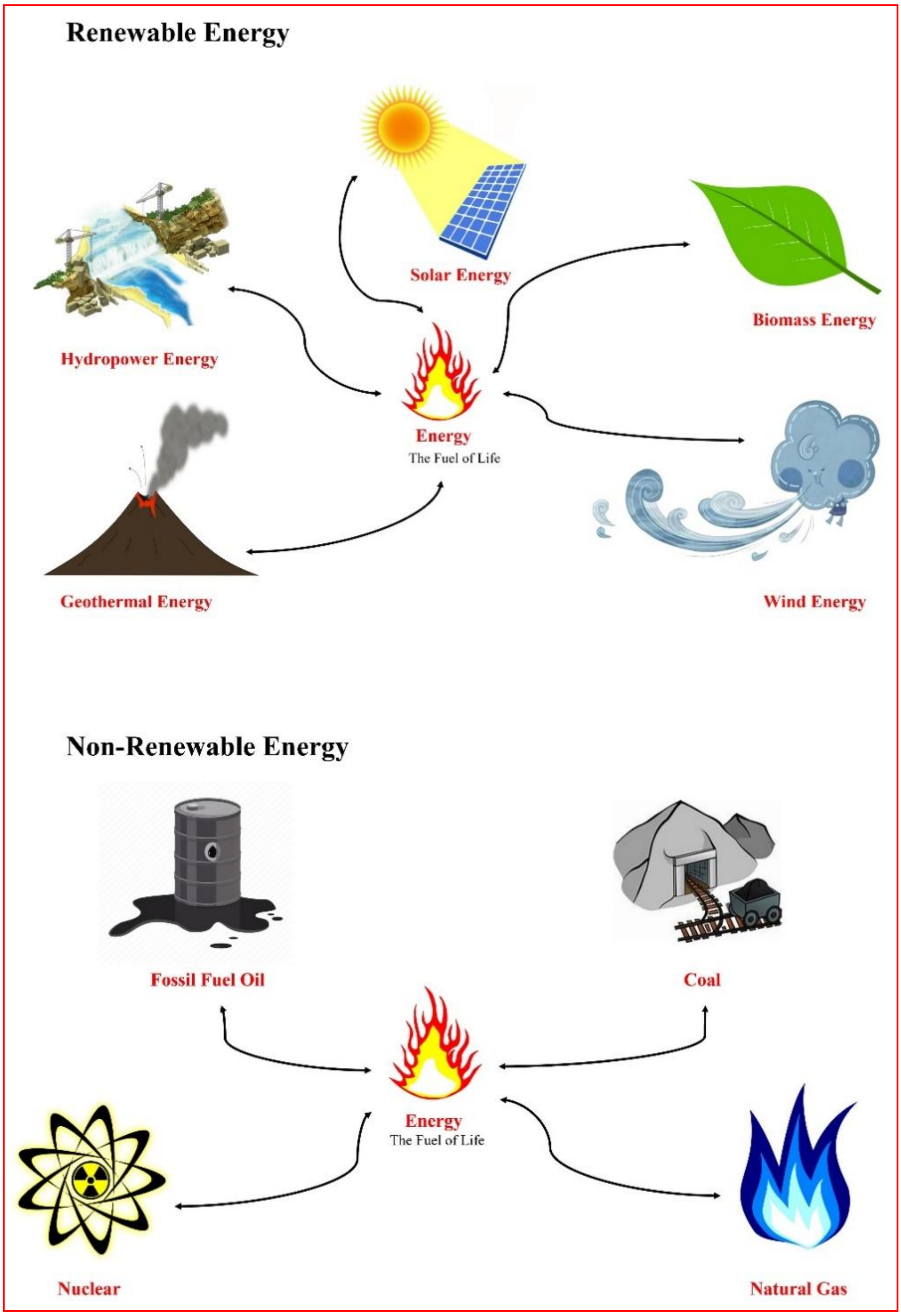

Figure 1.1. Types of energy resources.

Although fossil fuels offer high energy density, but their unsustainability leads to harmful environmental results, including smog formation and acid precipitation [1]. Consequently, there is a rising emphasis on the research and advancement of renewable energy resources namely solar, wind, hydroelectric power and nuclear power to fulfill the energy needs of the world with more sustainable manner. As an alternative energy source, nuclear power stands with both advantages and disadvantages. One of the main advantages is that it does not produce smoke, providing a cleaner form of energy compared to fossil fuels. Additionally, nuclear power provides more energy per unit mass of nuclear fuel. However, the disposal of radioactive waste from nuclear power plants can be a major concern, as it can be harmful to all living species [2]. Furthermore, nuclear powers viability hinges on geographical and climatic dependent, it requires extensive safety measures making it an expensive energy source. Nevertheless, many researchers believe that sustainable energy sources like wind, water, solar as well as geothermal are constantly renewable and readily accessible for use [3,4]. In the future decades, these sources might be extremely important for supplying the world's energy needs. The schematic representation of energy resources and their types is shown in Figure 1.1.

The graphical representation in Figure 1.2 illustrates the generation of electricity across the world (using renewable and non-renewable resources) from 2010 to 2022.

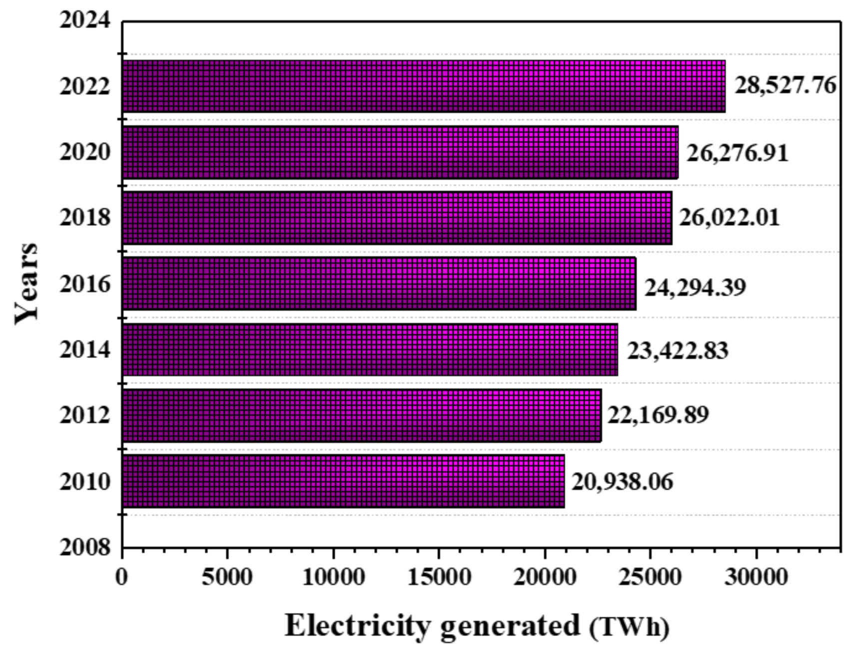

Figure 1.2. World electricity generation from 2010 to 2022.

It is clear that there was a consistent increase in power production throughout the decade. In 2010, the total amount of electricity generated was 20,938.06 Terawatt hours (TWh), and by 2022, this number had increased to 28,527.76 TWh [5]. This increase can likely be attributed to several factors, including the growing population and the increasing use of new technologies such as electric vehicles and household gadgets, all of which heavily rely on electricity as their primary power source.

1.2. Energy Scenario in India

India with a population of 1.42 billion is the most populated country. The vast population of India requires a significant amount of energy, making it challenging to meet the energy demand. India has a long history of prioritizing renewable energy sources. The Indian government established the Commission for Additional Sources of Energy in 1981, which later evolved into the Department of Non-Conventional Energy Sources in 1982 [6]. To meet its future energy demands, India took significant steps by expanding the Ministry of Non-Conventional Energy Sources in 1992, later rebranding it as the Ministry of New and Renewable Energy in 2006 [7]. Among the various renewable energy resources, particular attention has been given to the National Solar Mission, as emphasized by Nigam in 2016 [8]. This initiative aims to utilize 40,000 MW and 60,000 MW of solar power through rooftop and ground-mounted solar panels, indicating a strategic focus on solar energy development. In the broader context, Schmid et al. underscore the challenges India faces regarding energy security, especially in light of the Electricity Act of 2003 and subsequent tariff policies from 2006 [9]. These challenges likely stem from the need to balance energy demands with sustainable practices and regulatory frameworks.

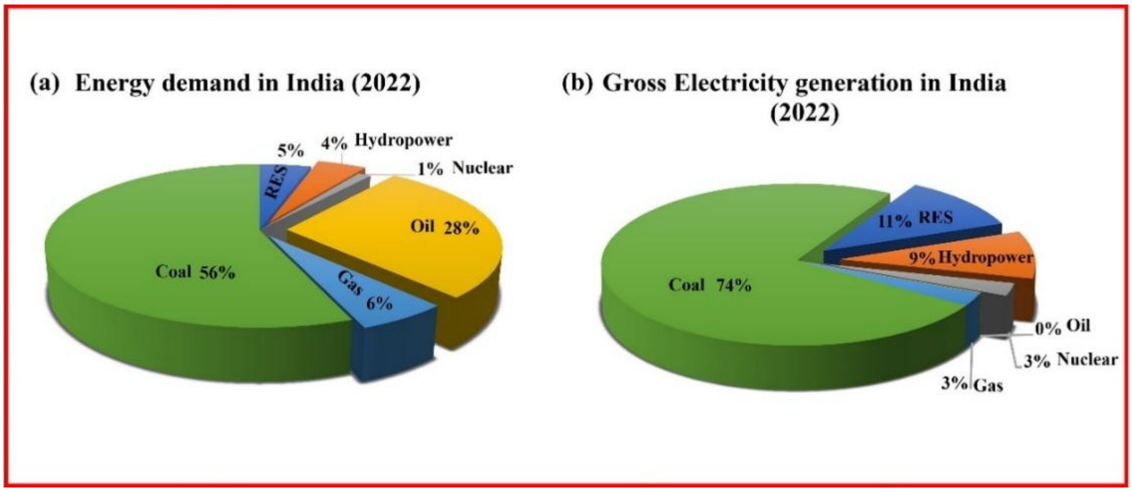

Figure 1.3. (a) The energy demand and (b) the total energy generation in India for the year 2022.

Concurrently, Garg et al. stress the imperative of boosting energy production from renewable sources and slashing greenhouse gas emissions by 20% [10]. This emphasis aligns with India's efforts to prioritize renewable energy, as highlighted by the National Solar Mission, and reflects a broader commitment to environmental sustainability and energy security. Figure 1.3(a) shows that in 2022, the majority of the energy demand was for coal (56%) whereas the availability of renewable energy sources (RES) was only 5%, with hydro accounting for 4%, gas 6%, nuclear 1%, and oil 28%, respectively [5]. Figure 1.3(b) illustrates the sources of electricity generated, in which 74% of the electricity was generated by burning coal and the remaining electricity was generated from RES. Asif et al. examined the challenges surrounding the expansion of renewable energy technologies in the world and India [11]. It noted that the proposed ultra large-scale solar and wind farms would occupy only a fraction of the country's available land and near-offshore areas. This insight highlights the potential for significant renewable energy development without substantial land use implications, reinforcing ongoing efforts to prioritize renewable energy. Mathews et al. proposed that increasing the capacity of renewable energy resources in growing countries namely China and India can lead to successful energy security [12].

However, one of the main disadvantages of renewable energy is its intermittency, as it is dependent on weather conditions. The availability of "solar" and "wind" energy can vary depending on the time of day and season [13]. However, advances in energy storage technology, namely batteries and supercapacitors are helping to mitigate this issue. These devices allow for the storage of excess energy generated by renewable sources, making them available for use when it is not being produced, such as at night or during calm weather. Improving the capacity and efficiency of energy storage technology is crucial in increasing the reliability and stability of renewable energy systems. Research and development in this range are ongoing and new advancements in "energy storage" devices are expected in the future [14].

1.3. Classification of energy storage devices

Energy storage devices are broadly classified into several categories, including electrical (capacitor, supercapacitor, battery, fuel cell and superconducting magnetic storage devices), mechanical (hydroelectric, flywheel, and compressed air storage systems), chemical (hydrogen, liquid nitrogen, and biofuels), thermal (steam accumulator, cryogenic liquid air, ice storage, and hot bricks), and biological (starch, glucose, and glycogen) systems [15]. However, the current reports suggest that meeting both the economic and technical requirements across various applications appears to be challenging for any of the aforementioned energy storage devices. It is important to note that renewable energy sources namely “solar” and “wind” power are not always predictable and can be difficult for grid operators to control their energy generation [16]. In this regard, energy storage systems can help to address this issue and promote green energy utilization over traditional fossil fuels for electricity generation. With increasing concerns about the exhaustion of traditional fuels and their consequence on the environment and global warming, there is a noticeable trend moving towards electrochemical power systems namely supercapacitors, fuel cells, and batteries to deliver clean energy. These systems are cleaner and more environmentally friendly than fuel combustion systems. They also benefit from being driven by reactions at interfaces rather than by volume-dependent heat-engine cycles, enhancing their efficiency and reliability. Energy storage in electrochemical devices, such as batteries and supercapacitors, relies on chemical reactions occurring at the interfaces between electrodes and electrolytes. These reactions are affected by factors like the surface morphology, physical properties, and chemical characteristics of the materials used in the system [17–19]. This allows for the efficient storage and release of energy based on the design and materials used in the system. This is different from traditional heat-engine cycles, which store and release energy through changes in volume. The main energy storage devices that have been commercialized include capacitors, batteries, fuel cells, and supercapacitors. While they all contain a positive electrode and a negative electrode, they operate through different mechanisms. In each of these devices, energy transfer takes place at the electrolyte-electrode interface. A conventional capacitor uses a dielectric between two oppositely charged electrodes, while supercapacitors, fuel cells, and batteries use an electrolyte solution and a separator to avoid electrical short circuits occurring between the two electrodes. In fuel cells and batteries, redox reactions occur at the cathode and anode, converting chemical energy into electrical energy [20–22]. To have a better understanding regarding energy storage devices the upcoming sections provide thorough explanations of batteries, capacitors, fuel cells, and supercapacitors.

1.3.1. Battery

A battery is an equipment that stores electrical energy in chemical form and transforms it into electrical energy by allowing the movement of electrons through a circuit. Batteries come in different shapes, sizes, and chemical compositions. They have a positive and negative terminal and the flow of electrons between them powers connected devices (see Figure 1.4). Batteries are categorized into two types: primary and secondary. Primary batteries, such as dry cells and some alkaline batteries are single-use and cannot be recharged. Secondary batteries, on the other hand, can be recharged and used multiple times. For example, “lead-acid, nickel-cadmium, and lithium-ion batteries” [23].

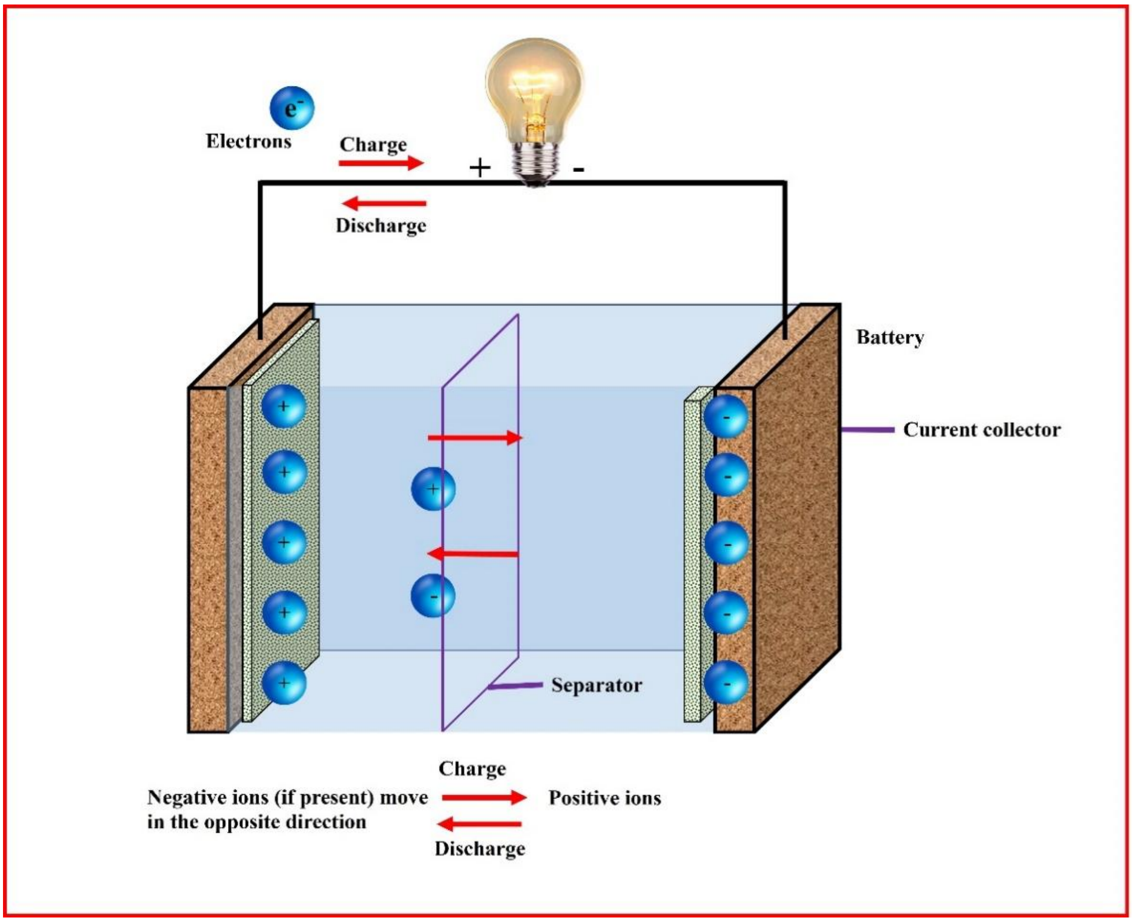

Figure 1.4. Charging-discharging activity in a battery.

1.3.2. Capacitor

Conventional capacitors store energy electrostatically by accumulating charges on opposite electrodes. During the charging process, the capacitor is linked to a voltage supply, which creates a potential difference between the electrodes, causing positive and negative charges to move toward the oppositely polarized electrodes. When the capacitor is fully charged, it acts as a small voltage source to a load in a circuit and the current will stop flowing once charge balance is achieved. Fundamentally, the capacitor acts like a temporary voltage source, providing a burst of energy until its stored voltage and the load's voltage become equal.

The following equation is used to determine the capacitor's capacitance, or its capacity to hold charge [24].

$$C = {}^{Q}\!/_{V} \tag{1.1}$$

where "Q" is the charge stored and "V" is the voltage across the capacitor.

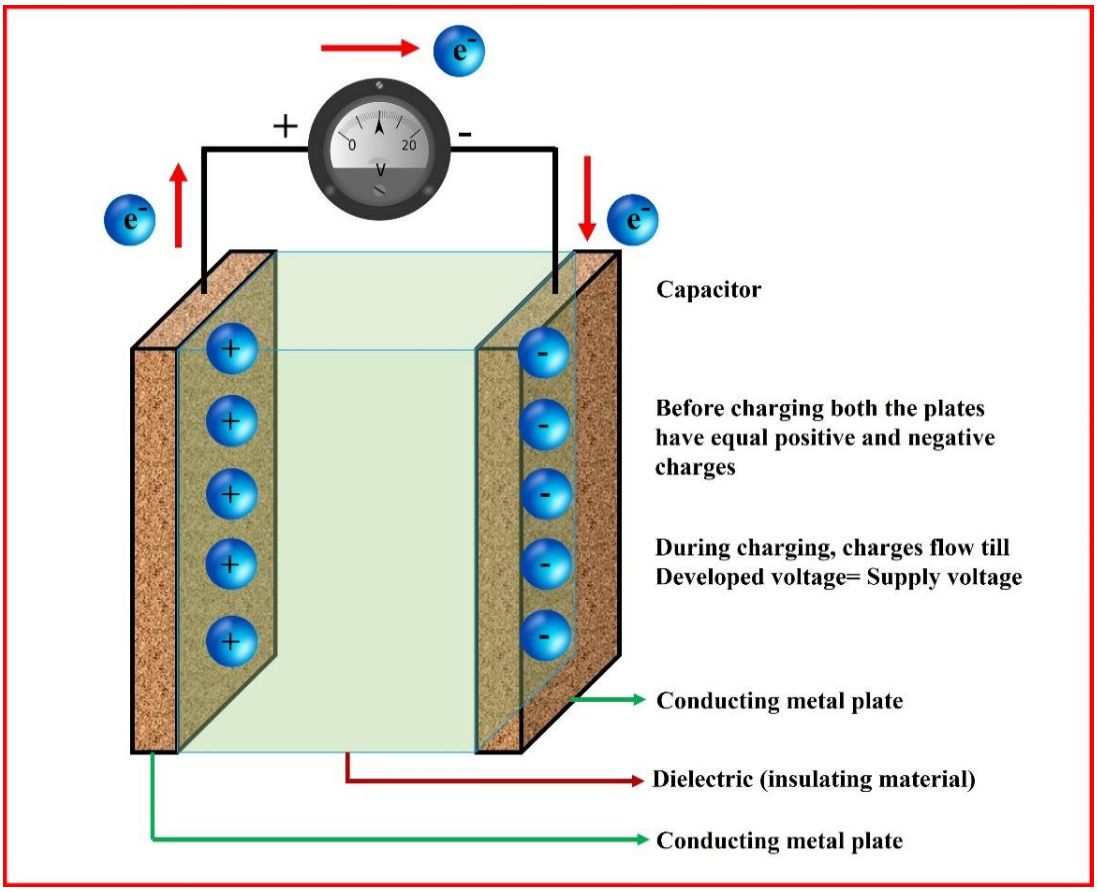

Figure 1.5. Charge storage process in capacitors.

The capacitance of a capacitor is affected by several factors, including the area "A" of the electrodes, the permittivity of free space "ε_0", and the separation distance "d" between the electrodes. These factors are connected as described by equation (1.2), which defines the capacitance of the capacitor [25].

$$C = \frac{\varepsilon_0 A}{d} \tag{1.2}$$

The capacity of a capacitor can also be represented by equation (1.3) when the gap between the parallel plates is filled with a dielectric material. The capacitance of a capacitor is primarily decided by the properties of the dielectric, the area of the capacitor's plates, and the distance between the electrodes [26].

$$C = \frac{\varepsilon\varepsilon_0 A}{d} \tag{1.3}$$

where “ε” is the permittivity of the dielectric substance. Figure 1.5 illustrates a capacitor with a dielectric material located between the conducting plates. The dielectric material prevents any movement of electrons or charges. The capacitor stores energy in the form of static electricity. Initially, both plates have positive and negative charges in equal amounts. When an external voltage source is linked to the capacitor, the positive end of the source attracts electrons from the plate connected to it, depositing them on the plate linked to the negative end. As a result, charges build up on both plates—one plate is negatively charged and the other is positively charged. The movement of electrons continues until the developed voltage is equal to the supplied voltage. During discharging, a load is connected to the circuit, and electrons move from the negatively charged plate to the positively charged plate through the circuit, causing the connected load to function [27,28]. The energy density *(ED)* and power rating of a capacitor are the two main variables that affect its performance. The equation (1.4) represents the energy density, which is the quantity of energy stored per unit volume and is directly correlated with the capacitance of the capacitor [29].

$$ED = \frac{1}{2} CV^2 \tag{1.4}$$

where “ED” denote the energy density, “C” is the capacitance and “V” is the potential across electrodes.

The maximum power handling capacity of a capacitor is determined by the energy rate delivery per unit of time. Some capacitors also take into account internal components like electrode material, current collectors, and dielectrics, which mutually contribute to the equivalent series resistance (ESR) of the capacitor. In such cases, the maximum power of the capacitor can be represented by equation (1.5) [24,29].

$$PD = \frac{V^2}{4ESR} \tag{1.5}$$

Conventional capacitors have relatively low *ED*, but they exhibit *PD* because of their electrostatic mechanism of charge storage.

1.3.3. Fuel cell

Fuel cells stand out as remarkable devices that leverage chemical reactions to generate electricity continuously. In contrast to batteries with finite energy stores, fuel cells operate as long as they have a steady supply of fuel and oxygen. This sustained functionality relies on redox reactions. Hydrogen (H_2) is a common fuel, and when fed into the cell, it splits into positively charged protons and electrons (see Figure 1.6). While the electrons (e^-) migrate via an outer electric circuit to initiate an electrical current, the protons (H^+) pass via a membrane. Conversely, when airborne oxygen (O_2) joins forces with protons and electrons to make water (H_2O), some heat is released. This combination of chemical reactions and electrical flow makes them a promising clean energy technology. Fuel cells possess a high energy degree, enabling them to keep a significant amount of energy in a compact space [30]. However, their power output, indicating the amount of electricity they produce at a given time, can vary depending on the type of fuel cell [30,31].

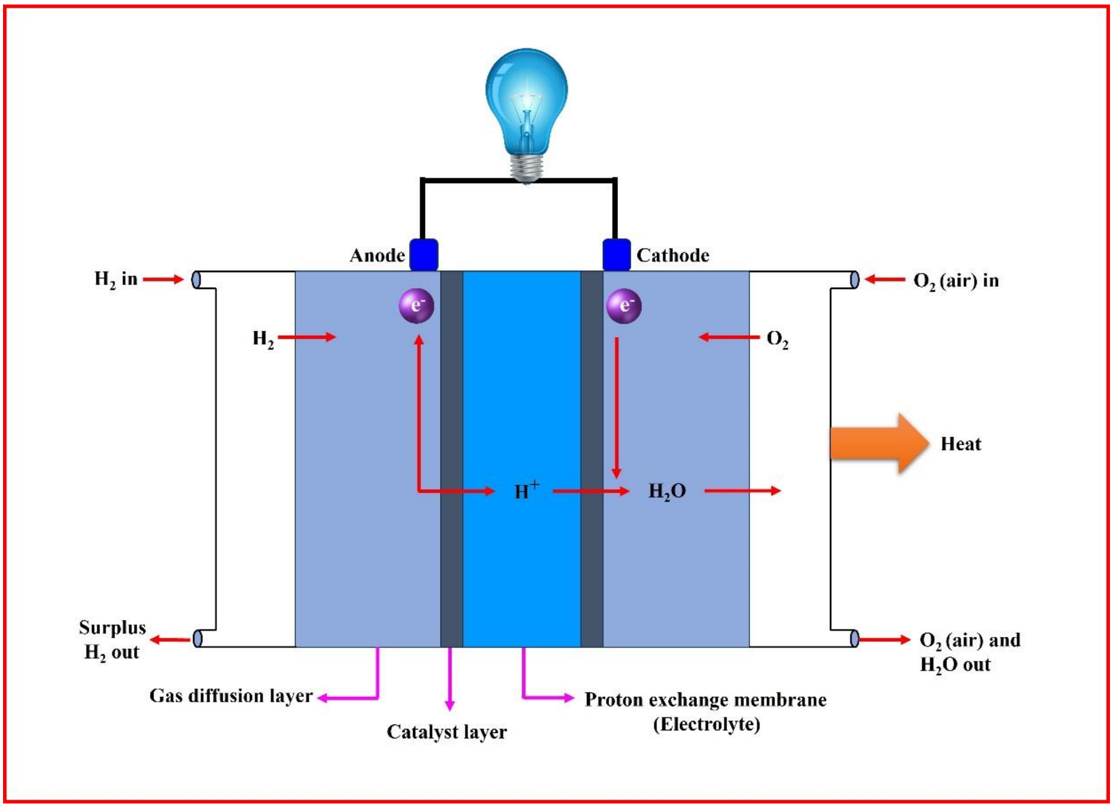

Figure 1.6. Fuel cell proton exchange membrane.

1.3.4. Supercapacitor

Supercapacitors, which have "high power densities and excellent energy densities," are energy storage devices that fill the void left by batteries and fuel cells [32]. Simply, the main advantage of supercapacitors over capacitors can be explained in terms of capacitance, a capacitor charged to 1 volt (V) with 1 farad (F) of capacitance will provide 1 ampere (A) current for 1 second time. It is worth noting that in practice, capacitors do not have a capacitance of 1F, but rather in microfarads. In many electronic applications, capacitances in microfarads are sufficient to power the device. In contrast to conventional capacitors, supercapacitors have capacitances in farads (F), which means that they can store electrical charges a million times more than capacitors [33,34]. In circumstances in which transportation of energy is required at a slow rate over a longer period, the most suitable choice would be a battery with a high ED and a low PD.

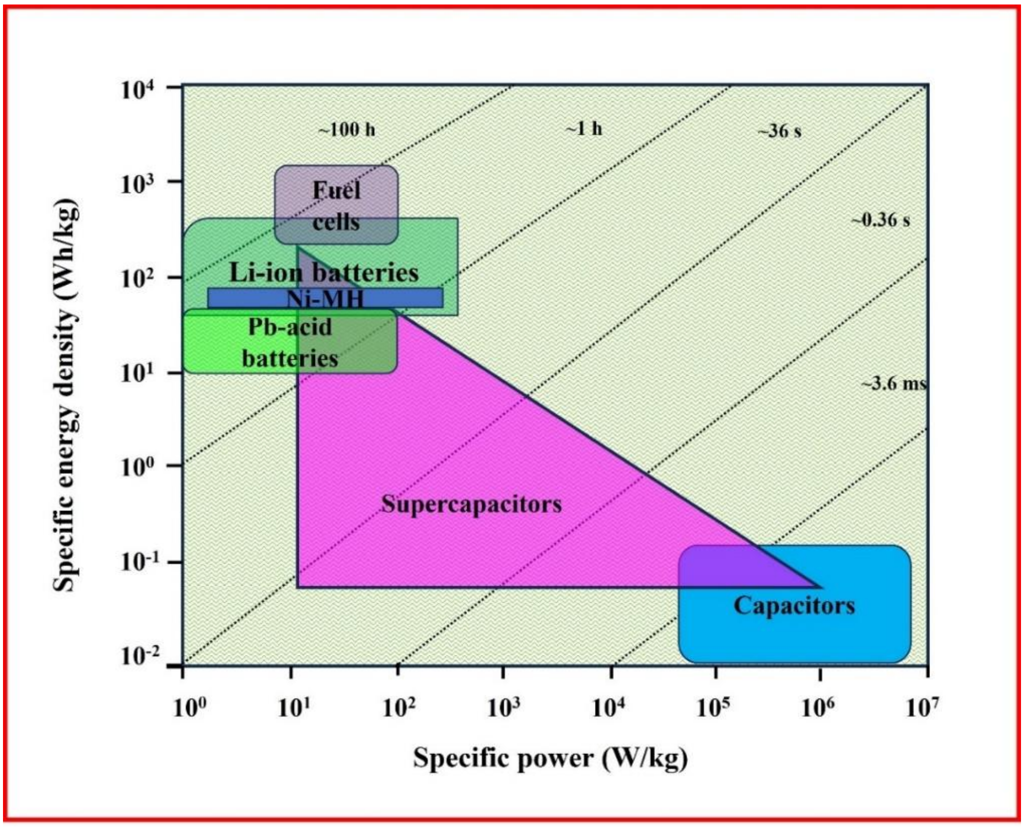

Figure 1.7. Ragone plot of an energy storage device.

On the other hand, a supercapacitor with greater power density and intermediate energy density would be a preferable choice in circumstances when energy needs to be provided quickly over a short period. Therefore, when quick energy transfer is needed, supercapacitors are frequently chosen over other electrochemical devices [35,36].

A helpful visual representation of the performance capabilities of various electrochemical storage equipment is provided by the Ragone plot in Figure 1.7, which can be used to compare the ED and PD of different devices [37]. According to observations, fuel cells exhibit the greatest specific energy density while simultaneously demonstrating the lowest specific power density in contrast to lithium-ion batteries, capacitors, and supercapacitors. Similarly, capacitors have the highest specific power density but the lowest specific energy density. Supercapacitors have more specific power density than batteries and fuel cells. The Ragone plot suggests that a rechargeable vehicle run by a battery, which has a high energy density, can travel a greater distance before the battery needs to be recharged. On the other hand, a vehicle powered by a supercapacitor, which has a high-power density, can accelerate faster. The kinetic process in a battery is driven by redox transitions of the materials inside it, which causes the volume of the battery to change. These sudden volume changes reduce the lifespan of batteries and limit their power delivery compared to supercapacitors. Therefore, supercapacitors are a preferred option for fast recharging, rapid power delivery, and long durability (cycle life) over other electrochemical devices [38,39]. Table 1.1 provides a comprehensive evaluation of the characteristics of fuel cells, batteries, and supercapacitors [40-41].

Table 1.1: Comparison between fuel cells, batteries and supercapacitors.

S. No	**Fuel Cells**	**Batteries**	**Supercapacitors**
1	Fuel cells produce electricity by reacting hydrogen with oxygen.	Chemical energy is converted to electrical energy by battery cells.	Energy is stored at the junction between the electrode and electrolyte, commonly referred to as either supercapacitors or electrochemical capacitors.
2	The total weight of the fuel cell ranges from 20 g to under 5 kg.	The weight of the battery can vary from 1 g to more than 10 kg.	The weight of a supercapacitor ranges from a minimum of 1 g to a maximum of 230 g.
3	It operates between +25°C and +90°C in temperature.	It operates between -20°C and +65°C in temperature.	It can function within a temperature range of -40°C to +85°C.

Table 1.1 Continued

4	The charging process generally spans from 10 to 300 h.	Charging of batteries typically takes one to ten hours.	Charging typically takes a few mili seconds (ms) to second (s).
5	The efficiency of energy is over 82%.	The energy efficiency can reach up to 90%.	It possesses rapid recharge capability and high cyclic stability, achieving an energy efficiency of 95%.
6	It remains reliable for a period extending from 1500 to 10000 h.	It has the capability to withstand cycles within the range of 150 to 1500 h.	It maintains excellent reliability even after 50000 h or an unlimited number of cycles.
7	The operating voltage of fuel cells is 0.6 V.	It can operate within the voltage range of 1.25 to 4.2 V.	It operates within a wide range, spanning from 2.3 to 2.75 V
8	Calculating specific capacitance in farads (F) is challenging.	The determination of capacitance is not applicable.	The capacitance falls within the range of 100 mF to 1500 F.
9	It is employed in the direct generation of electricity.	It is utilized for long extent backup.	It can serve as a short-term backup.

Above mentioned table findings signifies that supercapacitors can use in applications where rapid energy storage and release are vital, such as regenerative braking systems in vehicles, peak power saving in power plants, and smoothing power delivery in renewable energy systems [42,44]. Supercapacitors have an extended cycle span compared to batteries and fuel cells, making them appropriate for applications where frequent charge-discharge cycles are required without degradation. While batteries are better suited for storing large amounts of energy over longer periods and supercapacitors can provide bursts of power quickly. Supercapacitors can be used in conjunction with batteries to enhance total performance and efficiency, especially in hybrid energy storage systems.

1.4. Types of supercapacitors

Based on their charge storage techniques and the makeup of their electrodes, supercapacitors are often separated into three types: hybrid supercapacitors, electrochemical double layer capacitors (EDLCs), and pseudocapacitors [45]. The details of each kind of supercapacitor are as follows:

- **Electrochemical double layer capacitor (EDLC)**

In an EDLC, two electrodes are connected to current collectors and submerged in an electrolyte, with a separator in the center to allow for ion flow and prevent short-circuiting.

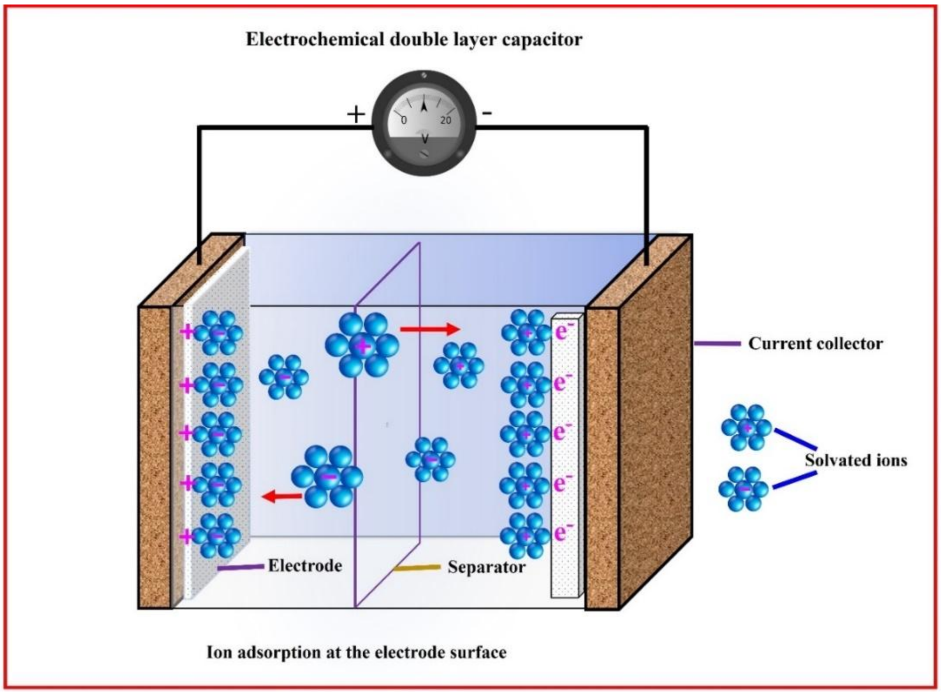

Figure 1.8. Charge storage process in electrical double layer capacitor (EDLC).

When a voltage is employed between the two electrodes, the charge is stored at the electrode-electrolyte junction due to the electrostatic force of attraction (as shown in Figure 1.8). Enhancing the electrode-specific surface area can increase the charge storage capacity. Due to the lack of faradaic charge transfer and the presence of ion adsorption (an electrostatic process), EDLCs have high PDs, quick charging and discharging times, and excellent cycle stabilities [46–48]. When a voltage is applied to an EDLC, charge is stored at the point of contact across the electrodes and electrolyte due to electrostatic attraction. An increase in the surface area of the electrodes may lead to a greater capacity for charge storage. Because ion adsorption process and faradaic charge transfer are present, a double layer forms at the electrode-electrolyte boundary throughout the charging procedure as electrons go from the positive electrode to the negative electrode and cations and anions move to the positive and negative electrodes, respectively. The capacitance of the EDLC is determined by the width of the double layer, and this process is reversed after discharging. The electrolyte concentration does not vary during the charge-discharge cycle because there is neither net ion exchange across the electrode and electrolyte nor charge transfer inside the electrode-electrolyte junction [49,50]. Indeed, while EDLCs offer numerous benefits, they do have some limitations. These include lower energy density, a restricted voltage range, and relatively limited specific capacitance [51]. However, these shortcomings have been addressed by pseudocapacitor supercapacitor devices.

➢ Pseudocapacitors

Pseudocapacitors have a charge storage process that relies on reversible oxidation-reduction reactions at or near the electrode surface, causing in higher capacitance and energy density compared to EDLCs (see Figure 1.9). Their capacitance is roughly 10-100 times greater than EDLCs and the charge storage varies linearly with charging potential, making it reliant on electron transmission as opposed to charge buildup in the double layer. The example of a nickel oxide pseudocapacitor's charge storing mechanism is shown in Figure 1.9. Usually, the oxidation state of nickel in nickel oxide (NiO) is +2.

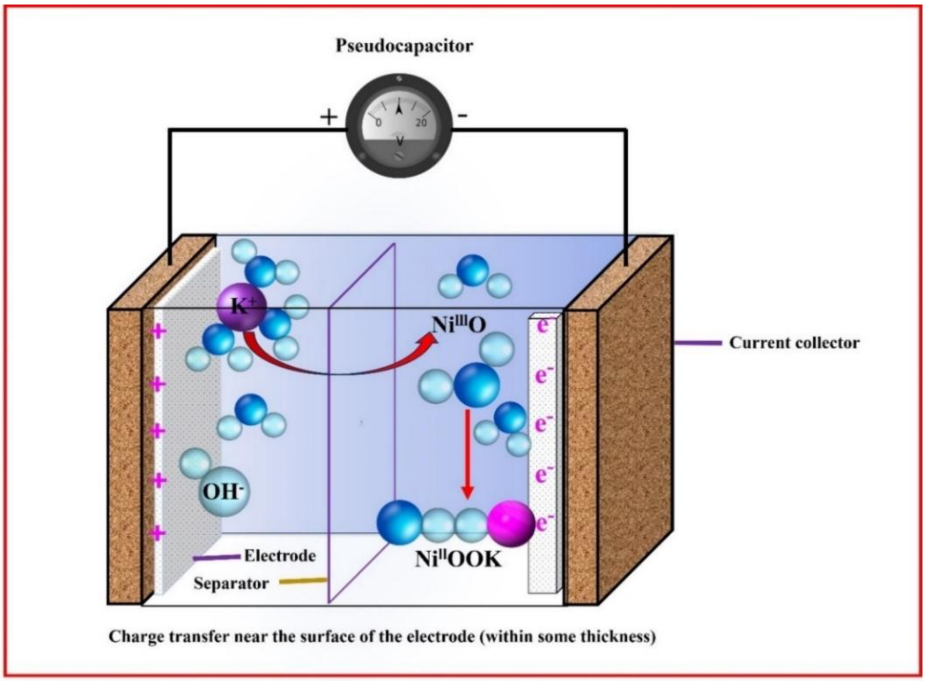

Figure 1.9. Example of nickel oxide pseudocapacitor mechanism in potassium hydroxide electrolyte (KOH).

During charging, KOH electrolyte ions interact with the nickel oxide, leading to the oxidation of nickel. This process often involves the loss of electrons to the electrolyte.

Consequently, the oxidation state of nickel increases, potentially reaching +3 in NiO electrodes. This change in oxidation state is crucial for NiO's effective charge storage [52]. During discharge, the reverse reaction occurs, returning nickel to its initial oxidation state and enabling the capacitor to release stored energy. It's also worth noting that pseudocapacitance coexists with double layer capacitance and different materials exhibit distinct faradaic mechanisms due to unique physical processes [53,54].

Furthermore, pseudocapacitors can be categorized into three main types [55,56].

(a) Underpotential deposition: Underpotential deposition (UPD) occurs when a monolayer of metal ions is formed above their redox potential at the surface of a different metal. This happens reversibly, as protons or metal ions adsorb onto the surface of the bulk electrolyte. The underpotential coating of lead (Pb) on a gold (Au) electrode is one illustration of this, as shown in Figure 1.10(a).

(b) Redox transitions: When ions are electrochemically adsorbed on or close to the surface of the electrode material, redox transitions take place, which are then followed by faradaic reactions, allowing pseudocapacitors to store energy. Electrode materials namely transition metal oxides, ruthenium oxide in its hydrous form (see Figure 1.10(b)), and conducting polymers, undergo reversible redox reactions and can be used in pseudocapacitors. Additionally, conducting polymers also demonstrate electrochemical doping-dedoping, which is the process of adding or eliminating electrons from the polymer through the function of an electric field. This enables the storage of energy in the form of electrical charge [57].

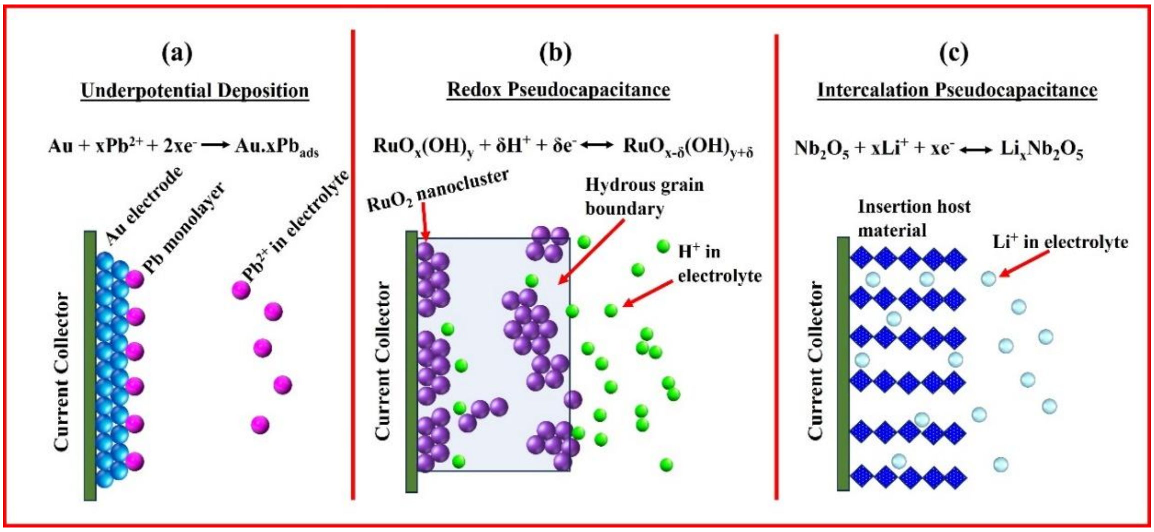

Figure 1.10. The electrodes in pseudocapacitors give rise to three distinct faradaic mechanisms, each dependent on the materials properties.

(c) Intercalation: Intercalation is a process in which ions penetrate through the layers or tunnels of a redox-active material, resulting in a faradaic transition without altering the material's crystallographic phase. An example of this is when lithium ions intercalate through the layers of Nb_2O_5 in a lithium electrolyte, as seen in Figure 1.10(c). Pseudocapacitors positively have higher capacity and ED contrasted to Electric Double-Layer Capacitors (EDLCs). However, their drawback lies in lower cycle stability, which can negotiate the overall performance and reliability of pseudocapacitors over extended usage periods. Nevertheless, these limitations have been addressed by hybrid supercapacitor devices.

➢ Hybrid Supercapacitors

Hybrid supercapacitors utilize mutually electrostatic and pseudocapacitive charge storage systems, which eliminates the limitations of each individual mechanism. This results in superior specific capacity and enhanced specific energy contrasted to traditional EDLCs. Additionally, these devices have excellent power density and cycle stability. Hybrid supercapacitors and their electrodes can be grouped into various categories depend on the materials employed for fabrication. One example is asymmetric hybrid supercapacitor electrode material, which is composed of one EDLC material and one pseudocapacitor material. In general, the negative and positive electrodes of asymmetric hybrids are made of carbon-based and pseudocapacitive materials, respectively [58,59]. Battery-type hybrid supercapacitor electrodes are composed of one battery electrode and one supercapacitor electrode. These hybrids address the requirements for both high PD and high ED. It can be achieved by combining a elevated ED battery-type electrode with an extreme PD supercapacitor electrode, resulting in rapid recharging times, exceptional power density, and improved cycle lifespan for the hybrid supercapacitors. The composite electrode, which combines conducting polymer, metal oxide, and carbon-based materials in one electrode, is another kind of hybrid electrode utilized in supercapacitors. The carbon-oriented materials offer an elevated surface area capacitive charge layer (electric double layer) that improves the electrolyte-pseudocapacitive material interface [60,61]. Further, the pseudocapacitive materials undergo faradaic reactions, which raise the capacitance of the composite electrode. The synergistic mechanism between carbon-based and pseudocapacitive materials improves the operational potential window, specific capacitance, corrosion stability, and cycle stability. Hybrid supercapacitors exhibit symmetric or asymmetric types based on their configuration.

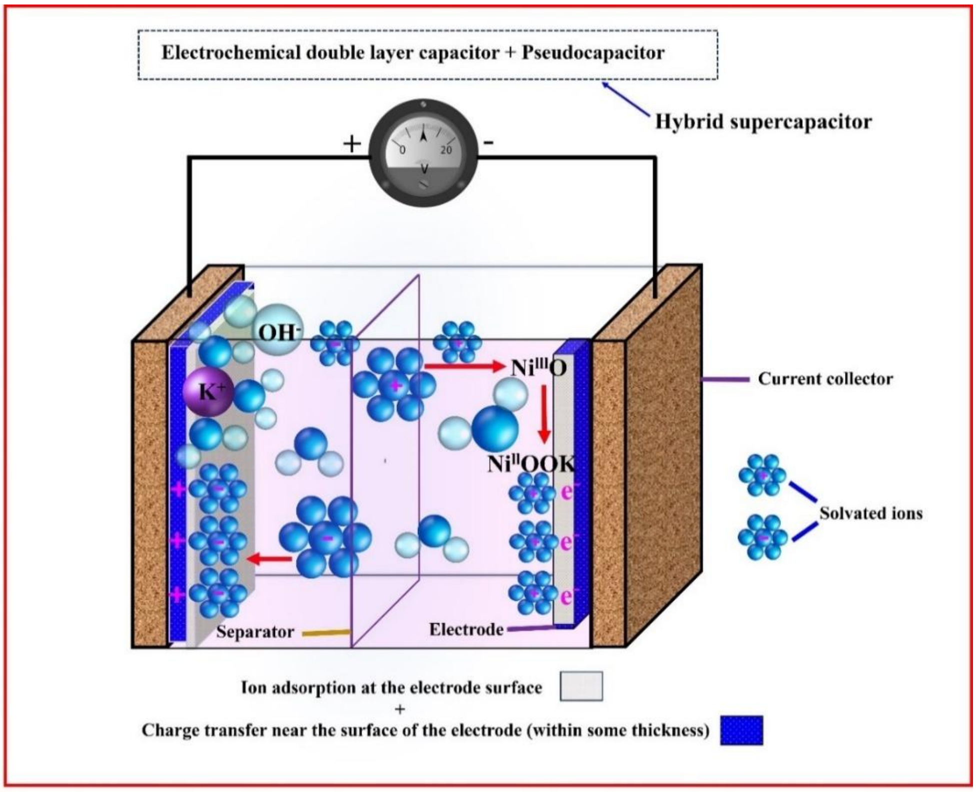

Figure 1.11. Generalized energy storage process in hybrid supercapacitors.

The electrodes of symmetric hybrid supercapacitors consist of two similar pseudocapacitive and EDLC materials. Asymmetric hybrid devices are made up of two electrodes of dissimilar materials, which achieve more energy and power densities than symmetric supercapacitors. However, symmetric supercapacitors are easier to fabricate and cost-effective. The characteristics of a symmetric supercapacitor can be obtained by considering a single electrode. Hybrid supercapacitors that utilize dissimilar materials for each electrode have a substantial impact on the overall properties of the device. The operational voltage of each electrode can limit the reflection of individual characteristics in the device behavior. In asymmetric designs, the electrochemical characteristics of the supercapacitor are determined by the overall device, rather than the individual electrodes. As an example, a combination of NiO, activated carbon, and conducting polymer can demonstrate dual charge storage mechanisms, encompassing both EDLC and pseudocapacitance. In this type, the redox reaction takes place via NiO within the KOH electrolyte (see Figure 1.11) and ion adsorption takes place via activated carbon. If we combine NiO, activated carbon, and conducting polymer, the charge storage mechanism will exhibit both EDLC (from the activated carbon) and pseudocapacitive properties (from the redox transitions of the conducting polymer and metal oxide) [62,63]. The components used to construct supercapacitors, such as electrode materials, current collector, electrolyte and separator are crucial for determining their performance in the real world. Each component of the supercapacitor is described individually as follows.

1.5. Different electrode materials used in supercapacitors

➢ Category I: Electric double layer electrode materials

Commercially, various carbon allotropes namely activated carbon, carbon blacks, carbon aerogels, graphene, and carbon nanotubes (CNT) show EDLC behavior (see Figure 1.12) and find its applications as electrode materials in supercapacitors [64,65].

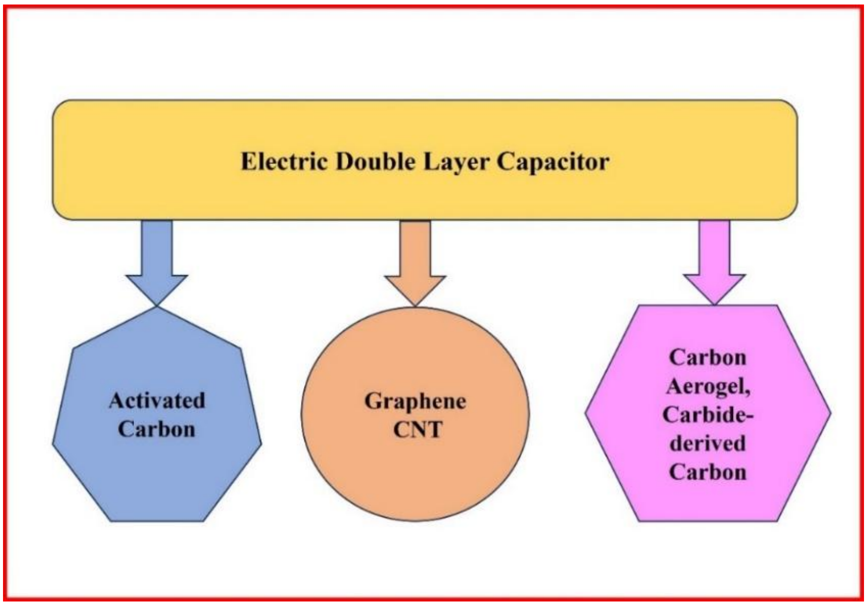

Figure 1.12. Various EDLC electrode materials.

These materials exhibit superior characteristics such as increased conductivity, elevated surface area, temperature stability, corrosion resistance, and porosity, all while maintaining a relatively low cost. Each type of EDLC electrode material is described individually as follows.

1. Graphene

Graphene is a 2D carbon allotrope that may be produced using a variety of techniques. It is distinguished by the hexagonal arrangement of carbon atoms. High electron mobility graphene is produced by mechanical exfoliation, and transparent, conductive graphene sheets are produced via ultrasonic exfoliation. Chemical processes like the reduction of graphite oxide, microwave-assisted reduction, and chemical vapor deposition are employed to produce ultrapure-grade graphene by splitting monolayer carbon. This remarkable material has widespread applications in various fields, including solar cells, light-emitting diodes (LEDs), and mobile touch screens [66].

2. Carbon Nano Tubes (CNT)

Carbon nanotubes (CNTs), an allotrope of carbon resembling a rolled-up unbroken mesh of graphene hexagons at the nanoscale, present in two forms: “Single-walled nanotubes (SWNT) and Multi-Walled Nanotubes (MWNT)” [67]. SWNTs, with an outer diameter of 3 nm, exhibit an energy bandgap in the range of 0-2 eV, displaying metallic or semiconducting properties. On the other hand, MWNTs consist of multiple concentric tubes with a 3.4 Å interlayer distance. CNT synthesis methods involve arc discharge, laser vaporization, and chemical vapor deposition. CNTs discover applications throughout a range of domains, such as sensors, hydrogen storage, solar cell construction, charge storage, and electrochemical capacitors [68].

3. Carbon aerogel

Carbon aerogels are fabricated through the pyrolysis of organic precursors in the existence of catalysts, exhibiting significant porosity, with 50% of pores measuring less than 100 nm [69]. These materials exhibit remarkable properties like density, extreme electrical conduction, and huge exterior area. Carbon-based materials are created via a variety of processes, such as chemical vapour, thermal, and electrochemical activation methods [70]. Carbon aerogels with fine porosity and enhanced surface area were successfully synthesized by Li et al. (2006), yielding a greater capacitance of 110.06 F/g [71].

4. Carbide-derived Carbon

Walter Mohun's extensive research in 1959 focused on the by-products generated during the high-temperature production of $SiCl_4$ [72]. Following this, from 1960 to 1980, Russian scientists adopted halogen treatment as a key method for synthesizing carbon aerogel (CDC). Various techniques, including chlorine treatment, vacuum processes, and hydrothermal decomposition, were utilized in the synthesis. A greater surface area, improved electrical conductivity, and higher porosity with micron-sized pores are some of the distinguishing characteristics of CDC. CDC is positioned as an extremely efficient electrode material for electric double layer capacitors (EDLC) because of these properties.

The interaction of the de-isolated ion in the electrolyte with the pores has a vital function in improving charge screening and confinement, thereby minimizing resistance loss and enhancing capacitance. In aqueous electrolytes, CDC demonstrates a 190 F/g capacitance, while in organic electrolytes, it reaches around 180 F/g [73].

5. Activated Carbon

Activated carbon, obtained as a by-product (ash) through the coal pyrolysis process, is a cost-effective form of carbon with an extremely porous organization and a substantial surface area of approximately 300 m^2/g [74]. This variant is known for its versatility and finds applications in a diverse range of fields including industry, medicine, environmental management, agriculture, alcoholic beverage purification, fuel preservation, gas purification, chemical processes, and mercury scrubbing [75]. The fabrication of activated carbon can be done via physical activation or chemical activation methods [76].

➢ Category II: Pseudocapacitor Electrode Materials

Pseudocapacitor electrode materials possessing the ability to facilitate rapid and reversible redox reactions, along with a substantial capacitance contrasted to carbon-composed materials, are identified as pseudocapacitive electrode materials. Specifically, conducting polymers and metal oxides are considered excellent contenders for energy storage technologies. Among the array of metal oxides, widely utilized supercapacitor electrode materials are RuO_2, MnO_2, CoO_2, V_2O_5, NiO, and bismuth-based oxides, recognized for their high specific capacitance and small resistance [77]. Pseudocapacitor electrode materials namely metal oxides and conducting polymers are described individually as follows.

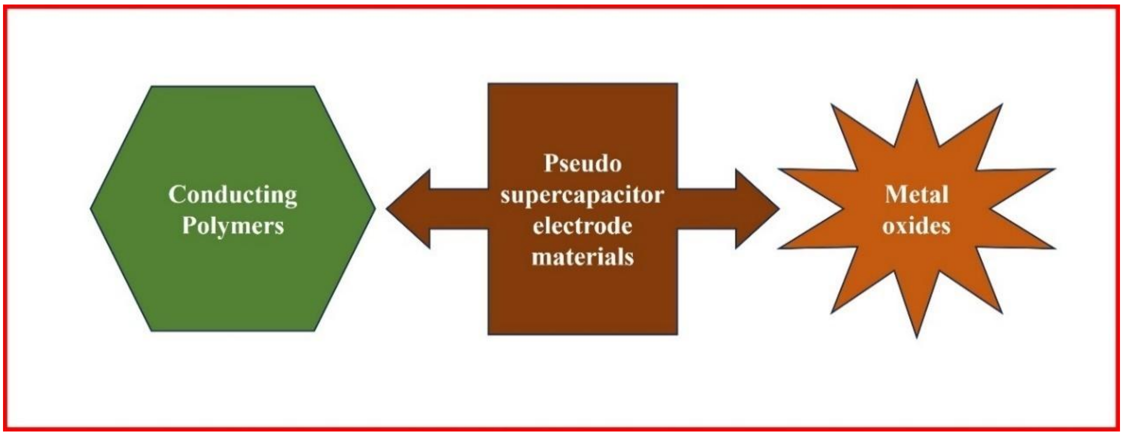

Figure 1.13. Different kinds of Pseudocapacitor electrode materials.

1. Metal oxide as electrode materials

It is commonly acknowledged that one of the utmost effective electrode materials for pseudo capacitors is ruthenium metal oxide (RuO_2). In an aqueous electrolyte, RuO_2 displays a capacitance that ranges from 270 to 350 F/g with a maximum current density of 400 mA/cm^3 [78]. This material demonstrates high capacitance, particularly in acidic electrolytes. In the charging and discharging duration, a redox reaction occurs, contributing to its electrochemical performance. RuO_2 also exhibits favorable characteristics, including low equivalent series resistance, elevated power, energy density, excellent cyclic stability, reversibility, and conductivity [79]. When sulphuric acid is used as the electrolyte, RuO_2 is stated to have a maximum capacitance of 750 F/g [80]. But, with the known expensive nature of RuO_2, it is crucial to keep this cost factor in mind when considering it for application. So, researchers are actively exploring alternative metal oxide materials to overcome this hurdle. Recently researchers have explored some alternative metal oxide electrode materials such as manganese oxide (MnO_2), cobalt oxide (CoO_2), nickel oxide (NiO), vanadium pentoxide (V_2O_5), and bismuth oxychloride (BiOCl) [81-83]. Among these metal oxides, V_2O_5 and BiOCl are gaining extensive attention due to their standout characteristics: superior theoretical capacitance, larger conductivity, excellent cycle stability, and wide potential window. These unique properties make them prime contenders in diverse energy-related endeavors such as batteries, solar cells, and supercapacitors [84,85].

(a) Vanadium Pentoxide (V_2O_5)

Vanadium pentoxide (V_2O_5) and its composite materials are getting the attention of researchers for their potential in cutting-edge technologies. V_2O_5 is abundant, affordable, and environmentally friendly, making it a very attractive choice. Both the bulk form and thin films of V_2O_5 have interesting physical and chemical features that can be used for many practical applications. These include batteries, energy-saving windows, light switches, solar panels for roofs, and rear-view mirrors [86]. They are appropriate for use in multicolour electrochromic devices due to their presentation of photochromic and electrochromic capabilities [87]. Vanadium oxides represent a category of transition metal oxides characterized by vanadium oxidation states typically spanning from +2 to +5. It holds considerable significance in technological applications due to its unique properties. These oxides exhibit distinct characteristics based on their compositions, including electrical, optical, and chemical properties, setting them apart from other transition metal oxides and finding utility across various fields. Primarily known as low-mobility semiconductors with predominantly n-type conductivity, thin films of vanadium oxides exhibit enhanced physicochemical properties at lower thicknesses. Vanadium pentoxide, for instance, serves as an excellent cathode material, accommodating Li ions within its tetrahedral sites, facilitating their insertion and deinsertion. This phenomenon, termed electrochromism, manifests as a color change during the intercalation mechanism of cations [88].

Moreover, vanadium oxides undergo transitions in their electrical behavior when exposed to temperature variations, shifting from insulator to semiconductor to metallic states [89]. They also demonstrate thermochromic behavior, altering color in response to temperature changes, thereby affecting optical transmittance, reflectance, and emissivity. Gasochromism, wherein the oxides change color upon exposure to organic gases, enables applications in gas sensing, particularly for detecting hydrogen in organic environments [90]. Beyond its role in sensing applications, vanadium pentoxide serves as a catalyst in various chemical reactions, such as the contact process for sulfuric acid production. Additionally, in thin film form, it enhances oxygenated dehydrogenation reactions. These oxides exhibit versatility in sensing oxygen levels, pH, and infrared radiation, with their conductivity varying between p-type and n-type depending on substrate and temperature conditions [91].

Vanadium oxides possess a remarkable variety, with more than 15 distinct stable phases found in their binary system with oxygen. These phases showcase vanadium in various oxidation states, including the well-known V^{2+} (VO), V^{3+} (V_2O_3), V^{4+} (VO_2), and the highest achievable state, V^{5+} (V_2O_5). Interestingly, intermediate phases like V_4O_9, V_6O_{13}, and V_3O_7 bridge the gap between V_2O_5 and VO_2. The intermediate phases between VO_2 and V_2O_3 are termed as Magneli phases. Another set of possible phases are V_nO_{2n}, where n=2 [92-94]. In the composition range from VO to V_2O_5 in the vanadium-oxygen system, the phase relationship is illustrated by the diagram (see Figure 1.14(a)) [95-97]. Figure 1.14(a) shows the equilibrium oxygen pressures over different vanadium oxide phases as a function of temperature. These phases, characterized by varying compositions, were observed to coexist at different temperature ranges [98]. Among the different phases vanadium pentoxide (V_2O_5), is the most stable vanadium oxide. Vanadium oxide V_2O_5 crystallizes in an orthorhombic unit cell structure within the P_{mmn} space group. Its lattice parameters are characterized by a = 11.510 Å, b = 3.563 Å, and c = 4.369 Å. Notably, the b and c dimensions are frequently interchanged [99]. Within this structure, vanadium atoms are surrounded (enveloped) by oxygen atoms, forming distorted trigonal bipyramidal shapes (see Figure 1.14(b)).

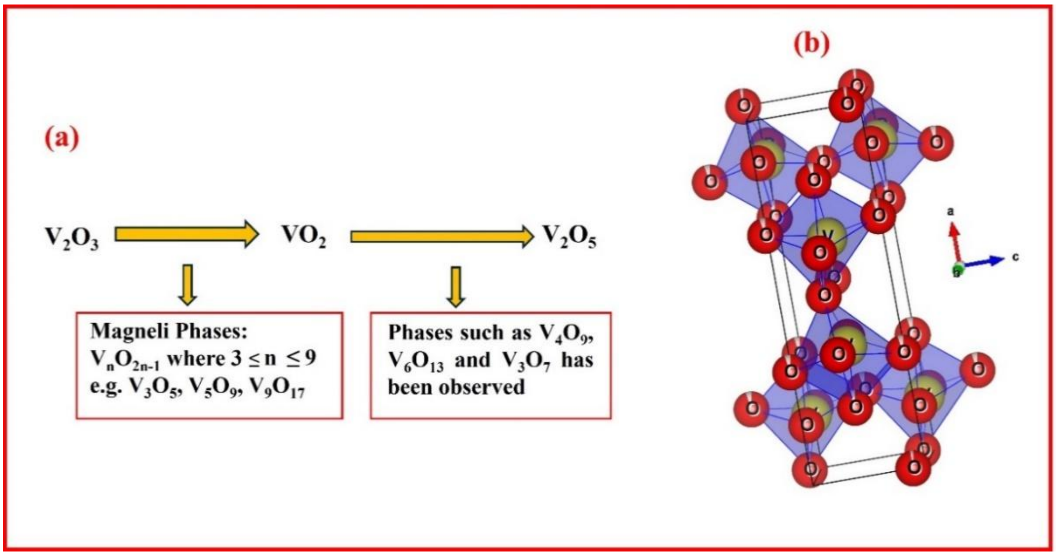

Figure 1.14. (a) Oxidation States of Vanadium Oxide (Including major and intermediate forms) (b) Orthorhombic unit cell crystal structure of V_2O_5.

This distorted trigonal bipyramidal structure creates a larger surface area for the vanadium atoms compared to a simpler arrangement. With a larger surface area, more vanadium atoms are available to participate in the chemical reactions at the electrode-electrolyte junction. In addition, the distorted shape might also influence the electronic properties of vanadium atoms, making them more reactive. This can improve the rate and efficiency of the chemical reactions crucial for storing and releasing energy in pseudocapacitors [100]. In this favor, ***Liang et al. (2024)*** reported a study on vanadium oxide enriched with oxygen vacancies, synthesized through a solvothermal approach followed by heat treatment. This material showcased an impressive rate performance, achieving 411.98 mAh/g, along with exceptional cycling lifespan, retaining 92.8% capacity after 1500 cycles. The improved electrochemical characteristics of the vanadium oxide are ascribed to an increased presence of oxygen vacancies. These vacancies offer additional active sites for zinc-ion storage, expand layer spacing, and enhance the conductivity of vanadium pentoxide [101]. ***Ingole et al. (2024)*** detailed the fabrication of hierarchically structured nanoporous vanadium pentoxide transparent material, grown on a fluorine-doped tin oxide substrate. The structural examination confirmed the formation of a pure orthorhombic structure for the vanadium pentoxide, while microscopy images depicted a well-organized three-dimensional spongy-like porous architecture. The deposition method, employing automatic spray pyrolysis, demonstrated exceptional conformality, enabling the fabrication of high-aspect-ratio three-dimensional structured nanoporous vanadium pentoxide electrodes tailored for advanced supercapacitor applications [102]. In addition, ***Pullanchiyodan et al. (2023)*** demonstrated the construction of an asymmetric supercapacitor device utilizing a two-dimensional transition metal dichalcogenide (molybdenum disulfide) as the negative electrode and a transition metal oxide (vanadium pentoxide) as the positive electrode. Electrochemical and galvanostatic charge-discharge analyses were conducted on both the positive vanadium pentoxide and negative molybdenum sulfide electrodes in a three-electrode setup. The results indicated stable operating potentials of -0.9 V and 1.0 V for molybdenum sulfides and vanadium pentoxide electrodes, respectively. By combining these positive and negative electrodes with an aqueous electrolyte containing 1 M sodium sulphate, an asymmetric device with a broad functioning potential of 2.0 V was created [103].

V_2O_5's structure and conductivity make it an excellent electrode material for pseudocapacitors overall. Pseudocapacitors use reversible chemical reactions instead of the physical separation of charges that ordinary capacitors use to store energy. In V_2O_5 electrodes, these reactions involve ions from the electrolyte interacting with the oxide surface and injecting charge. This process is similar to batteries but with less extreme voltage changes. V_2O_5 is an appealing metal oxide due to its capability to exhibit several oxidation states. These multiple oxidation states provide more opportunities for charge storage reactions to arise within a pseudocapacitor [104].

(b) Bismuth oxychloride (BiOCl)

The use of bismuth-based oxide materials has increased significantly, as has attention paid to them in a number of applications, such as photocatalytic materials, gas sensors, energy storage devices, and catalysts. Their non-toxic properties and affordability, together with their noteworthy qualities including high oxygen content, excellent conductivity, and dielectric behaviour, are the main reasons for their popularity. Furthermore, because bismuth-based compounds react redoxibly in aqueous electrolytes throughout the -1–0 V potential limit, they have the potential to function as negative electrodes [105]. Numerous researchers have documented the use of bismuth oxides and hydroxides as pseudocapacitors in the context of supercapacitor applications. The electrodeposition approach was utilized for the synthesis of a composite material consisting of bismuth oxide adorned with titania nanotube arrays. Investigations were conducted into how the morphology of the bismuth oxide state was affected by deposition parameters, such as current density and time. The capacitance that was obtained at the greatest level was 430 mF/cm^2 [106]. Among the family of bismuth-based oxides, BiOCl as electrode material shows its influence due to its unique combination of properties and versatile functionality [107]. Bismuth oxychloride possesses a unique crystal structure with lattice parameters a=b= 3.890 Å, c= 7.370 Å (see Figure 1.15). Within the crystal structure, each bismuth (Bi) atom serves as a central point, bonded to four oxygen (O) atoms and four halogen (Cl) atoms, forming a distinctive ten-sided shape known as a decahedron. Notably, these eight bonded atoms can be viewed as composing two square faces, with each containing two oxygen and two chlorine atoms.

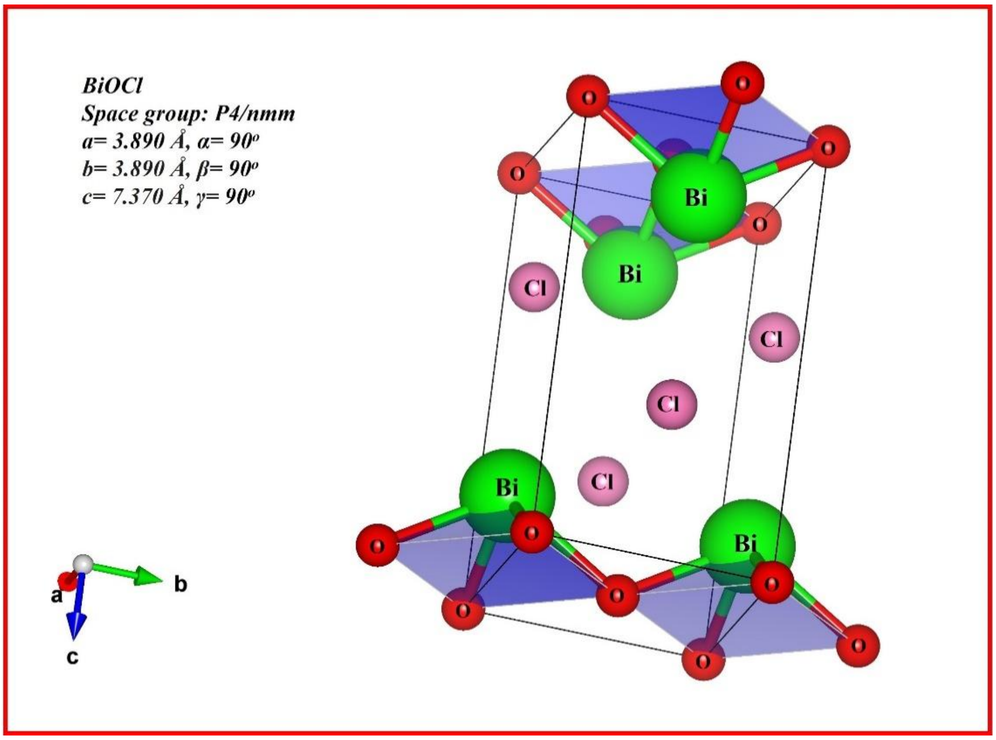

Figure 1.15. Crystal structure of BiOCl.

Positively charged sheets, comprising two bismuth atoms and three oxygen atoms $[Bi_2O_3]^{2+}$, are positioned between double layers of negatively charged chlorine ions (Cl^-), resulting in the establishment of the BiOCl layer [108]. This unique arrangement develops into a tetragonal crystal system, characterized by a square base for the unit cell replicating the entire structure. The stacking of these layers along a specific direction (c-axis) defines the overall structure. The internal layers of BiOCl are bound by strong covalent bonds, but their interaction between layers depends on weaker van der Waals forces. It allows flexibility within the crystal structure, this layered configuration enhances BiOCl's suitability for energy storage systems. Because its structure offers ample active sites for ion insertion and extraction through the charging and discharging phases in electrochemical energy storage systems [109].

BiOCl has the potential for various energy storage technological applications, spanning from rechargeable batteries to supercapacitors and electrochemical capacitors. In lithium-ion batteries, BiOCl can be utilized as a negative electrode material, offering high capacities and improved cycling lifespan compared to conventional graphite-based anodes. Its redox-active nature and favorable electrochemical properties make it a viable candidate for next-generation lithium-ion battery technologies, contributing to elevated EDs and longer cycle life [110]. BiOCl-based electrodes can also be utilized in supercapacitors to store electrical energy via rapid faradaic redox reactions. Among the notable new developments in electrode materials is BiOCl, which exhibits an excellent 90.3% cycle lifespan along with an extreme capacitance value of 1242 F/g at 1 A/g current density. A capacitance of 124 F/g was obtained in the setting of an asymmetric cell with the configuration BiOCl/activated carbon, retaining an amazing 82% retention even after experiencing 3000 cycles [111]. BiOCl's increased specific surface area and conductivity lead to improved cycling stability, power density, and capacitance, making it a suitable material for higher-performance supercapacitor devices used in energy delivery and storage systems. Moreover, BiOCl can be integrated into electrochemical capacitors (ECs) or pseudocapacitors, where it functions as both an electrode and an electrolyte material. The reversible redox reactions of bismuth and oxygen species allow effective charge storage, leading to high energy densities and long cycle life in EC-based energy storage systems. Given the abundance of sodium resources and the growing interest in sodium-ion battery technology, BiOCl shows capability as an electrode material in sodium-ion batteries [112]. Its electrochemical characteristics can be tailored for the storage of sodium, providing a more environmentally friendly option for energy storage than lithium-based systems. It can also help to further the development of sodium-ion battery technologies for use in grid-scale energy storage applications.

In the present research work, V_2O_5 and BiOCl have been specifically chosen among various metal oxides because the selection of electrode materials involves careful consideration of multiple factors, including synthesis method, cost, production efficiency, as well as chemical and electrochemical stability. To address these considerations, an approach prioritizing ease, cost-effectiveness, and convenience in the preparation of V_2O_5 and BiOCl was chosen. Sol-gel and solvothermal methods were employed to synthesize these materials, with solvothermal methods enabling the generation of diverse morphologies for BiOCl. The resulting nanoparticles exhibit favorable characteristics, such as high chemical, and electrochemical stability. This strategic selection and preparation methodology enhances the overall suitability of V_2O_5 and BiOCl as electrode materials for supercapacitor applications.

2. Conducting polymers

These materials, predominantly utilized in pseudo-capacitor electrode components, are valued for their swift and reversible oxidation/reduction processes as well as their commendable electrical conductivity. The commonly utilized conducting polymers encompass polyaniline, polypyrrole, and polythiophene. The synthesis of these polymers can be carried out using chemical or electrochemical methods.

(a) Polyaniline (PANI)

Polyaniline (PANI) is an outstanding conducting polymer that has gathered significant attention for its diverse applications in electronics, sensors, energy storage, and corrosion protection [113]. Its unique properties stem from its distinctive chemical structure, characterized by the repetitive arrangement of aniline monomers as shown in Figure 1.16. At its core, polyaniline consists of a chain-like structure composed of aniline units. Aniline ($C_6H_5NH_2$) is an aromatic amine compound with a benzene ring and an amino group ($-NH_2$) attached. In the polymerization process, multiple aniline molecules undergo oxidative coupling reactions, forming covalent bonds between their aromatic rings. The "delocalization of π-electrons" along the polymer chain allows for efficient charge transport, enabling PANI to conduct electricity [114]. This conductivity can be further enhanced by doping, a process in which additional molecules, ions, or groups are introduced into the polymer matrix to modify its electronic properties.

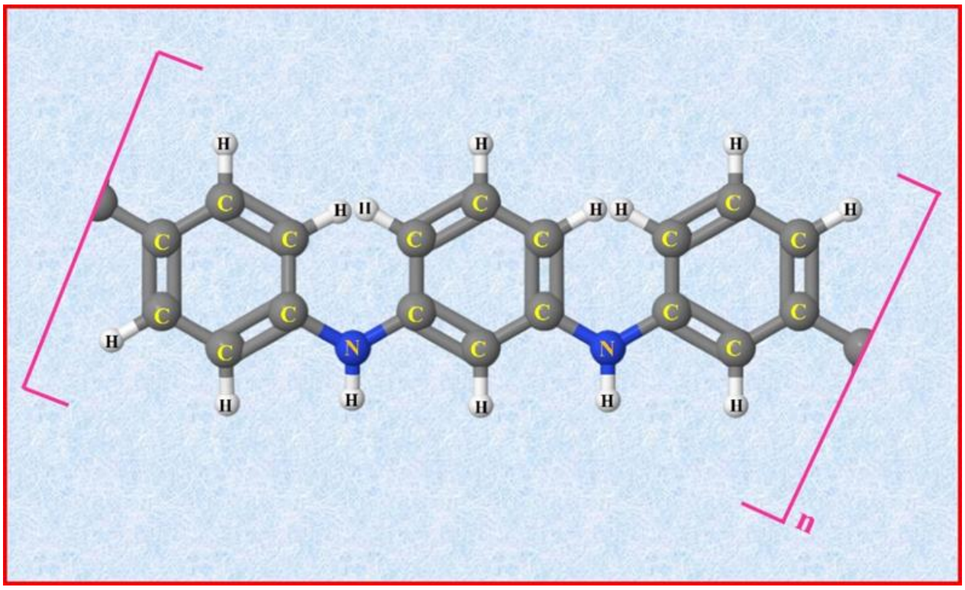

Figure 1.16. Chemical structure of Polyaniline (PANI).

Doping introduces charge carriers into the polymer, increasing its conductivity. Common dopants for PANI include acids such as hydrochloric acid (HCl) or camphorsulfonic acid (CSA), which protonate the nitrogen atoms in the polymer backbone. In addition to its electrical conductivity, polyaniline exhibits intriguing redox properties. It can undergo reversible oxidation and reduction reactions, switching between different oxidation states. The most common forms of PANI include the fully oxidized emeraldine salt and the partially reduced emeraldine base. The oxidation state of PANI influences its color, with the emeraldine salt appearing dark blue or green and the emeraldine base exhibiting a reddish-orange. This tunability of color and conductivity makes PANI an attractive material for various applications, including electrochromic devices and chemical sensors [115].

PANI is an admired material for supercapacitor devices that store energy electrochemically. Unlike other conducting polymers, PANI utilizes its entire volume for charge storage, leading to high capacitances (up to 950 F/g) [116]. It functions through redox reactions, changing oxidation states as it stores and releases energy. However, PANI has drawbacks. The charging and discharging process (doping/dedoping) causes the polymer to swell, shrink, and crack, reducing its lifespan (cycle stability). Additionally, PANI can degrade at high voltages, limiting its operating range. To address these limitations, researchers are creating composite electrodes that combine PANI with other materials namely graphene, metal oxides, carbon nanotubes, etc. A recent study by ***Yan et al. (2010)*** demonstrated a successful approach using a simple chemical method for PANI-based graphene oxide-carbon nanotube composite. The fabricated composite electrode achieved exceptional capacitance (1035 F/g) and impressive stability (only 6% capacitance loss after 1000 cycles) [117]. Similar to this, ***Ahmad et al***. (2021) investigated the use of a polyaniline/copper oxide nanocomposite in supercapacitors. At 0.5 mA/cm^2, the created nanocomposite demonstrated an areal capacitance of 169 F/cm^2 and a maximum capacitance of 486.9 F/g. The superior function of the nanocomposite electrode was linked to its low solution resistance and charge-transfer resistance, as evidenced by electrical impedance spectroscopy [118].

In conclusion, PANI offers high capacitance and efficient charge storage mechanisms, but its practical application is hindered by issues of mechanical stability and voltage limitations. Through innovative composite strategies, such as those integrating graphene, metal oxides, and carbon nanotubes, researchers are making significant steps toward overcoming these challenges, paving the way for improved supercapacitor devices with enhanced performance and longevity in various applications.

(b) Polypyrrole (PPy)

Polypyrrole (PPy) also stands as a cornerstone in the domain of conducting polymers, owing to its remarkable electrical conductivity, facile synthesis, and versatile applications across various fields such as electronics, sensors, energy storage, and biomedicine [119]. Polypyrrole possesses a distinctive chemical structure that forms the basis of its fascinating properties and varied functionalities. The chemical structure of polypyrrole is emblematic of its monomeric unit, pyrrole. Pyrrole, a five-membered aromatic heterocycle, serves as the fundamental building block in the polymerization of polypyrrole. The polymerization process involves the oxidative coupling of pyrrole monomers, leading to the formation of a polymer chain with a conjugated π-electron system. In its pristine form, polypyrrole consists of a linear chain of pyrrole units interconnected through carbon-carbon (C-C) bonds, resulting in a polymeric backbone characterized by alternating single and double bonds. Structurally, each pyrrole monomer comprises a pyrrole ring with four carbon atoms and one nitrogen atom. The carbon atoms form the framework of the ring (see Figure 1.17), while the nitrogen atom contributes to the aromaticity of the system, enhancing its stability and conjugation.

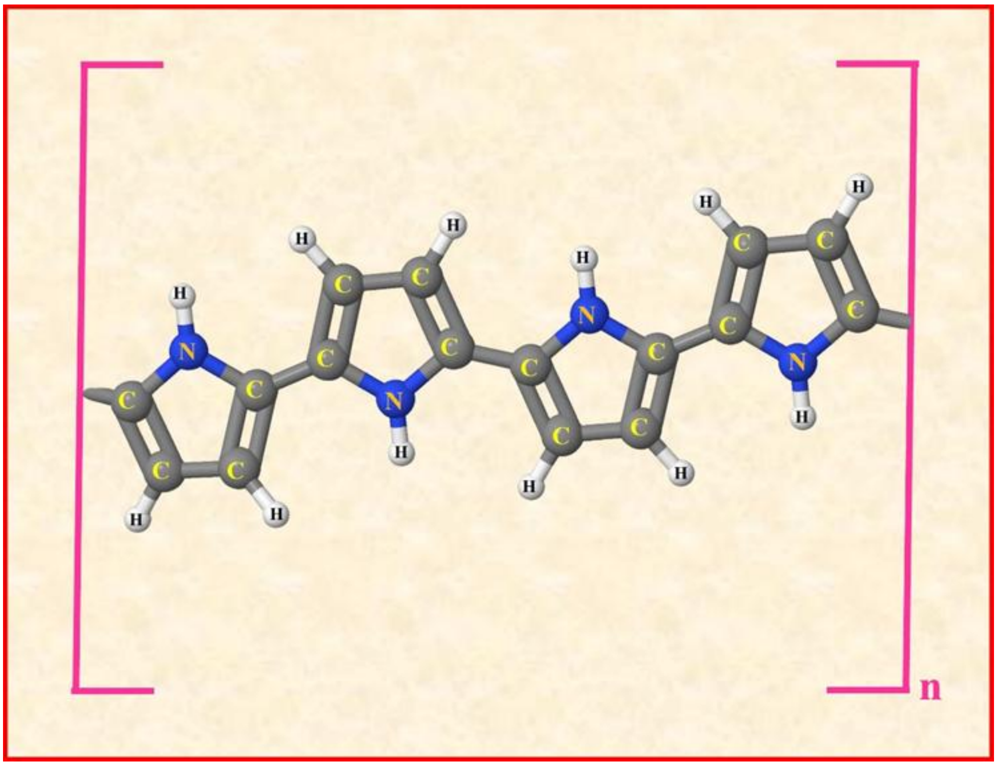

Figure 1.17. Chemical structure of polypyrrole (PPy).

The presence of delocalized π-electrons within the pyrrole ring imparts conductivity to the polymer chain, facilitating the efficient transport of charge carriers along its backbone. This inherent conductivity is a hallmark feature of polypyrrole and renders it suitable for various electronic and electrochemical applications [120]. The chemical structure of polypyrrole is not limited to its pristine form but can be modulated and tailored to accommodate specific requirements through doping and functionalization. Doping implies the inclusion of dopant molecules or ions into the polymer matrix, which induces changes in its electronic properties and enhances its performance. Common dopants for polypyrrole include inorganic ions (e.g., Cl^-, Br^-, I^-) and organic molecules (e.g., polystyrene sulfonate), which interact with the polymer chain via electrostatic interactions or charge transfer processes [121]. Furthermore, the chemical structure of polypyrrole can be modified through functionalization, wherein chemical groups or moieties are attached to the polymer backbone to introduce desired functionalities or improve compatibility with other materials. Functionalization strategies encompass methods such as grafting, polymerization of pyrrole derivatives, and post-polymerization modification. These approaches enable the incorporation of specific functional groups (e.g., hydroxyl, carboxyl, amino) or biomolecules (e.g., DNA, proteins) into the polymer structure, broadening its scope of uses in areas such as biosensing, drug delivery, and tissue engineering.

For the creation of electrodes, PPy is a polymeric material that has been extensively researched. It is prized for its remarkable qualities, which include high conductivity, quick charge/discharge rates, significant energy density, ease of synthesis, dense mass, flexibility, and affordability [122]. PPy exhibits a notably high volumetric specific capacitance (400–500 F/cm^3) and flexibility, allowing it to be molded into various shapes without compromising its electrochemical performance [123]. Researchers have demonstrated the excellent flexibility of PPy-based supercapacitors with hydrogel electrolytes, maintaining strong electrochemical performance [124]. Consequently, PPy finds applications in manufacturing flexible, highly capacitive, and lightweight supercapacitors, as well as flexible electronic devices like wristwatches, roll-up displays, smartphones, wearable sensors, smart textiles, and more. This has sparked considerable interest among researchers for future energy storage and electronic applications [125]. However, two main challenges hinder PPy's wider application in high-performance supercapacitors: i) the disparity between theoretical capacitance predictions and practical values, and ii) reduced cycling lifespan during long-term charge-discharge processes, a common issue for most conducting polymers. To address these challenges, several effective strategies have been developed: i) synthesizing PPy with tailored morphology and/or structure, ii) fabricating various PPy composites with carbon materials or metal oxides, and iii) designing novel configurations for PPy-based supercapacitors [126]. These strategies aim to optimize PPy's capacitance while significantly enhancing its cycling stability, covering the tactic for its broader utilization in advanced energy storage systems.

(c) Polythiophene (Pth)

Polythiophene, recognized for its semiconducting properties, exhibits exceptional mechanical stability, optical transparency, thermal resilience, and electrical stability, coupled with a notable bandgap energy [127]. Its application in solar cells is attributed to its ability to seamlessly integrate with metal electrodes and its overall stability [128]. When polythiophene is doped with n-type semiconductor materials, it establishes a unique hybrid with exceptional electrical and optical properties. The presence of double bonds in the Pth structure enhances its conductivity, facilitating the generation of polarons and bipolarons through redox processes. This unique feature makes it a versatile material suitable for use in polymer batteries, electrochromic devices, and solar cells [129]. ***Laforgue et al. (1999)*** synthesized polythiophene using a chemical approach, resulting in an active material with a large capacity of 40 mA h/g and exceptional cycle stability, maintaining capacity over 500 cycles [130]. Supercapacitors constructed with these prepared polythiophene-based electrodes demonstrated a specific capacity of 260 F/g at a current density of 2.5 mA/cm^2. In summary, the electrochemical activity of polythiophene as a supercapacitor electrode material is influenced by circumstances such as fabrication approach, substrate, and morphology. Polythiophene shows potential for supercapacitors, yet it still faces limitations. Despite advances enhancing its performance, it lags behind materials such as polyaniline and polypyrrole in critical aspects. Polythiophene-based supercapacitors suffer from rapid power density loss and lower overall capacitance. Overcoming these challenges requires continued development to achieve competitiveness with alternative options [131].

In the present research work, polyaniline (PANI) and polypyrrole (PPy) were selected as electrode materials within the domain of conducting polymers because they exhibit the following unique properties that are pivotal for the present study [132-136].

- **High Electrical Conductivity:** Both PANI and PPy exhibit a noteworthy level of electrical conductivity compared to their counterparts. This characteristic is paramount for facilitating efficient charge transport and overall conductivity within electrode applications, encompassing batteries, supercapacitors, and sensors.

- **Superior Processability:** PANI and PPy are renowned for their straightforward synthesis and processing capabilities. They can be meticulously crafted into thin films or coatings using established methods like chemical oxidation, electrodeposition, or solution casting. This inherent versatility in processing empowers the precise tailoring of their morphology and structure to flawlessly align with the specific prerequisites of experimental design.
- **Robust Environmental Stability:** PANI and PPy demonstrate a commendable degree of resilience against environmental factors such as oxidation and degradation. This stability is a crucial trait for applications where electrodes are susceptible to exposure to fluctuating conditions over extended durations. It guarantees long-term performance and unwavering reliability.
- **Doping Versatility:** Both polymers possess the remarkable ability to undergo doping with a variety of dopants (e.g., acids for PANI, dopant ions for PPy). This process significantly modifies their electrical, chemical, and structural properties. This versatility empowers the optimization of the electrodes for targeted functions, such as augmenting charge storage capacity in energy storage devices or refining sensitivity in sensors.
- **Applicability in Diverse Fields:** PANI and PPy boast extensive utilization across various applications, including batteries, supercapacitors, sensors, corrosion protection coatings, and more. Their compelling conductivity, processability, stability, and doping versatility render them ideal candidates for the present research objectives outlined in this thesis.

By possessing this exceptional confluence of properties, PANI and PPy stand out as the optimal choice for the electrode materials employed within this research endeavor.

Category III: Hybrid Electrode Materials

Hybrid supercapacitor electrode materials are categorized into two main types: asymmetric and composite electrode materials (see Figure 1.18). As for asymmetric hybrid supercapacitors, they incorporate both EDLC and pseudocapacitive electrode materials, allowing for an arrangement of faradaic and non-faradaic storage mechanisms.

Typically, carbon-based materials are employed in the negative electrode, while pseudo-active materials are used in the positive electrode.

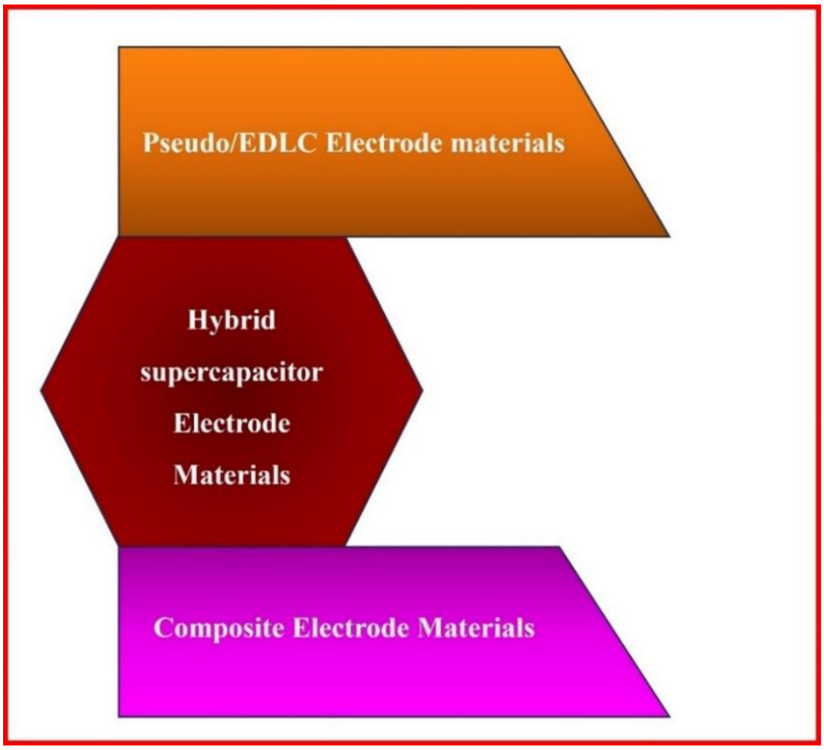

Figure 1.18. Types of hybrid electrode materials.

This configuration results in an asymmetrical hybrid supercapacitor that exhibits superior energy density and power density compared to EDLC, as well as enhanced cyclic lifespan compared to pseudocapacitors [137]. In composite electrodes, an interaction is achieved by integrating carbon-dependent components with either metal oxides or conducting polymers. This combination allows for the simultaneous occurrence of mutually physical and chemical charge storage processes within a singular electrode. The incorporation of faradaic reactions serves to amplify the capacitance of pseudoactive components [138].

1. Pseudo/EDLC electrode materials

Pseudocapacitive materials are mixed with carbon-based materials including graphene, carbon nanotubes, and activated carbon to provide a wide range of pseudo/EDLC electrode materials. Examples of pseudocapacitive materials include “transition metal oxides like ruthenium oxide, manganese oxide, and vanadium oxide, as well as conducting polymers such as PANI and PPy” [139]. These materials synergistically enhance electrode performance by facilitating additional redox reactions, thereby boosting overall capacitance and efficiency in Pseudo/EDLC systems.

2. Composite electrode materials

Materials become composite when two substances are mixed in a manner that renders them permanently inseparable. Carbon-based materials support charge transfer, enabling double-layer charge storage through their large surface area. Better energy and power densities in the composite materials are the result of this enlargement of the interface between capacitive components and electrolytes [140]. The prospect of combining carbon-based materials with conducting polymers is particularly encouraging, as it enables the mixing of the two most cost-effective materials, resulting in significant stable pseudocapacitance. As an example, ***Ren et al. (2015)*** formed a composite electrode of molybdenum disulfide/polyaniline (MoS_2/PANI) with activated carbon, resulting in outstanding stable electrochemical performance, showcasing high energy density and power density [141].

In the present research work, the focus is on utilizing V_2O_5-PANI and PPy/BiOCl nanocomposites as electrode materials for supercapacitors. This choice is significant for several reasons [142-145]:

1. **Enhanced Capacitance**: V_2O_5-PANI and PPy-BiOCl nanocomposites combine the high capacitance of pseudocapacitive materials (such as V_2O_5 and BiOCl) with the strong conductivity and stability of polymers (PANI and PPy). This combination results in electrodes that can store a larger amount of charge compared to individual component forms.
2. **Improved Cycling Stability**: Supercapacitors require materials that can withstand numerous charge-discharge cycles without significant degradation. Both V_2O_5 and BiOCl are known for their stability in electrochemical processes, while PANI and PPy contribute to mechanical robustness and structural integrity. This ensures that the nanocomposite electrodes maintain their performance over extended operational lifetimes.
3. **Facilitated Charge Transfer**: The nanoscale architecture of these composites facilitates rapid electron and ion transport, crucial for achieving high power densities in supercapacitors. This attribute is essential for applications requiring quick charge and discharge cycles.
4. **Environmental Friendliness**: Utilizing materials like V_2O_5 and BiOCl reduces reliance on rare or toxic elements, aligning with sustainable development goals.

Additionally, polymers such as PANI and PPy are often synthesized from readily available and environmentally benign precursors.

5. **Versatility in Applications**: The versatility of V_2O_5-PANI and PPy-BiOCl nanocomposites allows for their potential application in various fields beyond supercapacitors, including sensors, UV shielding, actuators, and energy storage systems.

All things considered, the selection of V_2O_5-PANI and PPy-BiOCl nanocomposites as supercapacitor electrode materials reflects a calculated mixture of electrochemical performance, stability, and environmental sustainability, making them viable options for developing energy storage systems. In addition to their promising electrochemical properties for supercapacitor applications, this thesis delves into the optical applications of V_2O_5-PANI nanocomposites. These materials present unique optical characteristics due to the synergistic properties of vanadium pentoxide (V_2O_5) and polyaniline (PANI), which enhance light absorption and modulation capabilities. The study investigates how the incorporation of V_2O_5 into PANI matrices can lead to improved optical properties, including tunable band gaps and increased UV shielding efficiency.

1.6. Other components of supercapacitors

➢ Current collectors

The components responsible for collecting the electrical current produced at the electrodes and connecting it with external networks are known as current collectors. Batteries and supercapacitors are two examples of electrical energy storage systems whose behavior is significantly influenced by these current collectors. Strong mechanical strength, high electrical conduction, low density, sustainability, and large electrochemical stability are just a few of the qualities that the perfect current collectors for supercapacitors should have. Despite the numerous advantages, metals have a major drawback in their lower electrochemical stability which decreases the performance of supercapacitors at high voltage levels. Additionally, metal-based current collectors are limited in their application under acidic electrolytic conditions as these materials tend to deteriorate in acidic environments, negatively impacting the electrochemical performance of the device. Materials including aluminium, iron, nickel, copper, stainless steel, and alloys are frequently used as current collectors [146].

Nickel-based (nickel foam and nickel foil) current collectors are widely employed in supercapacitor applications because of their superior mechanical strength, high electrical conductivity, low contact resistance with electrode components, and relatively low cost [143-146]. Nickel foam with an interior porous surface and increased contact area shows remarkable capacitance compared to nickel foil, which has a flat surface. Throughout the supercapacitor's cycle life, resistance within the device may grow due to the deterioration of the electrode, current collector, and active material as the number of cycles increases. To address this issue, polymeric binding materials like nafion, polyvinylidene fluoride (PVDF), polytetrafluoroethylene, and others are combined with the active material to ensure it remains firmly attached to the current collector over an extended time [147].

➢ Electrolyte

The electrolyte is a crucial component of electrochemical supercapacitors solid or quasi-solid electrolytes and liquid electrolytes [148]. These classifications of electrolytes are illustrated in Figure 1.19. The characteristics required of electrolytes in supercapacitors are [149,150]: (i) High ionic conductivity. (ii) A broad potential window. (iii) Small ionic radius. (iv) Excellent electrochemical stability. (v) Low resistance. (vi) Low volatility. (vii) Low toxicity. (viii) Low cost. (ix) High purity and easy availability. Aqueous electrolytes are widely utilized for research purposes due to their affordability and ease of handling during device fabrication and assembly. They offer lower resistance, higher concentration of ions compared to neutral electrolytes, lower volatility, and reduced flammability compared to other electrolytes (see Figure 1.19), which enhances safety in environments with strict safety protocols. Compared to organic and ionic liquid electrolytes, aqueous electrolytes have conductivities that are one to two orders of magnitude higher. Regrettably, aqueous electrolytes have a very narrow potential window that only extends to 1.23 V. In energy storage devices, various types of electrolytes such as alkaline, acidic, and neutral are used in aqueous form. However, acidic and neutral electrolytes have a higher rate of corrosion on electrodes compared to alkaline electrolytes [151,152]. Despite the limitations of low specific capacitance, low ionic conductivity, high volatility, flammability, toxicity, and cost, organic electrolytes are highly required due to their broad electrochemical potency window of 2.5 to 2.8 V. In comparison, aqueous electrolytes have a relatively narrow potential window. Ionic liquid electrolytes offer a wider electrochemical stability window compared to aqueous electrolytes, however, their high viscosity leads to lower ionic conductivity.

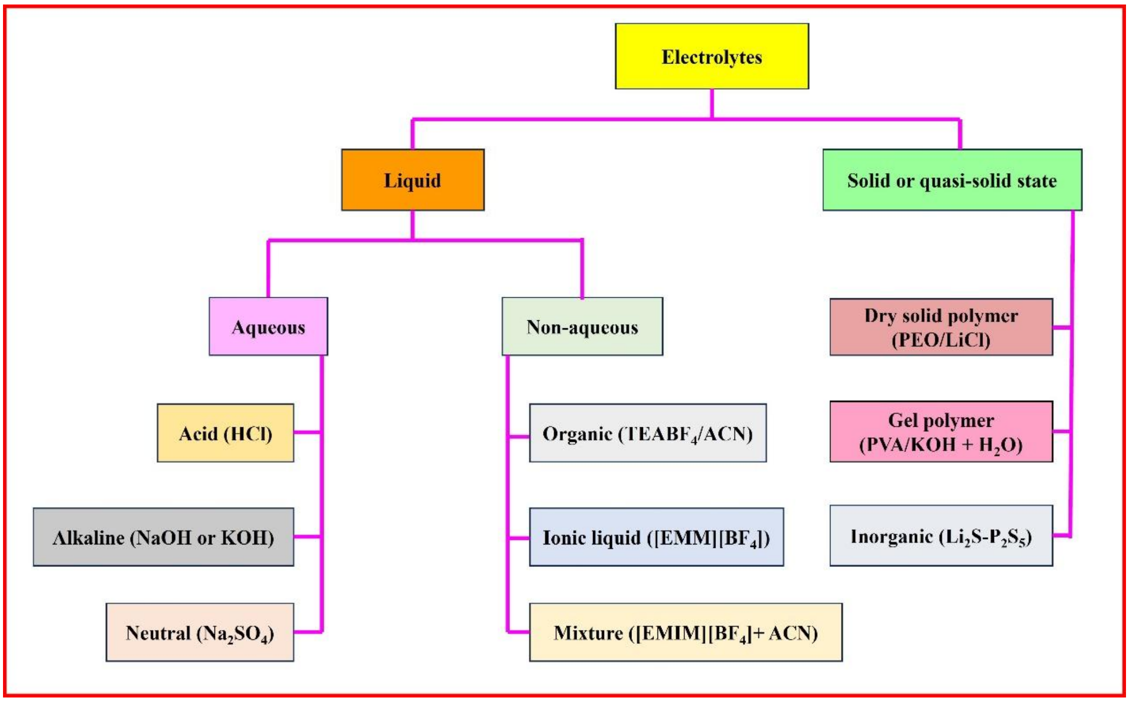

Figure 1.19. Categorization of electrolytes.

Liquid electrolytes have a smaller thickness, which might cause leaks in devices and reduce their functionality. Supercapacitors are great for short-term energy storage, but if they are broken, liquid-based devices could leak and endanger the environment. It is helpful to utilise solid or quasi-solid state electrolytes to address the problem of liquid leakage in devices. However, the low ionic conductivity of these solid-state electrolytes leads to a decrease in capacitance and energy density. Therefore, compared to electrochemical supercapacitors utilising alternative electrolytes, those based on aqueous electrolyte exhibit superior capacitance, energy density, and power density. The higher ion concentration and smaller ionic radius of aqueous electrolytes are responsible for this superiority [153,154].

➢ Separator

The separator in a supercapacitor acts as a barrier between its two electrodes, promoting ion movement through the bulk electrolyte while preventing short circuits. Separators can be made from various materials, including paper, glass, ceramics, and polymers [155,156]. Requirements of separator: (i) The separators must have non-conductive properties. (ii) They should allow for the permeation of electrolyte ions and exhibit low ionic resistance. (iii) They must be able to withstand volume and pressure fluctuations in the system to prevent swelling. (iv) The separators must be readily wetted by the electrolytes.

1.7. Advantages of supercapacitors

Supercapacitors have the following advantages over other energy storage devices [157–159].

(i) High specific power: The specific power of an electrochemical supercapacitor, ranging from 1 to 10 kW/kg, is significantly greater than that of lithium-ion batteries, which is around 150 W/kg. In electrochemical supercapacitors, electrical charges are stored at and near the electrode surface, rather than throughout the entire electrode. This results in faster charge-discharge rates compared to fuel cells and batteries, making them ideal for high-power delivery applications.

(ii) Long cycle life: In general, the faradaic processes in batteries involve a change in phase and conversion of electrode materials that are irreversible. On the other hand, the reactions in energy storage systems are reversible, giving them exceptional cyclic stability. The lifespan of energy storage systems can reach up to 30 years, with a significant number of charge-discharge cycles ranging from 50000 to 1 million cycles. In comparison, lithium-ion batteries have a cycle life of just 5 to 10 years, with a maximum of 1000 to 10000 cycles.

(iii) Long shelf life: If rechargeable batteries are left unused for an extended period, they deteriorate and become useless due to corrosion and self-discharge. Conversely, supercapacitors maintain their capacitance and can be fully recharged to their original state, even after long periods of inactivity.

(iv) High efficiency: During the charge-discharge process, supercapacitors are reversible throughout the entire potential window, and the energy loss due to heat dissipation is minimal and manageable. Additionally, the cycle efficiency of supercapacitors is quite impressive, with a rate of nearly 95% even when operating at a power density of 1 kW/kg .

(v) Wide operating temperature: Supercapacitors are capable of functioning in extremely low and high temperatures, ranging from -40 to 85°C. This reliability makes them a popular choice for use in military applications where energy must be sustained in challenging conditions.

(vi) Environmental friendliness: Generally, the materials used in the manufacture of supercapacitors are non-toxic, and the resulting waste by-products can be disposed of easily and safely.

(vii) Safety: Supercapacitors are considered safer than batteries, particularly lithium-ion batteries, which can explode due to heat dissipation and thermal rundown conditions.

1.8. Challenges for supercapacitors

While supercapacitors have many advantages over fuel cells and batteries, they still face challenges in some areas [160–162].

(i) Low energy density: Supercapacitors have a lower energy density (around 5 Wh/kg) than batteries (>50 Wh/kg). The cost is increased overall when using a large number of supercapacitors or a single, massive supercapacitor for applications that demand a high energy capacity.

(ii) High cost: The price of the electrode materials, electrolyte, separator, and other components are some of the elements that affect the cost of making a supercapacitor. Despite their high cost, high surface area carbon materials and transition metal oxides like RuO_2 are frequently found in commercial supercapacitors for practical uses. Additionally, the cost increases significantly if organic electrolytes are used instead of aqueous electrolytes.

To get beyond these restrictions and encourage the broad application of supercapacitors in many industries, more effective electrode materials must be found.

1.9. Applications of supercapacitors

Solutions for portable energy storage are becoming more and more necessary. Because of their high energy densities, batteries, and fuel cells currently dominate the industry. Supercapacitors' high PD and lengthy cycle life, however, are making them more and more popular in some applications where high power delivery is essential. In such applications, supercapacitors are becoming the preferred choice over other energy storage devices [163–166]. Some examples of these applications are listed below.

(i) Public sector: (a) Supercapacitors are utilized in digital cameras to produce flashes.

(b) Blueshift's portable speakers, manufactured by Sam Beck, use supercapacitors to provide up to 6 hours of playback time after just 5 minutes of charging.

(c) For security applications that require quick and temporary power supply, supercapacitors are utilized.

(ii) Transport and automotive industry: (a) Electrical vehicles that require high current for fast charging utilize supercapacitors.

(b) Supercapacitors play a significant role in regenerative braking systems as they quickly recover and store braking energy.

(iii) Defence and military-based applications: In defense and military applications, various tools such as communication devices, navigators, sensors, radar systems, torpedoes, electromagnetic pulse weapons, radar antenna, missiles, and GPS, are utilizing supercapacitors because of their requirement for large power and long cycle lifespan.

(iv) Memory backup: Supercapacitors provide backup power to devices such as PC cards, RAM, and SRAM during unexpected power outages, thereby preventing data loss.

(v) Medical purpose: Supercapacitors can serve as backup power sources for medical equipment to prevent potential failures during power outages.

1.10. Organization of thesis

Chapter 1 provides an overview of energy resources, including their classification and current accessibility. The utilization and excessive use of non-renewable energy sources result in numerous repercussions, such as the greenhouse effect, ozone depletion, and rising sea levels due to ice melting. To address this issue, there is a rising emphasis on the utilization of renewable resources. Various methods of generating energy from renewable sources were explored, along with the challenges encountered in the advancement of energy storage gadgets. Subsequently, the limitations in storing energy derived from renewable sources and the complexities associated with storing a specific amount of power using energy storage devices were deliberated. The discussion further extends to the role of supercapacitors, recent advancements, and their applications in energy storage. It offers brief overview of the concepts, types, and uses of supercapacitors while contrasting them, in terms of PD and ED, with batteries and fuel cells. It also describes the various methods of charge storage, the materials used for the electrodes, the benefits and drawbacks of supercapacitors, and their most recent uses.

Chapter 2 presents an extensive review of the literature concerning electrode materials such as V_2O_5, BiOCl, PANI, and PPy for supercapacitors. It explores diverse techniques employed in synthesizing these electrode materials. Furthermore, the chapter addresses the current research gap and defines the objectives of the thesis.

Chapter 3 presents the experimental methods and procedures for conducting polymers, manufacturing and characterizing metal oxides, and conducting polymer-based nanocomposite electrodes for supercapacitor cells.

Chapter 4 presents the in situ polymerization of anilinium hydrochloride over V_2O_5 was used to prepare PANI nanocomposites with varying weight percentages of V_2O_5 (10, 20, and 30 wt.%). V_2O_5 nanoparticles were synthesized using a simple chemical approach and their purity was confirmed through Rietveld refinement. For fabricated electrode materials, the pair of redox peaks as well as their shape in cyclic voltammetry suggests the faradic pseudocapacitive properties. Among all prepared electrodes, 20 wt% V_2O_5-PANI (PV2) nanocomposite demonstrates a maximum capacitance of 820.5 F/g with a decent capacitive lifespan of 88 % after 1000 charge-discharge phases. Besides this, the ignition of a red LED using three PV2//PV2 symmetric devices connected in series underscores its potential to advance energy storage applications.

Chapter 5 provides the UV-shielding efficiency and visible light transmittance of V_2O_5: PANI nanocomposites where V_2O_5 acts as a UV absorber. UV-visible study shows that different optical parameters changed considerably after doping and facilitated UV shielding efficiency of the prepared nanocomposites in the area of interest. The weight concentration of 30% V_2O_5 in the PANI matrix showed a 93% increase in UV shielding efficiency with respect to PANI in the UVB region. Distinct changes including red shift, narrowing of the band gap, better polarizability, tuned refractive index as well as dissipation factor could provide valuable insight into the design and development of new and superior UV shielding materials.

Chapter 6 gives the effects of different solvents for BiOCl synthesis by solvothermal method to study its electrochemical and physical characteristics. In this chapter ethylene glycol (EG), diethylene glycol (DEG), and triethylene glycol (TEG) are used to prepare different 3D hierarchical BiOCl nanostructures. Among all three prepared samples, BiOCl synthesized using TEG as the solvent (BT), exhibits a marigold flower-like morphology with a higher specific area. However, the BT electrode exhibits the highest specific capacitance due to its elevated electrical conductivity and expanded surface area, leading to a diminished potential drop in the galvanometric charge-discharge study. In three electrode configurations, an extreme capacitance of 665 F/g at 0.5 A/g was observed in an aqueous electrolyte solution with 93.8% cyclic stability after 2000 cycles. For the two electrodes system, a symmetric supercapacitor cell was constructed with a BT//BT configuration and demonstrates an extreme ED of 15.6 Wh/kg at 838 W/kg PD.

Chapter 7 provides the electrochemical properties of 3D porous PPy-BiOCl (wt.% of PPy 5,7, and 9) nanocomposites. The prepared BP1 (5 wt.%) nanocomposite supported on nickel foam textile exhibits high battery-type charge storage ability in an aqueous electrolyte solution. The galvanometric charge-discharge study showed an excellent capacitance of 659 F/g at 1 A/g. In the presence of an aqueous electrolyte, a symmetric supercapacitor cell was constructed with two matching 3D porous BP1 electrodes. This configuration unveiled an impressive ED of 24.0 Wh/kg at a PD of 750.0 W/kg. To illustrate its practical viability, two BP1//BP1 symmetric devices were linked in series, successfully powering a red LED for approximately 50 s with good light intensity. This underscores the practical potential of the BP1 electrode in energy storage systems.

Chapter 8 summarizes the key findings and observations from the study, emphasizing the major outcomes. It also identifies further research areas and potential future scope.

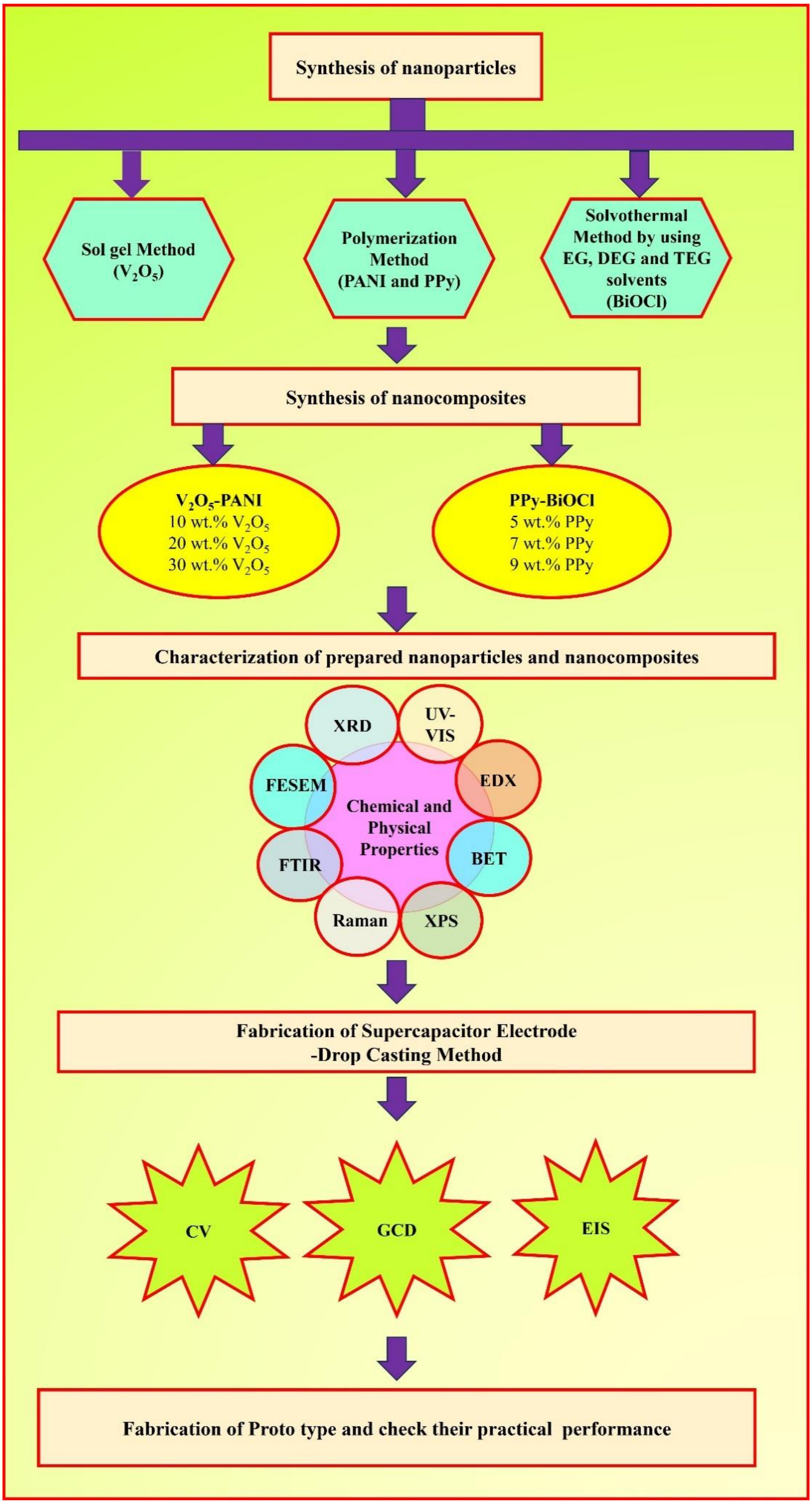

Figure 1.20. Schematic workflow of the thesis.

References

[1] Liu J, Cao G, Yang Z, Wang D, Dubois D, Zhou X, et al. Oriented nanostructures for energy conversion and storage. ChemSusChem: 2008;1:676–97.

[2] Chen X, Paul R, Dai L. Carbon-based supercapacitors for efficient energy storage. Natl Sci Rev 2017;4:453–89.

[3] Liu L, Zhao H, Lei Y. Review on Nanoarchitectured Current Collectors for Pseudocapacitors. Small Methods 2019;3.

[4] Vangari M, Pryor T, Jiang L. Supercapacitors: Review of Materials and Fabrication Methods. Journal of Energy Engineering 2013;139:72–9.

[5] Yolcan OO. World energy outlook and state of renewable energy: 10-Year evaluation. Innovation and Green Development 2023;2:100070.

[6] Davies MP, Banerjee R, Gupta A. Non-Conventional Energy Development in India. A report of studies conducted through a Fulbright grant to India. 1998:04-32.

[7] Blondeel M, Van de Graaf T. Toward a global coal mining moratorium? A comparative analysis of coal mining policies in the USA, China, India and Australia. Climatic Change. 2018;150(1):89-101.

[8] Yenneti K. The grid-connected solar energy in India: Structures and challenges. Energy strategy reviews. 2016;11:41-51.

[9] Schmid G. The development of renewable energy power in India: Which policies have been effective? Energy Policy 2012;45:317–26.

[10] Garg P. Energy Scenario and Vision 2020 in India. vol. 3. 2012.

[11] Asif M, Muneer T. Energy supply, its demand and security issues for developed and emerging economies. Renewable and Sustainable Energy Reviews 2007;11:1388–413.

[12] Mathews JA, Reinert ES. Renewables, manufacturing and green growth: Energy strategies based on capturing increasing returns. Futures 2014;61:13–22.

[13] Bauhofer W, Kovacs JZ. A review and analysis of electrical percolation in carbon nanotube polymer composites. Compos Sci Technol 2009;69:1486–98.

[14] Afif A, Rahman SM, Tasfiah Azad A, Zaini J, Islam MA, Azad AK. Advanced materials and technologies for hybrid supercapacitors for energy storage – A review. J Energy Storage 2019;25.

[15] Bryan AM, Santino LM, Lu Y, Acharya S, D’Arcy JM. Conducting Polymers for Pseudocapacitive Energy Storage. Chemistry of Materials 2016;28:5989–98.

[16] Poonam, Sharma K, Arora A, Tripathi SK. Review of supercapacitors: Materials and devices. J Energy Storage 2019;21:801–25.

[17] Eftekhari A. The mechanism of ultrafast supercapacitors. J Mater Chem A Mater 2018;6:2866–76.

[18] Wang J, Wang J, Kong Z, Lv K, Teng C, Zhu Y. Conducting-Polymer-Based Materials for Electrochemical Energy Conversion and Storage. Advanced Materials 2017;29.

[19] Li X, Wei B. Supercapacitors based on nanostructured carbon. Nano Energy 2013;2:159–73.

[20] Pawar SA, Patil DS, Shin JC. Electrochemical battery-type supercapacitor based on chemosynthesized Cu_2S-Ag_2S composite electrode. Electrochim Acta 2018;259:664–75.

[21] Huang YY, Lin LY. Synthesis of Ternary Metal Oxides for Battery-Supercapacitor Hybrid Devices: Influences of Metal Species on Redox Reaction and Electrical Conductivity. ACS Appl Energy Mater 2018;1:2979–90.

[22] Toupin M, Brousse T, Bélanger D. Charge storage mechanism of MnO_2 electrode used in aqueous electrochemical capacitor. Chemistry of Materials 2004;16:3184–90.

[23] Itani K, De Bernardinis A. Review on New-Generation Batteries Technologies: Trends and Future Directions. Energies. 2023;16(22):7530.

[24] Jayalakshmi M, Balasubramanian K. Simple capacitors to supercapacitors-an overview. International Journal of Electrochemical Science. 2008;3(11):1196-217.

[25] Nishino A. Capacitors: operating principles, current market and technical trends. Journal of power sources. 1996;60(2):137-47.

[26] Sun J, Luo B, Li H. A review on the conventional capacitors, supercapacitors, and emerging hybrid ion capacitors: past, present, and future. Advanced Energy and Sustainability Research. 2022;3(6):2100191.

[27] Dupont MF, Donne SW. Charge storage mechanisms in electrochemical capacitors: Effects of electrode properties on performance. J Power Sources 2016;326:613–23.

[28] Wang Y, Song Y, Xia Y. Electrochemical capacitors: Mechanism, materials, systems, characterization and applications. Chem Soc Rev 2016;45:5925–50.

[29] Wang G, Lu Z, Li Y, Li L, Ji H, Feteira A, Zhou D, Wang D, Zhang S, Reaney IM. Electroceramics for high-energy density capacitors: current status and future perspectives. Chemical Reviews. 2021 ;121(10):6124-72.

[30] Reid O, Saleh FS, Easton EB. Determining electrochemically active surface area in PEM fuel cell electrodes with electrochemical impedance spectroscopy and its application to catalyst durability. Electrochim Acta 2013;114:278–84.

[31] Cruz-Manzo S, Chen R. Electrochemical impedance study on estimating the mass transport resistance in the polymer electrolyte fuel cell cathode catalyst layer. Journal of Electroanalytical Chemistry 2013;702:45–8.

[32] Gu D, Ding C, Qin Y, Jiang H, Wang L, Shen L. Behavior of electrical charge storage/release in polyaniline electrodes of symmetric supercapacitor. Electrochim Acta 2017;245:146–55.

[33] Wu TH, Hesp D, Dhanak V, Collins C, Braga F, Hardwick LJ, et al. Charge storage mechanism of activated manganese oxide composites for pseudocapacitors. J Mater Chem A Mater 2015;3:12786–95.

[34] Gerasimov GN, Gromov VF, Ilegbusi OJ, Trakhtenberg LI. The mechanisms of sensory phenomena in binary metal-oxide nanocomposites. Sens Actuators B Chem 2017;240:613–24.

[35] Augustyn V, Simon P, Dunn B. Pseudocapacitive oxide materials for high-rate electrochemical energy storage. Energy Environ Sci 2014;7:1597–614.

[36] Ozoemena KI, Kebede M. Next-Generation Nanostructured Lithium-Ion Cathode Materials: Critical Challenges for New Directions in R&D. Nanomaterials in Advanced Batteries and Supercapacitors. 2016:1-24.

[37] Sharma P, Bhatti TS. A review on electrochemical double-layer capacitors. Energy conversion and management. 2010;51(12):2901-12.

[38] Liu Y, Soucaze-Guillous B, Taberna PL, Simon P. Understanding of carbon-based supercapacitors ageing mechanisms by electrochemical and analytical methods. J Power Sources 2017;366:123–30.

[39] Mahon PJ, Paul GL, Keshishian SM, Vassallo AM. Measurement and modelling of the high-power performance of carbon-based supercapacitors. Journal of power sources. 2000;91(1):68-76.

[40] Winter M, Brodd RJ. What are batteries, fuel cells, and supercapacitors?. Chemical reviews. 2004;104(10):4245-70.

[41] Bagotsky VS, Skundin AM, Volfkovich YM. Electrochemical power sources: batteries, fuel cells, and supercapacitors. John Wiley & Sons; 2015.

[42] Ghosh A, Lee YH. Carbon-based electrochemical capacitors. ChemSusChem 2012;5:480–99.

[43] Muzaffar A, Ahamed MB, Deshmukh K, Thirumalai J. A review on recent advances in hybrid supercapacitors: Design, fabrication and applications. Renewable and Sustainable Energy Reviews 2019;101:123–45.

[44] Libich J, Máca J, Vondrák J, Čech O, Sedlaříková M. Supercapacitors: Properties and applications. J Energy Storage 2018;17:224–7.

[45] Luo Z, Liu L, Yang X, Luo X, Bi P, Fu Z, Pang A, Li W, Yi Y. Revealing the charge storage mechanism of nickel oxide electrochromic supercapacitors. ACS applied materials & interfaces. 2020;12(35):39098-107.

[46] Zhao B, Chen D, Xiong X, Song B, Hu R, Zhang Q, et al. A high-energy, long cycle-life hybrid supercapacitor based on graphene composite electrodes. Energy Storage Mater 2017;7:32–9.

[47] Xing J, Liao M, Zhang C, Yin M, Li D, Song Y. The effect of anions on the electrochemical properties of polyaniline for supercapacitors. Physical Chemistry Chemical Physics 2017;19:14030 41.

[48] Wang F, Wu X, Yuan X, Liu Z, Zhang Y, Fu L, et al. Latest advances in supercapacitors: From new electrode materials to novel device designs. Chem Soc Rev 2017;46:6816–54.

[49] Forse AC, Merlet C, Griffin JM, Grey CP. New perspectives on the charging mechanisms of supercapacitors. J Am Chem Soc 2016;138:5731–44.

[50] Taylor SR, Gileadi E. Physical interpretation of the Warburg impedance. Corrosion. 1995;51(09).

[51] Ehsani A, Heidari AA, Shiri HM. Electrochemical Pseudocapacitors Based on Ternary Nanocomposite of Conductive Polymer/Graphene/Metal Oxide: An Introduction and Review to it in Recent Studies. Chemical Record 2019;19:908–26.

[52] Balamurugan J, Nguyen TT, Aravindan V, Kim NH, Lee SH, Lee JH. All ternary metal selenide nanostructures for high energy flexible charge storage devices. Nano Energy 2019;65:103999.

[53] Liu Y, Jiang SP, Shao Z. Intercalation pseudocapacitance in electrochemical energy storage: recent advances in fundamental understanding and materials development. Materials Today Advances. 2020;7:100072.

[54] Raza W, Ali F, Raza N, Luo Y, Kim KH, Yang J, et al. Recent advancements in supercapacitor technology. Nano Energy 2018;52:441–73.

[55] Mei W, Chen H, Sun J, Wang Q. The effect of electrode design parameters on battery performance and optimization of electrode thickness based on the electrochemical-thermal coupling model. Sustain Energy Fuels 2019;3:148–65.

[56] Patil SS, Bhat TS, Teli AM, Beknalkar SA, Dhavale SB, Faras MM, et al. Hybrid Solid State Supercapacitors (HSSC's) for High Energy & Power Density: An Overview. Engineered Science 2020;12:38–51.

[57] Senthilkumar ST, Selvan RK, Lee YS, Melo JS. Electric double layer capacitor and its improved specific capacitance using redox additive electrolyte. Journal of Materials Chemistry A. 2013;1(4):1086-95.

[58] Javed MS, Khan AJ, Asim S, Shah SSA, Najam T, Siyal SH, et al. Insights to pseudocapacitive charge storage of binary metal-oxide nanobelts decorated activated carbon cloth for highly-flexible hybrid-supercapacitors. J Energy Storage 2020;31.

[59] Wang Y, Ding Y, Guo X, Yu G. Conductive polymers for stretchable supercapacitors. Nano Res 2019;12:1978–87.

[60] Zhang C, Zeng J, Xu C, Gao T, Wang X. Electric Double Layer Capacitors Based on Porous Three-Dimensional Graphene Materials for Energy Storage. J Electron Mater 2021;50:3043–63.

[61] Yang I, Kim SG, Kwon SH, Lee JH, Kim MS, Jung JC. Pore size-controlled carbon aerogels for EDLC electrodes in organic electrolytes. Current Applied Physics 2016;16:665–72.

[62] Ke Q, Wang J. Graphene-based materials for supercapacitor electrodes – A review. Journal of Materiomics 2016;2:37–54.

[63] Yu Y, Cui C, Qian W, Xie Q, Zheng C, Kong C, et al. Carbon nanotube production and application in energy storage. Asia-Pacific Journal of Chemical Engineering 2013;8:234–45.

[64] Vinodh R, Gopi CV, Yang Z, Deviprasath C, Atchudan R, Raman V, Yi M, Kim HJ. Novel electrode material derived from porous polymeric organic framework of phloroglucinol and terephthaldehyde for symmetric supercapacitors. Journal of Energy Storage. 2020;28:101283.

[65] Muchuweni E, Mombeshora ET, Martincigh BS, Nyamori VO. Recent Applications of Carbon Nanotubes in Organic Solar Cells. Front Chem 2022;9.

[66] Saliger R, Bock V, Petricevic R, Tillotson T, Geis S, Fricke J. Carbon aerogels from dilute catalysis of resorcinol with formaldehyde. Journal of Non-Crystalline Solids. 1997;221(2-3):144-50.

[67] Pekala RW, Alviso CT, Lu X, Gross J, Fricke J. New organic aerogels based upon a phenolic-furfural reaction. Journal of non-crystalline solids. 1995;188(1-2):34-40.

[68] Li J, Wang X, Huang Q, Gamboa S, Sebastian PJ. Studies on preparation and performances of carbon aerogel electrodes for the application of supercapacitor. J Power Sources 2006;158:784–8.

[69] Presser V, Heon M, Gogotsi Y. Carbide-derived carbons - from porous networks to nanotubes and graphene. Adv Funct Mater 2011;21:810–33.

[70] Zhai Z, Zhang L, Du T, Ren B, Xu Y, Wang S, Miao J, Liu Z. A review of carbon materials for supercapacitors. Materials & Design. 2022;221:111017.

[71] Devi R, Kumar V, Kumar S, Bulla M, Jatrana A, Rani R, et al. Recent advancement in biomass-derived activated carbon for waste water treatment, energy storage, and gas purification: a review. J Mater Sci 2023;58:12119–42.

[72] Iqbal S, Khatoon H, Hussain Pandit A, Ahmad S. Recent development of carbon based materials for energy storage devices. Mater Sci Energy Technol 2019;2:417–28.

[73] Sevilla M, Mokaya R. Energy storage applications of activated carbons: supercapacitors and hydrogen storage. Energy & Environmental Science. 2014;7(4):1250-80.

[74] Majumdar D, Maiyalagan T, Jiang Z. Recent Progress in Ruthenium Oxide-Based Composites for Supercapacitor Applications. ChemElectroChem 2019;6:4343–72.

[75] Li Q, Zheng S, Xu Y, Xue H, Pang H. Ruthenium based materials as electrode materials for supercapacitors. Chemical Engineering Journal 2018;333:505–18.

[76] Yu F, Pang L, Wang HX. Preparation of mulberry-like RuO_2 electrode material for supercapacitors. Rare Metals 2021;40:440–7.

[77] Sun J, Wu C, Sun X, Hu H, Zhi C, Hou L, Yuan C. Recent progresses in high-energy-density all pseudocapacitive-electrode-materials-based asymmetric supercapacitors. Journal of materials chemistry A. 2017;5(20):9443-64.

[78] Zhu J, Zhang D, Zhu Z, Wu Q, Li J. Review and prospect of MnO_2-based composite materials for supercapacitor electrodes. Ionics (Kiel) 2021;27:3699–714.

[79] Tang XN, Zhu SK, Ning J, Yang XF, Hu MY, Shao JJ. Charge storage mechanisms of manganese dioxide-based supercapacitors: A review. Xinxing Tan Cailiao/New Carbon Materials 2021;36:702–10.

[80] Yang L, Zhu Q, Yang K, Xu X, Huang J, Chen H, et al. A Review on the Application of Cobalt-Based Nanomaterials in Supercapacitors. Nanomaterials 2022;12(22):4065.

[81] Temam AG, Alshoaibi A, Getaneh SA, Awada C, Nwanya AC, Ejikeme PM, Ezema FI. Recent progress on V_2O_5 based electroactive materials: Synthesis, properties, and supercapacitor application. Current Opinion in Electrochemistry. 2023;38:101239.

[82] Xu K, Wang L, Xu X, Dou SX, Hao W, Du Y. Two dimensional bismuth-based layered materials for energy-related applications. Energy Storage Materials. 2019;19:446-63.

[83] Yan Y, Li B, Guo W, Pang H, Xue H. Vanadium based materials as electrode materials for high performance supercapacitors. J Power Sources 2016;329:148–69.

[84] Le TK, Pham PV, Dong CL, Bahlawane N, Vernardou D, Mjejri I, Rougier A, Kim SW. Recent advances in vanadium pentoxide (V_2O_5) towards related applications in chromogenics and beyond: fundamentals, progress, and perspectives. Journal of Materials Chemistry C. 2022;10(11):4019-71.

[85] Xia C, Hong WT, Kim YE, Choe WS, Kim DH, Kim JK. Metal-Organic Decomposition-Mediated Nanoparticulate Vanadium Oxide Hole Transporting Buffer Layer for Polymer Bulk-Heterojunction Solar Cells. Polymers. 2020;12(8):1791.

[86] Navone C, Baddour-Hadjean R, Pereira-Ramos JP, Salot R. A kinetic study of electrochemical lithium insertion into oriented V_2O_5 thin films prepared by rf sputtering. Electrochimica Acta. 2008 ;53(8):3329-36.

[87] Iida Y, Kaneko Y, Kanno Y. Fabrication of pulsed-laser deposited V_2O_5 thin films for electrochromic devices. Journal of materials processing technology. 2008;197(1-3):261-7.

[88] Cui HN, Teixeira V, Meng LJ, Wang R, Gao JY, Fortunato E. Thermochromic properties of vanadium oxide films prepared by dc reactive magnetron sputtering. Thin Solid Films. 2008 ;516(7):1484-8.

[89] Hormoz S, Ramanathan S. Limits on vanadium oxide Mott metal-insulator transition field-effect transistors. Solid-State Electronics. 2010;54(6):654-9.

[90] Fateh N, Fontalvo GA, Cha L, Klünsner T, Hlawacek G, Teichert C, Mitterer C. Synthesis–structure relations for reactive magnetron sputtered V_2O_5 films. Surface and Coatings Technology. 2008;202(8):1551-5.

[91] Su Q, Lan W, Wang YY, Liu XQ. Structural characterization of β-V_2O_5 films prepared by DC reactive magnetron sputtering. Applied Surface Science. 2009;255(7):4177-9.

[92] Yang H, Jin W, Wang L. Synthesis and characterization of V_2O_5-doped SnO_2 nanocrystallites for oxygen-sensing properties. Materials Letters. 2003;57(22-23):3686-9.

[93] Allersma T, Hakim R, Kennedy TN, Mackenzie JD. Structure and physical properties of solid and liquid vanadium pentoxide. The Journal of Chemical Physics. 1967;46(1):154-60.

[94] Kämper A, Hahndorf I, Baerns M. A molecular mechanics study of the adsorption of ethane and propane on V_2O_5 (001) surfaces with oxygen vacancies. Topics in Catalysis. 2000;(1):77-84.

[95] Haber J, Witko M, Tokarz R. Vanadium pentoxide I. Structures and properties. Applied Catalysis A: General. 1997;157(1-2):3-22.

[96] Kumar A, Singh P, Kulkarni N, Kaur D. Structural and optical studies of nanocrystalline V_2O_5 thin films. Thin Solid Films. 2008;516(6):912-8.

[97] Goodenough JB. Metallic oxides. Progress in solid state chemistry. 1971;5:145-399.

[98] Jiang Y, Liu J. Definitions of pseudocapacitive materials: a brief review. Energy & Environmental Materials. 2019;2(1):30-7.

[99] Umeshbabu E, Ranga Rao G. Vanadium pentoxide nanochains for high-performance electrochemical supercapacitors. J Colloid Interface Sci 2016;472:210–9.

[100] Zylbersztejn AM, Mott NF. Metal-insulator transition in vanadium dioxide. Physical Review B. 1975;11(11):4383.

[101] Liang F, Chen M, Zhang S, Zou Z, Ge C, Jia S, Le S, Yu F, Nong J. Electrochemical Activation in Vanadium Oxide with Rich Oxygen Vacancies for High-Performance Aqueous Zinc-Ion Batteries. ACS Sustainable Chemistry & Engineering. 2024;12(13):5117-28.

[102] Ingole RS, Kadam SL, Tiwari NG, Nakate UT, Mangiri R, Kulkarni SB, Lokhande BJ, Ok JG. Hierarchically Structured 3D Nanoporous Vanadium Oxide Transparent Electrodes for Next-Generation Supercapacitors. Advanced Sustainable Systems. 2024:2300535.

[103] Pullanchiyodan A, Haridasan GT, Sreeram P, Das A, TM Balakrishnan N, Raghavan P, Hegde AC. High-Potential Aqueous Asymmetric Supercapacitor Based on 2D Molybdenum Disulfide and Vanadium Pentoxide Electrodes. Energy & Fuels. 2024.

[104] Xu X, Qian Y, Wang C, Bai Z, Wang C, Song M, Du Y, Xu X, Wang N, Yang J, Qian Y. Enhanced charge transfer and reaction kinetics of vanadium pentoxide for zinc storage via nitrogen interstitial doping. Chemical Engineering Journal. 2023;451:138770.

[105] Devi N, Ray SS. Performance of bismuth-based materials for supercapacitor applications: A review. Mater Today Commun 2020;25.

[106] Shinde NM, Ghule BG, Raut SD, Narwade SH, Pak JJ, Mane RS. Hopping Electrochemical Supercapacitor Performance of Ultrathin BiOCl Petals Grown by a Room-Temperature Soft-Chemical Process. Energy and Fuels 2021;35:6892–7.

[107] Lv X, Lam FL, Hu X. A review on bismuth oxyhalide (BiOX, X= Cl, Br, I) based photocatalysts for wastewater remediation. Frontiers in Catalysis. 2022;2:839072.

[108] Vinoth S, Ong WJ, Pandikumar A. Defect engineering of BiOX (X= Cl, Br, I) based photocatalysts for energy and environmental applications: Current progress and future perspectives. Coordination Chemistry Reviews. 2022;464:214541.

[109] Ahmad I, Shukrullah S, Naz MY, Ullah S, Assiri MA. Designing and modification of bismuth oxyhalides BiOX (X= Cl, Br and I) photocatalysts for improved photocatalytic performance. Journal of Industrial and Engineering Chemistry. 2022;105:1-33.

[110] Mengting Z, Kurniawan TA, Duan L, Song Y, Hermanowicz SW, Othman MH. Advances in BiO X-based ternary photocatalysts for water technology and energy storage applications: Research trends, challenges, solutions, and ways forward. Reviews in Environmental Science and Bio/Technology. 2022;21(2):331-70.

[111] Hong W, Wang L, Liu K, Han X, Zhou Y, Gao P, et al. Asymmetric supercapacitor constructed by self-assembled camellia-like BiOCl and activated carbon microspheres derived from sweet potato starch. J Alloys Compd 2018;746:292–300.

[112] Dutta S, Pal S, Ahammed N, Sahoo S, Chatterjee S, De S. Enhanced Electrochemical Performance of BiOCl Nanoflower-RGO Based Supercapacitor in the Presence of Redox Additive Electrolyte. ECS Journal of Solid State Science and Technology. 2023;12(9):091002.

[113] Bhadra J, Alkareem A, Al-Thani N. A review of advances in the preparation and application of polyaniline based thermoset blends and composites 2052.

[114] Namsheer K, Rout CS. Conducting polymers: a comprehensive review on recent advances in synthesis, properties and applications. RSC Adv 2021;11:5659–97.

[115] Tanguy NR, Thompson M, Yan N. A review on advances in application of polyaniline for ammonia detection. Sens Actuators B Chem 2018;257:1044–64.

[116] Wang K, Huang J, Wei Z. Conducting polyaniline nanowire arrays for high performance supercapacitors. The Journal of Physical Chemistry C. 2010;114(17):8062-7.

[117] Yan J, Wei T, Fan Z, Qian W, Zhang M, Shen X, Wei F. Preparation of graphene nanosheet/carbon nanotube/polyaniline composite as electrode material for supercapacitors. Journal of Power Sources. 2010;195(9):3041-5.

[118] Ahmad MW, Anand S, Fatima A, Yang DJ, Choudhury A. Facile synthesis of copper oxide nanoparticles-decorated polyaniline nanofibers with enhanced electrochemical performance as supercapacitor electrode. Polymers for Advanced Technologies. 2021;32(10):4070-81.

[119] Huang Y, Li H, Wang Z, Zhu M, Pei Z, Xue Q, et al. Nanostructured Polypyrrole as a flexible electrode material of supercapacitor. Nano Energy 2016;22:422–38.

[120] Shimoga G, Palem RR, Choi DS, Shin EJ, Ganesh PS, Saratale GD, et al. Polypyrrole-based metal nanocomposite electrode materials for high-performance supercapacitors. Metals (Basel) 2021;11.

[121] Fan LZ, Maier J. High-performance polypyrrole electrode materials for redox supercapacitors. Electrochem Commun 2006;8:937–40.

[122] Ates M, Alperen C. Polythiophene-based reduced graphene oxide and carbon black nanocomposites for supercapacitors. Iranian Polymer Journal (English Edition) 2023;32:1241–55.

[123] Huang Y, Li H, Wang Z, Zhu M, Pei Z, Xue Q, Huang Y, Zhi C. Nanostructured polypyrrole as a flexible electrode material of supercapacitor. Nano Energy. 2016;22:422-38.

[124] Ren Y, Liu Y, Wang S, Wang Q, Li S, Wang W, Dong X. Stretchable supercapacitor based on a hierarchical PPy/CNT electrode and hybrid hydrogel electrolyte with a wide operating temperature. Carbon Energy. 2022;4(4):527-38.

[125] Sumdani MG, Islam MR, Yahaya AN, Safie SI. Recent advancements in synthesis, properties, and applications of conductive polymers for electrochemical energy storage devices: A review. Polymer Engineering & Science. 2022;62(2):269-303.

[126] Yao H, Zhang F, Zhang G, Luo H, Liu L, Shen M, Yang Y. A novel two-dimensional coordination polymer-polypyrrole hybrid material as a high-performance electrode for flexible supercapacitor. Chemical Engineering Journal. 2018;334:2547-57.

[127] Kim HJ, Lee MY, Kim JS, Kim JH, Yu H, Yun H, Liao K, Kim TS, Oh JH, Kim BJ. Solution-Assembled Blends of Regioregularity-Controlled Polythiophenes for Coexistence of Mechanical Resilience and Electronic Performance. ACS applied materials & interfaces. 2017;9(16):14120-8.

[128] Shokry A, Karim M, Khalil M, Ebrahim S, El Nady J. Supercapacitor based on polymeric binary composite of polythiophene and single-walled carbon nanotubes. Sci Rep 2022;12.

[129] Sahoo R, Lee TH, Pham DT, Luu THT, Lee YH. Fast-Charging High-Energy Battery-Supercapacitor Hybrid: Anodic Reduced Graphene Oxide-Vanadium(IV) Oxide Sheet-on-Sheet Heterostructure. ACS Nano 2019;13:10776–86.

[130] Laforgue A, Simon P, Sarrazin C, Fauvarque JF. Polythiophene-based supercapacitors. Journal of power sources. 1999 Jul 1;80(1-2):142-8.

[131] Meng Q, Cai K, Chen Y, Chen L. Research progress on conducting polymer based supercapacitor electrode materials. Nano Energy. 2017;36:268-85.

[132] Das TK, Prusty S. Review on conducting polymers and their applications. Polymer-plastics technology and engineering. 2012;51(14):1487-500.

[133] Ates M, Karazehir T, Sezai Sarac AJ. Conducting polymers and their applications. Current Physical Chemistry. 2012;2(3):224-40.

[134] Kumar D, Sharma RC. Advances in conductive polymers. European polymer journal. 1998;34(8):1053-60.

[135] Agobi AU, Louis H, Magu TO, Dass PM. A review on conducting polymers-based composites for energy storage application. J. Chem. Rev. 2019;1(1):19-34.

[136] Han Y, Dai L. Conducting polymers for flexible supercapacitors. Macromolecular chemistry and physics. 2019;220(3):1800355.

[137] Chatterjee DP, Nandi AK. A review on the recent advances in hybrid supercapacitors. Journal of Materials Chemistry A. 2021;9(29):15880-918.

[138] Gonçalves JM, da Silva MI, Toma HE, Angnes L, Martins PR, Araki K. Trimetallic oxides/hydroxides as hybrid supercapacitor electrode materials: a review. Journal of materials chemistry A. 2020;8(21):10534-70.

[139] Najib S, Erdem E. Current progress achieved in novel materials for supercapacitor electrodes: mini review. Nanoscale Advances. 2019;1(8):2817-27.

[140] Yi XS. An introduction to composite materials. Composite Materials Engineering 2017;1:1–61.

[141] Ren L, Zhang G, Yan Z, Kang L, Xu H, Shi F, Lei Z, Liu ZH. Three-dimensional tubular MoS_2/PANI hybrid electrode for high rate performance supercapacitor. ACS applied materials & interfaces. 2015;7(51):28294-302.

[142] Zegebreal LT, Tegegne NA, Hone FG. Recent progress in hybrid conducting polymers and metal oxide nanocomposite for room-temperature gas sensor applications: A review. Sensors and Actuators A: Physical. 2023:114472.

[143] Raza MA, Rehman ZU, Tanvir MG, Maqsood MF. Metal oxide-conducting polymer-based composite electrodes for energy storage applications. InRenewable Polymers and Polymer-Metal Oxide Composites 2022 (pp. 195-251). Elsevier.

[144] Thomas SW, Khan RR, Puttananjegowda K, Serrano-Garcia W. Conductive polymers and metal oxide polymeric composites for nanostructures and nanodevices. InAdvances in Nanostructured Materials and Nanopatterning Technologies 2020 (pp. 243-271). Elsevier.

[145] Mohite DD, Chavan SS, Lokhande PE, Sutar KB, Dubal S, Rednam U, Al-Asbahi BA, Kumar YA. Metal oxide-based nanocomposites as advanced electrode materials for enhancing electrochemical performance of Supercapacitors: A comprehensive review. Materials Today: Proceedings. 2024.

[146] Kar KK. Handbook of Nanocomposite Supercapacitor Materials III. Cham: Springer International Publishing; 2021.

[147] Abdisattar A, Yeleuov M, Daulbayev C, Askaruly K, Tolynbekov A, Taurbekov A, et al. Recent advances and challenges of current collectors for supercapacitors. Electrochem Commun 2022;142.

[148] Pal B, Yang S, Ramesh S, Thangadurai V, Jose R. Electrolyte selection for supercapacitive devices: A critical review. Nanoscale Adv 2019;1:3807–35.

[149] Iqbal MZ, Zakar S, Haider SS. Role of aqueous electrolytes on the performance of electrochemical energy storage device. Journal of Electroanalytical Chemistry 2020;858.

[150] Ye W, Wang H, Ning J, Zhong Y, Hu Y. New types of hybrid electrolytes for supercapacitors. Journal of Energy Chemistry 2021;57:219–32.

[151] Mendhe A, Panda HS. A review on electrolytes for supercapacitor device. Discov Mater 2023;3.

[152] Baig MM, Khan MA, Gul IH, Rehman SU, Shahid M, Javaid S, et al. A Review of Advanced Electrode Materials for Supercapacitors: Challenges and Opportunities. J Electron Mater 2023;52:5775–94.

[153] Sharma P, Kumar V. Study of electrode and electrolyte material of supercapacitor. Materials today: proceedings. 2020;33:1573-8.

[154] Singh A, Bhardwaj R, Mishra RK, Sundramoorthy AK, Gupta V, Arya S. Potential of functional gel polymers as electrolytes for supercapacitors. Ionics. 2023;29(10):3831-51.

[155] Kar KK. Handbook of Nanocomposite Supercapacitor Materials III. Cham: Springer International Publishing; 2021.

[156] Qin B, Han Y, Ren Y, Sui D, Zhou Y, Zhang M, et al. A Ceramic-Based Separator for High-Temperature Supercapacitors. Energy Technology 2018;6:306–11.

[157] Kondrat S, Kornyshev AA. Pressing a spring: What does it take to maximize the energy storage in nanoporous supercapacitors? Nanoscale Horiz 2016;1:45–52.

[158] Shi K, Yang X, Cranston ED, Zhitomirsky I. Efficient Lightweight Supercapacitor with Compression Stability. Adv Funct Mater 2016;26:6437–45.

[159] Choi HJ, Kim JH, Kim HK, Lee SH, Lee YH. Improving the Electrochemical Performance of Hybrid Supercapacitor using Well-organized Urchin-like TiO_2 and Activated Carbon. Electrochim Acta 2016;208:202–10.

[160] Xu Y, Ye J, Zhou D, Su L. Research progress on applications of calcium derived from marine organisms. Scientific reports. 2020;10(1):18425.

[161] Salanne M, Rotenberg B, Naoi K, Kaneko K, Taberna PL, Grey CP, Dunn B, Simon P. Efficient storage mechanisms for building better supercapacitors. Nature Energy. 2016;1(6):1-0.

[162] Liu H, Liu X, Wang S, Liu HK, Li L. Transition metal based battery-type electrodes in hybrid supercapacitors: A review. Energy Storage Mater 2020;28:122–45.

[163] Huang S, Zhu X, Sarkar S, Zhao Y. Challenges and opportunities for supercapacitors. Apl Materials. 2019;7(10).

[164] Ates M. A review on conducting polymer coatings for corrosion protection. J Adhes Sci Technol 2016;30:1510–36.

[165] Meer S, Kausar A, Iqbal T. Trends in Conducting Polymer and Hybrids of Conducting Polymer/Carbon Nanotube: A Review. Polymer - Plastics Technology and Engineering 2016;55:1416–40.

[166] Shi K, Yang X, Cranston ED, Zhitomirsky I. Efficient Lightweight Supercapacitor with Compression Stability. Adv Funct Mater 2016;26:6437–45.

Chapter 2

Literature Review, Research Gap, and Objectives

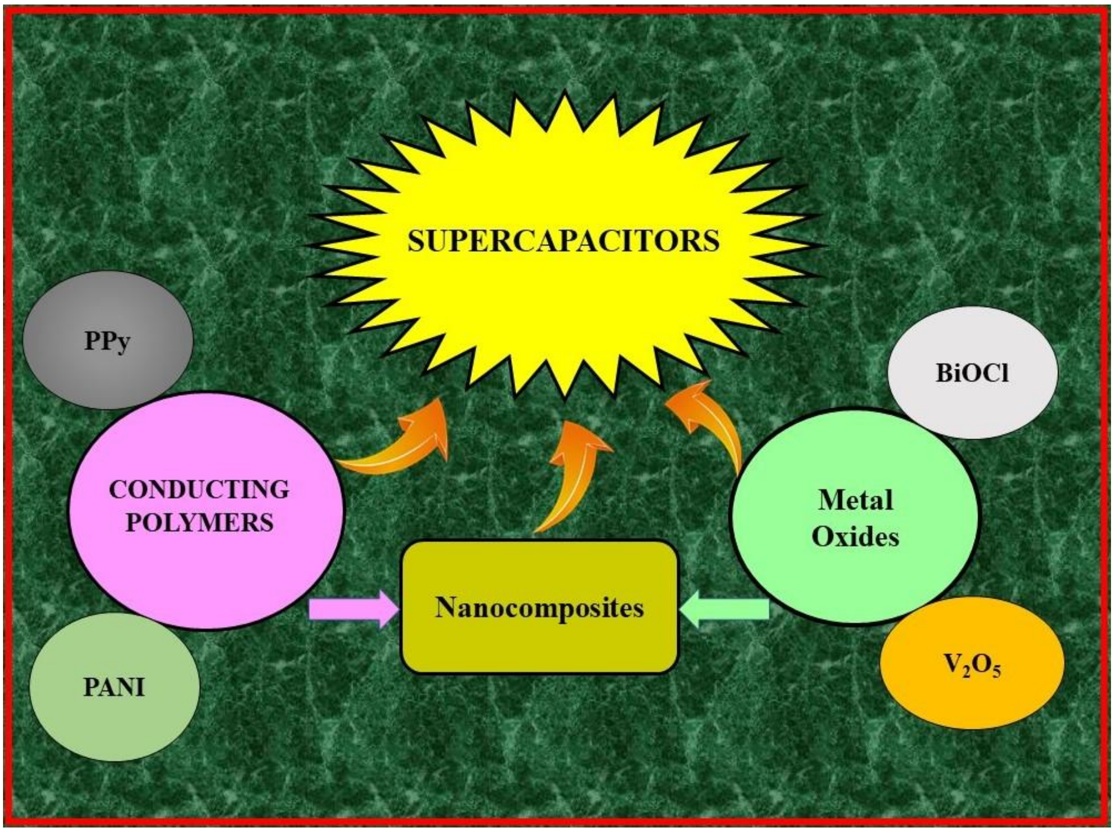

This chapter specifies a broad review of the current advances in the use of conducting polymers for electrode material in supercapacitors. It particularly emphasizes the significance of PANI and PPy, in combination with metal oxides such as V_2O_5 *and BiOCl. Furthermore, the chapter addresses the present research gap and defines the objectives of the present study.*

2.1. Literature Review

This chapter offers a broad review that investigates the research conducted on Vanadium Pentoxide (V_2O_5), Bismuth Oxychloride (BiOCl), Polyaniline (PANI), and Polypyrrole (PPy) as electrode materials for supercapacitors. It provides a comprehensive understanding of these materials' properties and their potential for enhancing supercapacitor performance.

- ***Wang et al. (2015)*** fabricated a three-dimensional composite of graphene and polyaniline using a hydrothermal process. This method included polymerizing polyaniline in a solution of graphene oxide. The resultant material is porous and three-dimensional, with an outstanding specific capacity of 648 F/g at a low current density of 0.5 A/g. Even with a high current density of 20.0 A/g, it maintains a large capacity of 356 F/g. After 1000 charge-discharge cycles lifespan, it still has a capacity of 537 F/g at 1.0 A/g. These findings demonstrate the composite's tremendous potential as an electrode material for supercapacitors [1].
- ***Balasubramanian et al. (2015)*** present a straightforward and eco-friendly method for synthesizing carbon-coated vanadium pentoxide with a distinctive flowery structure in a single step. They thoroughly investigate the structural, and supercapacitive attributes of this material. Remarkably, the carbon-coated flowery vanadium pentoxide demonstrates an impressive specific capacitance of 417 F/g and a good cycle lifespan after 2000 continuous charge-discharge cycles. Additionally, they construct a two-electrode symmetric device to assess its electrochemical performance, revealing a peak specific capacitance of 101 F/g at a scan rate of 2 mV/s [2].
- ***Simotwo et al. (2016***) developed freestanding, binder-free electrodes from high purity polyaniline nanofibers using a single electrospinning process. The nanofibers' extremely high polyaniline content (93 wt.%) was obtained by mixing ultrahigh molecular weight poly(ethylene oxide) with polyaniline in solution, ensuring the necessary chain entanglements for electrospinning. Polyaniline and polyaniline-carbon nanotube electrodes showed competitive specific capacitances of 308 and 385 F/g, respectively, at a current density of 0.5 A/g. After 1000 cycles, polyaniline and polyaniline-carbon nanotube-based electrodes retained specific capacitance at 70% and 81.4%, respectively. The porous three-dimensional electrode structure, which is made up of nonwoven interconnected nanostructures, is responsible for the electrodes' promising electrochemical performance [3].
- ***Huang et al. (2016)*** highlighted a significant challenge in the cycling lifespan of bendable supercapacitors using conducting polymers as electrodes, attributed to

structural breakdown from repetitive counterion flow during charging/discharging. They introduced supercapacitors constructed with facilely electropolymerized polypyrrole, demonstrating ultrahigh capacitance retentions. These electropolymerized polypyrrole supercapacitors retained over 97%, 91%, and 86% of their capacitance after 15000, 50000, and 100000 charging/discharging cycles, respectively. Impressively, they sustained over 230000 charging/discharging cycles while retaining approximately half of their initial capacitance, marking an unprecedented achievement in long-term cycling stability. The fully controllable electropolymerization process exhibited superiority in molecular ordering, facilitating uniform stress distribution and charge transfer within the electrodes. Remarkably, even after being left at ambient conditions for 8 months, the electropolymerized polypyrrole supercapacitors maintained their excellent electrochemical performance without degradation. These extremely stable supercapacitors, coupled with excellent flexibility and scalability, hold significant promise for the commercialization of flexible and wearable electronics [4].

- ***Zhao et al. (2016)*** described the fabrication of polypyrrole nanowires under mild conditions using ferric chloride as an oxidant. These polypyrrole nanowires, with a width of 120 nm, exhibit numerous nanogaps or pores due to their intertwined nanostructures. Importantly, the polypyrrole nanowires were utilized as electrode materials for supercapacitors. Upon electrochemical testing, it was observed that the electrode based on polypyrrole nanowires exhibited a large specific capacitance of 420 F/g at 1.5 A/g and a good rate capability of 272 F/g at 18.0 A/g [5].
- ***Zheng et al. (2017)*** reported the successful synthesis of tungsten-doped vanadium pentoxide nanobelts through a facile hydrothermal route combined with calcination. The results indicate the successful doping of tungsten atoms into the crystal lattice of the vanadium pentoxide matrix, leading to the formation of homogeneous solid solutions of tungsten-doped vanadium pentoxide nanobelts. The electrochemical properties of these nanobelts as supercapacitor electrodes were investigated using cyclic voltammetry and galvanostatic charge-discharge methods. The tungsten-doped vanadium pentoxide nanobelts exhibited excellent capacity and good rate capability. Specifically, their specific capacitance was measured as 407, 381, 350, 328, 295, and 273 F/g at current densities of 0.5, 1, 2, 5, 10, and 20 A/g, respectively. Additionally, these nanobelts demonstrated excellent energy densities of 246 and 165 W h/kg at power densities of 0.99 and 39.60 kW/kg [6].
- ***Xu et al. (2017)*** have developed ternary composite of graphene/activated carbon/polypyrrole for use as an electrode material in supercapacitors. This composite

was synthesized through vacuum filtration and anodic constant current deposition methods. The activated carbons situated between graphene sheets served as flexible substrates for the deposition of polypyrrole nanoparticles. By adjusting different deposition current densities and deposition times, morphologies and electrochemical performances of the nanocomposite electrodes were tailored and optimized. Notably, graphene/activated carbon/polypyrrole electrode demonstrated a maximum areal specific capacitance of 906 mF/cm^2 with a polypyrrole loading mass of 2.75 mg/cm^2 (equivalent to a specific capacitance of 178 F/ g) at a current density of 0.5 mA/cm^2. Even after 5000 charge-discharge cycles, the capacitance retention remained at 64.4%, and after 500 stretching–bending cycles at a current density of 3 mA/cm^2, it remained at 83.6%. These flexible, free-standing, and binder-free graphene/activated carbon/polypyrrole electrodes hold significant promise for use in flexible energy storage devices [7].

- ***Wang et al. (2017)*** demonstrated the synthesis of nanostructured polyaniline with varying morphologies by controlling hydrothermal conditions, and then composited them with graphene sheets for use as electrode materials in supercapacitors. Specifically, ultrathin polyaniline layers, ranging from 10 to 20 nm in total thickness, were uniformly combined with graphene sheets through a two-step hydrothermal-assisted chemical oxidation polymerization process. Alternatively, polyaniline nanofibers with diameters of 50 to 100 nm were obtained through a one-step direct hydrothermal process. Due to their ultrathin layer and porous structure, the graphene/polyaniline composites in sheet form exhibited specific capacitances ranging from 532.3 to 304.9 F/g at scan rates of 2 to 50 mV/s [8].
- ***Nie et al. (2017)*** introduced a simple and eco-friendly method to fabricate uniform polyaniline thorn/BiOCl chip heterostructures at low temperatures without the requirement of surfactants. In this approach, bismuth sulfide nanowires acted as sacrificial templates and a bismuth source for BiOCl, facilitating the concurrent formation of HCl-doped polyaniline conductive arrays and BiOCl chips supported on residual Bi_2S_3 nanowires. Consequently, the resultant polyaniline thorn/BiOCl chip nanocomposite demonstrated superior electrochemical performance as electrode materials for supercapacitors in neutral media. This included increased specific capacitance, enhanced rate capability, and reduced charge-transfer resistance compared to individual polyaniline nanofibers. These improvements were attributed to the distinctive hierarchical nanostructure of the polyaniline thorn/BiOCl chip and the synergistic interaction between ionizable BiOCl and the polyaniline chain [9].

- ***Palsaniya et al. (2018)*** detailed the synthesis of nanocomposites consisting of polyaniline, graphene, and molybdenum disulfide, with equal weight proportions of graphene and molybdenum disulfide. These nanocomposites were created via in-situ oxidative polymerization of polyaniline, along with binary nanocomposites of polyaniline-graphene. Analysis of their morphology confirmed the formation of well-dispersed composite materials. The ternary composite exhibited a distinct interlayered structure of graphene and molybdenum disulfide, enclosing polyaniline nanorods. This unique arrangement conferred exceptional supercapacitive properties to the ternary composite, making it ideal for energy storage applications, as evidenced by its improved cyclic stability. Measurements conducted on symmetric supercapacitor of the ternary composite polyaniline-graphene-molybdenum disulfide demonstrated a notably high specific capacitance of 142.30 F/g under galvanostatic charge-discharge cycles, surpassing that of binary composites. The substantial enhancement in cyclic stability led to a remarkable capacitance retention of 98.11%, compared to approximately 40% for pure polyaniline and approximately 60-96% for binary composites [10].
- ***Liu et al. (2018)*** conducted a study where they synthesized a nickel vanadate-polyaniline composite through an in situ chemical bath method. Their findings revealed that this composite exhibited exceptional electrochemical properties, boasting a specific capacitance value of 2565.7 F/g at a scan rate of 5 mV/s, along with a wide potential window and excellent rate capability. These characteristics surpassed those observed in both nickel vanadate and polyaniline electrodes. The enhanced electrochemical performance was attributed to the synergistic interaction between nickel vanadate and polyaniline. Furthermore, they fabricated a symmetric, flexible, and transparent supercapacitor using the nickel vanadate-polyaniline composite as the working electrode. This device showcased a maximum areal capacitance of 58.5 mF/cm^2 at a scan rate of 5 mV/s [11].
- ***Hou et al. (2018)*** reported the synthesis of vanadium pentoxide (V_2O_5) nanosheets through a V_2O_5 xerogel solvothermal reaction in ethanol solvent at 200 °C for 12 hours. These nanosheets offer enhanced ion accessibility and provide a larger surface area for electrochemical reactions. Remarkably, V_2O_5 electrodes achieved a specific capacitance of 298 F/g with robust rate capability. Even after 10,000 cycles at 200 mV/s, the capacitance retained an impressive 85% retention rate. Additionally, asymmetric supercapacitors were constructed using V_2O_5 nanosheets and active carbon electrodes, resulting in a specific capacitance of 13.2 F/g at 1 A/g current density [12].

- ***Hong et al. (2018)*** introduced two electrode materials for a new asymmetric supercapacitor (ASC): self-assembled camellia-like bismuth oxychloride (BiOCl) and monodispersed activated carbon microspheres (AC). The activated carbon, synthesized from a renewable carbon source, served as the positive electrode, exhibiting a specific capacitance of 208 F/g at 1 A/g with 87.6% capacitance retention after 3000 cycles. Additionally, they proposed an efficient method for preparing bismuth oxychloride with controllable morphology, revealing its camellia-like morphology with a mesoporous structure. As the negative electrode in the asymmetric supercapacitor, the bismuth oxychloride electrode demonstrated a specific capacitance of 1243 F/g at 1 A/g, with 90.3% capacitance retention after 3000 cycles at 5 A/g. Combining activated carbon and bismuth oxychloride, the full asymmetric supercapacitor cell exhibited a maximum capacitance of 124 F/g at 0.5 A/g and good cycling stability, retaining 82% of the initial specific capacitance after 3000 cycles at 1 A/g [13].
- ***Dutta et al. (2019)*** investigated the utilization of BiOCl nanosheets as anode material for sodium-ion batteries, employing a novel electrolyte sodium perchlorate-tetraethylene glycol dimethyl ether. This electrolyte prevents dendrite formation on the anode surface, facilitating easy characterization and material analyses. In situ, PEIS revealed distinct electrochemical phases, which were further analyzed using XRD, Raman, and TEM techniques. During sodiation, BiOCl undergoes conversion to metallic Bi alongside $NaBiO_3$ and NaCl. Subsequent insertion results in the formation of Na_3Bi alloy along with NaBi and BiO compounds. Upon desodiation, sodium is extracted from the system, leaving behind Bi and NaBi as irreversible products. The study also identified previously undetected phases including NaBi, BiO, $NaBiO_3$, and Na_3BiO_4, indicating a complex multistep interaction between sodium ions and ionically layered oxychloride nanosheets. This mechanism differs from the lithium system, where only Li_3Bi formation was predicted, while NaBi and other compounds were observed in this study. In addition to the mechanistic investigation, the authors reported a new sodium-ion full cell (BiOCl-PB) capable of achieving a voltage of approximately 2.2 V [14].
- ***Zhu et al. (2019)*** have introduced self-supported ultrathin bismuth nanosheets through a straightforward method involving in situ topotactic transformation using BiOCl as the primary template, termed TRA-BiOCl. Theoretical calculations suggest that the space left by TRA-BiOCl after the release of O and Cl atoms is ample for the reversible charge/discharge process of Bi ↔ Bi_2O_3. This spaciousness, coupled with the unique structure, facilitates rapid electron transfer, reduces activation energy, and enhances

stability. Consequently, TRA-BiOCl demonstrates a high capacity of 366 mA h/g (nearly reaching the theoretical capacity of 384.7 mA h/g) and exhibits good stability, retaining 82% of its capacity after 5000 cycles. Moreover, a $NiCo_2O_4$//TRA-BiOCl full battery is constructed, showcasing a high energy density of 116 Wh/kg [15] .

- ***Khalaj et al. (2019)*** presented a novel graphene/cobalt oxide/polypyrrole ternary nanocomposite synthesized via a two-step technique. Cobalt oxide nanoparticles were initially integrated into graphene sheets using a chemical precipitation method. Subsequently, a conductive polypyrrole thin film was deposited onto the surface through in-situ polymerization. These nanocomposites were then applied onto copper/copper hydroxide substrates prepared via alkaline solution immersion. Electrochemical assessments in a three-electrode system revealed a notable specific capacitance of 422 F/g at a scan rate of 10 mV/s and 385 F/g at a current density of 1 A/g in 6 M potassium hydroxide. Additionally, an energy density of 13.4 Wh/kg was achieved at a power density of 250 W/kg. The improved electrochemical performance of the ternary nanocomposite stems from the synergistic interactions among its three constituents [16].
- ***Mariappan et al. (2019)*** conducted a study where they synthesized ternary hybrid nanocomposites employing different weight ratios of reduced graphene oxide, polypyrrole (PPy), and either cobalt ferrite or iron oxide using a hydrothermal approach. They found specific capacitance values of 261 F/g, 141 F/g, 108 F/g, and 68.3 F/g at 1 A/g in 1 M lithium nitrate electrolyte for compositions comprising 37 wt.% reduced graphene oxide /58 wt.% polypyrrole /5 wt.% iron oxide, 32 wt.% reduced graphene oxide/54 wt.% polypyrrole /14 wt.% iron oxide, 37 wt.% reduced graphene oxide /58 wt.% polypyrrole /5 wt.% cobalt ferrite, and 32 wt.% reduced graphene oxide /54 wt.% polypyrrole /14 wt.% cobalt ferrite, respectively [17].
- ***Mezgebe et al. (2019)*** present an uncomplicated method for controlling the core/shell architecture of manganese dioxide nanorods and polyaniline through in-situ hydrothermal polymerization. The structure and morphology of the resulting polyaniline-coated manganese dioxide nanorods were meticulously characterized, and their capacitance enhancement was thoroughly investigated. Experimental findings unveiled that the specific capacitance of the manganese dioxide-polyaniline nanocomposite (with 40% manganese dioxide relative to aniline monomer) reached 665 F/g at a current density of 1 A/g, surpassing that of pristine manganese dioxide (273 F/g) and pristine polyaniline (434 F/g). Moreover, the nanocomposite retained 82% of its original capacitance after 1500 consecutive cyclic voltammetry cycles at a scan rate of 100 mV/s [18].

- ***Rauhala et al. (2020)*** addressed the limited stability of polyaniline as an electrode material for electrochemical energy storage due to its vulnerability to degradation. They proposed enhancing durability through two methods: incorporating a carbonaceous support and applying thermal treatments. The study focused on investigating the degradation of a composite consisting of polyaniline and acid-treated multi-walled carbon nanotubes when utilized as a positive electrode in a lithium-ion cell. The composite was prepared by facile ultrasonic-assisted mixing of aqueous colloids, followed by processing into binder-free electrodes and vacuum heat treatment (120–180 °C). Polyaniline alone displayed poor cycling stability, attributed to declining conductivity and alterations in particle morphology. The inclusion of acid-treated multi-walled carbon nanotubes was found to mitigate these changes and enhance the electrochemical accessibility of polyaniline within the composite. Furthermore, heat treatment improved the composite's stability during open circuit conditions by facilitating polymer cross-linking. However, this stabilizing effect diminished with prolonged cycling. Post-cycling electrode analysis revealed dedoping and side reactions with the electrolyte in both pristine and heat-treated composites, albeit to a greater extent in the pristine composite [19].
- ***Wang et al. (2020)*** reported the electrochemical performance of a polyaniline-coated polylactic acid/multi-walled carbon nanotubes composite film electrode in two commonly used electrolytes: sulfuric acid (acidic) and sodium sulfate (neutral). They found that the optimal aqueous electrolyte for polyaniline-based electrodes in supercapacitors was a mixed electrolyte containing 1.1 mol/L sulfuric acid and 0.1 mol/L sodium sulfate. Compared to the standard acidic electrolyte (1.0 mol/L sulfuric acid), this mixed electrolyte enhanced the specific capacitance by 17.28%. Analysis of the electrode and electrolytes after electrochemical cycles revealed that the addition of neutral electrolyte sodium sulfate effectively inhibited the acid-induced hydrolysis of polyaniline. This inhibition led to improvements in specific capacitance and cycling stability [20].
- ***Viswanathan et al. (2020)*** investigated a nanocomposite consisting of reduced graphene oxide and vanadium pentoxide synthesized through a chemical method, with a composition of 7.69% reduced graphene oxide and 92.31% vanadium pentoxide by weight. They examined the role of faradaic vanadium pentoxide in storing high energy when combined with reduced graphene oxide. Parameters obtained from the linear discharge approach include a specific capacitance of 120.62 F/g, a specific capacity of 144.74 C/g, an energy density of 24.12 Wh/kg, a power density of 2.647 kW/kg, and a

columbic efficiency of 79.22% at a current density of 2 A/g. The nanocomposite maintained 100% of its initial specific capacitance over 5000 cycles and retained 38% of its initial specific capacitance [21].

- ***Shinde et al. (2021)*** introduced a room-temperature method for fabricating ultrathin bismuth oxychloride supercapacitor electrode material on three-dimensional nickel foam, employing a simple solution-based approach. The resulting free-standing bismuth oxychloride ultrathin petal-type electrode material underwent thorough characterization for crystal structure, surface morphology, and surface area using various analytical techniques, before being applied in electrochemical supercapacitors. Electrochemical analysis revealed an optimal specific capacitance of 379 F/g at a current density of 1.25 A/g. Assembled symmetric electrochemical supercapacitor devices with two identical bismuth oxychloride electrodes and a 6 M potassium hydroxide electrolyte yielded an excellent energy density of 12 Wh/kg and power density of 1125 W/kg, with approximately 80% retention over 5000 cycles [22].
- ***Fu et al. (2021)*** presented a microwave synthetic method to grow vanadium pentoxide on graphene, which is notable for its simplicity, speed, energy efficiency, and effectiveness. This method yielded uniform vanadium pentoxide nanoparticles, approximately 20 nm in size, evenly dispersed on graphene. The resulting vanadium pentoxide/graphene composites were utilized in symmetrical supercapacitors, demonstrating maximum specific capacitances of 673.2 F/g at 1 A/g current density, along with 96.8% capacitance retention after 10,000 cycles at 1 A g^{-1}. Moreover, the assembled devices exhibited an outstanding energy density of 46.8 Wh/kg at 499.4 W/kg power density characteristics [23].
- ***Rajkumar et al. (2021)*** reported the synthesis of iron cobalt oxide/polyaniline through an in-situ polymerization method, aiming to explore its suitability as an electrode material for supercapacitors. The iron cobalt oxide/polyaniline composite underwent comprehensive characterization using various physico-chemical techniques. Electrochemical analyses, including cyclic voltammetry (CV), galvanostatic charge-discharge (GCD), and electrochemical impedance spectroscopy (EIS), were employed to assess its performance. Their results demonstrated a notable specific capacity value of 940 C/g at a current density of 1 A/g through GCD measurements. This impressive capacitive behavior was attributed to the material's porous nanorod-like structure, which provided a large number of active sites, facilitating efficient ion and electron transport. The straightforward one-step fabrication process further underscored the material's

potential as an electrode material for advanced energy storage systems, emphasizing its high specific capacity and promising applicability [24].

- ***Li et al. (2021)*** stated the synthesis of nickel cobalt tetrasulfide nanoneedles via a two-step hydrothermal approach on nickel foam. Subsequently, a layer of polypyrrole was applied onto the surface of the nickel-cobalt tetrasulfide nanoneedles through in-situ polymerization. The resulting nickel-cobalt tetrasulfide-polypyrrole composite was evaluated for its potential in supercapacitor applications, revealing a capacitance of 1842.8 F/g at 1 A/g. Furthermore, an asymmetric supercapacitor device, featuring an activated carbon negative electrode and nickel-cobalt tetrasulfide-polypyrrole positive electrodes, showcased an energy density of 41.2 Wh/kg at 402.2 W/kg, along with remarkable charge-discharge cycling stability (92.8% retention after 5000 cycles). These findings highlight the promising prospects of nickel-cobalt tetrasulfide-polypyrrole electrodes as materials for energy storage applications [25].
- ***He et al. (2022)*** reported the performance of a wood aerogel/polypyrrole composite electrode, demonstrating its remarkable areal capacitance of 7.68 F/cm^2 at a current density of 1.0 mA/cm^2. They observed an acceptable capacitance retention of 82.6% over 10,000 cycles at 10 mA/cm^2. Furthermore, they achieved an impressive energy density of 20 Wh/kg at a power density of 161.6 W/kg using a symmetrical supercapacitor device employing the wood aerogel-based electrode [26].
- ***Kenesi et al. (2022)*** conducted a study where they synthesized a nanocomposite consisting of polyaniline cadmium oxide graphene oxide using the co-precipitation method. They then assessed its electrochemical performance, revealing promising results. The polyaniline cadmium oxide graphene oxide nanocomposite displayed superior electrochemical properties, boasting a specific capacity of 647 F/g, an energy density of 116.6 W h/kg, and a power density of 388 W/kg when compared to alternative electrodes. Stability tests indicated initial capacity maintenance of approximately 82% after 500 charge-discharge cycles, suggesting favorable electrochemical stability. Additionally, impedance spectroscopy studies revealed lower internal and charge transfer resistance in the nanocomposite electrode materials [27].
- ***Bi et al. (2022)*** have presented the synthesis of V^{4+}-rich vanadium pentoxide/carbon aerogel composites as electrode materials for supercapacitors using in-situ hydrolysis-condensation processing. The presence of carbon aerogel facilitates the deposition of amorphous vanadium oxide and catalyzes the crystallization of V^{4+}-rich vanadium pentoxide nanosheets at significantly lower temperatures. The uniform distribution of vanadium pentoxide nanosheets within carbon aerogel provides a large specific area and

numerous reactive sites, while carbon aerogel also enhances electrical conductivity and structural integrity synergistically. Furthermore, the abundance of V^{4+} ions enhance the intrinsic electrical conductivity of vanadium pentoxide, facilitates ion diffusion, and catalyzes electrochemical reactions. As a result, V^{4+}- rich vanadium pentoxide/carbon aerogel exhibits significantly enhanced specific capacitance, reaching 405 F/g at 0.5 A/g current density [28].

- ***Feng et al. (2023)*** describe the fabrication of high-performance negative electrodes using bismuth carbonate ($Bi_2O_2CO_3$) nanosheets wrapped around bismuth oxide (Bi_2O_3) arrays, employing a combination of electrical substitution, oxidative calcination, and hydrothermal methods. The resulting copper foam/Bi_2O_3/$Bi_2O_2CO_3$ structure exhibits a surface with cross-linked laminar features, effectively shortening the path for electrolyte penetration. Through direct replacement growth of Bi on copper substrates, subsequent composites are achieved, enabling improved adhesion between the electrode material and the collector, facilitating charge transfer, and achieving ultrahigh loadings of 13.2 mg/cm^2 [29].
- In addressing the energy density challenge of supercapacitors, ***Rohith R et al. (2023)*** propose a novel solution: a hybrid electrode combining polyaniline (PANI) and vanadium pentoxide V_2O_5 nanoparticles. Synthesized via an organic-mediated self-stabilized polymerization method, PANI, when paired with nanostructured V_2O_5, exhibits a synergistic effect, overcoming the limitations of individual materials. Through meticulous evaluation in both three and two-electrode symmetric configurations, the PANI:V_2O_5 hybrid electrode showcases impressive electrochemical performance. Notably, among the varied compositions studied, PANI:V_2O_5 = 3:1 ratio electrode emerges as exceptional, boasting a gravimetric capacitance of 498 F/g at a current density of 1 A/g. Even under high current densities, such as 20 A/g, this electrode maintains 84% of its initial capacitance [30].
- ***Temam et al. (2023)*** deliver a broad review of vanadium pentoxide (V_2O_5) as a promising electroactive material for supercapacitors. However, the widespread adoption of V_2O_5 is hindered by its low conductivity and lacking cycling lifespan. To address these issues, researchers have proposed various strategies including structural, morphological, and electronic property modifications, as well as doping and the formation of nanocomposites. These approaches aim to enhance the performance of V_2O_5-based electrodes by mitigating the limitations [31].
- ***Vishwakarma et al. (2024)*** synthesized V_2O_5 using both solvothermal and hydrothermal methods. Their findings revealed a notable difference in the specific capacitance of

V_2O_5 produced by the two methods. Specifically, V_2O_5 synthesized via the hydrothermal method exhibited a two-fold extension in capacitance compared to that produced by the solvothermal method. Their experimental findings indicated that V_2O_5 nanoparticles synthesized through hydrothermal means could offer a capacitance of 121 F/g, while those synthesized via solvothermal methods yielded a capacitance of 72 F/g. These results were obtained at a current density of 1 A/g within the potential range of 0 to 0.45 V in an aqueous electrolyte [32].

2.2. Research gap identification

After reviewing various works of literature on metal oxides and conductive polymers for renewable energy storage systems, the following research gaps have emerged:

a) While V_2O_5 has commonly been synthesized for supercapacitor electrodes using methods like solvothermal or hydrothermal processes, there is a notable absence of studies employing the facile sol-gel method.

b) Despite extensive research on V_2O_5-PANI nanocomposites synthesized through the electropolymerization method and their electrochemical performance, there is a lack of investigations into synthesizing these nanocomposites through in situ polymerization, particularly with varied weight percentages of V_2O_5 in PANI.

c) The electrochemical performance of V_2O_5-PANI nanocomposites in 6 M potassium hydroxide (KOH) electrolytes is seldom documented in the literature.

d) There is a lack of research on synthesizing BiOCl as an electrode material using different solvents such as ethylene glycol (EG), diethylene glycol (DEG), and triethylene glycol (TEG) for supercapacitor applications.

e) The study into PPy-BiOCl nanocomposite electrode materials for supercapacitor applications, along with their practical feasibility, is notably absent in the literature.

To address the identified research gaps, the present study aims to investigate optimal metal oxides and conducting polymers, synthesizing their nanocomposites through user-friendly techniques for energy storage applications. The study will prioritize the production of these materials in large quantities, with a focus on eco-friendliness, easy accessibility, and cost-effectiveness for the betterment of society.

2.3. Objectives of the Present Work

The main aim and objectives of the study of the present research are:

a) Preparation and characterization of metal oxides nanoparticles to study their various properties.
b) Synthesis of the conducting polymers and fabrication of nanocomposite.
c) Prepared nanocomposite will be characterized with different techniques in order to check their utility in applications for renewable energy sources.

References

[1] Wang J, Xian H, Peng T, Sun H, Zheng F. Three-dimensional graphene-wrapped PANI nanofiber composite as electrode material for supercapacitors. Rsc Advances. 2015;5(18):13607-12.

[2] Balasubramanian S, Purushothaman KK. Carbon coated flowery V_2O_5 nanostructure as novel electrode material for high performance supercapacitors. Electrochimica Acta. 2015;186:285-91.

[3] Simotwo SK, DelRe C, Kalra V. Supercapacitor electrodes based on high-purity electrospun polyaniline and polyaniline–carbon nanotube nanofibers. ACS applied materials & interfaces. 2016 Aug 24;8(33):21261-9.

[4] Huang Y, Zhu M, Pei Z, Huang Y, Geng H, Zhi C. Extremely stable polypyrrole achieved via molecular ordering for highly flexible supercapacitors. ACS Applied Materials & Interfaces. 2016;8(3):2435-40.

[5] Zhao J, Wu J, Li B, Du W, Huang Q, Zheng M, Xue H, Pang H. Facile synthesis of polypyrrole nanowires for high-performance supercapacitor electrode materials. Progress in Natural Science: Materials International. 2016;26(3):237-42.

[6] Zheng J, Zhang Y, Jing X, Wang Q, Hu T, Xing N, Meng C. Improvement of the specific capacitance of V2O5 nanobelts as supercapacitor electrode by tungsten doping. Materials Chemistry and Physics. 2017;186:5-10.

[7] Xu L, Jia M, Li Y, Zhang S, Jin X. Design and synthesis of graphene/activated carbon/polypyrrole flexible supercapacitor electrodes. RSC advances. 2017;7(50):31342-51.

[8] Wang R, Han M, Zhao Q, Ren Z, Guo X, Xu C, Hu N, Lu L. Hydrothermal synthesis of nanostructured graphene/polyaniline composites as high-capacitance electrode materials for supercapacitors. Scientific reports. 2017;7(1):44562.

[9] Nie G, Lu X, Wang W, Chi M, Jiang Y, Wang C. One-dimensional polyaniline thorn/BiOCl chip heterostructures: self-sacrificial template-induced synthesis and electrochemical performance. Materials Chemistry Frontiers. 2017;1(5):859-66.

[10] Palsaniya S, Nemade HB, Dasmahapatra AK. Synthesis of polyaniline/graphene/MoS_2 nanocomposite for high performance supercapacitor electrode. Polymer. 2018;150:150-8.

[11] Liu X, Wang J, Yang G. In situ growth of the $Ni_3V_2O_8$@ PANI composite electrode for flexible and transparent symmetric supercapacitors. ACS applied materials & interfaces. 2018;10(24):20688-95.

[12] Hou ZQ, Yang ZG, Gao YP. Synthesis of vanadium oxides nanosheets as anode material for asymmetric supercapacitor. Chemical Papers. 2018;72(11):2849-57.

[13] Hong W, Wang L, Liu K, Han X, Zhou Y, Gao P, Ding R, Liu E. Asymmetric supercapacitor constructed by self-assembled camellia-like BiOCl and activated carbon microspheres derived from sweet potato starch. Journal of Alloys and Compounds. 2018;746:292-300.

[14] Dutta PK, Myung Y, Kulangaramadom Venkiteswaran R, Mehdi L, Browning N, Banerjee P, Mitra S. Mechanism of Na-ion storage in BiOCl anode and the sodium-ion battery formation. The Journal of Physical Chemistry C. 2019;123(18):11500-7.

[15] Zhu Q, Cheng M, Yang X, Zhang B, Wan Z, Xiao Q, Yu Y. Self-supported ultrathin bismuth nanosheets acquired by in situ topotactic transformation of BiOCl as a high performance aqueous anode material. Journal of materials chemistry A. 2019;7(12):6784-92.

[16] Khalaj M, Sedghi A, Miankushki HN, Golkhatmi SZ. Synthesis of novel graphene/Co_3O_4/polypyrrole ternary nanocomposites as electrochemically enhanced supercapacitor electrodes. Energy. 2019;188:116088.

[17] Mariappan CR, Gajraj V, Gade S, Kumar A, Dsoke S, Indris S, Ehrenberg H, Prakash GV, Jose R. Synthesis and electrochemical properties of rGO/polypyrrole/ferrites nanocomposites obtained via a hydrothermal route for hybrid aqueous supercapacitors. Journal of Electroanalytical Chemistry. 2019;845:72-83.

[18] Mezgebe MM, Xu K, Wei G, Guang S, Xu H. Polyaniline wrapped manganese dioxide nanorods: Facile synthesis and as an electrode material for supercapacitors with remarkable electrochemical properties. Journal of Alloys and Compounds. 2019;794:634-44.

[19] Rauhala T, Davodi F, Sainio J, Sorsa O, Kallio T. On the stability of polyaniline/carbon nanotube composites as binder-free positive electrodes for electrochemical energy storage. Electrochimica Acta. 2020;336:135735.

[20] Wang Q, Li J, Wang D, Niu J, Du P, Liu J, Liu P. Enhanced electrochemical performance of polyaniline-based electrode for supercapacitors in mixed aqueous electrolyte. Electrochimica Acta. 2020;349:136348.

[21] Viswanathan A, Shetty AN. Reduced graphene oxide/vanadium pentoxide nanocomposite as electrode material for highly rate capable and durable supercapacitors. Journal of Energy Storage. 2020;27:101103.

[22] Shinde NM, Ghule BG, Raut SD, Narwade SH, Pak JJ, Mane RS. Hopping electrochemical supercapacitor performance of ultrathin BiOCl petals grown by a room-temperature soft-chemical process. Energy & Fuels. 2021;35(8):6892-7.

[23] Fu M, Zhuang Q, Zhu Z, Zhang Z, Chen W, Liu Q, Yu H. Facile synthesis of V_2O_5/graphene composites as advanced electrode materials in supercapacitors. Journal of Alloys and Compounds. 2021;862:158006.

[24] Rajkumar S, Elanthamilan E, Merlin JP, Sathiyan A. Enhanced electrochemical behaviour of $FeCo_2O_4$/PANI electrode material for supercapacitors. Journal of Alloys and Compounds. 2021 Sep 5;874:159876.

[25] Li J, Zou Y, Li B, Xu F, Chu H, Qiu S, Zhang J, Sun L, Xiang C. Polypyrrole-wrapped $NiCo_2S_4$ nanoneedles as an electrode material for supercapacitor applications. Ceramics International. 2021;47(12):16562-9.

[26] He W, Qiang H, Liang S, Guo F, Wang R, Cao J, Guo Z, Pang Q, Wei B, Sun J. Hierarchically porous wood aerogel/polypyrrole (PPy) composite thick electrode for supercapacitor. Chemical Engineering Journal. 2022;446:137331.

[27] Kenesi AG, Ghorbani M, Lashkenari MS. High electrochemical performance of PANI/CdO nanocomposite based on graphene oxide as a hybrid electrode materials for supercapacitor application. International Journal of Hydrogen Energy. 2022;47(91):38849-61.

[28] Bi W, Deng S, Tang H, Liu Y, Shen J, Gao G, Wu G, Atif M, AlSalhi MS, Cao G. Coherent V^{4+}-rich V_2O_5/carbon aerogel nanocomposites for high performance supercapacitors. Science China Materials. 2022;65(7):1797-804.

[29] Feng Z, Zhang B, Ji P, Hu R, Gao B, Wang X, Meng YL, Song XZ, Tan Z. Bi_2O_3@ $Bi_2O_2CO_3$ Heterostructure Electrode for Significant Enhancement of Electrochemical Capacity. ACS Applied Energy Materials. 2023;6(17):8808-17.

[30] Rohith R, Prasannakumar AT, Manju V, Mohan RR, Varma SJ. Flexible, symmetric supercapacitor using self-stabilized dispersion-polymerised polyaniline/V_2O_5 hybrid electrodes. Chemical Engineering Journal. 2023;467:143499.

[31] Temam AG, Alshoaibi A, Getaneh SA, Awada C, Nwanya AC, Ejikeme PM, Ezema FI. Recent progress on V_2O_5 based electroactive materials: Synthesis, properties, and supercapacitor application. Current Opinion in Electrochemistry. 2023;38:101239.

[32] Vishwakarma N, Mashangva TT, Kumar M, Srivastava A, Sharma A. Impact of hydrothermal and solvent-thermal synthesis on the electrochemical performance of V_2O_5. Materials Letters. 2024 :136137.

Chapter 3

Materials and Methods

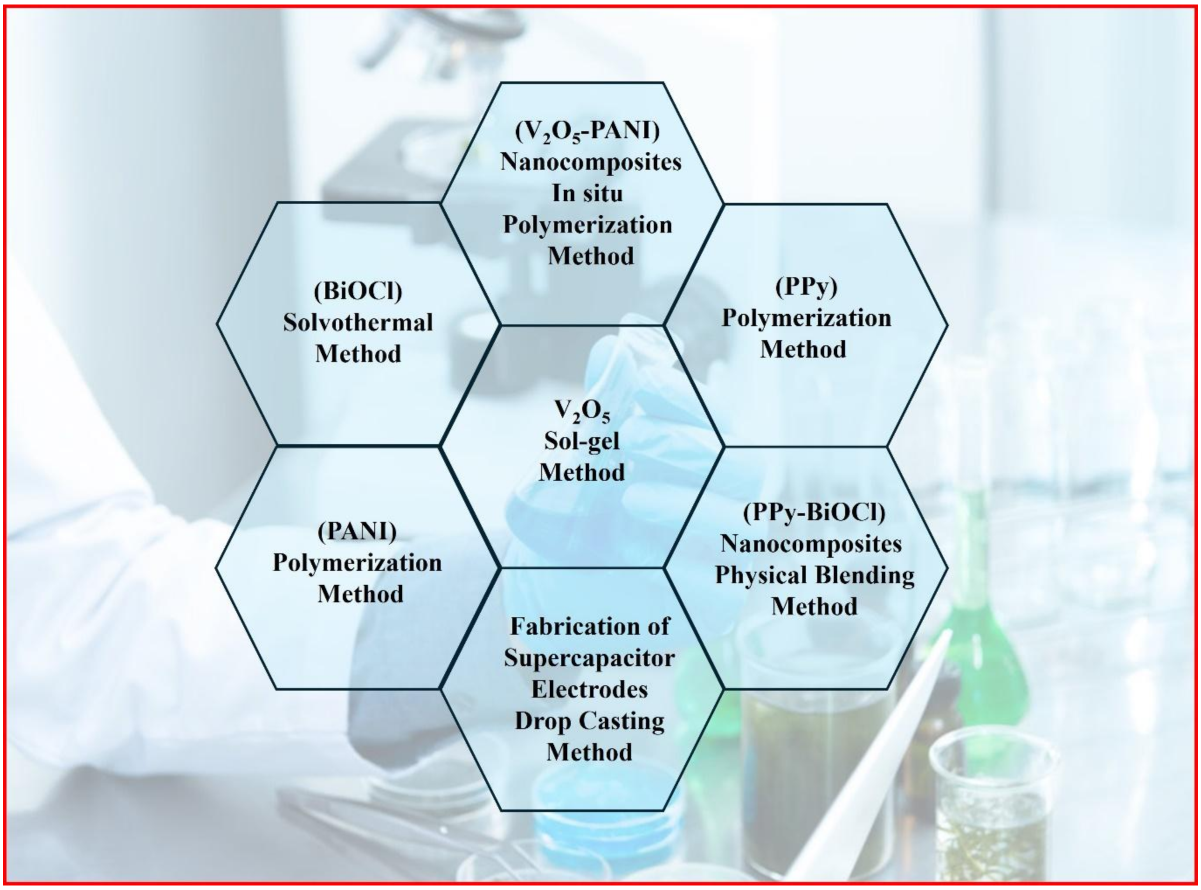

This chapter focuses on the experimental techniques utilized and the methodology described for preparing and characterizing metal oxides and conducting polymers for Supercapacitor applications.

3.1. Materials

Table 3.1 displays details about the precursor compounds, reagents, and other chemicals utilized in the current study.

Table 3.1 Materials utilized in the present work.

Chemicals	Provider	Molecular weight (g/mol)
Ammonium metavanadate	LOBA Chemie	116.98
Ammonium peroxydisulfate	LOBA Chemie	228.20
Nitric acid	LOBA Chemie	63.01
Ethanol	LOBA Chemie	46.068
Anilinium hydrochloride	LOBA Chemie	129.60
N-methylpyrrolidone	LOBA Chemie	99.133
Potassium hydroxide	LOBA Chemie	56.11
Hydrochloric acid	LOBA Chemie	36.46
Acetylene black	MIT Corporation	12.01
Conducting nickel foam	Nanoshel	----
Polyvinylidene fluoride	MIT Corporation	~1,000,000
Ethylene glycol	LOBA Chemie	62.07
Diethylene glycol	LOBA Chemie	106.12
Triethylene glycol	LOBA Chemie	150.17
Bismuth (III) nitrate	LOBA Chemie	394.99
Sodium chlorate	SIGMA	106.44
Pyrrole	LOBA Chemie	67.09
Ferric chloride hexahydrate	LOBA Chemie	270.29
Methyl orange	LOBA Chemie	327.33

3.2. Synthesis Process

3.2.1. Sol gel synthesis of V_2O_5

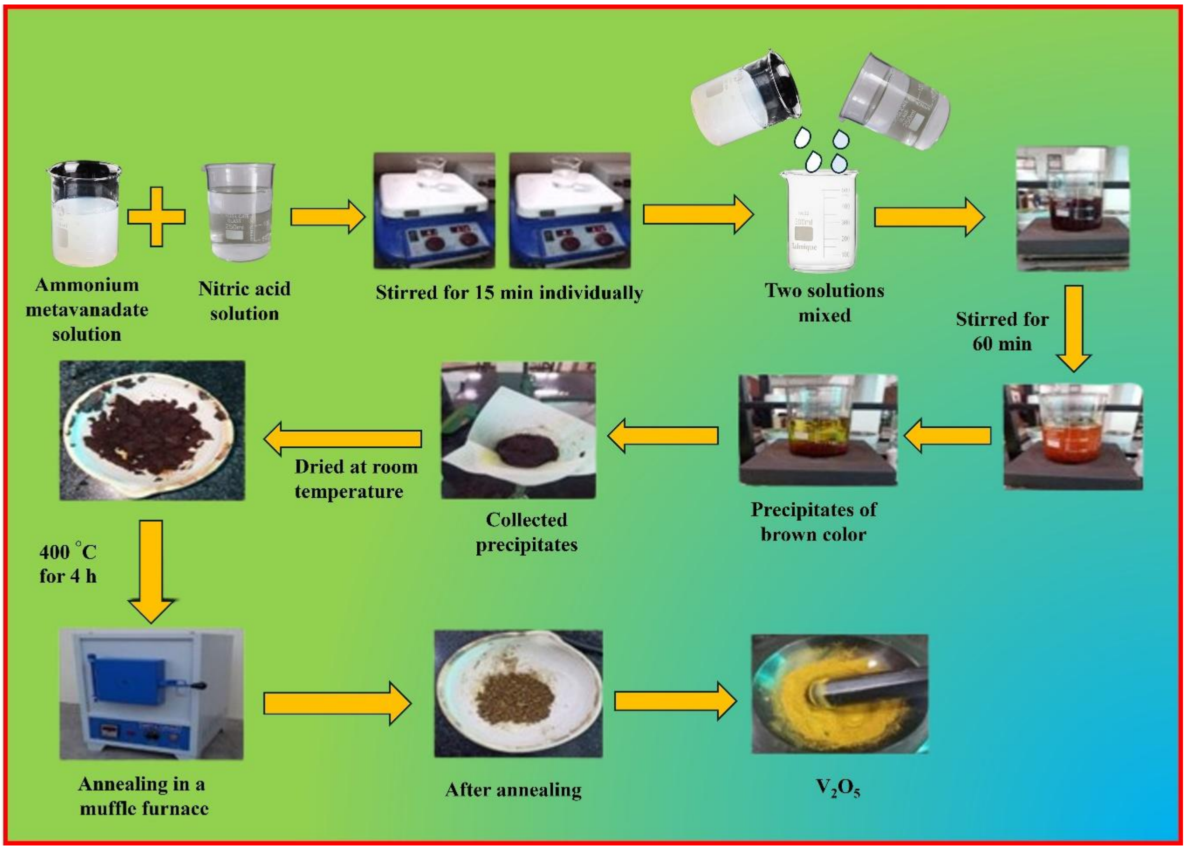

Figure 3.1. Preparation of V_2O_5 by Sol-gel method.

The sol-gel process is a wet chemical technique used for creating various nanostructures, particularly metal oxide nanoparticles. In this method, a molecular precursor, often a metal alkoxide, is dissolved in water or alcohol. Heating and stirring then facilitate its conversion into a gel through hydrolysis or alcoholises. As the gel is initially wet, suitable drying methods are employed based on the desired properties and application. Once dried, the gels are transformed into powder form and subjected to calcination. The sol-gel method provides cost-effectiveness, and its modest reaction temperature enables precise control over the chemical composition of the resulting products. For the preparation of V_2O_5 metal oxide in this study, 7 gm of ammonium metavanadate and 3.37 ml of nitric acid were dissolved individually in 150 ml of distilled water and stirred for 15 min. Afterward, the two solutions were mixed in a beaker and stirred for 60 min. Later, the solution was allowed to settle down for the next 24 h, resulting in the formation of precipitates of brown color. The precipitates were collected and to dry at room temperature for 4 days. The final product was subjected to annealing in a muffle furnace at 400 °C for 4 h (see Figure 3.1).

3.2.2. Synthesis of PANI and their nanocomposites

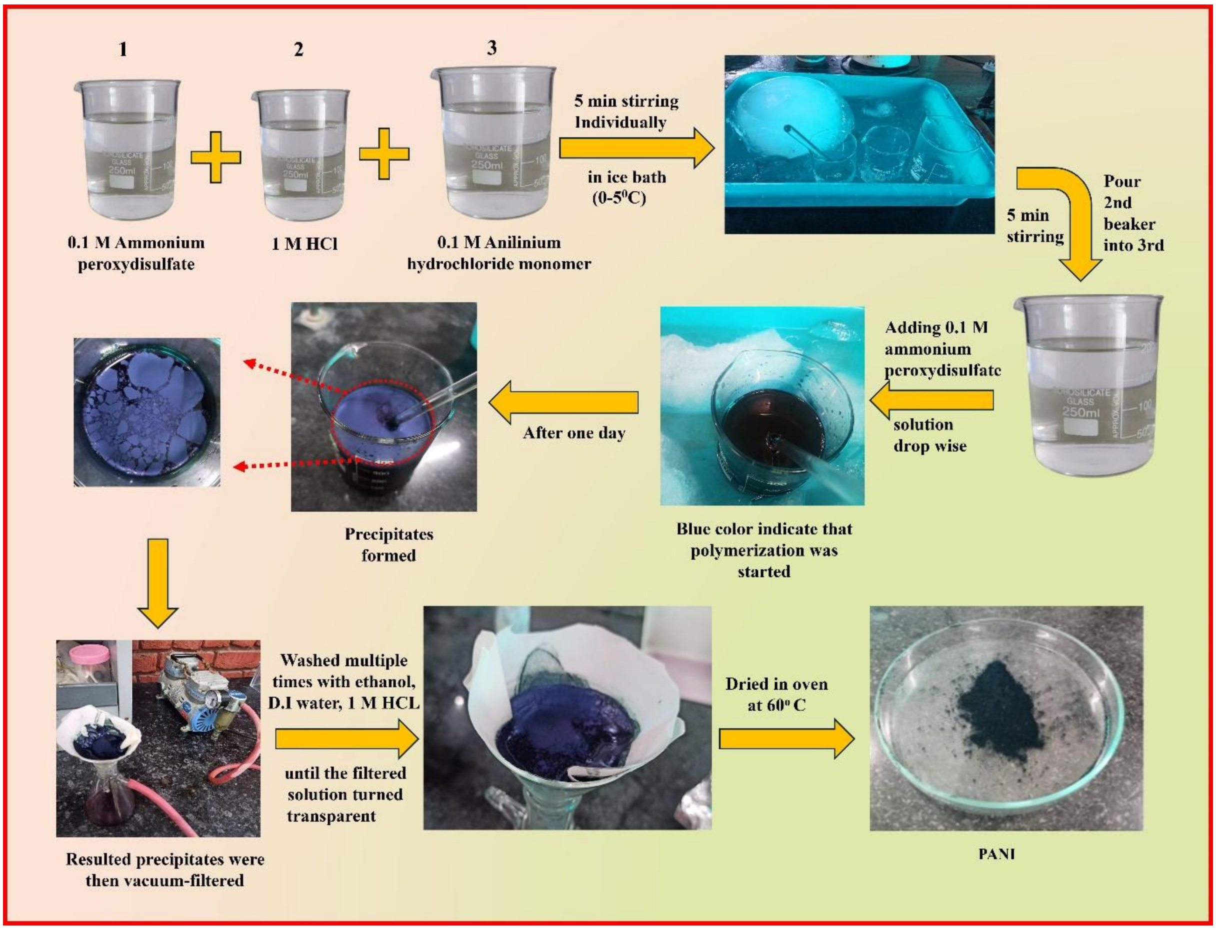

Figure 3.2. Synthesis of PANI by polymerization method.

Polyaniline (PANI) is synthesized through the polymerization of aniline monomers. The chemical oxidative polymerization method is used to synthesize PANI polymer. This method involves the oxidative polymerization of aniline monomers using various oxidizing agents such as ammonium persulfate (APS), ferric chloride ($FeCl_3$), hydrogen peroxide (H_2O_2), or potassium dichromate ($K_2Cr_2O_7$). Typically, aniline monomers are dissolved in an acidic medium, and the oxidizing agent is added slowly to initiate the polymerization process. This method is widely used due to its simplicity and scalability. Polyaniline is synthesized by oxidative polymerization of 0.1 M anilinium hydrochloride monomer in 1 M HCl with an equimolar amount of ammonium persulfate ($(NH_4)_2S_2O_8$) solution and cooled in the ice bath (0–4 °C). It took 14 h to complete the polymerization reaction with the dropwise addition of ($(NH_4)_2S_2O_8$) solution to the monomer. The resulting mixture is then vacuum-filtered and washed multiple times with 1 M HCl, ethanol, and distilled water until the filtered solution turns transparent. Finally, the obtained precipitates are dried in a vacuum oven at 60 °C for 8 h. Similarly, polyaniline nanocomposites were also prepared with the addition of 10, 20, and 30 wt.% of V_2O_5 in 0.1 M anilinium hydrochloride solution named PV1, PV2, and PV3, respectively. Figure 3.2 shows the synthesis process of PANI.

3.2.3. Solvothermal synthesis of BiOCl

A solvothermal process occurs within a closed environment where a solvent, either aqueous or non-aqueous, is present at a temperature exceeding the boiling point of the solvent and under elevated pressure. In this study, a one-step solvothermal method is used to synthesize different BiOCl 3D hierarchical nanostructures via various synthesis solvents such as ethylene glycol (EG), diethylene glycol (DEG), and triethylene glycol (TEG) . In the synthesis method 1.458 g of $Bi(NO_3)_3.5H_2O$ dissolved in 75 ml of EG, DEG, and TEG solvents individually and ultrasonicated solution for 20 min. After the ultrasonication process, 0.318 g of $NaClO_3$ is added to the solution and again ultrasonicated for 20 min.

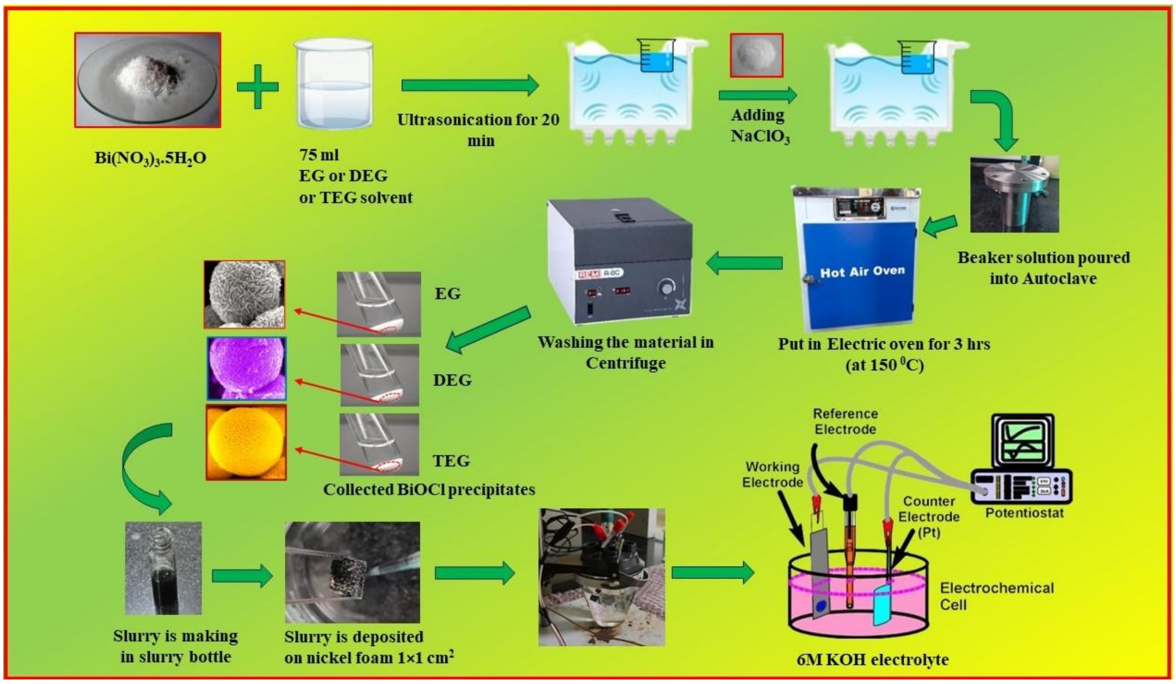

Figure 3.3. Solvothermal synthesis of BiOCl and their electrodes testing in a three-electrode system.

Subsequently, the resulting solution is poured into a 100 ml autoclave and heated for 3 h at 150 ^{0}C in a hot air oven. Once the mixture solution is cooled to room temperature, centrifugation is employed to collect the produced precipitates. These collected precipitates are afterward subjected to seven washes with deionized water to remove any impurities in the solution. Finally, the material endured drying in an oven at 60°C for 12 h. The workflow of the synthesis method is illustrated in Figure 3.3.

3.2.4. Synthesis of PPy and their nanocomposites

Polypyrrole (PPy) is synthesized through the polymerization of pyrrole monomers. The chemical oxidative polymerization method is used to synthesize PPy polymer.

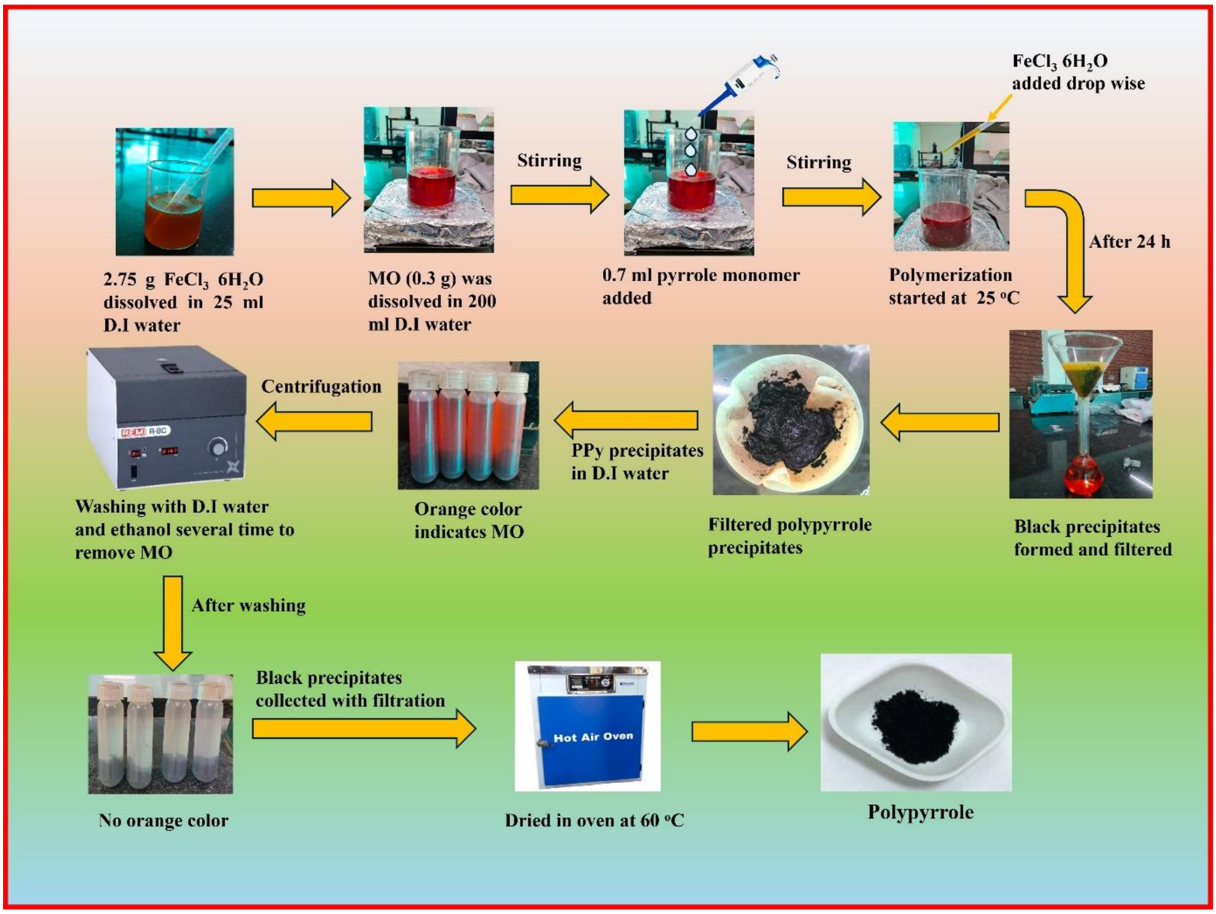

Figure 3.4. Synthesis of PPy by oxidative polymerization method.

This method involves the oxidative polymerization of pyrrole monomers using $FeCl_3$ as an oxidizing agent. In this study, 0.2 g of methyl orange is mixed in 200 ml of deionized water in a beaker. Subsequently, 0.70 ml of pyrrole monomer is added to create mixture “A”. Separately, 2.6 g of ferric chloride hexahydrate is dissolved in 25 ml of deionized water to prepare an oxidant solution, labeled solution “B”. Solution “B” is then added to mixture “A” in a 300 ml beaker. The polymerization process occurred at room temperature, specifically 25°C. Afterward, the resultant products are gathered through filtration and underwent washing using a centrifugation machine. Water and ethanol are employed as medium for washing to eliminate the oxidant, methyl orange, and oligomers. Figure 3.4 displays the synthesis procedure of PPy by the oxidative polymerization method. PPy-BiOCl nanocomposites are fabricated via a physical blending method, as depicted in Figure 3.5. The weight ratios of PPy in BiOCl are 5%, 7%, and 9%. The nanocomposite components undergo thorough mixing using a mortar and pestle to achieve a homogeneous blend.

Figure 3.5. The physical blending process is employed to produce the PPy-BiOCl nanocomposites.

3.2.5. Fabrication of Supercapacitor Electrodes

A three-electrode apparatus is being used to conduct the electrochemical examination at room temperature. The electrodes include the working electrode (ink-loaded nickel foam), reference electrode (Ag/AgCl), and counter electrode (platinum wire). The experiment is being carried out with 6 M KOH as the electrolyte. The mixture of active material V_2O_5-PANI, acetylene black, and Polyvinylidene fluoride (PVDF) binder are used to develop electrodes by weight ratio of 80:10:10. Firstly, the mixture is properly grinded and an adequate amount of N-Methyl-2-pyrrolidone (NMP) is added to form the ink, which is further ultrasonicated for 20 min. Afterward, nickel foam is dipped in a solution of HCl and ultrasonicated for 25 min to remove any oxide layer or impurities. Later, the nickel foam is rinsed with deionized water to eliminate any remaining acid. After removing any impurities, nickel foam is immersed in ethanol for a couple of minutes and then rinsed in the deionized water. Finally, the nickel foam is dried in a vacuum oven.

The previously formed ink is dropped cast onto nickel foam and subjected to vacuum conditions at 60 ^{0}C for 12 h to dry. Figure 3.6 shows various steps involved in fabricating the nanocomposite working electrode. A similar methodology is adopted for the preparation of V_2O_5, PANI, BiOCl, PPy, and PPy-BiOCl electrodes.

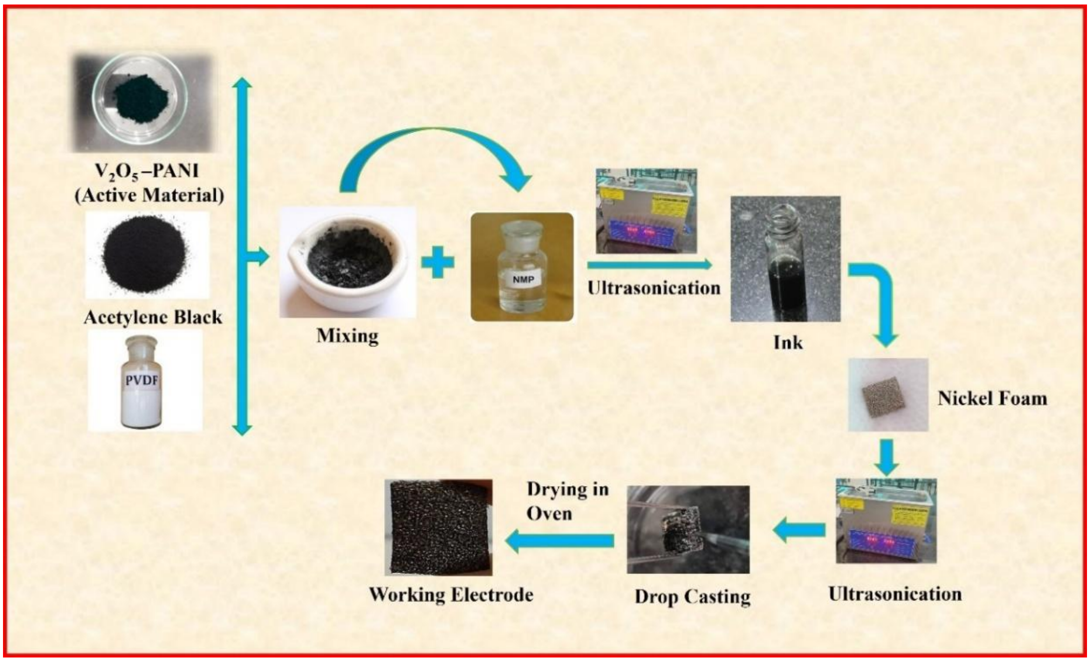

Figure 3.6. Fabrication of Supercapacitor electrodes.

3.3. Characterization Techniques

The sample's structural, morphological, optical, and electrochemical features were explored through a series of characterization techniques.

3.3.1. X-ray diffraction (XRD)

X-ray diffraction stands out as a comprehensive and non-destructive method for analyzing the crystalline properties of materials, identifying phases, and determining unit cell features. When incident rays interact with a material sample, it leads to constructive interference. According to "Bragg's law ($n\lambda = 2dsin\theta$), the path difference between the reflected beams must be an integer multiple of the X-ray wavelength" [1]. When samples are scanned over various 2θ angles, the resulting data is displayed as a plot of 2θ versus diffraction intensity. To conduct these analyses, a Bruker D8 Gen 10 theta/theta powder X-ray diffractometer was utilized. This instrument utilizes Cu Kα radiation, with a wavelength of 0.1542 nm, and is used at 40 kV voltage and 30 mA current. Every sample's diffraction pattern was captured at a rate of 5 degrees per second, spanning a 2θ range from 5 to 80 degrees. Obtained outcomes were then compared with corresponding samples in the standard JCPDS database.

3.3.2. Field emission scanning electron microscope (FESEM)

The electrochemical activity of an electrode in a supercapacitor is heavily influenced by the particle size and shape. To visualize the diverse micro- and nano-sized morphological features of the samples created for this study, electron microscopy was employed. This advanced technique applies a focused beam of electrons to capture high-resolution images of a specimen. In electron microscopy, electrons are generated by an electron gun and then focused onto the sample through a series of electromagnetic lenses. Upon striking the sample, these electrons interact with its atoms, generating various signals such as secondary electrons, back-scattered electrons, and X-rays [2, 3]. These signals are detected and utilized to create an image of the sample's surface. Field Emission Scanning Electron Microscopy (FESEM) offers numerous advantages over other microscopy techniques. It provides high-resolution images of surface morphology, topography, and composition. Furthermore, FESEM enables the analysis of samples at high magnification and under various conditions, including vacuum and low temperatures. For visualizing the micro- and nano-sized morphological features of the catalyst samples in this study, a JEOL field emission scanning electron microscope (FESEM) was applied. The FESEM boasts a versatile range of features, including a magnification range of 25 to 1,000,000, an accelerating voltage range of 0.1 kV to 30 kV, and a probe current range from a few pA to 200 nA. In sample preparation, electrode samples without carbon were mounted onto an aluminum stub using a double adhesive conductive carbon tape, while carbon-containing materials were affixed using copper tape and silver paste adhesive. Before image acquisition, a conductive coating approximately 10 nm thick was applied by sputtering the samples with a thin layer of Au for about 5 minutes.

3.3.3. Energy-dispersive X-ray spectroscopy (EDX)

EDX, referred to as energy dispersive spectroscopy (EDS) as well, serves as a non-destructive analytical technique employed to glean insights into the chemical composition of a sample. Widely utilized in materials science, geology, and biological sciences, EDX functions by detecting the X-rays emitted when a sample is bombarded with a beam of high-energy electrons [4, 5]. These emitted X-rays stem from the energy transfer occurring when the incident electron beam collides with the sample's atoms. The energy of these X-rays is characteristic of the originating element. Collected by a detector, the X-rays' energies are measured to deduce the elemental composition of the sample. This process generates a spectrum of X-ray energies corresponding to the elements present, with each element producing a distinct set of X-ray energies. Consequently, EDX enables the identification and quantification of elements within the sample. In conjunction with scanning electron microscopy (FESEM), EDX offers both elemental analysis and high-resolution imaging of the sample surface. In the context of this study, an EDX detector was utilized to acquire in-situ EDX spectra of various samples during electron microscope imaging. However, owing to extreme magnification and material heterogeneity, the EDX spectrum may vary based on the imaging area. Hence, all EDX images and data presented in this study solely serve to identify the presence of specific elements in the sample rather than determine its precise composition.

3.3.4. Fourier-Transform Infrared Spectroscopy (FTIR)

FTIR is a valuable technique employed to investigate the vibrational properties of molecular bonds within a sample. It assesses the absorption or transmission of infrared radiation, offering insights into the sample's chemical composition and functional groups. In operation, FTIR directs an infrared light beam through the sample, where it interacts with the chemical bonds present. Various types of bonds absorb energy at distinct frequencies, which are detected and transformed into a spectrum of infrared radiation absorbed or transmitted by the sample. This spectrum, akin to a unique "fingerprint," unveils the chemical composition of the sample, enabling qualitative and quantitative analysis. FTIR finds applications across chemistry, materials science, and biology for the identification, characterization, and quantification of diverse samples, including polymers, proteins, and pharmaceuticals [6]. In this study, an FTIR spectrophotometer (Perkin Elmer Spectrum BX, USA) was utilized, employing spectroscopic grade potassium bromide (KBr) in the dried form at 40°C. Spectra were obtained over a range from 400 to 4000 cm^{-1}.

3.3.5. Thermogravimetric Analysis (TGA)

TGA involves monitoring the change in weight of a material as it undergoes heating or cooling, offering insights into its thermal stability. The sample is placed in a furnace, which is then subjected to a constant rate of heating or cooling, while the sample's weight is continuously monitored. The variation in sample weight is recorded as a function of temperature or time. TGA is frequently utilized to assess the thermal stability of polymers, composites, and other materials, as well as to explore their thermal decomposition behavior [7]. TGA can be coupled with additional techniques such as FTIR or mass spectrometry to provide information on the chemical composition of the sample as it experiences temperature changes. In this study, the Perkin Elmer thermoanalytical instrument was employed to generate TGA curves of the prepared samples under an inert nitrogen atmosphere, with a heating rate of 10 °C/min from room temperature to 600 °C. Various properties of the samples, including weight percentage, activation energy, oxygen index, and residual weight percentage, were determined through TGA. For the thermal analysis, approximately 50 mg of powdered sample was precisely weighed and placed in a clean alumina crucible. After loading the crucible into the Q600 SDT thermal analysis instrument (TA Instruments), both heating and cooling cycles were programmed to ramp up at a rate of 10 °C/min from room temperature to 600°C. The peak temperature was maintained for 30 minutes, and each sample underwent testing at least twice to ensure reproducibility.

3.3.6. Ultraviolet-visible (UV-Vis) Spectroscopy

UV-Vis absorption spectroscopy serves as a widely utilized analytical technique for gauging the amount of light absorbed by a sample within the ultraviolet and visible regions of the electromagnetic spectrum. The underlying principle lies in molecules containing bonding and non-bonding electrons, which can absorb photons from the UV (250-400 nm) and visible (400-750 nm) spectra, leading to excitation to higher anti-bonding orbitals [8]. This technique finds utility in both qualitative and quantitative analyses. By quantifying the light absorbed by a sample at a specific wavelength, it becomes possible to detect the presence of certain compounds or functional groups. Moreover, UV-Vis spectroscopy allows for the determination of compound concentration in a solution using the Beer-Lambert law. This law correlates the amount of light absorbed to the concentration of the absorbing species and the path length of the sample [9].

$$A = \frac{I_o}{I} = aLc \qquad (3.1)$$

In the Beer-Lambert law, denoted by Equation 3.1, symbols are defined as follows: A represents absorbance, I_o signifies the intensity of incident light, and I denotes the intensity of transmitted light. Parameters a, L, and c correspond to the molar absorptivity (extinction coefficient), path length through the sample, and concentration of the compound, respectively.

3.3.7. Raman spectroscopy

Raman spectroscopy provides detailed insights into molecular vibrations, interactions, and crystal structures. It serves as a non-contact and non-destructive technique for chemical analysis. A Raman spectrometer typically comprises an excitation light source, sample collection optics, monochromator, and a detector. Its operational principle relies on the inelastic scattering of monochromatic light. When a monochromatic laser beam strikes the sample, light scatters in various directions. "Rayleigh scattering" occurs when the frequency of scattered radiation matches the frequency of the incident radiation. Stokes and anti-Stokes scattering take place when the scattered radiation frequency is respectively lower or higher than that of the incident radiation [10]. A Raman spectrum is typically depicted as intensity versus wavelength shift and can be recorded over a wavenumber range of 4000-10 cm^{-1}. In the present work, a

RENISHAW spectrophotometer equipped with a laser source emitting at a wavelength of 532 nm was utilized for Raman spectroscopy analysis.

3.3.8. X-ray photoelectron spectroscopy (XPS)

XPS was employed to analyze the chemical composition and electronic states of the samples. The photoelectric effect is the underlying basis of XPS, where electrons from incoming photons interact with the surface of the sample to produce photoelectrons. These emitted photoelectrons were then captured and measured by an electron spectrometer, generating an energy spectrum [11]. Using the XPS apparatus, the elemental content and electronic structure of the produced samples were examined, specifically the Thermoscientific NEXA model.

3.3.9. Brunauer-Emmett-Teller (BET)

BET theory describes the physical adsorption of gas molecules onto a solid surface and is a foundational method for measuring the specific surface area of materials. BET theory is applicable to multilayer adsorption systems and typically employs non-reactive probing gases to measure surface area. Nitrogen (N_2) is the most commonly used gas for BET analysis, which is generally performed at the boiling point of nitrogen. Although nitrogen is the primary adsorbate, other gases such as argon, carbon dioxide, and water can also be used to measure surface area under different conditions, though less frequently. The specific surface area is inherently dependent on the measurement scale and the adsorbate's properties, such as its adsorption cross-section. Consequently, the specific surface area values obtained through BET analysis can vary based on the adsorbate used. For the present study, N_2 adsorption-desorption isotherms were employed to analyze the surface area and pore size distributions of the samples, with all measurements conducted using an Autosorb iQ.

3.3.10. Electrochemical Characterization

Electrochemical investigations were conducted on metal oxides, conducting polymers, and their composites using a half-cell setup, which employed a three-electrode system with potassium hydroxide (KOH) aqueous solution as the electrolyte.

Figure 3.7. Electrochemical workstation Autolab PGSTAT204.

Specifically, the electrodes utilized were Ag/AgCl, platinum wire, and the synthesized metal oxides, conducting polymers, and their composites coated onto nickel foam, serving as the reference, counter, and working electrodes, respectively. All electrochemical assessments were carried out using an electrochemical apparatus manufactured by Autolab PGSTAT204 (see Figure 3.7). In electrochemical investigations, the three-electrode (half-cell) system is typically employed to determine specific electrochemical properties of a material, while a two-electrode (full-cell) system is recommended for assessing the performance of supercapacitor (SC) devices [13]. In the three-electrode setup, comprising working, reference, and counter electrodes, all are immersed in an electrolyte solution. As depicted in Figure 3.8, the electrochemical workstation controller oversees the current flow from the counter to the working electrode by gauging the potential difference between the working and reference electrodes. This resultant current is directly proportional to the voltage established between the working and reference electrodes.

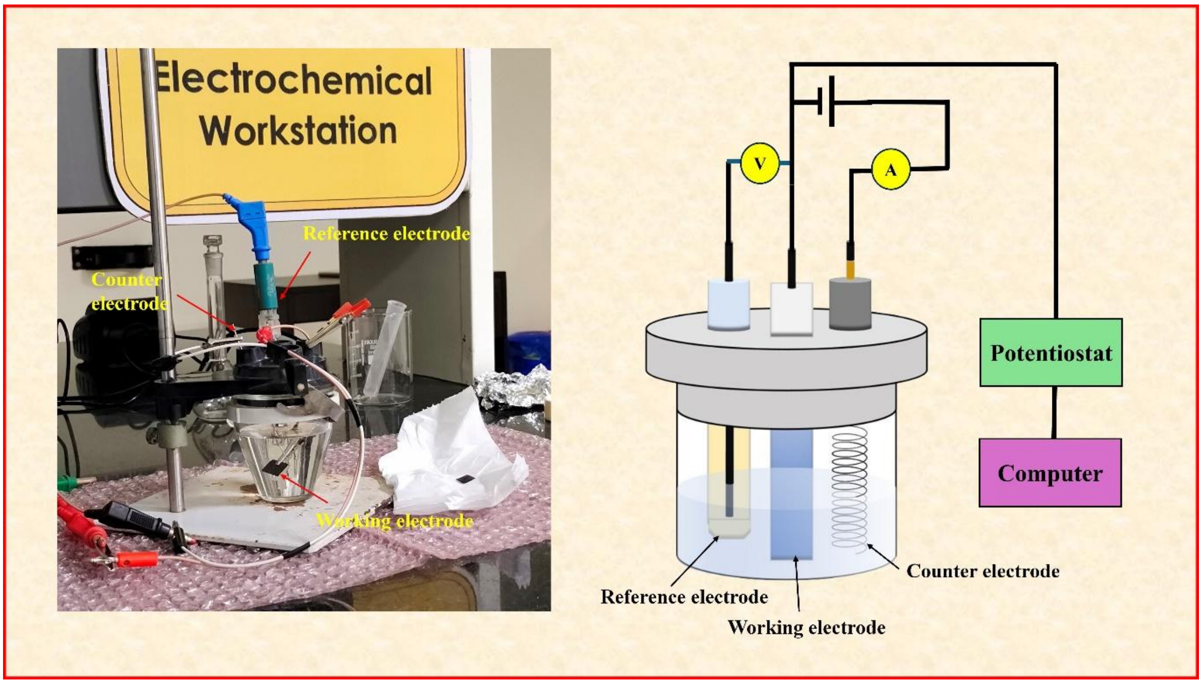

Figure 3.8. A schematic representation of a three-electrode electrochemical (half-cell) system.

It is then converted to a voltage signal by a current-to-voltage (I/V) converter and subsequently recorded by the data acquisition system over time. It's important to highlight that an ideal electrometer should possess a sufficiently high electrical resistance to maintain zero input current [14]. This is crucial because any current passing through a reference electrode has the potential to alter the actual potential, thus impacting the precision of the data collected.

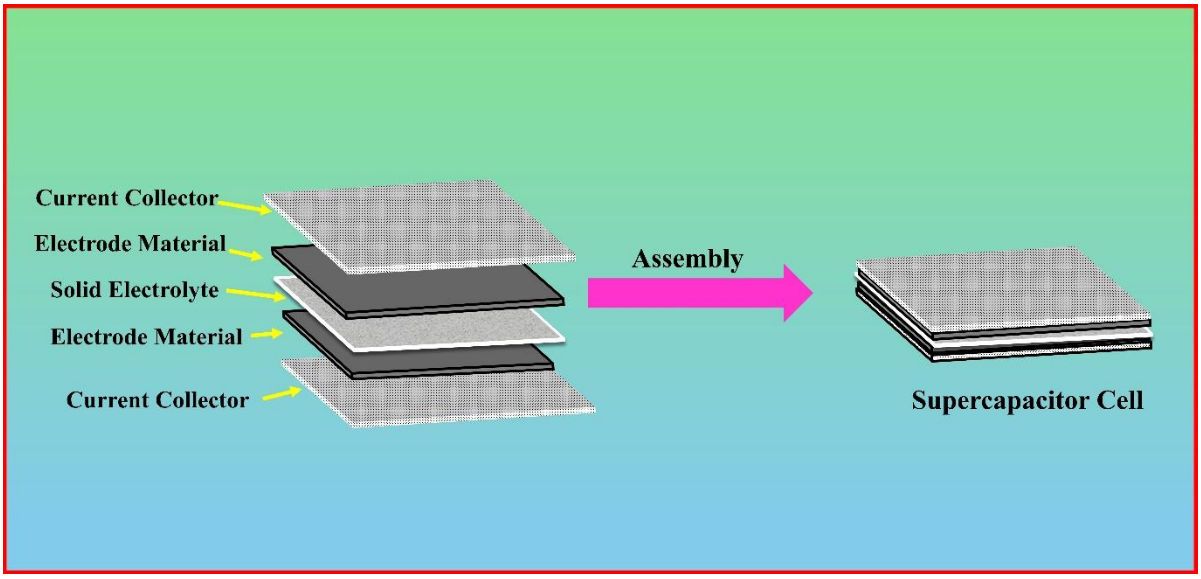

Figure 3.9. Schematic of two electrode setup.

In a two-electrode (full-cell) setup, two working electrodes are placed together with a solid electrolyte acting as a separator. This configuration resembles a packed supercapacitor cell and provides a more accurate depiction of the electrodes' electrochemical behavior within the device [15]. Figure 3.9 illustrates a schematic of this setup. The working electrodes of the half-cells exhibit double the potential window compared to the electrodes in the full cells, as per the specified potential window on the electrochemical system.

Various techniques, such as cyclic voltammetry (CV), galvanostatic charge-discharge (GCD), and electrochemical impedance spectroscopy (EIS), can be utilized to investigate the electrochemical capacitive performance of developed materials. Assessing the electrochemical characteristics of thin layers is particularly crucial for their utilization as active electrodes in supercapacitor devices. CV, GCD), and EIS analyses are conducted on synthesized metal oxides, conductive polymers, and their composite electrodes within a three-electrode system. These investigations aim to evaluate their electrochemical performance in a constructed supercapacitor cell.

- **Cyclic voltammetry** (CV)

Cyclic voltammetry provides insights into various parameters such as potential window, redox activities, reproducibility, capacitance, ion transport kinetics, and material resilience. During cyclic voltammetry, potential is applied between the reference and working electrodes, while the working electrodes and counter concurrently capture current. A typical CV, as depicted in Figure 3.10 (a), showcases distinctive features: the rectangular shape designating the EDLC nature of the electrode material, and the existence of oxidation and reduction peaks in the positive and negative potential range signifying battery-type behavior [16].

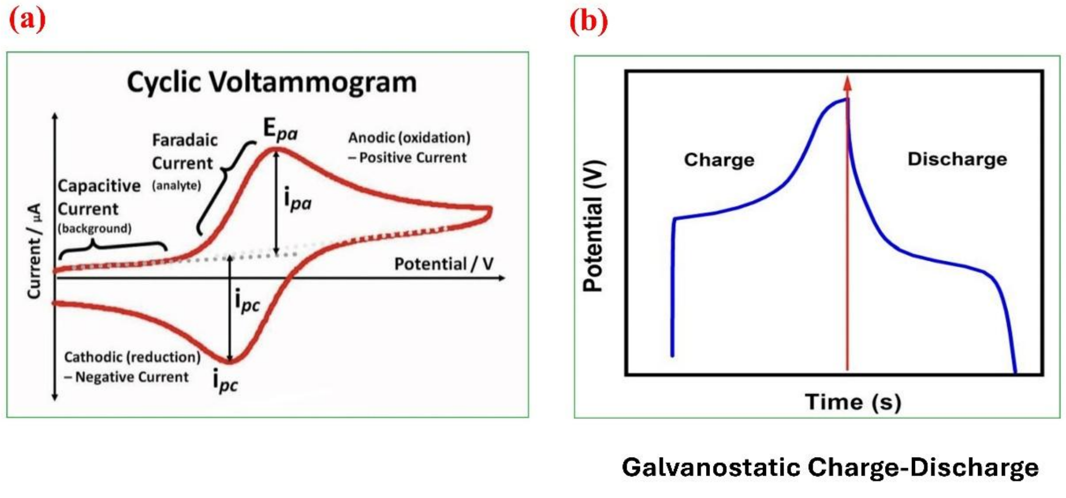

Figure 3.10. (a) A typical cyclic voltammetry curve (b) Schematic diagram of a GCD curve.

- **Galvanostatic charge-discharge (GCD)**

GCD analysis is widely employed to measure important parameters such as power density, energy density, specific capacitance, cycling stability, and Coulombic efficiency. In this study, the electrode receives a steady current that is delivered in both positive and negative directions; the current direction changes at a predetermined cut-off voltage. As seen in Figure 3.10 (b), the GCD curve's form exposes the electrode materials' energy storage process. A pseudo-capacitive diffusion-controlled redox process usually has a nonlinear, plateau-shaped curve. On the other hand, perfect Electric Double-Layer Capacitors (EDLC) exhibit symmetrical features and flawlessly linear profiles [17].

- **Electrochemical Impedance Spectroscopy (EIS)**

EIS is a versatile technique employed in scientific inquiry to elucidate the electrical characteristics of materials, particularly electrode materials. Rather than simply observing a material's behavior under a single condition, researchers employ EIS to investigate its response across a range of conditions. In the present study, the experiment is conducted under open circuit conditions, where no direct connection to an external electrical circuit is established. A small alternating current (AC) voltage with an amplitude of 10 millivolts is applied to the system [18].

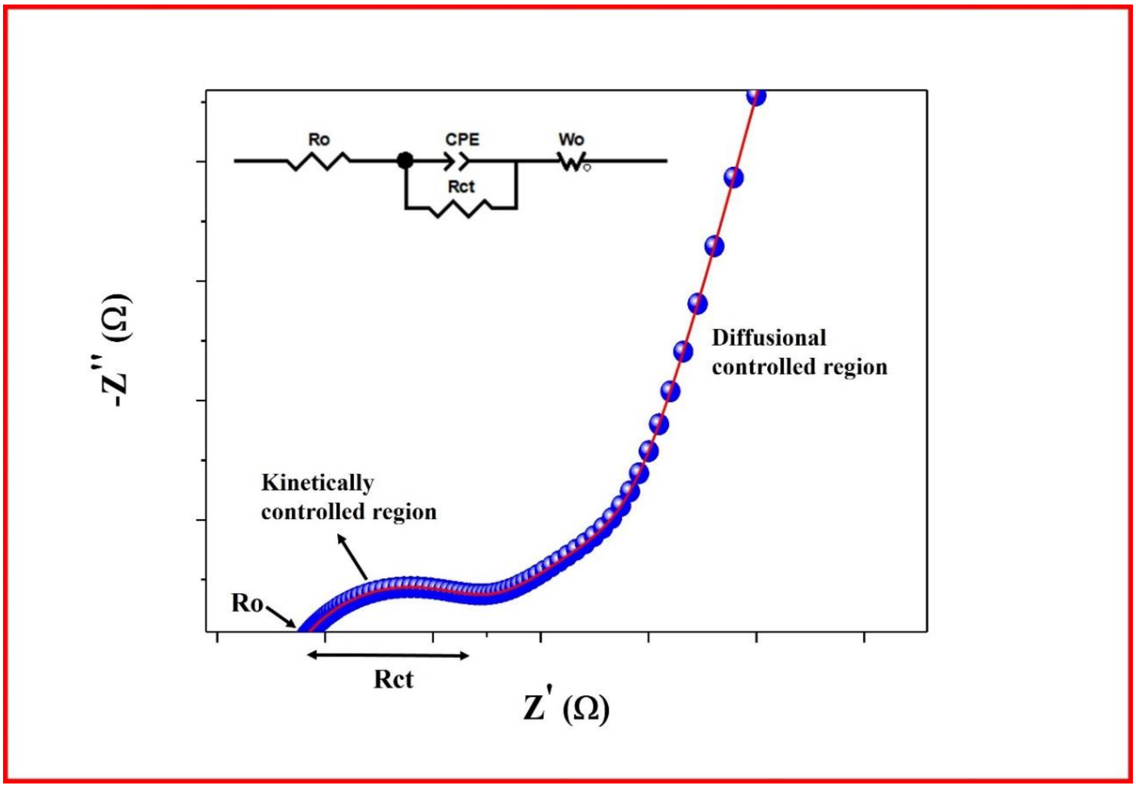

Figure 3.11. Schematic EIS curve with fitted equivalent circuit.

Researchers systematically vary the frequency of this voltage signal, sweeping from a low of 0.01 Hz to a high of 100 kHz. This approach allows for a comprehensive examination of how the material reacts to different electrical signals. The resulting data is typically visualized using a Nyquist plot, Figure 3.11 a graphical representation of impedance as a function of frequency. Within this plot, an inset often presents a model that effectively fits the experimental data, aiding in interpretation. One key parameter of interest is the charge transfer resistance (Rct), which can be inferred from the semicircular feature frequently observed in the EIS curve. This parameter provides valuable insights into the material's ability to facilitate the movement of charges. Furthermore, the intersection of the semicircle with the horizontal axis yields information about the solution resistance (Ro), reflecting the resistance associated with the electrolyte solution surrounding the electrode. The size of the semicircle itself indicates Rct, with a larger semicircle suggesting greater charge transfer resistance and hence a more hindered charge movement within the material [19, 20]. Lastly, consideration is given to the Warburg impedance (represented by W), which reflects the diffusion of ions within the material. Overall, EIS facilitates a comprehensive understanding of the electrical behavior of electrode materials, with implications spanning diverse fields such as energy storage, corrosion mitigation, and sensor technology.

References

[1] Ameh ES. A review of basic crystallography and x-ray diffraction applications. The international journal of advanced manufacturing technology. 2019;105(7):3289-302.

[2] Abd Mutalib M, Rahman MA, Othman MH, Ismail AF, Jaafar J. Scanning electron microscopy (SEM) and energy-dispersive X-ray (EDX) spectroscopy. InMembrane characterization 2017:161-179.

[3] Abdul Khalil HP, Chong EW, Owolabi FA, Asniza M, Tye YY, Rizal S, Nurul Fazita MR, Mohamad Haafiz MK, Nurmiati Z, Paridah MT. Enhancement of basic properties of polysaccharide-based composites with organic and inorganic fillers: A review. Journal of Applied Polymer Science. 2019;136(12):47251.

[4] Leng Y. Materials characterization: introduction to microscopic and spectroscopic methods. John Wiley & Sons; 2013.

[5] Goldstein JI, Newbury DE, Michael JR, Ritchie NW, Scott JH, Joy DC. Scanning electron microscopy and X-ray microanalysis. springer; 2017.

[6] Stuart BH. Infrared spectroscopy: fundamentals and applications. John Wiley & Sons; 2004.

[7] Loganathan S, Valapa RB, Mishra RK, Pugazhenthi G, Thomas S. Thermogravimetric analysis for characterization of nanomaterials. InThermal and rheological measurement techniques for nanomaterials characterization 2017:67-108.

[8] Perkampus HH. UV-VIS Spectroscopy and its Applications. Springer Science & Business Media; 2013.

[9] Swinehart DF. The beer-lambert law. Journal of chemical education. 1962;39(7):333.

[10] Cialla-May D, Schmitt M, Popp J. Theoretical principles of Raman spectroscopy. Physical Sciences Reviews. 2019;4(6):20170040.

[11] Andrade JD. X-ray photoelectron spectroscopy (XPS). Surface and Interfacial Aspects of Biomedical Polymers: Volume 1 Surface Chemistry and Physics. 1985:105-95.

[12] Sinha P, Datar A, Jeong C, Deng X, Chung YG, Lin LC. Surface area determination of porous materials using the Brunauer–Emmett–Teller (BET) method: limitations and improvements. The Journal of Physical Chemistry C. 2019;123(33):20195-209.

[13] Li X, Qu J, Hu Z, Xie H, Yin H. Electrochemically converting Sb2S3/CNTs to Sb/CNTs composite anodes for sodium-ion batteries. International Journal of Hydrogen Energy. 2021 ;46(33):17071-83.

[14] Zhang F, Liu J, Ivanov I, Hatzell MC, Yang W, Ahn Y, Logan BE. Reference and counter electrode positions affect electrochemical characterization of bioanodes in different bioelectrochemical systems. Biotechnology and bioengineering. 2014;111(10):1931-9.

[15] Lv H, Pan Q, Song Y, Liu XX, Liu T. A review on nano-/microstructured materials constructed by electrochemical technologies for supercapacitors. Nano-Micro Letters. 2020 ;12:1-56.

[16] Iro ZS, Subramani C, Dash SS. A brief review on electrode materials for supercapacitor. International Journal of Electrochemical Science. 2016;11(12):10628-43.

[17] Liu Q, Dong X, Xiao G, Zhao F, Chen F. A novel electrode material for symmetrical SOFCs. Advanced materials. 2010;22(48):5478-82.

[18] Sharma S, Chand P. Supercapacitor and electrochemical techniques: A brief review. Results in Chemistry. 2023;5:100885.

[19] Bredar AR, Chown AL, Burton AR, Farnum BH. Electrochemical impedance spectroscopy of metal oxide electrodes for energy applications. ACS Applied Energy Materials. 2020;3(1):66-98.

[20] Ogihara N, Kawauchi S, Okuda C, Itou Y, Takeuchi Y, Ukyo Y. Theoretical and experimental analysis of porous electrodes for lithium-ion batteries by electrochemical impedance spectroscopy using a symmetric cell. Journal of The Electrochemical Society. 2012;159(7):A1034.

Chapter 4

Enhanced Electrochemical Performance of in situ Polymerized V_2O_5-PANI Nanocomposites for Supercapacitors Application

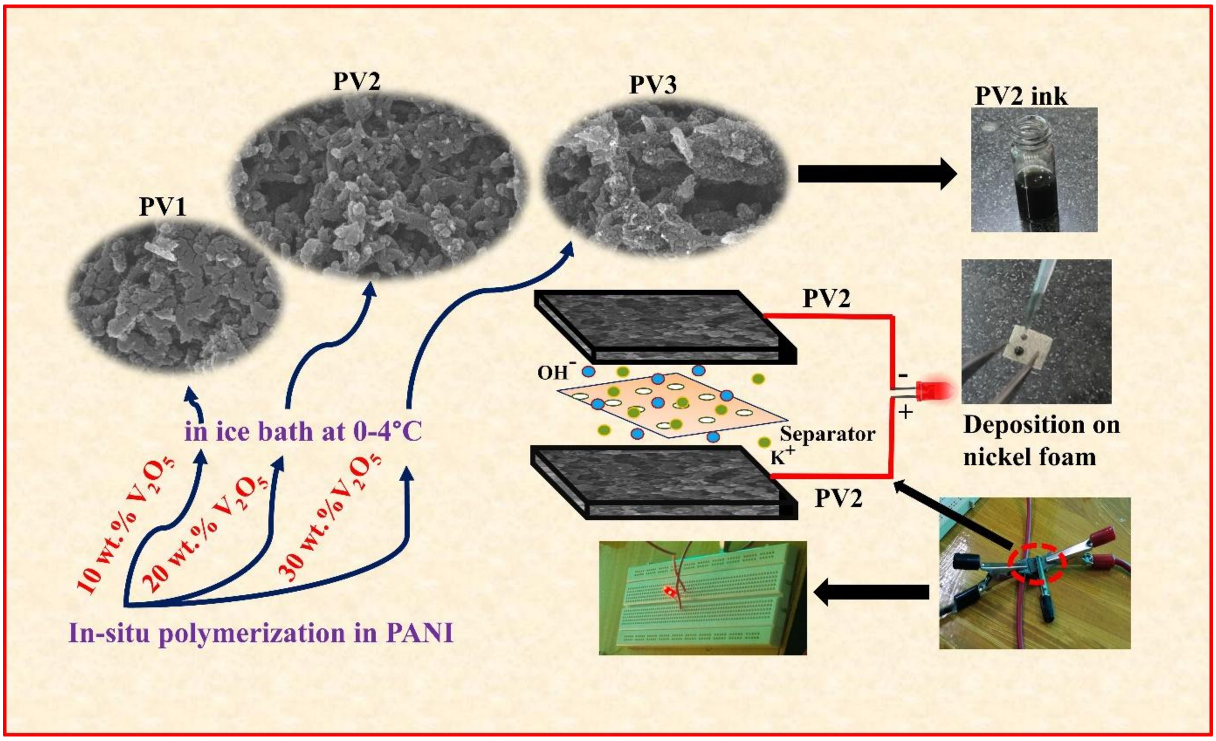

In this chapter, the preparation of PANI nanocomposites with varying V_2O_5 *weight percentages (10%, 20%, and 30%) was achieved through in situ polymerization of anilinium hydrochloride over* V_2O_5*. The* V_2O_5 *nanoparticles were synthesized via a straightforward chemical method, and their purity was verified through Rietveld refinement, which confirmed the advantageous electrochemical properties of* V_2O_5*, characterized by a high oxidation state of vanadium (*V^{+5}*) that facilitates efficient electron storage. The electrochemical performance of the fabricated electrode materials was analyzed using cyclic voltammetry (CV), which revealed a pair of redox peaks indicative of faradic pseudocapacitive behavior. Among the various electrodes, the 20 wt%* V_2O_5*-PANI (PV2) nanocomposite exhibited the highest capacitance of 820.5* Fg^{-1} *at 1* $A\ g^{-1}$*, along with a commendable cycle stability. The PV2 electrode also demonstrated a low charge transfer resistance (Rct) of 0.5* Ω *and a reduced solution resistance (Ro) of 0.31* Ω *in a 6 M KOH electrolyte, contributing to its superior electrochemical performance. The enhanced capacitance and stability of PV2 were attributed to its well-ordered structure and increased active sites, as observed through FESEM, which facilitate efficient ion and electron transfer. Furthermore, the symmetric supercapacitor configuration of PV2 electrodes showed impressive energy and power densities of 4.6* $Wh\ kg^{-1}$ *and 80.7* $W\ kg^{-1}$*, respectively. Notably, the ability to power a red LED using three PV2//PV2 symmetric devices connected in series highlights its potential for advancing energy storage applications.*

4.1. Introduction

With gradual growth in the demand for high-performance energy storage systems, supercapacitors become the first choice of researchers due to having an extensive range of potential applications, namely; backup power sources, electronic fuses, power supply devices for electric vehicles, etc. owing to their ability to provide long life cycle, quick charge–discharge rates, superior power density (PD), and low cost of maintenance [1–4]. These properties make them well-suited for use in hybrid electric motor vehicles and compact electronic gadgets, which are becoming prevalent in today's society. Various research groups are actively working to expand the performance of supercapacitors and to upgrade new ways to use them in a variety of applications. Although supercapacitors have many advantages over batteries, but the main limitation of supercapacitors is that they have lower energy density (ED) compared to batteries [5,6]. Supercapacitors are grouped into two categories based on the nature of electrode material utilized in their manufacturing: electric double layer capacitors (EDLC) and pseudocapacitors [7,8]. EDLC capacitors rely solely on elevated surface area carbon electrode material, supported by essential parts namely as electrolytes solution and current collectors, while pseudocapacitors use RuO_2, NiO, MnO_2, Fe_3O_4, V_2O_5 metal oxides and conductive polymers [9–11]. In electric double layer capacitors, charges are separated at the electrode-electrolyte junction and stored through electrostatic means. In contrast, pseudocapacitors exhibit fast, reversible faradic redox reactions on the electrode surface, resulting in greater capacitance and high ED than electric double layer capacitors. Conducting polymers are appealing materials for use in pseudocapacitors due to their high specific capacitance, controllable electrical conductivity, fast charge–discharge process, and low cost [12–14]. Among the various conducting polymer, PANI has gained significant attention from researchers because of its high specific capacitance, favorable environmental strength, exceptional electrical conductivity, and synthesis process [15]. Zhang et al. investigated the electrochemical performance of polyaniline in 0.1 M neutral electrolytes and reported that the produced polymer has a reasonable capacity of 187 F/g at 1 A/g of current density (CD) [16]. Despite of its positive features, the use of conductive PANI is limited due to its poor cycle lifespan in the charge-discharge process. Consequently, many studies aim to improve the operational efficiency and specific capacitance of PANI. One such common approach to enhance polyaniline electrochemical properties is by incorporating inorganic nano additives namely graphene or metal oxide nanoparticles in a polymer matrix. These additives can significantly alter the electrical, optical, and dielectric attributes of the developing nanocomposite pseudocapacitors [17–20]. The addition of inorganic nanoparticles in the polymer matrix creates a higher specific surface area or smaller diffusion path due to the greater porosity. This allows faster transport of electrolyte ions and can boost the adsorption–desorption of electroactive species, resulting in increased current and superior performance of electrode for supercapacitors application [21]. Among the various metal oxides, Vanadium oxide (V_2O_5) has received significant consideration in recent years due to its layered structure, high oxidation state and ability to easily diffuse in electrolyte ions, which allows high capacitance storage capability. Kannagi et al. reported a specific capacitance of 431 F/g for the V_2O_5 spheres electrode [22]. However, the electronic conductivity of V_2O_5 is relatively limiting its application in supercapacitors. Therefore, composite materials consisting of V_2O_5 and PANI have the potential to manage the problems (poor stabilities of PANI and low conductivity of V_2O_5), resulting in superior properties for supercapacitors. These composites have a synergistic effect on enhancing surface area, minimizing particle dimension, preventing particle cluster, improving cyclic lifespan, and providing extra pseudocapacitance. The presence of V_2O_5 in the composite offers physical and mechanical strength for the polymer and acts as a charge storage material, while the PANI provides strong conductivity due to its flexible and polymeric nature. This results in significantly better performance compared to the individual component materials. Tuning of the potential window by making the use of appropriate electrolyte solution effectively improve the performance of the electrode in the supercapacitor. Roy et al. reported V_2O_5-PANI nanocomposites and his finding demonstrates that V_2O_5-PANI electrode can reach a maximum specific capacitance of 538 F/g at a lower CD of 1 A/g in 1 M H_2SO_4 electrolyte [23]. Bai et al. also reported that V_2O_5-PANI nanocomposites can achieve the largest capacitance of 450 F/g at 1 A/g of CD in a 5 M LiCl electrolyte solution [24]. The widely used electrolyte, H_2SO_4 is highly corrosive and can damage the conductive electrodes, which can reduce the performance and lifetime of the supercapacitor [25]. Another commonly employed electrolyte, LiCl has relatively low ionic conductivity, which can limit the efficiency of charge transfer. On the other hand, KOH electrolyte is an ideal alternative because it offers a well-balanced combination of ionic conductivity, solubility, and compatibility with a diverse array of electrode materials [26]. Thus, the diffusion of KOH electrolyte ions within the electrode is beneficial to achieve the high specific capacitance value. The conductivity of the electrolyte solution is also influenced by its concentration. Literature witnessed that 6 M concentration of KOH is often considered ideal for conductivity because it provides a high concentration of ions in the solution [26,27]. Below this optimum concentration of KOH, the available number of ions is not that much sufficient to cause ion-ion interaction but also at the same time they offer a scope of improvement in the conductivity by increasing the molar concentration. At concentration higher than 6 M results in ion-ion interactions which leads to the formation of clusters and hence making the solution ion deficient which results in a decrease in conductivity. In the study, V_2O_5-PANI nanocomposites were successfully synthesized via the in situ polymerization method. The work comprehensively investigated their structural, morphological and thermal properties. Additionally, electrochemical behavior of the synthesized V_2O_5-PANI nanocomposite materials was assessed in a 6 M KOH electrolyte solution after being deposited onto a nickel foam substrate.

4.2. Experimental Procedures

4.2.1. V_2O_5 synthesis

7 gm of ammonium metavanadate and 3.37 ml of nitric acid were dissolved individually in 150 ml of distilled water and stirred for 15 minutes. Afterward, the two solutions were mixed in a beaker and stirred for 60 minutes. Later, the solution was allowed to settle down for the next 24 hours, resulting in the formation of precipitates of brown color. The precipitates were collected and left to dry at room temperature for 4 days. The final product was subjected to annealing in a furnace at 400°C for 4 hours.

4.2.2. PANI and V_2O_5-PANI synthesis

Polyaniline was synthesized by oxidative polymerization of 0.1M anilinium hydrochloride monomer in 1M HCl with an equimolar amount of ammonium peroxydisulfate ($(NH_4)_2S_2O_8$) solution and cooled in the ice bath (0-4°C). It took 14 hours to complete the polymerization reaction with the dropwise addition of ($(NH_4)_2S_2O_8$) solution to the monomer. The resulting mixture was then vacuum-filtered and washed multiple times with 1M HCl, ethanol, and distilled water until the filtered solution turned transparent. Finally, the obtained precipitates were dried in a oven at 60 ^{0}C for 8 hours. Similarly, polyaniline nanocomposites were also prepared with the addition of 10, 20, and 30 wt.% of V_2O_5 in 0.1 M anilinium hydrochloride solution named as PV1, PV2, and PV3, respectively.

4.2.3. Fabrication of electrode

A mixture of V_2O_5-PANI, acetylene black, and polyvinylidene fluoride (PVDF) binder was used to develop electrodes with weight ratio of 80:10:10. Firstly, the mixture was properly grinded and an adequate amount of N-Methyl-2-pyrrolidone (NMP) was added to form the ink, which is further ultrasonicated for 20 minutes. Afterwards, nickel foam dipped in a solution of HCl and ultrasonicated for 25 minutes to remove any oxide layer or impurities [28]. Later, the nickel foam rinsed with deionized water to eliminate any remaining acid. Thereafter for the removal of any impurities nickel foam immersed in ethanol for couple of minutes and finally rinse in the deionized water. Finally, the nickel foam dried in a vacuum oven. The previously formed ink was drop casted onto nickel foam and subjected to vacuum conditions at 60 ^{0}C for 12 hours to dry. Similar methodology is adopted for the preparation of V_2O_5 and PANI electrodes.

4.3. Results and discussions

4.3.1. XRD study

The X-ray diffraction pattern of V_2O_5 displayed in Figure 4.1. The high-intensity peaks observed at $2\theta = 15.39^{0}$, 20.19^{0}, 26.15^{0}, $30.9^{0,}$ and 34.2^{0} corresponding to planes (200), (001), (110), (400), and (310), respectively, indicated the development of highly crystalline nanoparticles corresponding to the orthorhombic crystal structure (JCPDS no: 01-085-0601) with lattice parameters; a = 11.512 Å, b = 4.368 Å and c = 3.564 Å.

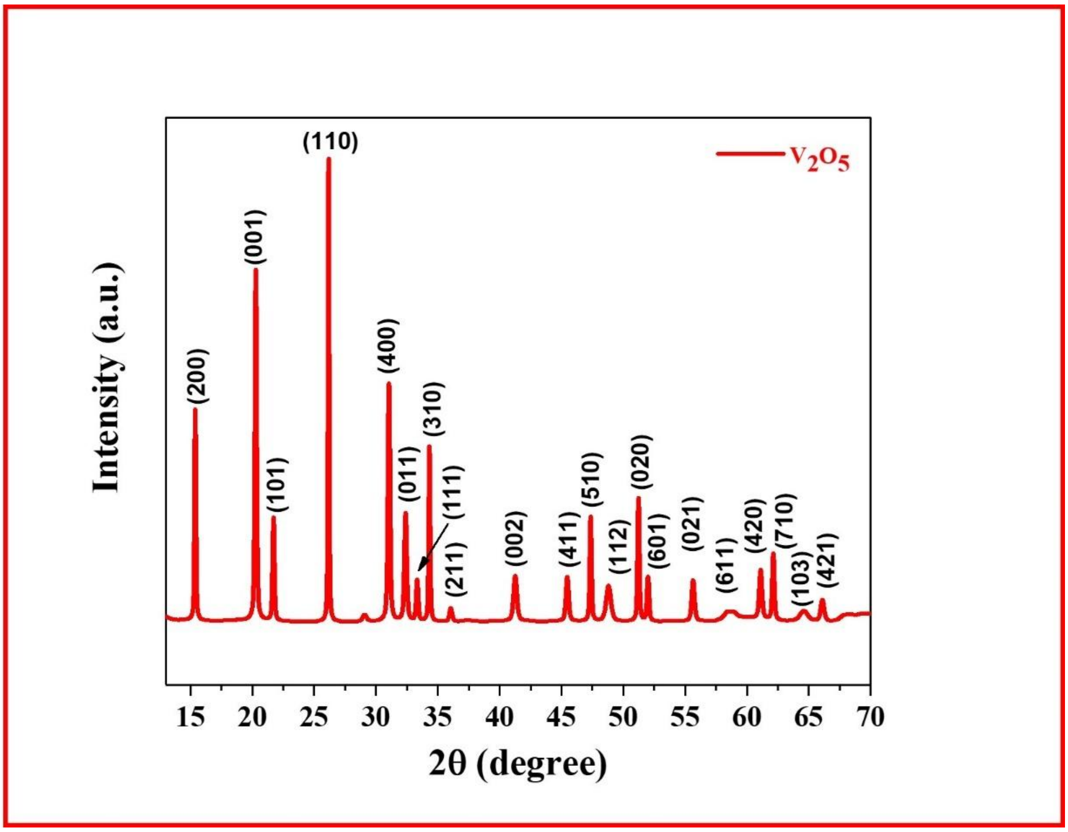

Figure 4.1. XRD of synthesized V_2O_5 metal oxide.

Rietveld analysis is used to explore the X-ray powder diffraction data by comparing the observed data with the available referred XRD data based on the proposed crystal structure [29,30]. By adjusting the various parameters of the crystal structure, the Rietveld method can eliminate inaccuracies and provide the most accurate representation of the crystal structure of the material. In the present work, Full Prof Suit software is used to refine the XRD data for the synthesized V_2O_5 powder sample. The Rietveld plot, shown in Figure 4.2, shows the peak shapes fitted by refining the Gaussian and Lorentzian contributions separately. The refined parameters include the zero-shift correction, phase fractions, unit-cell parameters, background parameters, and peak shape parameters. These parameters are adjusted iteratively until the best agreement between the observed and referred XRD patterns is achieved. The stable refinements and satisfactory fits, as indicated by the smoothness of the Yobs-Ycalc curve, illustrate the reliability of the Rietveld refinement process for the V_2O_5 nanoparticles (see Figure 4.2). The refined parameters had regular convergence, indicating that the result obtained by the refinement process is robust.

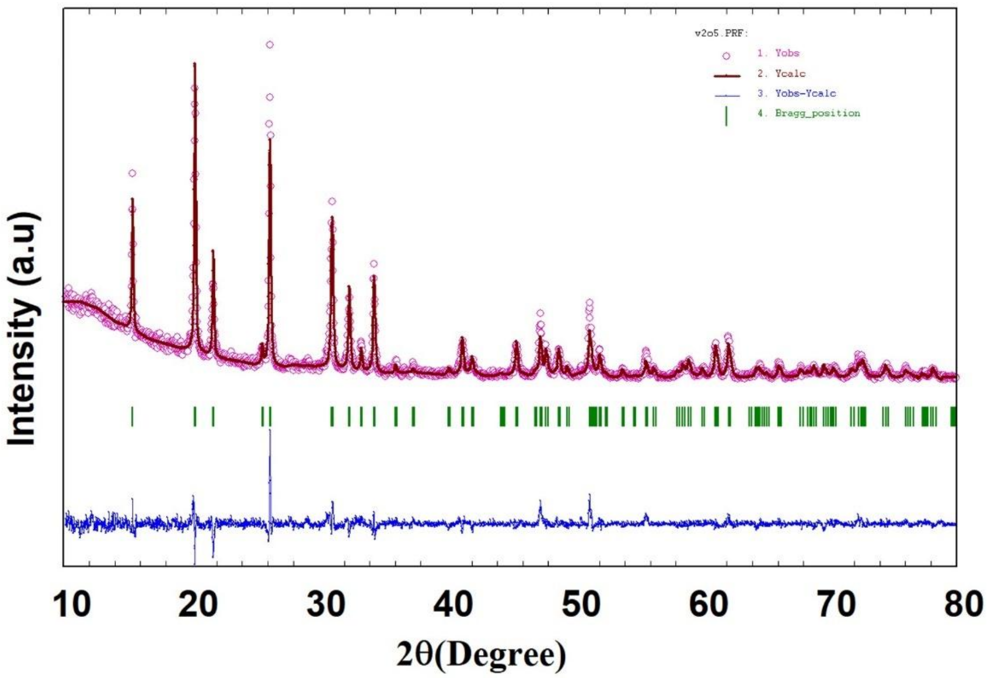

Figure 4.2. Rietveld refinement of V_2O_5. The pink circles lines show the experimental (Yobs) and the continuous brown shows simulated (Ycal) intensities. The tick mark indicates all the positions of the Bragg reflections.

The Bragg R-factor and weight fraction are commonly used indicators of the quality of the fit between the observed and referred XRD patterns and always appreciable to be lower in value. In the present work, the Bragg R-factor is 9.17 % and the weight fraction is 5.71 %, indicating a good fit. The resemblance of the results as obtained by fit indicator (χ^2) = 1.87 %, reveals the close mapping (see Figure 4.2) and reflects the high quality of the prepared V_2O_5 nanoparticles. Furthermore, the observed orthorhombic structure is of having space group ($Pmn2_1$) along with refined lattice parameters a= 11.48000 Å, b= 4.36000 Å, c= 3.55000 Å, and cell volume = 177.6874 (Å)^3. Williamson-Hall calculations are used to determine the micro-strain and crystallite size of V_2O_5 (see Figure 4.3) using the following equation [29].

$$\beta_t \cos\theta = \frac{k\lambda}{D} + 4\varepsilon \sin\theta \tag{4.1}$$

where β_t indicates FWHM in radian (obtained from the Rietveld refinement) of different peaks, θ(radian), ε , k , λ and D is the bragg angle in degree, lattice strain, shape factor, wavelength of X-ray and average crystallite size (nm) of the crystal, respectively.

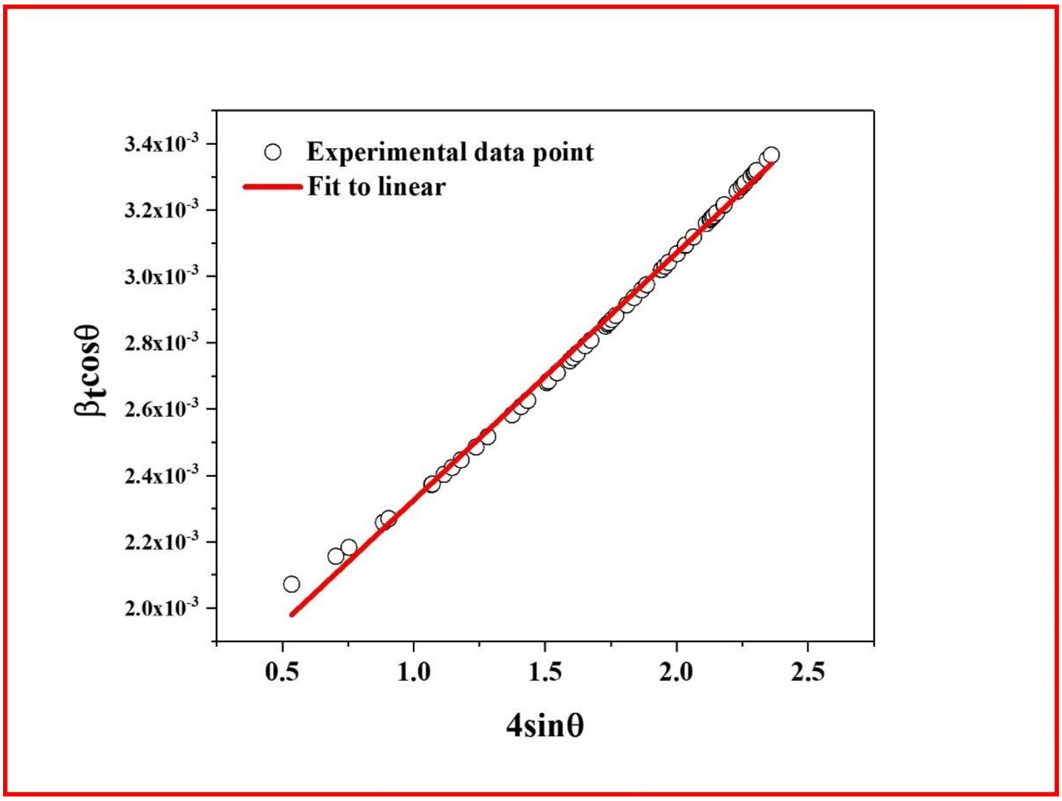

Figure 4.3. Williamson–Hall Plot for V_2O_5.

The average crystallite size (D) is calculated from the intercept $\left(\frac{k\lambda}{D}\right)$ and found to be 84.68 nm, whereas slope of plotted data is used to calculate the lattice strain (ε), which is given as 0.000074.

To have a further insight, Rietveld refinement is used to characterize and envisage the electron density inside the unit cell through GFourier software. The obtained concentration of the electron density helps to recognise the atomic position of the constituent elements within the unit cell. Following equation is used to compute the electron scattering density d(x,y,z) [30].

$$d(x,y,z) = \frac{1}{V}\sum_{hkl} |F_{(hkl)}|\, \mathrm{e}^{-2\pi i(hx+ky+lz-\alpha_{hkl})} \tag{4.2}$$

where $F_{(hkl)}$ is the amplitude of the structure factor, α_{hkl} is the phase angle of each Bragg reflection, and d(x, y, z) is the electron density at a positions (x, y, z) in a unit cell of volume (V). The representation of the electron density maps could be as either two- or three-dimensional Fourier map.

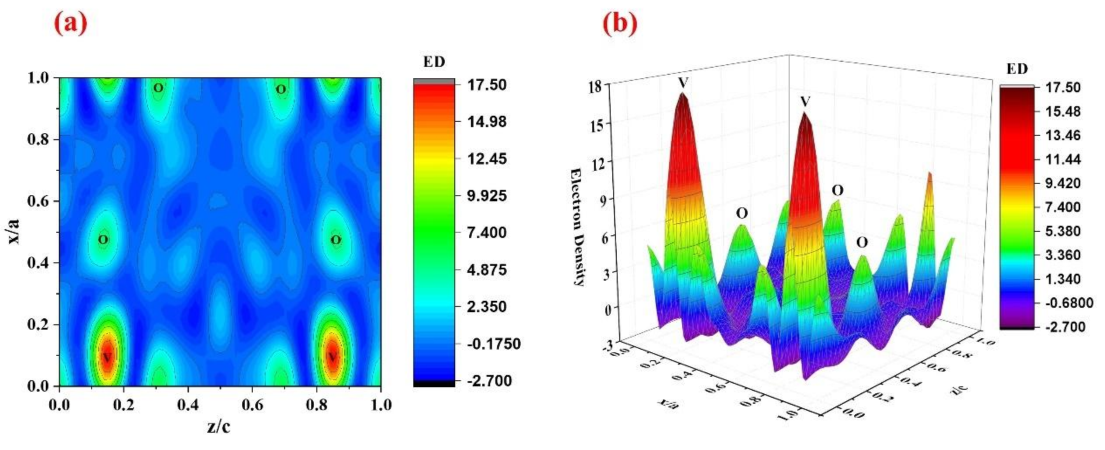

Figure 4.4. (a) Two-dimensions individual atoms electron density maps on the xz plane in the unit cell. (b) Map of the individual atoms electron densities in the unit cell of V_2O_5 in three-dimensions, electrons per cubic angstrom (e/Å^3), unit is used to estimate electron density.

Electron density distribution through 2D Fourier map helps to identify the different density level (see Figure 4.4(a)). Thicker electron density contour leads to indicate heavier element. Whereas 3D Fourier map helps to identify single electron density level by producing chicken-wire style network (see Figure 4.4(b)). Two and three-dimensional mapping of the V_2O_5 unit cell on the plane xz (y = 0) are shown in Figure 4.4(a-b). As it is evident from the figure that, green to red-brown-colored areas reflect increasing levels of electron density surrounding the vanadium (V) cation, and the rest of the area covered by the blue color represents the zero-level density contour. Meanwhile, the presence of oxygen anion reflected through cyan color indicates lower electron density than V cations observed through electron density indicator. In electron density maps (see Figure 4.4(a-b)), Vanadium ions exhibit a high electron density in their higher oxidation state (V^{+5}) which allows them to store and release a substantial number of electrons. These properties could be helpful in supercapacitor to attain high energy storage capacity.

XRD patterns of the prepared nanocomposites with different concentrations have been assessed and are given in Figure 4.5. Intensity of the peak is found to be better developed with concentrations preferably along (200) plane at 2θ=25.18^0, as well as embedded with low-intensity kink at an angle 13.7^0 and 20.76^0. The observed XRD pattern reflects that the peak profile of prepared nanocomposites are mostly similar to that of the free PANI (except the shift in the peak position towards lower angle side).

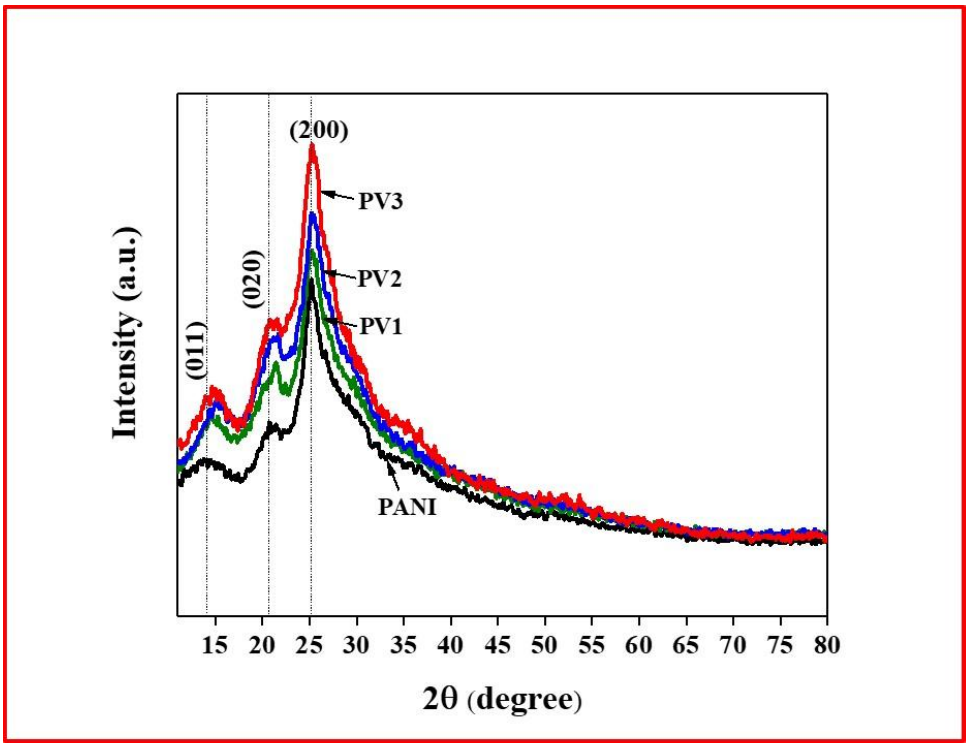

Figure 4.5. XRD patterns of PANI, PV1 (10 wt% V_2O_5-PANI), PV2 (20 wt% V_2O_5-PANI) and PV3 (30 wt% V_2O_5-PANI).

The observed intense peak corresponds to (200) shows that the PANI has some sort of crystallinity, which might be due to the high ordered system of the PANI developed because of regular repeated monomer units of PANI. However, the degree of crystallinity could also be affected by the crystallographics radii (0.18 nm) as well as the shape (spherical) of used monobasic acid (HCl) as a dopant [31]. Moreover, the absence of the V_2O_5 peaks in the nanocomposites might be due to the distortion in the crystal arrangement, which led to the transformation of V_2O_5 into amorphous state and hence in XRD pattern the free PANI peaks are predominant. Wrapping of the V_2O_5 by the polymer chain could be accepted as the possible reason. Another possible reason could be the acting of the PANI as a shell structure in the form of sheathe surrounding the core V_2O_5. The addition of V_2O_5 oxide induces a notable shift in the high-intensity peak (200) of PANI, towards the lower-angle side. This shift is evident by the observed changes in peak angles, which are -0.09^0, -0.32^0, and -0.01^0 for PV1, PV2, and PV3, respectively. However, the most significant shift is observed in PV1 and PV2 nanocomposites. This intriguing phenomenon can be attributed to the increased interchain spacing and enhanced interchain order within the PANI matrix, resulting in a pronounced delocalization of electrons would collectively contribute to creating better pathways for charge carriers to move through the material, leading to higher conductivity within PV1 and PV2 nanocomposites. This special property of nanocomposites proves to be highly advantageous by facilitating electron transport in supercapacitors and explained in electrochemical analysis section. On the other hand, the peak position for PV3 nanocomposite approaches towards higher angle side (as compare to PV1 and PV2) and in alignment with pure PANI peak position. This observation points towards the congregation of V_2O_5 oxide within the polymer matrix, seems to be responsible to limit the overall properties of the nanocomposite. The obtained results are further supported by estimating the chain separation (R) for the prepared samples by following expression [32].

$$R = \frac{5\lambda}{8\sin\theta} \tag{4.3}$$

The calculated values for V_2O_5, free PANI and for PV1, PV2 and PV3 are 1.50, 1.54, 1.55, 1.56 and 1.54 respectively. It is to be noted that the resemblance in the value of R for free PANI and PV3 clearly favours the dominance of PANI beyond the optimum doping concentration i.e. 20 wt.% of V_2O_5.

4.3.2 Morphological study

The morphology of fabricated V_2O_5 oxide was examined by FESEM and shown in Figure 4.6.

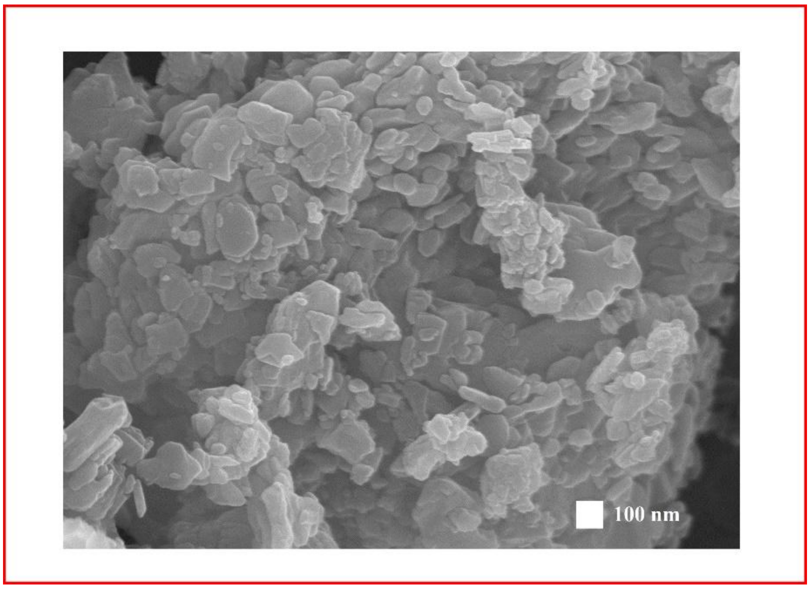

Figure 4.6. FESEM of V_2O_5.

It has been noted that V_2O_5 shows randomly orientated nanoflake-like morphology. The chemical composition of V_2O_5 is measured through energy dispersive X-ray (EDX) spectra displayed in Figure 4.7. The obtained elemental composition is 64.66 % and 35.34 % atomic percentages for V and O, respectively, which are in good concordance with the outcomes attained by electron density mapping (see Figure 4.4(a-b)). Furthermore, there were also observed additional peaks in the EDX spectrum. These peaks may arise due to gold coating used in sample testing because gold coating indeed shows its own characteristic peaks ~2-2.3 keV in the EDX spectrum due to its high atomic number and strong electron backscattering.

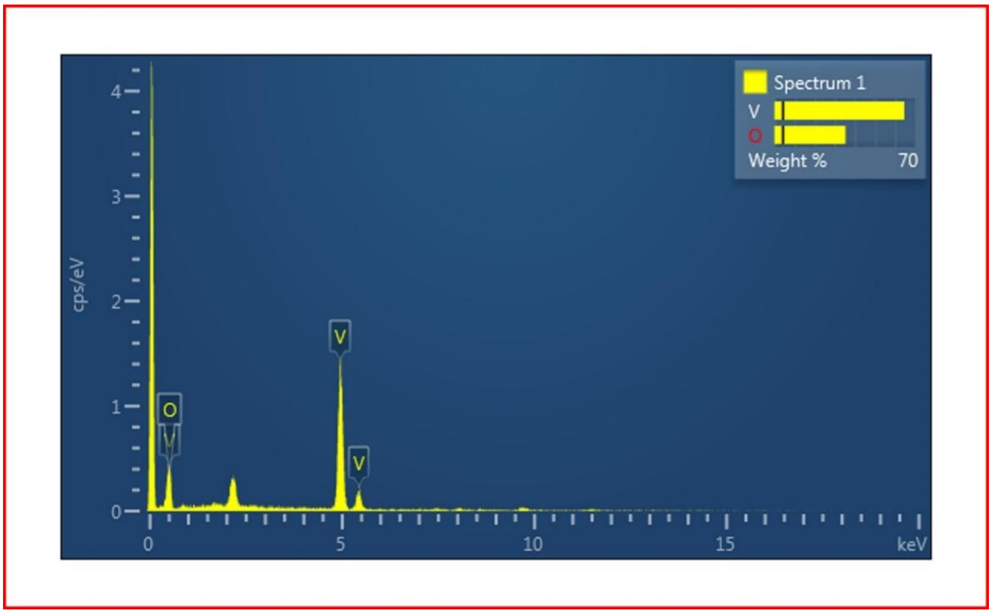

Figure 4.7. EDX spectrum of V_2O_5.

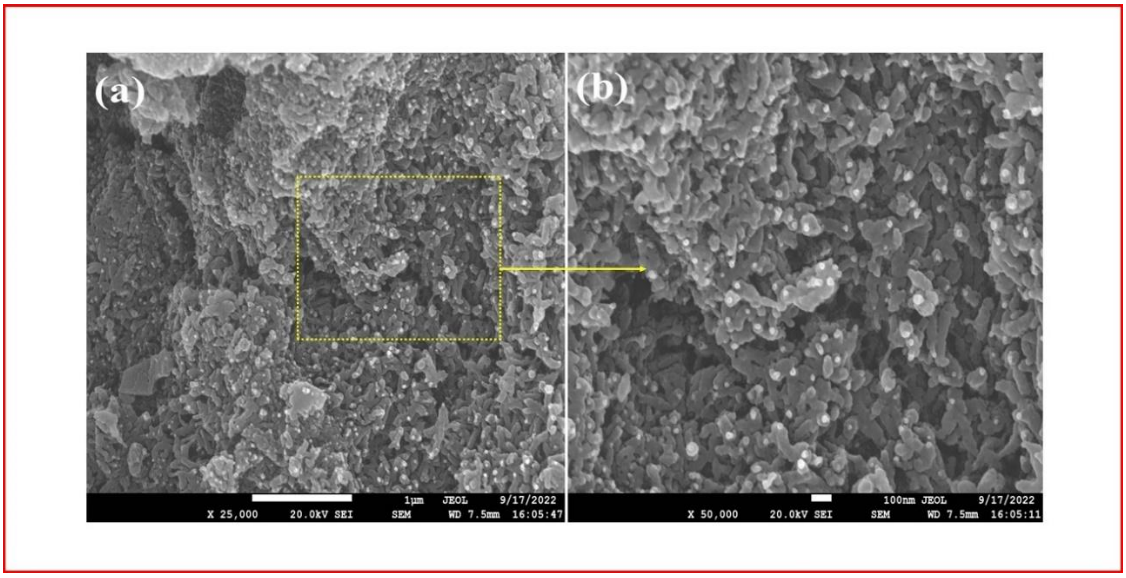

Figure 4.8. (a) Recorded FESEM images of PANI without magnification (b) with magnification.

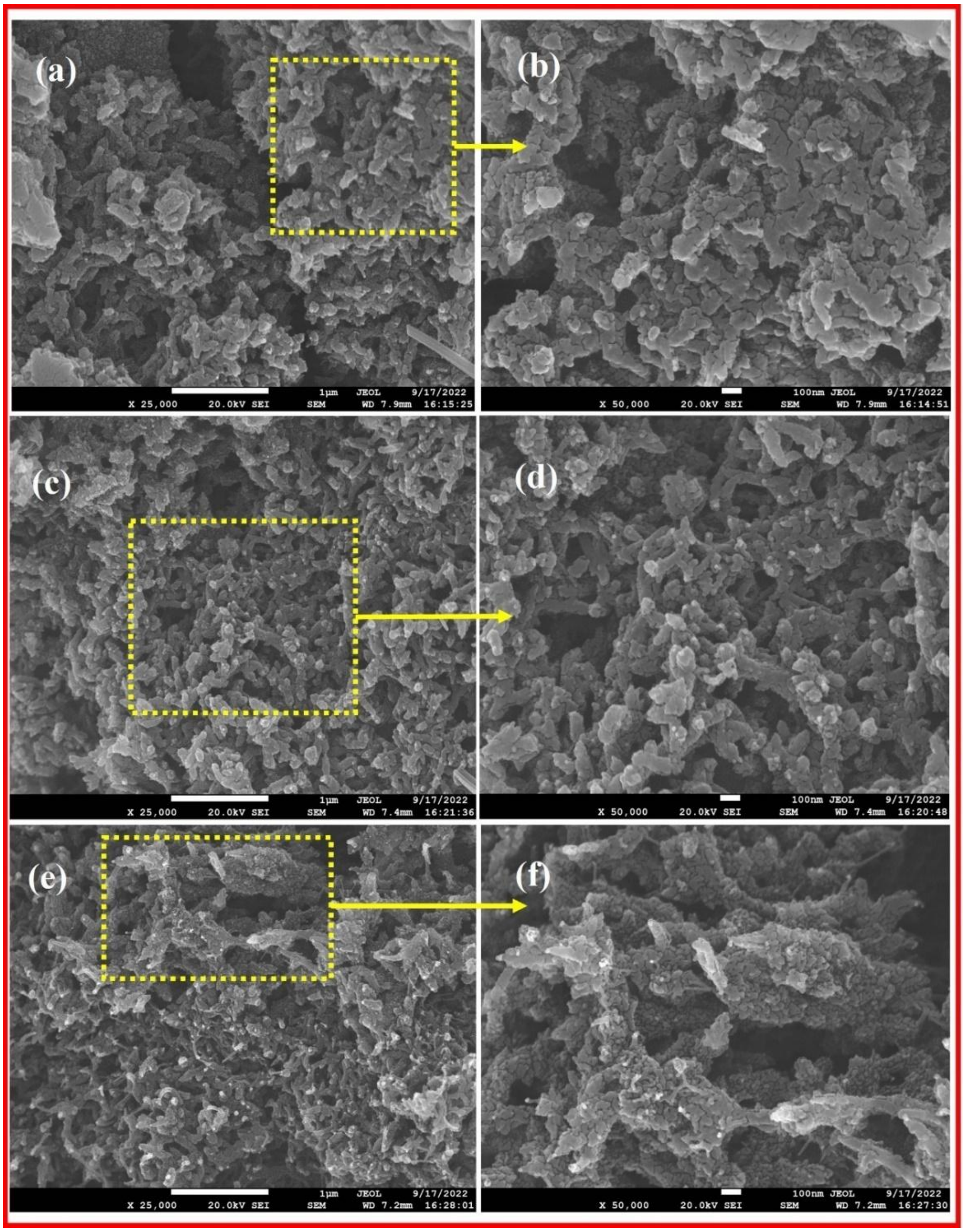

Figure 4.9. Recorded FESEM images of nanocomposites (a-b) PV1 (10 wt% V_2O_5-PANI) (c-d) PV2 (20 wt% V_2O_5-PANI) (e-f) PV3 (30 wt% V_2O_5-PANI).

The FESEM image of pure PANI displays the irregular porous morphology with randomly oriented grains as shown in Figure 4.8(a-b). Figure 4.9(a-f) shows the FESEM images for PV1, PV2 and PV3 nanocomposites, it has been observed that the irregular grains of PANI seem to align into uniform grains and lead to enhance porosity (see Figure 4.9(a–d)). This kind of morphological change is the result of uniform dispersion of filler (V_2O_5) in the polymer matrix [33]. The improved porosity as a result of grains alignment might be ascribed to the pi-basic character of the amino group, which permits the donation of their lone pair to the unoccupied valence orbitals of filler [34]. This led to provide more active sites for V_2O_5-PANI nanocomposites and improving the electrochemical performance of electrodes in supercapacitors. Furthermore, for the increased concentration i.e. PV3 nanocomposite shows aggregated morphology which could be ascribed to poor dispersion as well as the development of high stress inside the polymer matrix (see Figure 4.9(e-f)). Therefore, it is noted that the incorporation of nanoparticles up to 20 wt.% is sufficient to prevent nanoparticle aggregation for promoting superior nanocomposite properties. As a result, the capability of nanoparticles to grow uniformly with high porosity inside PANI matrix is inhibited at higher concentration (>20 wt.%), as shown in Figure 4.9 (d). Hence, it is concluded that the optimum concentration of V_2O_5 in the PANI should be up to 20 wt.% for ordered and porous morphology.

4.3.3. TGA study

The thermal stability of V_2O_5, PANI, PV1, PV2 and PV3 was studied by thermogravimetric analysis (TGA). In this analysis, TGA curves of weight loss % were recorded at temperatures ranging from room temperature to 600 ^{0}C for prepared samples (see Figure 4.10). The related thermal kinetics for prepared samples given in Table 4.1. The PANI, PV1, PV2 and PV3 showed three stages of weight loss. The first weight loss % observed below 110 ^{0}C arises mainly due to loss of water or volatile solvent and the unreacted acid trapped in the PANI [35]. The second weight loss % stage ranging between 114-263 ^{0}C, which attributes to the degradation of benzenoid ring structure of polymer or removal of dopant or acid from polymer (PANI) backbone. For third weight loss % stage, the temperature ranging from 277-570 ^{0}C commonly accountable to the thermal decomposition of the PANI chain [36]. Table 4.1. showed the weight loss % of V_2O_5, PANI, PV1, PV2 and PV3 at mid-point temperature of different stages. From the calculated results (see Table 4.1) it is clear that mid-point temperature range for first stage weight loss is alike for all the samples whereas in case of second and third stage a clear variation has been observed. At the end of degradation, the residue weight % for V_2O_5, PANI, PV1, PV2 and PV3 nanocomposites noted to be 98.2, 58.3, 60.2, 63.1 and 53.6 % respectively. It has been observed that weight loss % is less in PV2 (see Figure 4.10) i.e., more residue is left for PV2 nanocomposite which suggest that PV2 is more thermally stable than the other nanocomposites. The improved thermal stability observed in this study can be attributed to two factors: the inherent high thermal stability of V_2O_5 networks and the strong interactions between V_2O_5 particles and the polymer matrix. Specifically, the interaction between V_2O_5 and PANI chains restricts the thermal motion of macromolecules, increases the rigidity of macromolecular chains which leads to enhance the energy required for movement and breakage of polymeric chains. As a result, the mobility of PANI chains in the nanocomposite is reduced, which suppresses chain transfer reactions and slows down the degradation process. However, beyond 20 wt.% the stability of the composite is affected by the agglomeration as confirmed in FESEM.

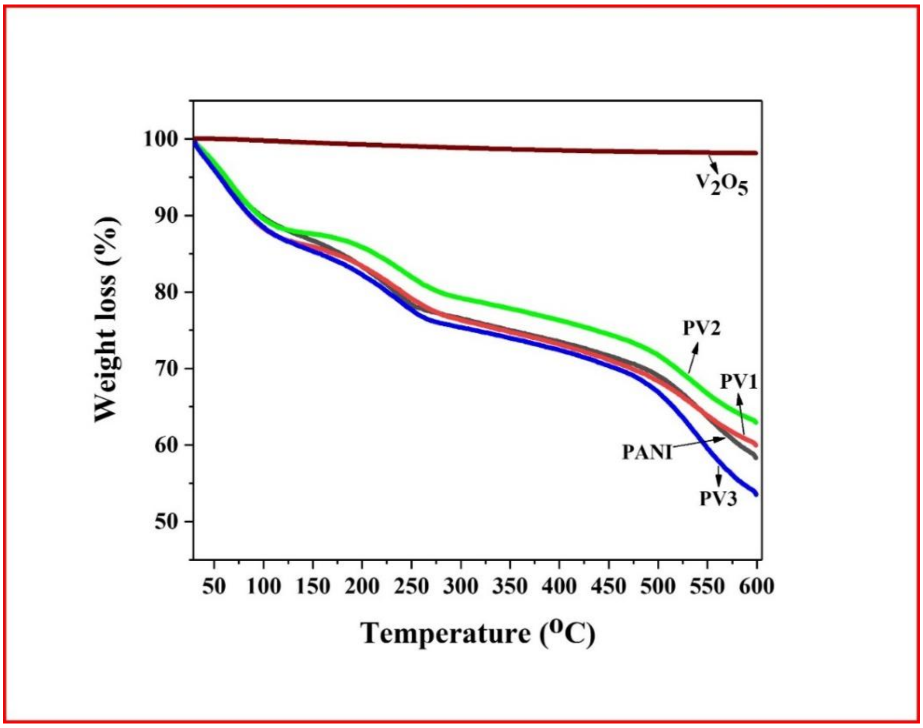

Figure 4.10. TGA curve of V_2O_5, PANI, PV1(10 wt% V_2O_5-PANI), PV2 (20 wt% V_2O_5-PANI) and PV3 (30 wt% V_2O_5-PANI).

Table 4.1. TGA data of PANI, PV1 (10 wt% V_2O_5-PANI), PV2 (20 wt% V_2O_5-PANI) and PV3 (30 wt% V_2O_5-PANI) nanocomposites.

Sample Name	First Stage		Second Stage		Third Stage	
	Mid-point (^{0}C)	Weight loss (%)	Mid-point (^{0}C)	Weight loss (%)	Mid-point (^{0}C)	Weight loss (%)
PANI	70	6.6	207	18	499	31
PV1	72	8.1	208	18	500	31.6
PV2	75	6.6	216	15.2	507	28
PV3	71	8.1	209	19	497	33

Further, the activation energy of the samples was calculated through the TGA using the Coats–Redfern method [37], and the values for V_2O_5, PANI, PV1, PV2, and PV3 nanocomposites were found to be 9.5, 5.6, 5.3, 5.2 and 5.4 KJ/mol respectively. Consequently, the PV2 nanocomposite demonstrates superior thermal stability compared to PV1, PV3, and PANI.

4.3.4. FTIR study

The FTIR (Fourier Transform Infrared Spectroscopy) spectrum of V_2O_5, PANI, PV1, PV2, and PV3 nanocomposites was recorded in the range of 400-4000 cm^{-1} (see Figure 4.11). The spectra of V_2O_5 shows three absorption band at 464.89, 829.52, and 1011.4 cm^{-1}. The absorption band at 464.89 cm^{-1} has been assigned the stretching modes of the oxygen, which are shared among three vanadium atoms and the peak located at 829.52 cm^{-1} corresponds to V-O-V vibrations [38]. Whereas the high absorption at 1011.4 cm^{-1} confirms the orthorhombic structure of V_2O_5 and is in agreement with XRD data [39].

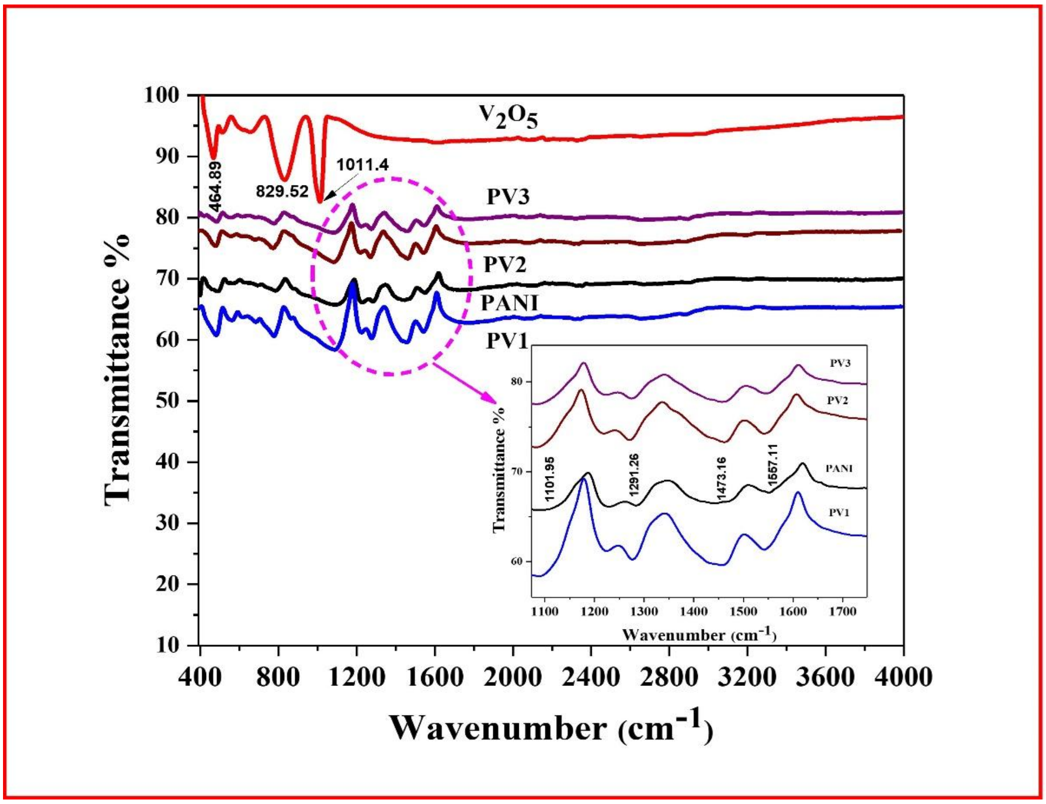

Figure 4.11. FTIR spectra of pure V_2O_5, PANI, PV1 (10 wt% V_2O_5-PANI), PV2 (20 wt% V_2O_5-PANI) and PV3 (30 wt% V_2O_5-PANI).

The prominent peak (1011.4 cm^{-1}) of orthorhombic V_2O_5 structures appeared due to the unshared stretching vibration of V=O [40]. PANI spectra show absorption peaks at 1101.95, 1291.26, 1473.16 and 1557.11 cm^{-1}. The absorption peak at 1101.95 cm^{-1} displays the stretching mode of C=N for quinoid rings and the peak appearing at 1291.26 cm^{-1} demonstrates the stretching of C-N in the amine group. The peak located at 1473.16 cm^{-1} attributes the stretching mode of two doubly bonded carbon (C=C) in the benzenoid ring and the absorption peak at 1557.11 cm^{-1} attributes the stretching vibration of two carbon (C=C) [36]. According to Figure 4.11 spectra of PANI nanocomposites it is found that after the incorporation of V_2O_5 into PANI matrix, there is a noteworthy increase in the intensity of (C=N) quinoid rings, (C-N) amine group, doubly bonded carbon (C=C) stretching and vibrational peaks (see inset of Figure 4.11). This effect indicates a decrease in the electrostatic and van der Waals interactions in the PANI matrix with the addition of V_2O_5, which allows the vibrational motion of bonds, leading to an increase in the dipole moments of these bonds [36]. A minor shift in the peak locations of several functional groups was observed towards a lower wavenumber with the addition of filler in the PANI matrix, which supports the existence of interfacial interactions between the two phases. The broadening of the peaks observed in the quinoid, amine, and doubly bonded carbon stretching groups points to the presence of intermolecular interactions between the two phases. These intermolecular contacts influence neighbouring molecules, leading to induce more vibrations.

4.3.5. Raman spectral analysis

The Raman spectrum of V_2O_5 is shown in Figure 4.12(a), where peaks located at 101, 145, 198, 284, 305, 406, 484, 531, 704, and 996 cm^{-1} correspond to the Raman signature of V_2O_5 crystal. Peak at 101 cm^{-1} is due to external T_y modes [45]. Most prominent low-wavenumber band at 145 cm^{-1} arises from the skeleton bending vibration, while the peaks at 198 and 284 cm^{-1} result from the bending vibrations of the O_c-V-O_b bond. Bending vibration (B) of V-O_c and bending vibration of the V-O_b-V bond occur at around 305 and 406 cm^{-1}. While the stretching vibration (S) of V-O_c bond and stretching vibration of the V-O_b-V bond occur at approximately 531 and 704 cm^{-1}, respectively. Peak at 145 cm^{-1} corresponding to the skeleton Raman mode, is indicative of the layered structure of V_2O_5 material. On the other hand, the peak at 996 cm^{-1}, corresponding to the stretching of vanadium atoms connected to oxygen atoms through double bonds (V=O), is indicative of the formation of V_2O_5 nanoparticles [45,46]. Raman spectrum of PANI, recorded with 785 nm excitation (see Figure 4.12(b)), displays various bands in the 1100-1700 cm^{-1} wavenumber range, which correspond to the stretching modes of various bands [47]. The Raman band at 1595.8 cm^{-1} represents the C-C stretching vibration of the benzene ring. The band at 1508 cm^{-1} corresponds to N-H deformation vibrations. The 1341-1352 cm^{-1} range gives information on carrier vibrations in PANI's C-N^+ polaronic structure. The band at 1233 cm^{-1} corresponds to the polaronic unit's C-N stretching mode. A strong Raman band at 1170 cm^{-1} corresponds to C-H vibrations in aromatic rings. The Raman band in the 1000–400 cm^{-1} region gives insight into the deformation vibrations of benzene rings [48]. Bands at 806.3 and 415 cm^{-1} correspond to in-plane and out-of-plane vibrations of the ring of the protonated emeraldine form of PANI [49]. Raman spectra of doped PANI with V_2O_5 displays no new peaks, indicating that the structure of the polymer remains unchanged without any deformation.

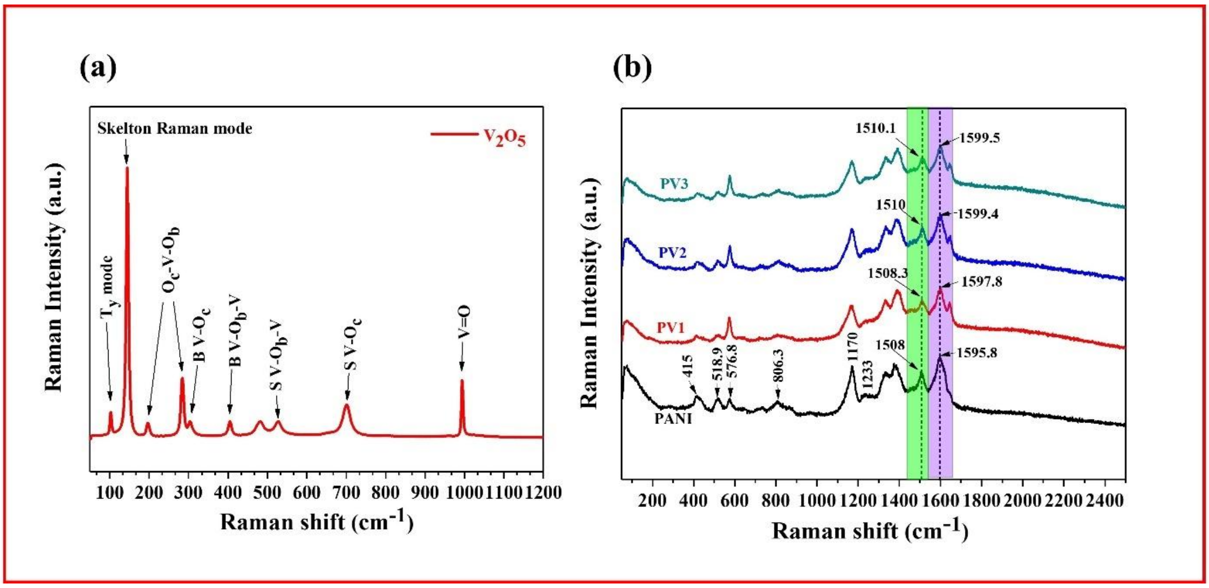

Figure 4.12. (a) Raman spectra of pure V_2O_5 (b) Raman spectra of pure PANI, PV1 (10 wt% V_2O_5-PANI), PV2 (20 wt% V_2O_5-PANI) and PV3 (30 wt% V_2O_5-PANI) samples.

Furthermore, Raman spectra towards higher wave number is commonly associated with a reduction in the chemical bond length of the molecules. In the case of PV1, PV2 and PV3, as the weight percent of V_2O_5 in the PANI matrix increases, the bond length of the V_2O_5 and PANI molecules is likely to decrease, leading to a shift in the Raman spectra towards higher wave numbers.

The observed slight blue shift in the Raman band from 1595 to 1599 cm^{-1} i.e. towards higher wavenumber could be arises due to introduction of the defects due to V_2O_5 inclusion. This leads to increase the vibrational frequencies of the chemical bonds in the PANI and hence due to the quantization of the energy levels the density of electronic state changes, induces changes in the electronic structure of the PANI [50].

4.3.6. Electrochemical study

The appropriate potential window is selected in the span of -0.01 to 0.5 V. A comparative cyclic voltammogram study of V_2O_5, PANI, PV1, PV2 and PV3 is shown in Figure. 4.13(a). CV shows pair of redox peaks C' and C'' correspond to K^+ extraction and insertion in V_2O_5 material [23,24]. The CV of PANI shows pair of peaks: A'/A'' at 0.308/0.199 V indicates the transition between leucoemeraldine and emeraldine states while peaks B'/B'' point toward the switching between emeraldine and pernigraniline states of polyaniline [51]. The CV curve of PV1, PV2 and PV3 shows the merging of V_2O_5 and PANI, indicating the effective assimilation of V_2O_5 in the polyaniline matrix. The CV curve (see Figure. 4.13(a)) of the V_2O_5, PANI, PV1, PV2 and PV3 electrodes at a scan rate of 10 mV/sec precisely illustrates a high unified area under the curve for PV2, suggesting that the PV1 as well as PV3 electrodes have poor electrochemical activity due to the low charge diffusion rate.

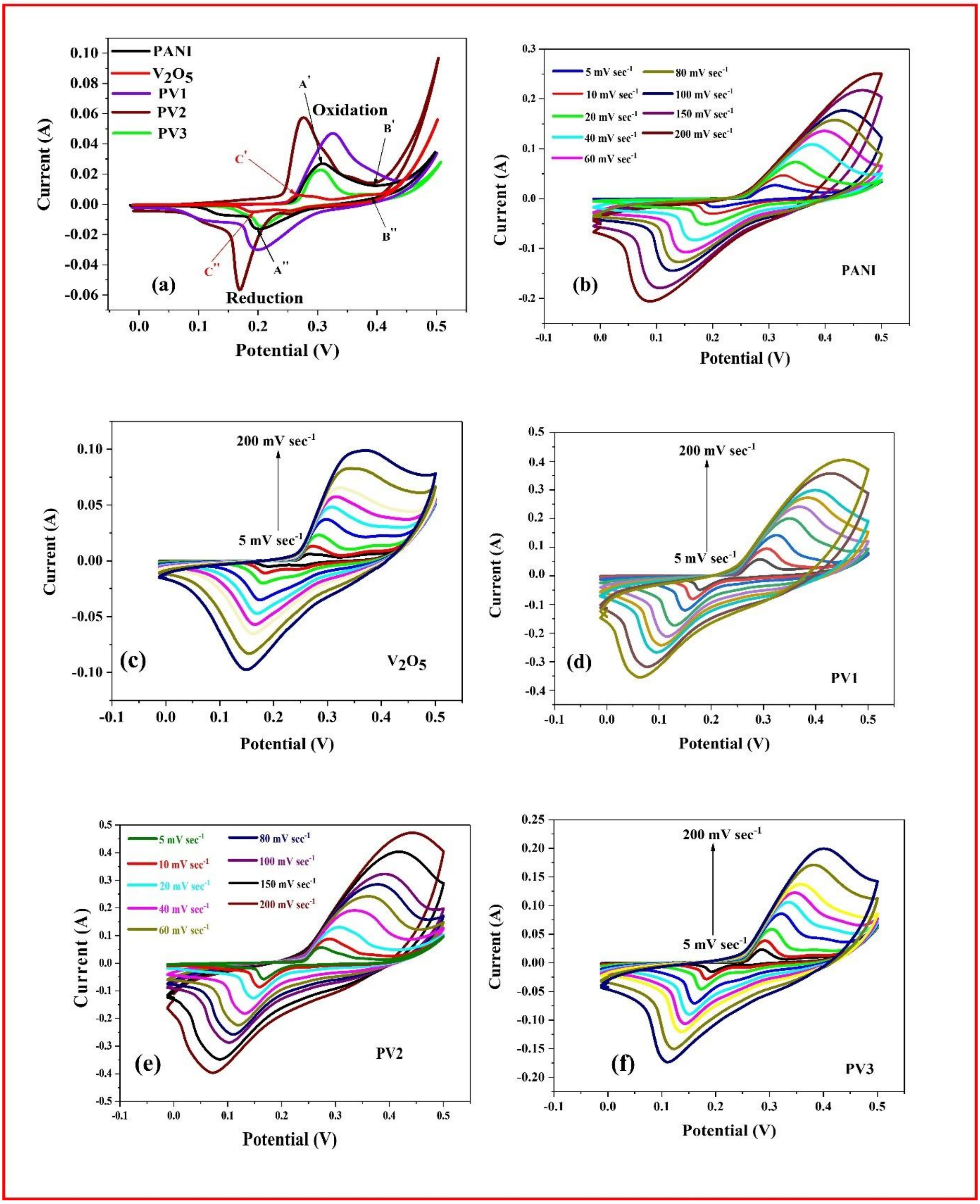

Figure 4.13. (a) Cyclic voltammogram of V_2O_5, PANI, PV1 (10 wt% V_2O_5-PANI), PV2 (20 wt% V_2O_5-PANI), and PV3 (30 wt% V_2O_5-PANI) at a 10 mV sec^{-1}. (b-f) CV curve of PANI, V_2O_5, PV1, PV2, and PV3 electrodes at different scan rates.

The electrode with a more contact area (PV2) provides a more appropriate alleyway for ion diffusion in the electrode peak and indicates outstanding faradic behavior [52].

The obtained geometry of CV curve for all samples is found to be different from that of rectangular shaped ideal electric double-layer behaviour of CV curve. This indicates the growth of the redox reaction and pseudocapacitive behavior of electroactive materials [53]. The CV curves of PANI, V_2O_5, PV1, PV2 and PV3 at different scanning rates such as 5, 10, 20, 40, 60, 80, 100, 150 and 200 mV sec^{-1} displayed in Figure 4.13(b-f) indicate that redox peak raises with the increment of scan rates. Furthermore, the movement of oxidation-reduction peaks in the direction of higher and lower potentials (See Figure 4.13(b-f)) reflects the strengthening of the electric polarization and viable kinetic irreversibility of the KOH ions on the electrode's surface [54]. Using the equation (4.4) the specific capacitance (C) can be determined [55].

$$C = \frac{A}{ms(V_a - V_c)} \tag{4.4}$$

where, "A" is the area under the CV curve, "m" is the loaded mass of material, "s" is the scan rate, "V_a" is anodic potential and "V_c" is cathodic potential.

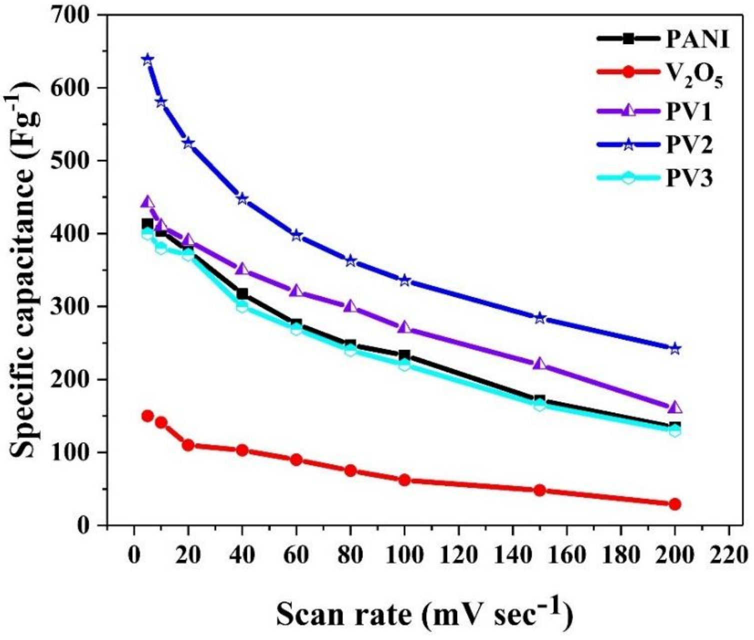

Figure 4.14. Specific capacitance of PANI, V_2O_5, PV1 (10 wt% V_2O_5-PANI), PV2 (20 wt% V_2O_5-PANI) and PV3 (30 wt% V_2O_5-PANI) at various scanning rates.

The calculated values of "*C*" for V_2O_5, PANI, PV1, PV2 and PV3 at 10 mV sec^{-1} scan rate found to be 140.98, 413, 442, 638 and 380 Fg^{-1} respectively. The variation of "*C*" with the increasing scan rate from 5 to 200 mV sec^{-1} (see Figure 4.14) can be described on the basis of the flow of KOH ions and charges inside the electrode materials.

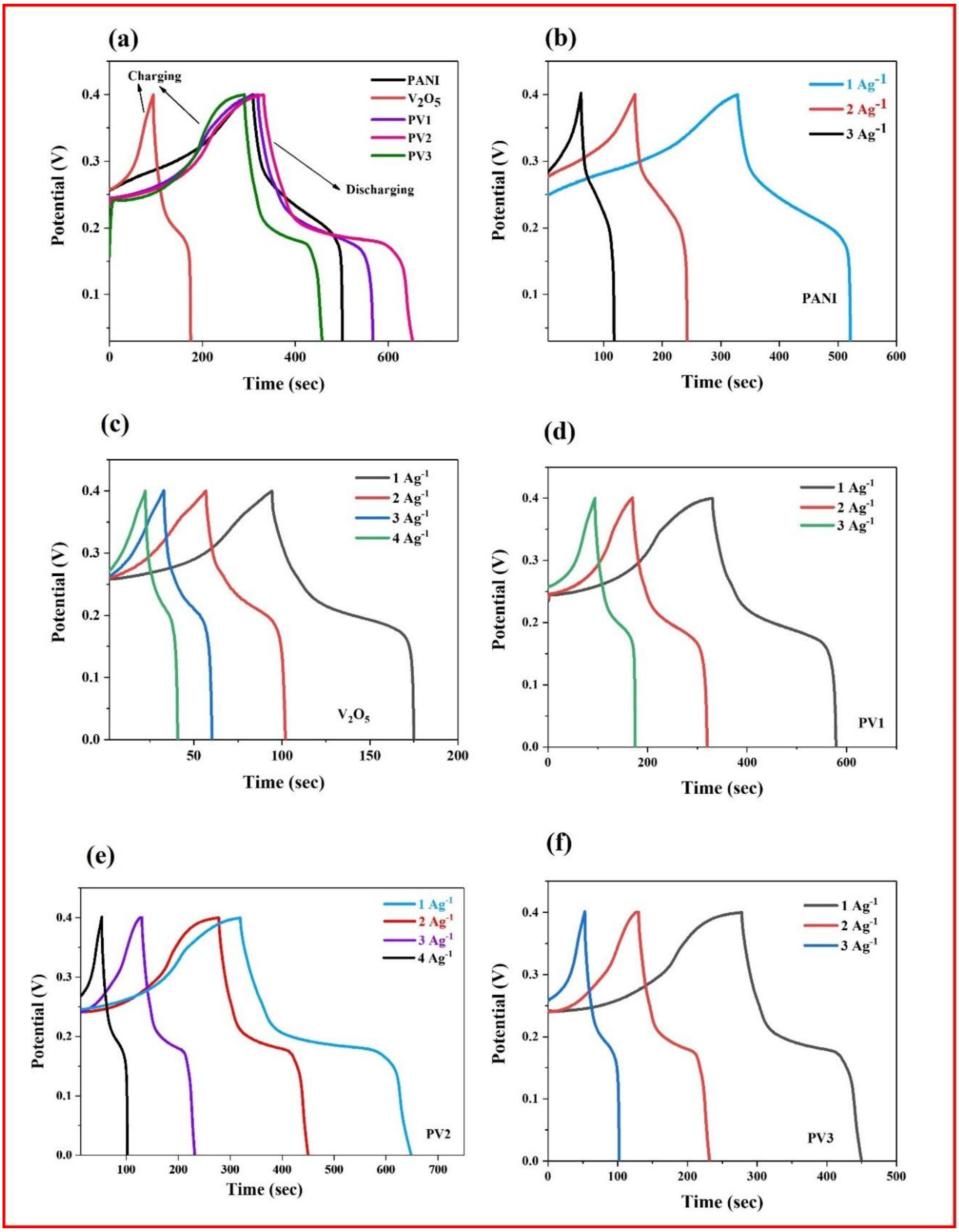

Figure 4.15. (a) GCD curve of V_2O_5, PANI, PV1 (10 wt% V_2O_5-PANI), PV2 (20 wt% V_2O_5-PANI) and PV3 (30 wt% V_2O_5-PANI) at a 1 Ag^{-1}. (b-f) GCD curve of PANI, V_2O_5, PV1, PV2 and PV3 at varied current densities.

At a lower scanning rate, the ions from the KOH solution have a plentiful time to contact the maximum surface area of the electrode materials. Consequently, the significant number of ions collected at the electrode surface leads to an improvement in the "C" value of the electrode. However, when the scan rates rise, the mobility of charges per unit of time increases, which results in a smaller amount of ion gathering at the interface of the electrode and gives a decrease in specific capacitance value. Thus, the CV study showed that the PV2 electrode is more suitable compared to PANI and V_2O_5.

The GCD study of the V_2O_5, PANI, PV1, PV2, and PV3 electrodes was conducted in the appropriate potential window range 0-0.4 V (see Figure 4.15(a)). In the GCD profile for all electrodes the peak corresponds to discharge curves demonstrated the non-linear behavior of electrodes and suggested that all of the fabricated electrode materials have pseudocapacitive properties [56]. The discharge time of PV2 is found to be widely extended signifying the higher charge storage capacity of the electrode. The specific capacitance (C) of fabricated electrodes can be calculated by using equation (4.5) [55].

$$C = \frac{It}{V} \tag{4.5}$$

where, "I" is current density, "t" is discharging time and "V" is potential window used in GCD curve.

The calculated values of "C" for V_2O_5, PANI, PV1, PV2 and PV3 electrodes at 1 Ag^{-1} current density are 190, 485, 618, 820.5, and 417 Fg^{-1} respectively are in accordance to CV study. Furthermore, the GCD curves of PANI, V_2O_5, PV1, PV2 and PV3 were examined at various current densities (see Figure 4.15(b-f)) and the "C" values were calculated using equation (4.5) and plotted in Figure 4.16(a). From the plot it is evident that PV2 electrode shows higher "C" values as compared to pure PANI, which further confirms the formation of a porous structure to improve the electrochemical activity of the electrode. Moreover, the obtained trend of the graph clearly depicts the gradual decrement of "C" with increase in current density, which is in good agreement with earlier reports [57-59].

The decrease in the "C" values might be due to diffusion effect which inhibits the further migration of electrolytic ions to the electrode. Hence, charge storage is no longer possible in the active area of the surface. For practical application it is important to check and analyze the long-term stability of the fabricated electrode.

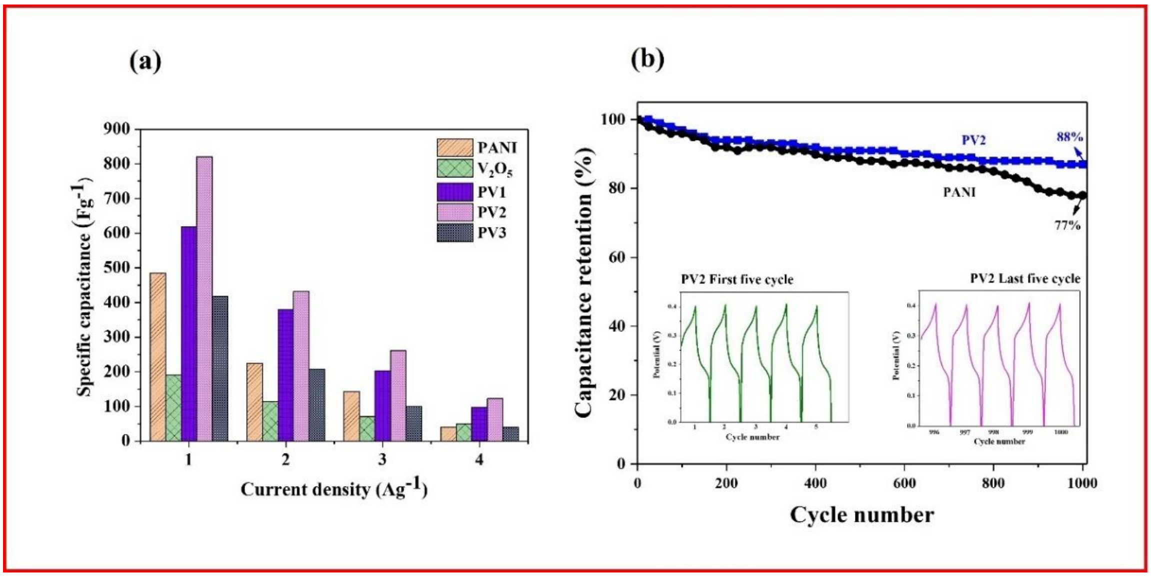

Figure 4.16. (a) Change of PANI, V_2O_5, PV1 (10 wt% V_2O_5-PANI), PV2 (20 wt% V_2O_5-PANI) and PV3 (30 wt% V_2O_5-PANI) specific capacitance at altered current densities. (b) Cyclic stability of PANI and PV2 electrodes.

Table 4.2. Comparison of Specific capacitance of PANI and PV2 (20 wt% V_2O_5-PANI) electrode with reported electrode materials.

Materials	Electrolyte	Current density (CD)	Specific capacitance (C) (Fg^{-1})	References
PANI-Coated MnO_2	1M H_2SO_4	0.5 $mAcm^{-1}$	257	[60]
PANI-Grafted MnO_2	1M H_2SO_4	0.5 $mAcm^{-1}$	407	[60]
PANI	2M H_2SO_4	0.1 Ag^{-1}	457	[61]
Hollow Carbon-PANI	2M H_2SO_4	0.1 Ag^{-1}	525	[61]
PANI/Fe_3O_4	1M H_2SO_4	0.5 Ag^{-1}	572	[62]
PANI-TiO_2	1M H_2SO_4	1 Ag^{-1}	732	[63]
MnS/GO/PANI	6M KOH	1 Ag^{-1}	773	[64]
PANI	1M H_2SO_4	0.2 Ag^{-1}	300	[65]
PANI-GO	1M H_2SO_4	0.2 Ag^{-1}	555	[65]
V_2O_5-PANI	1M H_2SO_4	1 Ag^{-1}	538	[23]
V_2O_5-PANI	5M LiCl	1 Ag^{-1}	450	[24]
V_2O_5-PANI	0.5M $LiClO_4$ propylene carbonate	1 Ag^{-1}	1115	[48]
PANI	**6M KOH**	**1 Ag^{-1}**	**485**	**Present work**
(20 wt% V_2O_5-PANI)	**6M KOH**	**1 Ag^{-1}**	**820.5**	**Present work**

Figure 4.16(b) shows the electrochemical stability of the PV2 electrode. The recorded retention rate of the capacitance is 88% up to 1000 cycles suggests the good stability of the fabricated electrode. It is to be noted that the inclusion of the V_2O_5 contribute to enhance the poor stability of the PANI i.e. 77%, helps to improve the retention rate and maintain up to 88%. A comparison of PANI and V_2O_5 doped PANI electrode capacitance with reported electrode materials has been shown in Table 4.2.

Electrochemical Impedance Spectroscopy (EIS) is the most important tool to analyze the electrochemical activity of electrode materials. Fig. 4.17(a-b) shows Nyquist plots of PANI, PV1, PV2 and PV3 electrodes.

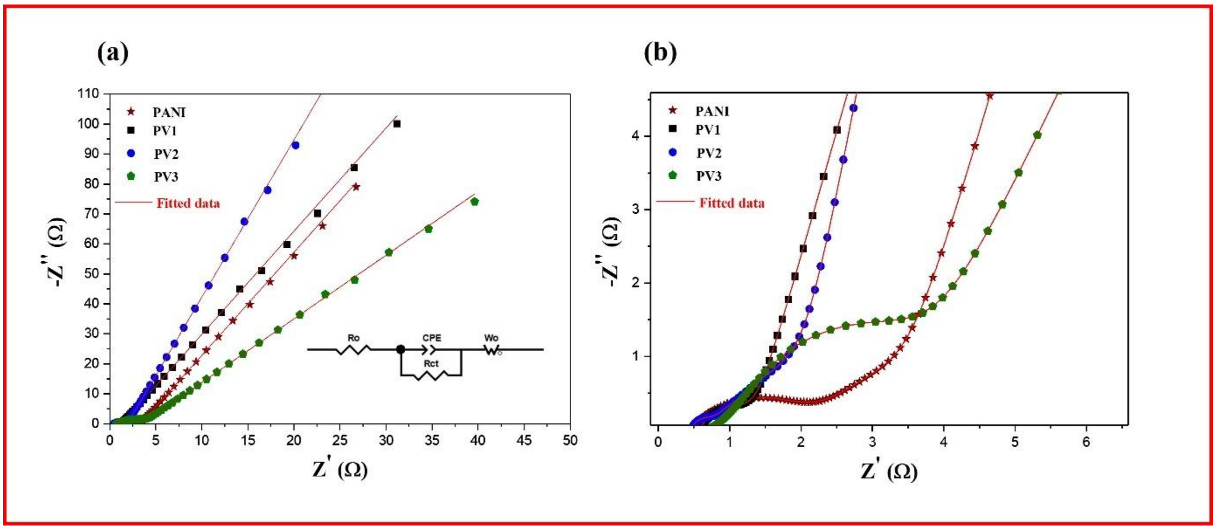

Figure 4.17. (a) Nyquist plot of PANI, PV1(10 wt% V_2O_5-PANI), PV2 (20 wt% V_2O_5-PANI) and PV3 (30 wt% V_2O_5-PANI) (b) magnified view of PANI, PV1, PV2 and PV3.

The Nyquist plot has also been further simulated using ZSimpWin (ver. 2.0) with an electrical equivalent circuit (shown in the inset of the Figure 4.17(a)) to confirm experimental findings of EIS. The simulated profiles for all samples are in good agreement with experimental data and are displayed by the red (solid) line. The impedance plots of PANI and its nanocomposites showing two different patterns, semi-circular portion at high frequencies and a linear component at low frequencies. In electrochemical impedance spectroscopy, the semi-circular section in the high-frequency region represents the charge transfer resistance (Rct) at the electrode-electrolyte interface. By extrapolating the curve of the real part Z′ in this region, the solution resistance (Ro) can also be determined. The electrode exhibits capacitor behavior in the low-frequency region, indicated by the slope of the straight line. The solution resistance (Ro) values of PANI, PV1, PV2, and PV3 were found to be 0.51, 0.52, 0.5, and 0.71 **Ω**, whereas electrodes exhibited Rct values of 1.6, 0.7, 0.31, and 2.4 **Ω** respectively. Figure 4.17(b) clearly indicates that PV2 electrodes displayed the lowest value of Ro and Rct. PV2 electrode has a smaller semicircle diameter than the PANI, PV1, and PV3 electrodes, signifying a lower charge transfer resistance in the electrode. PV2 electrode shows ideal capacitive behavior and could be confirmed from the observed trend in the low-frequency region which is closer to the imaginary axis (that is y-axis) than the other samples. Therefore, EIS study clearly demonstrated that PV2 electrode offered best supercapacitor performance.

To have further insight into our electrochemical investigation, we examined the storage mechanisms of the prepared electrodes. Charge storage primarily comprises three key elements: the initial two attributed from faradic surface redox reactions and intercalating (diffusion) pathways, giving rise to pseudo-capacitive behavior. Meanwhile, the third component is associated with interfacial effects, attributed to the creation of an electric double layer (EDL). These contributions were examined by analyzing the correlation between the CV peak current 'i' and scan rate 'v', as given by equations (4.6) and (4.7) [66].

$$i = av^b \tag{4.6}$$

$$\log(i) = \log(a) + b\log(v) \tag{4.7}$$

The 'b' parameter values can be determined from the slope of equation (4.7). In literature, it is reported that the 'b' value equal to 1 signifies pseudocapacitive behavior, while a value equal to 0.5 suggests a battery-like (diffusion-controlled) process, respectively [66]. The anode peaks in pure PANI, V_2O_5, PV1, PV2, and PV3 exhibit 'b' values of 0.66, 0.55, 0.67, 0.58, and 0.57, respectively (see Figure 4.18(a)). These values indicate that the specific capacitances of the electrodes are influenced by both diffusion-controlled and pseudocapacitive behavior. Further, the diffusion-controlled and pseudocapacitive contribution can be studied using the CV curves and equations (4.8) and (4.9)[67].

$$i(V) = K_1 v + K_2 v^{1/2} \tag{4.8}$$

$$\frac{i(V)}{v^{1/2}} = K_1 v^{1/2} + K_2 \tag{4.9}$$

The parameters 'K_1' and 'K_2' are tuneable quantities derived from the slope and y-axis intercept of the curves between '$i\ v^{-1/2}$'and '$v^{1/2}$'. The parameters 'K_1v' and '$K_2v^{1/2}$' represent the fractions that signify the capacitive and diffusion-type behavior, respectively. Figure 4.18(b) illustrates the fractions representing the contribution of battery-type (diffusion-controlled) process behavior of PANI, V_2O_5, PV1, PV2 and PV3. Based on the aforementioned calculations, the diffusion contributions for PANI are as follows: 72%, 69%, 64%, 59%, 52%, 46%, and 42% at a scan rate of 5, 10, 20, 40, 60, 80 and 100 mV sec^{-1}, respectively.

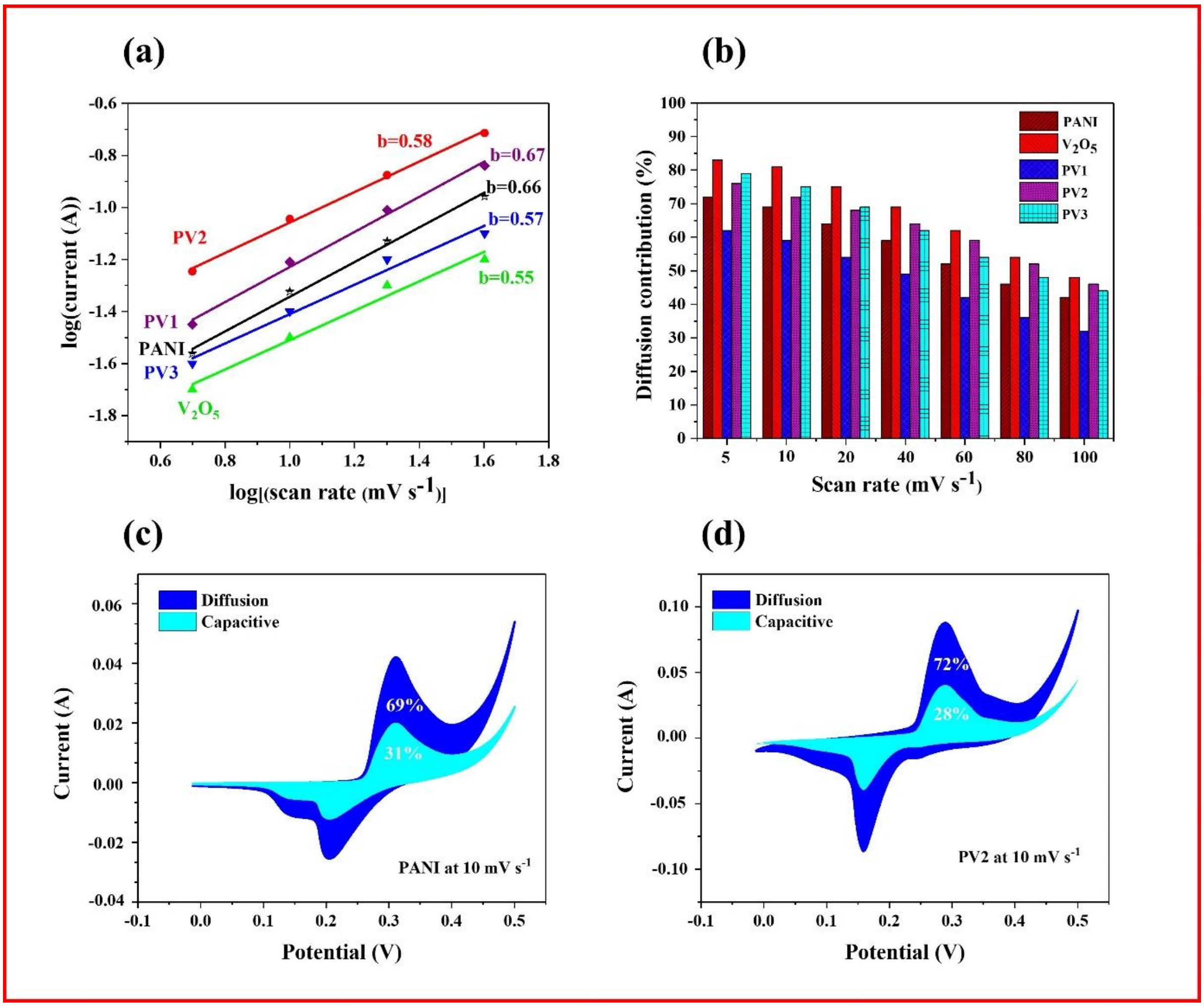

Figure 4.18. (a) Graph depicts the relationship between the log of peak current and the log of the scan rate for the anodic peaks. (b) Percentage of diffusion contribution by PANI, V_2O_5, PV1 (10 wt% V_2O_5-PANI), PV2 (20 wt% V_2O_5-PANI) and PV3 (30 wt% V_2O_5-PANI) at altered scan rates. (c-d) Separation of percentage contributions of capacitive and diffusion current of PANI and PV2 (20 wt% V_2O_5-PANI) with respect to a fixed scan rate of 10 mV sec^{-1}.

Similarly, for PV2, the ratios of diffusion contribution are, 76%, 72%, 68%, 64%, 59%, 52%, and 46% at a scan rate of 5, 10, 20, 40, 60, 80, and 100 mV sec^{-1} respectively. At a lower scanning rate, the electrolyte ions are granted additional time to effectively engage with the electrode materials, leading to a significant involvement through faradaic interactions. On the other hand, at higher scan rates, charge storage predominantly occurs through non-faradaic pathways due to the limited time for electrolyte-ion interaction with electrode materials. The cyclic voltammograms obtained at a scan rate of 10 mV sec^{-1} for PANI and PV2 electrode materials are depicted in Figure 4.18(c-d). The portion of the CV curve that looks in a blue color illustrates the current attributed to the battery-type (diffusion) mechanism and region shaded in cyan color represents the charge storage associated with the capacitive mechanism. Hence, the aforementioned outcomes clearly indicate that introducing V_2O_5 into the PANI matrix significantly improves its battery-type (diffusion) mechanism. The improved electrochemical performance of PV2 can be ascribed to several factors. Firstly, the distribution of V_2O_5 nanoparticles within porous PANI shortens the distance for electron transfer and ion diffusion, while the considerable specific surface area offers more sites for electrochemical reactions and improved pathways for ion diffusion within the composite structure [70]. Additionally, the crystalline V_2O_5 can contribute to capacitance via diffusion, as suggested by the energy storage mechanism. The presence of high-valence vanadium (V^{5+}) allows for the storage of more charges than low-valence vanadium (V^{4+} and V^{3+}) [71]. Furthermore, PV2 synergistically enhances electrical conductivity and structural integrity, resulting in an increased capacity for storing charges through diffusion-based mechanisms.

4.3.7. Practical applications of fabricated electrode

For practical purposes, we evaluated the performance of symmetrical PV2 electrodes within a 6 M KOH electrolyte to determine the amount of voltage that the electrochemical system could store. To achieve this, we immersed two electrodes in the electrolyte solution and supplied voltage through a direct current (DC) battery. Following the charging process, we measured the voltage stored within the electrochemical system using a multimeter.

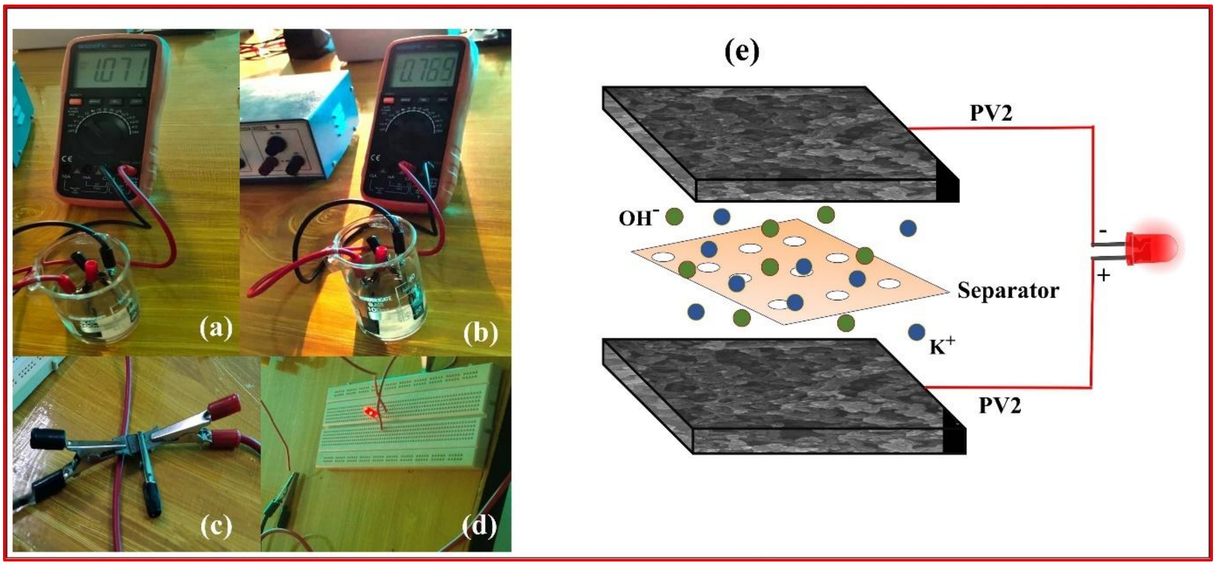

Figure 4.19. (a) Intial reading of two PV2 (20 wt% V_2O_5-PANI) immersed electrode in electrolyte solution. (b) reading of PV2 electrode in multimeter after 10 sec. (c) PV2//PV2 symmetrical assembled supercapacitor device. (d) ignition of a red LED using PV2//PV2 symmetric devices. (e) schematic of PV2//PV2 symmetical device.

The initial reading was recorded at 1.07 V (see Figure 4.19(a)). However, it rapidly decreased to 0.769 V (see Figure 4.19(b)), indicating that our electrochemical system can retain approximately 0.75 V over time. This implies that a stable potential of 0.75 V might be attainable for a symmetrical PV2 electrochemical system. Further, the PV2//PV2 symmetric supercapacitor device was assembled using two equal-sized PV2 electrodes with wet 6 M KOH Whatman filter as a separator (see schematics in Figure. 4.19(e)). However, for symmetrical device configuration, it is possible to calculate theoretical ED and PD by using three electrode outcomes. The ED (Wh kg^{-1}) and PD (W kg^{-1}) can be computed using equation (4.10) (4.11) [72].

$$ED = \frac{CV^2}{8 \times 3.6} \tag{4.10}$$

$$PD = \frac{ED}{T} \times 3600 \tag{4.11}$$

where "V", and "T" denote potential window, and discharging time/4 respectively for the PV2 electrode.

The ED and PD values for the PV2//PV2 symmetric device are 4.6 Wh kg^{-1} and 80.7 W kg^{-1} respectively at a 1 A g^{-1} of CD. In addition, to assess the practical viability of the PV2 electrode, a PV2//PV2 symmetrical supercapacitor device was established (see Figure 4.19(c)). Three cells were connected in series, charged using an external power source with a voltage of 3 volts, and subsequently discharged by illuminating a red LED. The successful illumination of the red LED by the PV2//PV2 device suggests that the PV2 electrode displays a potential candidate for next-generation energy storage devices.

4.4. Conclusions

In summary, V_2O_5 nanoparticles were successfully synthesized by sol-gel method and doped in PANI matrix with different wt.% using in situ polymerization method. The prepared nanoparticles were characterized through XRD to determine the electron density, microstrain and crystallite size via Rietveld refinement and Williamson-Hall calculations. Uniform dispersion of V_2O_5 inside the PANI matrix was confirmed through FESEM, showing the alignment of non-uniform grains to uniform grains giving a porous morphology for PV2 nanocomposites which is valuable for good electrochemical activity. FTIR and Raman spectra of the V_2O_5-PANI nanocomposites show shifts in peaks, providing evidence of the effective intercalation of V_2O_5 into the PANI matrix. In the electrochemical studies, among all electrodes PV2 electrode presented a prominent specific capacitance of 820.5 Fg^{-1} at a current density of 1 Ag^{-1} and demonstrated a decent cyclic lifespan with a capacity maintenance rate of 88% after 1000 cycles. Additionally, the PV2 electrode also delivered a good ED and PD of 4.6 Wh kg^{-1}

and 80.7 Wkg^{-1} respectively. Finally, the successful illumination of a red LED by the symmetric device strongly suggests that the PV2 electrode is a promising candidate for next-generation energy storage devices.

References

[1] Meng F, Ding Y. Sub-micrometer-thick all-solid-state supercapacitors with high power and energy densities. Advanced Materials. 2011;35(23):4098-102.

[2] Wu Q, Xu Y, Yao Z, Liu A, Shi G. Supercapacitors based on flexible graphene/polyaniline nanofiber composite films. ACS nano. 2010;4(4):1963-70.

[3] Weng Z, Su Y, Wang DW, Li F, Du J, Cheng HM. Graphene–cellulose paper flexible supercapacitors. Advanced Energy Materials. 2011;1(5):917-22.

[4] Hussain S, Yang X, Aslam MK, Shaheen A, Javed MS, Aslam N, Aslam B, Liu G, Qiao G. Robust TiN nanoparticles polysulfide anchor for Li–S storage and diffusion pathways using first principle calculations. Chemical Engineering Journal. 2020;391:123595.

[5] Hwang JY, Kim HM, Shin S, Sun YK. Designing a high-performance lithium–sulfur batteries based on layered double hydroxides–carbon nanotubes composite cathode and a dual-functional graphene–polypropylene–Al_2O_3 separator. Advanced Functional Materials. 2018;28(3):1704294.

[6] Liu H, Zhao D, Liu Y, Hu P, Wu X, Xia H. Boosting energy storage and electrocatalytic performances by synergizing $CoMoO_4$@ $MoZn_{22}$ core-shell structures. Chemical Engineering Journal. 2019;373:485-92.

[7] Zhang LL, Zhou R, Zhao XS. Graphene-based materials as supercapacitor electrodes. Journal of Materials Chemistry. 2010;20(29):5983-92.

[8] Wang G, Zhang L, Zhang J. A review of electrode materials for electrochemical supercapacitors. Chemical Society Reviews. 2012;41(2):797-828.

[9] Pandolfo AG, Hollenkamp AF. Carbon properties and their role in supercapacitors. Journal of power sources. 2006;157(1):11-27.

[10] Ghenaatian HR, Mousavi MF, Kazemi SH, Shamsipur M. Electrochemical investigations of self-doped polyaniline nanofibers as a new electroactive material for high performance redox supercapacitor. Synthetic metals. 2009;159(17-18):1717-22.

[11] Kötz R, Carlen MJ. Principles and applications of electrochemical capacitors. Electrochimica acta. 2000;45(15-16):2483-98.

[12] Bose S, Kuila T, Mishra AK, Rajasekar R, Kim NH, Lee JH. Carbon-based nanostructured materials and their composites as supercapacitor electrodes. Journal of Materials Chemistry. 2012;22(3):767-84.

[13] Frackowiak E, Beguin F. Carbon materials for the electrochemical storage of energy in capacitors. Carbon. 2001;39(6):937-50.

[14] Zhu J, Gu H, Luo Z, Haldolaarachige N, Young DP, Wei S, Guo Z. Carbon nanostructure-derived polyaniline metacomposites: electrical, dielectric, and giant magnetoresistive properties. Langmuir. 2012;28(27):10246-55.

[15] Gurunathan K, Murugan AV, Marimuthu R, Mulik UP, Amalnerkar DP. Electrochemically synthesised conducting polymeric materials for applications towards technology in electronics, optoelectronics and energy storage devices. Materials chemistry and physics. 1999;61(3):173-91.

[16] Zhang X, Ji L, Zhang S, Yang W. Synthesis of a novel polyaniline-intercalated layered manganese oxide nanocomposite as electrode material for electrochemical capacitor. Journal of Power Sources. 2007;173(2):1017-23.

[17] Mirmohseni A, Dorraji MS, Hosseini MG. Influence of metal oxide nanoparticles on pseudocapacitive behavior of wet-spun polyaniline-multiwall carbon nanotube fibers. Electrochimica Acta. 2012;70:182-92.

[18] Arjomandi J, Lee JY, Movafagh R, Moghanni-Bavil-Olyaei H, Parvin MH. Polyaniline/aluminum and iron oxide nanocomposites supercapacitor electrodes with high specific capacitance and surface area. Journal of Electroanalytical Chemistry. 2018;810:100-8.

[19] Eftekhari A, Li L, Yang Y. Polyaniline supercapacitors. Journal of Power Sources. 2017;347:86-107.

[20] Arjomandi J, Keramat Irad Mossa N, Jaleh B. Electrochemical synthesis and In situ spectroelectrochemistry of conducting NMPy-TiO_2 and ZnO polymer nanocomposites for Li secondary battery applications. Journal of Applied Polymer Science. 2015;132(8).

[21] Wei H, Gu H, Guo J, Cui D, Yan X, Liu J, Cao D, Wang X, Wei S, Guo Z. Significantly enhanced energy density of magnetite/polypyrrole nanocomposite capacitors at high rates by low magnetic fields. Advanced Composites and Hybrid Materials. 2018;1:127-34.

[22] Kannagi K. Super critically synthesized V_2O_5 spheres based supercapacitors using polymer electrolyte. Applied Surface Science. 2018;456:13-8.

[23] Roy A, Ray A, Sadhukhan P, Saha S, Das S. Morphological behaviour, electronic bond formation and electrochemical performance study of V_2O_5-polyaniline composite and its application in asymmetric supercapacitor. Materials Research Bulletin. 2018;107:379-90.

[24] Bai MH, Liu TY, Luan F, Li Y, Liu XX. Electrodeposition of vanadium oxide–polyaniline composite nanowire electrodes for high energy density supercapacitors. Journal of Materials Chemistry A. 2014;2(28):10882-8.

[25] Pal B, Yang S, Ramesh S, Thangadurai V, Jose R. Electrolyte selection for supercapacitive devices: a critical review. Nanoscale Advances. 2019;1(10):3807-35.

[26] Gilliam RJ, Graydon JW, Kirk DW, Thorpe SJ. A review of specific conductivities of potassium hydroxide solutions for various concentrations and temperatures. International Journal of Hydrogen Energy. 2007;32(3):359-64.

[27] Krishnan P, Biju V. Effect of electrolyte concentration on the electrochemical performance of RGO–KOH supercapacitor. Bulletin of Materials Science. 2021;44(4):288.

[28] Thakur YS, Acharya AD, Sharma S, Manhas SS. Synthesis and characterization of PANI doped V_2O_5 nanocomposites for supercapacitor application. Materials Today: Proceedings. 2023.

[29] Debnath S, Deb K, Saha B, Das R. X-ray diffraction analysis for the determination of elastic properties of zinc-doped manganese spinel ferrite nanocrystals ($Mn_{0.75}Zn_{0.25}Fe_2O_4$), along with the determination of ionic radii, bond lengths, and hopping lengths. Journal of Physics and Chemistry of Solids. 2019;134:105-14.

[30] Paswan SK, Kumari S, Kar M, Singh A, Pathak H, Borah JP, Kumar L. Optimization of structure-property relationships in nickel ferrite nanoparticles annealed at different temperature. Journal of Physics and Chemistry of Solids. 2021;151:109928.

[31] Gemeay AH, Mansour IA, El-Sharkawy RG, Zaki AB. Preparation and characterization of polyaniline/manganese dioxide composites via oxidative polymerization: Effect of acids. European polymer journal. 2005;41(11):2575-83.

[32] Pal R, Goyal SL, Rawal I. Selective methanol sensors based on polyaniline/V_2O_5 nanocomposites. Iranian Polymer Journal. 2022;31(4):519-32.

[33] Tanvidkar P, Nayak B, Kuncharam BV. Study of dual Filler Mixed Matrix Membranes with acid-functionalized MWCNTs and Metal-Organic Framework (UiO-66-NH_2) in Cellulose Acetate for CO_2 Separation. Journal of Polymers and the Environment. 2023;31(8):3404-17.

[34] Yusoff N. Graphene–polymer modified electrochemical sensors. InGraphene-based electrochemical sensors for biomolecules 2019(pp. 155-186). Elsevier.

[35] Saadattalab V, Shakeri A, Gholami H. Effect of CNTs and nano ZnO on physical and mechanical properties of polyaniline composites applicable in energy devices. Progress in Natural Science: Materials International. 2016;26(6):517-22.

[36] Liu D, Wang X, Deng J, Zhou C, Guo J, Liu P. Crosslinked carbon nanotubes/polyaniline composites as a pseudocapacitive material with high cycling stability. Nanomaterials. 2015;5(2):1034-47.

[37] Sharma S, Acharya AD, Thakur YS, Bhawna. Controlled synthesis of hierarchical BiOCl nanostructure with exposed {010} facets to yield enhanced photocatalytic performance for PMMA deterioration. Journal of Polymer Research. 2022;29(11):466.

[38] Suresh R, Giribabu K, Manigandan R, Kumar SP, Munusamy S, Muthamizh S, Stephen A, Narayanan V. New electrochemical sensor based on Ni-doped V_2O_5 nanoplates modified glassy carbon electrode for selective determination of dopamine at nanomolar level. Sensors and Actuators B: Chemical. 2014;202:440-7.

[39] Jain VM, Shah DV, Patel KK, Shah MS. Surfactant free synthesis and study of vanadium pentoxide nanostructure. Journal of Nano-and Electronic Physics.. 2020;12:02017.

[40] Webster S, Czerw R, Nesper R, DiMaio J, Xu JF, Ballato J, Carroll DL. Optical properties of vanadium oxide nanotubes. Journal of Nanoscience and Nanotechnology. 2004;4(3):260-4.

[41] Xiong C, Aliev AE, Gnade B, Balkus Jr KJ. Fabrication of silver vanadium oxide and V_2O_5 nanowires for electrochromics. ACS nano. 2008;2(2):293-301.

[42] Botewad SN, Pahurkar VG, Muley GG, Gaikwad DK, Bodkhe GA, Shirsat MD, Pawar PP. PANI-ZnO cladding-modified optical fiber biosensor for urea sensing based on evanescent wave absorption. Frontiers in Materials. 2020;7:184.

[43] Patil PT, Anwane RS, Kondawar SB. Development of electrospun polyaniline/ZnO composite nanofibers for LPG sensing. Procedia Materials Science. 2015;10:195-204.\

[44] Shan FK, Liu GX, Lee WJ, Shin BC. Stokes shift, blue shift and red shift of ZnO-based thin films deposited by pulsed-laser deposition. Journal of crystal growth. 2006;291(2):328-33.

[45] Su Q, Huang CK, Wang Y, Fan YC, Lu BA, Lan W, Wang YY, Liu XQ. Formation of vanadium oxides with various morphologies by chemical vapor deposition. Journal of alloys and compounds. 2009;475(1-2):518-23.

[46] Dhananjaya M, Prakash NG, Sandhya GL, Narayana AL, Hussain OM. Microstructure and supercapacitor properties of V_2O_5 thin film prepared by thermal evaporation method. Mech Mater Sci Eng. 2017.

[47] Ding J, Li X, Wang X, Zhang J, Yu D, Qiu B. Fabrication of vertical array CNTs/polyaniline composite membranes by microwave-assisted in situ polymerization. Nanoscale Research Letters. 2015;10:1-9.

[48] Rohom AB, Londhe PU, Mahapatra SK, Kulkarni SK, Chaure NB. Electropolymerization of polyaniline thin films. High Performance Polymers. 2014;26(6):641-6.

[49] Mohammed M, AbdulAmohsin S, Li Z, Zheng L. Enhanced photovoltaic conversion of ZnO/PANI/NiO_x heterostructure devices with ZnO nanorod array. Nano Express. 2020;1(3):030016.

[50] Jyoti J, Arya AK, Chockalingam S, Yadav SK, Subhedar KM, Dhakate SR, Singh BP. Mechanical, electrical and thermal properties of graphene oxide-carbon nanotube/ABS hybrid polymer nanocomposites. Journal of Polymer Research. 2020;27:1-6.

[51] Aamir A, Ahmad A, Shah SK, Ain NU, Mehmood M, Khan Y, Rehman ZU. Electro-codeposition of V_2O_5-polyaniline composite on Ni foam as an electrode for supercapacitor. Journal of Materials Science: Materials in Electronics. 2020;31:21035-45.

[52] Hao T, Liu Y, Liu G, Peng C, Chen B, Feng Y, Ru J, Yang J. Insight into faradaic mechanism of polyaniline@ $NiSe_2$ core-shell nanotubes in high-performance supercapacitors. Energy Storage Materials. 2019;23:225-32.

[53] Jadhav VV, Kore RM, Thorat ND, moon Yun J, Kim KH, Mane RS, O'Dwyer C. Annealing environment effects on the electrochemical behavior of supercapacitors using Ni foam current collectors. Materials Research Express. 2018;5(12):125004.

[54] Parveen N, Ansari SA, Al-Arjan WS, Ansari MO. Manganese dioxide coupled with hollow carbon nanofiber toward high-performance electrochemical supercapacitive electrode materials. Journal of Science: Advanced Materials and Devices. 2021;6(3):472-82.

[55] Iqbal M, Saykar NG, Arya A, Banerjee I, Alegaonkar PS, Mahapatra SK. High-performance supercapacitor based on MoS_2@ TiO_2 composite for wide range temperature application. Journal of Alloys and Compounds. 2021;883:160705.

[56] Rajkumar S, Elanthamilan E, Merlin JP, Sathiyan A. Enhanced electrochemical behaviour of $FeCo_2O_4$/PANI electrode material for supercapacitors. Journal of Alloys and Compounds. 2021;874:159876.

[57] Boukhalfa S, Evanoff K, Yushin G. Atomic layer deposition of vanadium oxide on carbon nanotubes for high-power supercapacitor electrodes. Energy & Environmental Science. 2012;5(5):6872-9.

[58] Ramesh S, Karuppasamy K, Msolli S, Kim HS, Kim HS, Kim JH. A nanocrystalline structured NiO/MnO_2@ nitrogen-doped graphene oxide hybrid nanocomposite for high performance supercapacitors. New Journal of Chemistry. 2017;41(24):15517-27.

[59] Nithya VD, Hanitha B, Surendran S, Kalpana D, Selvan RK. Effect of pH on the sonochemical synthesis of BiPO4 nanostructures and its electrochemical properties for pseudocapacitors. Ultrasonics sonochemistry. 2015;22:300-10.

[60] Jadhav SA, Dhas SD, Patil KT, Moholkar AV, Patil PS. Polyaniline (PANI)-manganese dioxide (MnO_2) nanocomposites as efficient electrode materials for supercapacitors. Chemical Physics Letters. 2021;778:138764.

[61] Lei Z, Chen Z, Zhao XS. Growth of polyaniline on hollow carbon spheres for enhancing electrocapacitance. The Journal of Physical Chemistry C. 2010;114(46):19867-74.

[62] Prasankumar T, Wiston BR, Gautam CR, Ilangovan R, Jose SP. Synthesis and enhanced electrochemical performance of PANI/Fe_3O_4 nanocomposite as supercapacitor electrode. Journal of Alloys and Compounds. 2018;757:466-75.

[63] Xie K, Li J, Lai Y, Liu Y, Zhang G, Huang H. Polyaniline nanowire array encapsulated in titania nanotubes as a superior electrode for supercapacitors. Nanoscale. 2011;3(5):2202-7.

[64] Yasoda KY, Kumar S, Kumar MS, Ghosh K, Batabyal SK. Fabrication of MnS/GO/PANI nanocomposites on a highly conducting graphite electrode for supercapacitor application. Materials Today Chemistry. 2021;19:100394.

[65] Xu J, Wang K, Zu SZ, Han BH, Wei Z. Hierarchical nanocomposites of polyaniline nanowire arrays on graphene oxide sheets with synergistic effect for energy storage. ACS nano. 2010;4(9):5019-26.

[66] Ning J, Xia M, Wang D, Feng X, Zhou H, Zhang J, Hao Y. Superior pseudocapacitive storage of a novel Ni_3Si_2/NiOOH/graphene nanostructure for an all-solid-state supercapacitor. Nano-Micro Letters. 2021;13:1-4.

[67] Wang S, Shao Y, Liu W, Wu Y, Hao X. Elastic sandwich-type GaN/MnO_2/MnON composites for flexible supercapacitors with high energy density. Journal of Materials Chemistry A. 2018;6(27):13215-24.

[68] Bi W, Huang J, Wang M, Jahrman EP, Seidler GT, Wang J, Wu Y, Gao G, Wu G, Cao G. V_2O_5–Conductive polymer nanocables with built-in local electric field derived from interfacial oxygen vacancies for high energy density supercapacitors. Journal of materials chemistry A. 2019;7(30):17966-73.

[69] Bi W, Wang J, Jahrman EP, Seidler GT, Gao G, Wu G, Cao G. Interface engineering V_2O_5 nanofibers for high-energy and durable supercapacitors. Small. 2019;15(31):1901747.

[70] Bi W, Jahrman E, Seidler G, Wang J, Gao G, Wu G, Atif M, AlSalhi M, Cao G. Tailoring energy and power density through controlling the concentration of oxygen vacancies in V_2O_5/PEDOT nanocable-based supercapacitors. ACS applied materials & interfaces. 2019;11(18):16647-55.

[71] Bi W, Deng S, Tang H, Liu Y, Shen J, Gao G, Wu G, Atif M, AlSalhi MS, Cao G. Coherent V^{4+}-rich V_2O_5/carbon aerogel nanocomposites for high performance supercapacitors. Science China Materials. 2022;65(7):1797-804.

[72] Wang Y, Zhang X, Li X, Liu Y, Wang X, Liu X, Xu J, Li Y, Liu Y, Wei H, Jiang P. Spontaneously grown $Ni(OH)_2$ on iron oxide nanoparticles with enhanced energy storage performance for electrodes of asymmetric supercapacitors. RSC advances. 2017;7(79):50358-66.

Chapter 5

Enhancing the optical and UV-shielding characteristics of polyaniline by incorporating V_2O_5 nanoparticles into polyaniline

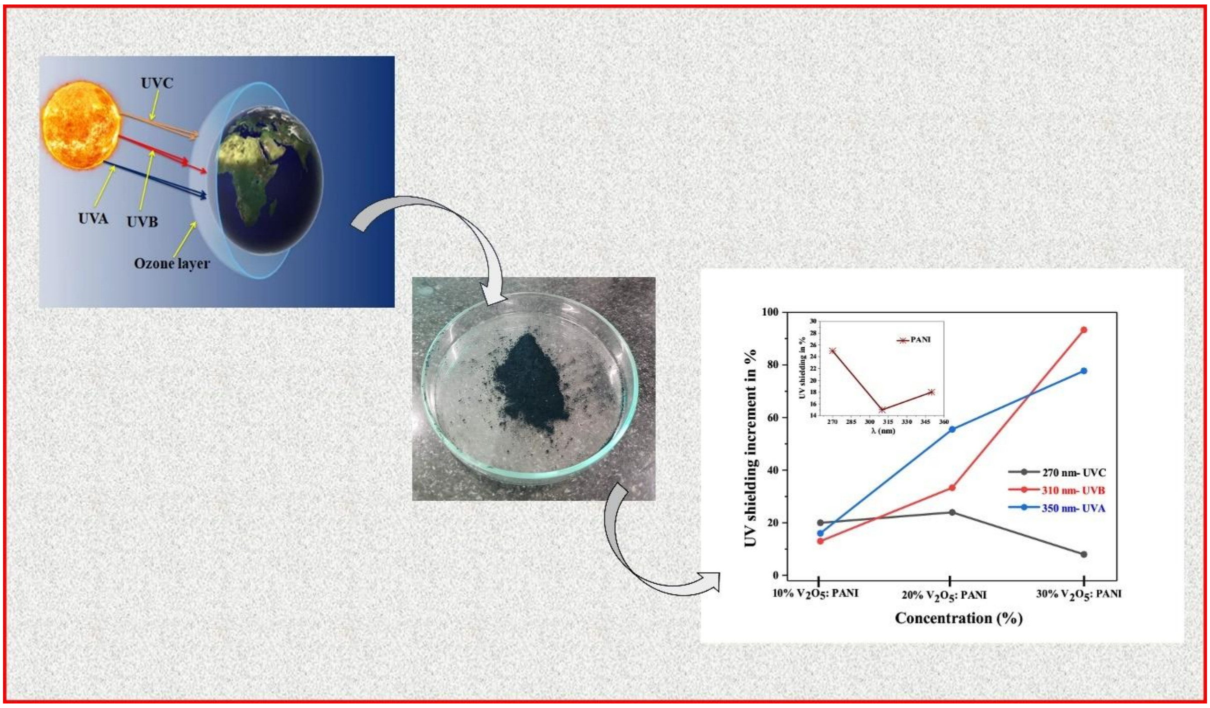

The goal of this research is to meet the scientific community's demand for UV protective materials, especially UV shielding coatings that are both transparent to visible light and effective in blocking UV radiation. To do this, we created conducting polymer nanocomposites of V_2O_5*:PANI by polymerizing* V_2O_5 *with PANI and utilizing ammonium persulfate as an oxidizing agent. This work examines the UV-shielding effectiveness and transmittance of these nanocomposites, in which* V_2O_5 *acts as a UV absorber. UV-visible spectroscopy demonstrated considerable changes in optical properties as a result of doping, increasing the UV shielding efficacy of the nanocomposites. Specifically, a 30% weight concentration of* V_2O_5 *in the PANI matrix resulted in a 93% improvement in UV shielding efficacy in the UVB region compared to pure PANI. The observed red shift, decreased band gap, enhanced polarizability, and modified refractive index and dissipation factor provide important insights into the design and advancement of new UV shielding materials.*

5.1. Introduction

Fabrication of a variety of polymer nanocomposites by incorporating various nanofillers to upgrade and diversify the properties of polymer materials has emerged as an area of growing research [1]. Composite materials based on inorganic filler and conductive polymers have drawn the keen attention of researchers to develop novel functional materials to meet the demands of contemporary engineering functions. It is important to note that polymerization as well as reaction conditions have a huge impact on the morphology, composition and physical attributes of conducting polymer nanocomposites. The attributes of polymer materials were reported to be improved and diversified by the addition of nanofillers as well as by reaction mechanism, particularly their superior optical features, UV shielding, and electrical conductivity [2–4]. Out of these numerous physicochemical properties of polymer nanocomposites, the shielding against UV light allows very special applications. Hazardous effect of UV radiation affects a variety of materials and living organisms. UV region covers the wavelength range of 100-400 nm and is divided into three bands; UVA (320 to 400 nm), UVB (290 to 320 nm), and UVC (100 to 290 nm), respectively. It is a well-acknowledged truth that the ozone layer blocks UVC completely along with a less portion of UVB. However, UVA and most of the parts of UVB rays get transmitted, resulting in photo-aging of the skin as well as the breakdown of several organic compounds, including polymers, bleaches, and tinctures [5]. Hence, there is a need to develop UV shielding material capable of blocking harmful UV rays present in the light spectrum. Polymer nanocomposites can be effective in managing the negative effects of UV light exposure because they have a high refractive index, helps to scatter UV light and exhibits good transparency in the visible region resulting in minimal impact on visible light transmission. These properties of polymer nanocomposites make them a promising candidate for UV shielding applications. Polymers are chosen as the base material due to their short price, ease of processing, visible transparency, lightweight, flexibility as well as potential to shield UV rays with good stability making them a versatile and practical choice for UV shielding applications.

In the past few decades implanting of inorganic UV absorbers namely TiO_2, ZnO, CuO, CdS, SiO_2, and CeO_2 in the polymer matrix has attracted the attention of the investigators due to the origin of unique properties and enhancement in the optical properties of the nanocomposites [6]. Zhang et al. reported ZnO/PMMA nanocomposite films and their result reveals that prepared ZnO/PMMA film can completely absorb UV radiation with good transparency in the visible region [7]. Wang et al. also prepared TiO_2/polyacrylate nanocomposite film with outstanding UV-shielding characteristics [8]. Doddapaneni et al.

reported CuO/PMMA nanocomposites and their findings demonstrate that the nanocomposites with CuO nanoparticles absorb UV rays more effectively than pure PMMA [9]. However, despite the ability to block UV rays, nanofillers lead to the generation of free radicals, which can further degrade the polymer matrix. These factors can lead to a reduction in the lifetime and applicability of the composite material. Hence there is a need to develop UV absorbers that alleviate limitation scarcity by stimulating the optical properties of the composite.

Conducting polymers are preferred over non-conducting polymers for UV shielding because they can absorb and disperse UV radiation as electrical energy, making them more effective in blocking UV light than non-conducting polymers. Furthermore, conducting polymers may be directly doped to change their electrical conductivity and optical characteristics, allowing them to be customized for specific UV shielding applications [10]. In this context, polyaniline (PANI) polymer is recommended as the basis matrix for nanofiller dispersion due to its unique qualities such as high refractive index and protective ability. PANI, a conductive polymer, is also noted for its durability and resistance to degradation due to strong chemical bonding in the repeating units of aniline. Additionally, PANI is a conjugated polymer that can absorb UV rays due to its electron-rich structure. PANI may also have a high extinction coefficient, making it an excellent choice for UV shielding applications [11]. These properties make PANI an attractive material for use in UV-blocking coatings, solar cells, rechargeable batteries, and sensors [12,13]. Whereas the existence of aromatic assembly in the PANI chain has low photostability which serves as a limitation in optical applications. Therefore, there is a need to enhance the photostability of PANI relating to UV absorption potential along with visible transparency.

V_2O_5 are a class of crystalline materials that have received broad consideration due to their high specific surface area, wide optical band gap, good electrical conductivity, excellent chemical and optical conductivity, etc. These special qualities of V_2O_5 ensure their applicability in technological applications such as solar cell optical windows, solar cell interfacial layers, gas sensors, catalysts, electrochromic devices, electrode material in supercapacitors and optical power limiting [14–18]. Hou et al. reported that V_2O_5 is a crucial material for photogenerated carriers, kinetic behaviours as well as for improving the ability of a material to absorb UV light [19]. Maruthi et al. studied that the addition of V_2O_5 in the PANI polymer matrix improves the dielectric behavior as well as the electromagnetic shielding ability of polymer nanocomposites and forms an efficient composite network between V_2O_5 and polymer [20]. Putrolaynen et al. reported V_2O_5 thin film and suggested that UV resistance can be improved with the help of some organic compounds [21]. To the best of our knowledge, the reported investigations have less focus on the optical properties as well as UV shielding effect of V_2O_5 as an inorganic filler in PANI matrix.

In this chapter, we studied the physical and optical properties of pure V_2O_5, pure PANI, and PANI doped with different weight percentages (10, 20, and 30 wt.%) of V_2O_5. We also investigated the extent to which V_2O_5 can alter the optical as well as UV shielding abilities of PANI and can be found at a later stage. Here, in this chapter in situ polymerization has been adopted to achieve the above-mentioned properties since it provides a regular dispersion of nanofiller in the polymer matrix.

5.2. Results and discussion

5.2.1. Structural properties

Figure 5.1 shows XRD patterns of V_2O_5, pure PANI, and PANI- with varying concentration of V_2O_5. Figure 5.1(a) shows the XRD pattern of V_2O_5 with diffraction peaks located at 2θ = 15.38°, 20.28°, 21.71°, 26.16°, 31.04°, 32.38°, 33.32°, 34.31°, 36.03°, 41.25°, 45.46°, 47.35°, 48.80°, 51.22°, 55.64° and 61.1° respectively (JCPDS-01-085-0601).

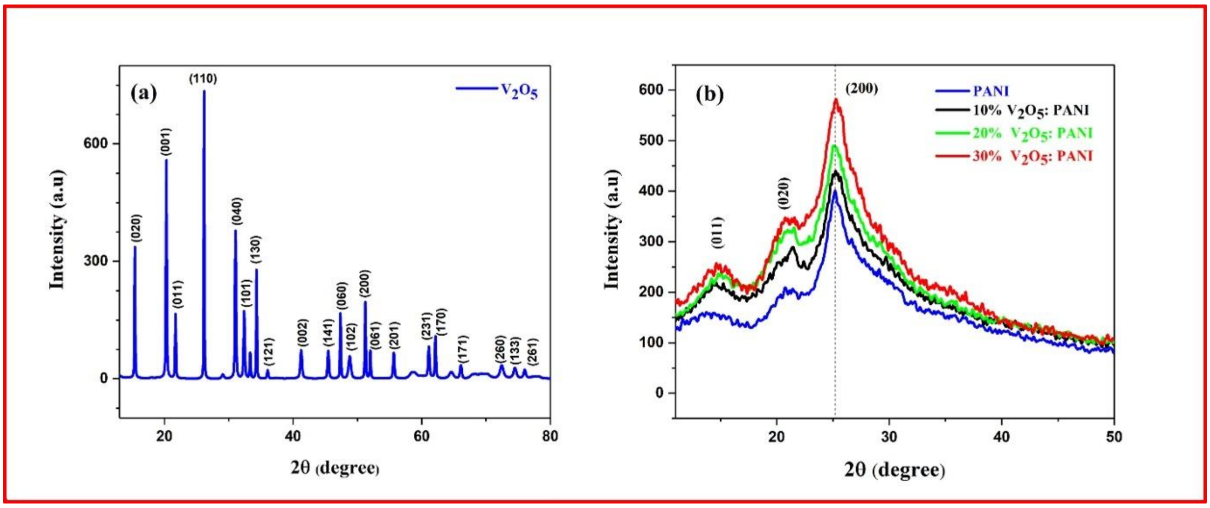

Figure 5.1. XRD patterns of (a) pure V_2O_5 (b) pure PANI and V_2O_5: PANI nanocomposites.

According to Scherrer's formula, the average crystalline size of V_2O_5 for the (0 2 0), (0 0 1), (0 1 1), (1 1 0), (0 4 0), (1 0 1), (1 1 1) and (1 3 0) diffraction peaks came out to be 62.83 nm with orthorhombic crystal structure [22]. The obtained results reflects that the as prepared V_2O_5 has good crystallinity, high purity with predominant orientation along (110) plane. The XRD patterns of pure polyaniline in Figure 5.1(b) show a relatively intense and wide band at 2θ = 25.2° with two distinct shoulders at 16° and 22°. The observed broad peak at 2θ = 25.2°

might be due to the overlapping between the prevailing (110) reflection of V_2O_5 and the peak associated to the pure PANI. Increase in the intensity of this peak with different doping concentration (10, 20, & 30 wt. %) as well as the absence of any impurity peak defines the excellent harmony between V_2O_5 and the polymer matrix. The obtained results reflects that the as prepared V_2O_5 has good crystallinity, high purity with predominant orientation along (110) plane.

5.2.2. Optical properties

5.2.2.1. UV-vis absorption and transmission

The absorption spectra of pure V_2O_5, PANI, and V_2O_5: PANI are shown in Figure 5.2. The pure PANI sample has a low absorbance, which increases as the V_2O_5 concentration in PANI is increased. Peak absorption intensity increased as V_2O_5 nanoparticle concentration increased because V_2O_5 as a doping agent can increase the surface area of PANI. In other words, the roughness of the PANI surface increases as the concentration of V_2O_5 increases, which gives light rays more possibilities to be absorbed. Hence, the strong absorption occurred. Further in the case of V_2O_5: PANI the graphs for all concentration follows the almost saturated trend for higher wavelength or we can say in the visible region due to its polymer-filler complexation. Hence, the prepared samples could be better applicable for UV shielding applications.

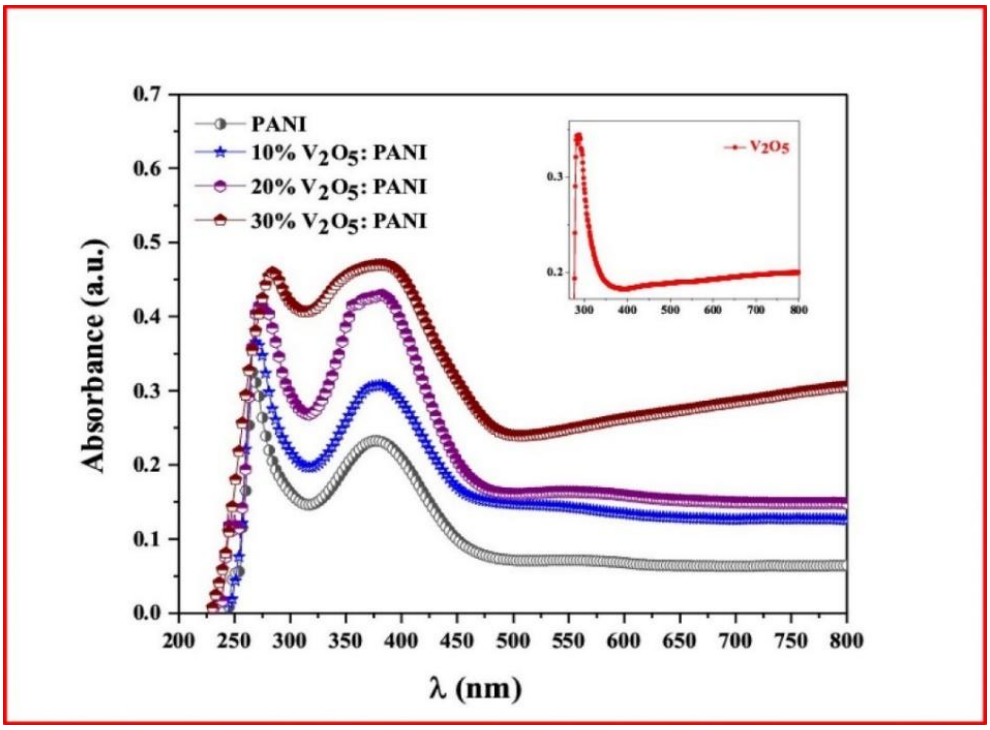

Figure 5.2. Absorption spectra of pure PANI, V_2O_5, and V_2O_5: PANI nanocomposites.

Figure 5.3 shows transmittance spectra of pure V_2O_5, PANI, and V_2O_5: PANI nanocomposites studied in the wavelength range (200-800 nm). Pure PANI shows good transparency more than 90% in the visible region. In contrast, the transmittance of PANI decreases with an increase in vanadium concentrations. It is conspicuous to note that the rough surface of PANI with V_2O_5 has provided high absorption, which results in poor PANI transmittance as V_2O_5 concentration increases.

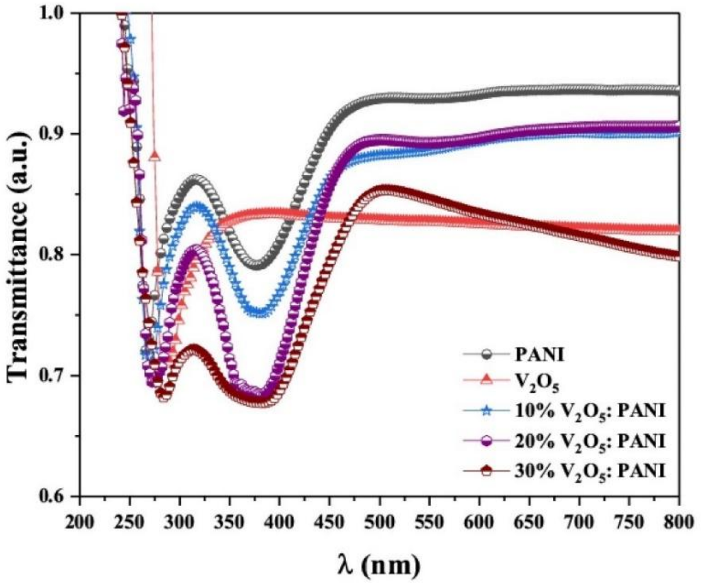

Figure 5.3. Transmittance spectra of pure PANI, V_2O_5, and V_2O_5: PANI nanocomposites.

Optical windows in devices are mainly used to protect optical equipment and electrical sensors from the surroundings. Moreover, a transmission level of at least 80% is required for optical window materials [23]. Therefore, these samples can be utilized as an optical window in optical devices because they show average transmittance in a wide wavelength range, which is above 80% for pure PANI and V_2O_5: PANI nanocomposites.

5.2.2.2. Optical parameters

Tauc's model is used to calculate the absorption edge of the transitions [24]

$$\alpha h\nu = C_1 (h\nu - E_g^{opti})^m \qquad (5.1)$$

where hν is the photon energy, C_1 is constant, E_g^{opti} is the optical energy band gap and α is the absorption coefficient. For allowed direct transition $\left(m = \frac{1}{2}\right)$. Figure 5.4 $(\alpha h\nu)^2$ vs $(h\nu)$ plot could be used to calculate the optical band gap. Polyaniline (PANI) exhibits two distinct optical band gaps: E_g $(B)^{opti}$, attributed to the π–π^* transitions of the benzenoid units, and E_g $(Q)^{opti}$, associated with the polaron/bipolaron transitions within the quinoid structures (Q-band) [25]. The incorporation of V_2O_5 leads to a reduction in both energy band gaps, due to an increase in localized states and structural defects within the band gap, indicating successful blending and strong interaction between V_2O_5 and the polymer matrix.

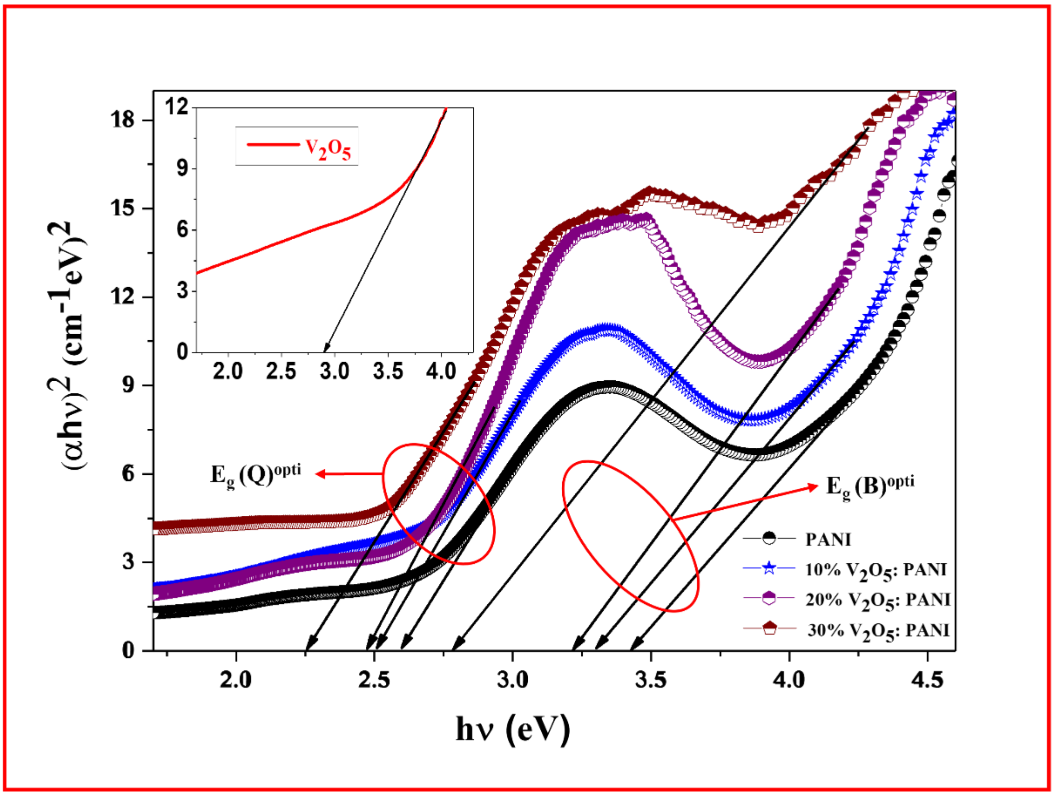

Figure 5.4. Plot of $(\alpha h\upsilon)^2$ vs $(h\upsilon)$ for PANI, V_2O_5 and V_2O_5: PANI nanocomposites.

The extinction coefficient k is calculated from the absorption coefficient using relation [26].

$$k = \frac{\alpha\lambda}{4\pi} \tag{5.2}$$

The absorption coefficient (α) indicates how far photons can travel through the material before being absorbed. The following relation has been used to determine the absorption coefficient (α) [27].

$$\alpha = \frac{2.303A}{t} \tag{5.3}$$

Since our sample is in solution form, the thickness '*t*' should be taken as the length of the cuvette, which is 1 cm. Therefore, the relationship between optical absorbance 'A' and thickness '*t*' can be simplified with 't' set to 1 cm. The dependency of '*k*' on the wavelength (λ) is shown in Figure 5.5. It clearly shows that the extinction coefficient decreases with increasing wavelength due to the light scattering mechanism and the values of '*k*' increase as the concentration of V_2O_5 increases. The initial decrease in the extinction coefficient within the UV range (280-310 nm) is primarily due to the higher photon energy. This energy is adequate to excite electrons from the valence band into the conduction band, effectively surpassing the optical band gap. On the other hand, the increase in extinction coefficient in the range of 310-400 nm with the concentration of V_2O_5 in the V_2O_5: PANI samples is attributed to the surface plasmon absorption phenomenon. In these polymer nanocomposites, this absorption leads to photon energy scattering or reflection, thereby hindering electron excitation in this spectral region [26].

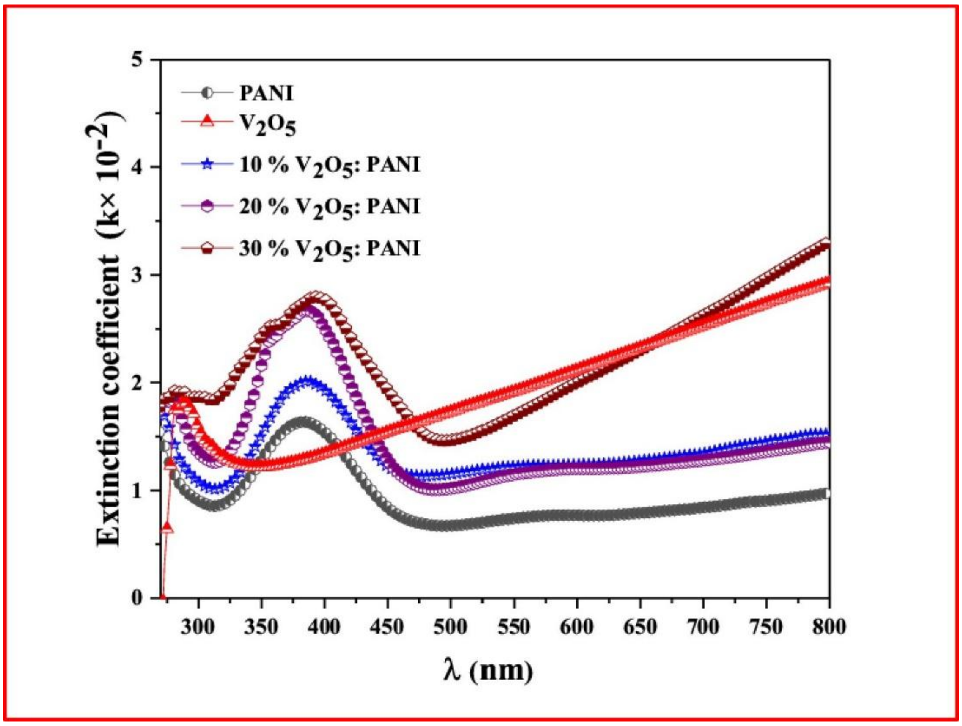

Figure 5.5. Extinction coefficient of V_2O_5, PANI, V_2O_5: PANI nanocomposites.

The refractive index (n) can be determined through the utilization of reflectance (R) and extinction coefficient (k) [28].

$$n = \left[\frac{4R}{(1-R)^2} - k^2\right]^{\frac{1}{2}} + \frac{(1+R)}{(1-R)} \tag{5.4}$$

The variations of refractive index with wavelength are shown in Figure 5.6 for the prepared sample. As the concentration of V_2O_5 increased, it has been observed that the values of the refractive index also increased. Hence, these materials with a high index of refraction can be used in waveguide technology, anti-reflection coatings, and manufacturing solar cells [29,30]. The imaginary (ε_i) and real (ε_r) components of the dielectric constant were estimated via the $\varepsilon_i = 2nk$ and $\varepsilon_r = n^2 - k^2$ relations. Figure 5.7 and Figure 5.8 depict the variation of ε_i and ε_r with wavelength for all samples [31]. Despite belonging to the same modality curves, the observed values of the real parts are much greater than those of the imaginary parts. The values of ε_i reflect how the dipole motion of the polymer matrix absorbs energy from the input electric field, and ε_r is associated with a formula that describes how much the speed of light will slow down in the material [32,33].

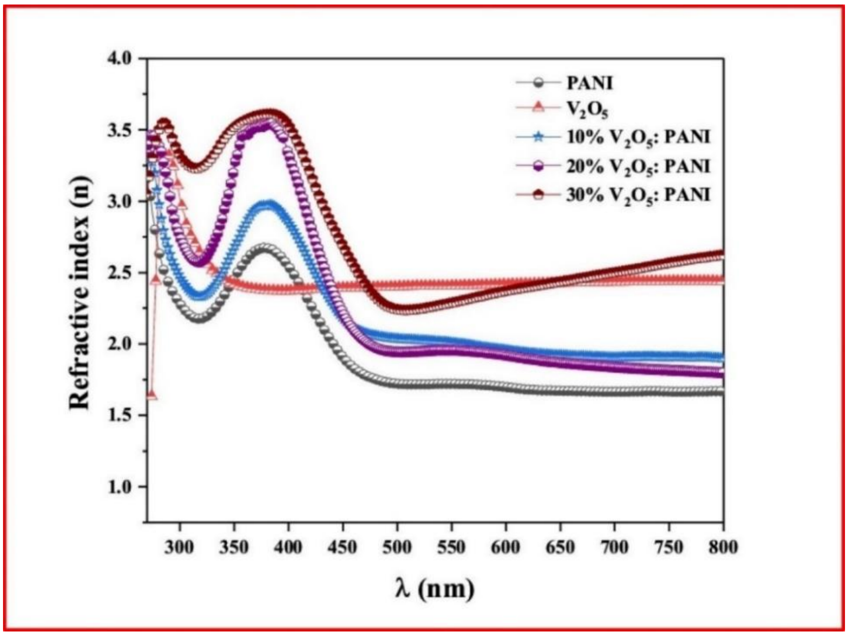

Figure 5.6. Variation of refractive index with wavelength of PANI, V_2O_5, and V_2O_5: PANI nanocomposites.

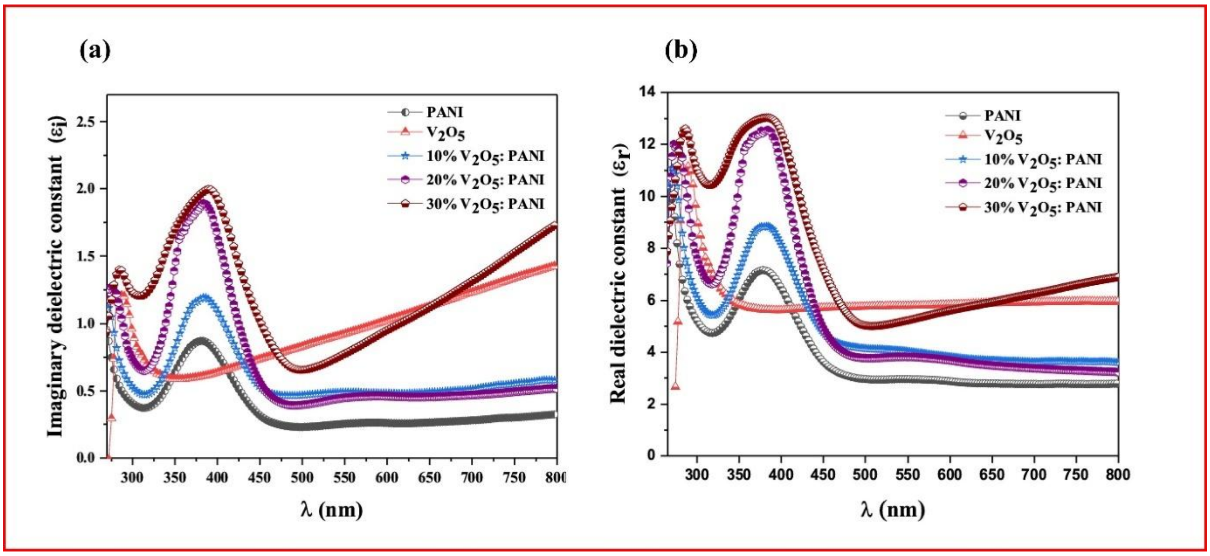

Figure 5.7. Plot of (a) imaginary part of the dielectric constant (b) real part of the dielectric constant for PANI, V_2O_5, and V_2O_5: PANI nanocomposites.

The relation (5.5) can be used to calculate the dissipation factor (tanδ), which is a measurement of mechanical power loss by the oscillator [34].

$$tan\delta = \frac{\varepsilon_i}{\varepsilon_r} \tag{5.5}$$

Figure 5.8 shows the dependence of dissipation factor vs λ for pure PANI, V_2O_5, and V_2O_5: PANI nanocomposites. It is clear that the dissipation factor increases as the concentration of V_2O_5 increases, indicating a direct relationship between V_2O_5 concentration and the material's propensity to dissipate energy. Wemple and DiDomenico's single oscillator model can be utilized to calculate the single-oscillator energy (E_o) and dispersion energy (E_d) [35–37].

$$n^2 - 1 = \frac{E_o E_d}{E_o^2 - (h\nu)^2} \tag{5.6}$$

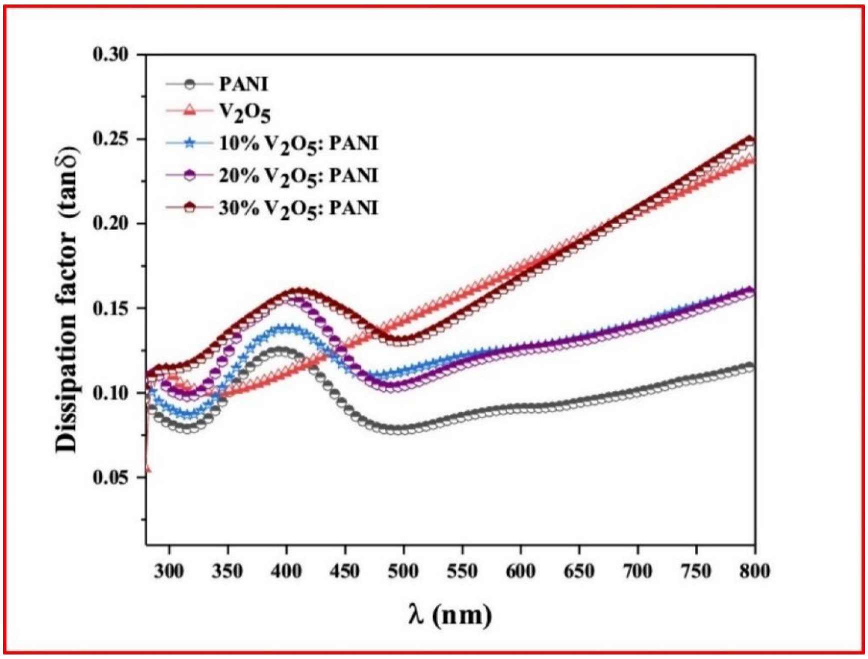

Figure 5.8. Variation of tan δ vs λ for PANI, V_2O_5, and V_2O_5: PANI nanocomposites.

In equation (5.6), E_0 is associated with the minimum direct band gap and corresponds to the energy difference between the center of gravity of the valence band and the conduction band. On the other hand, E_d is proportional to the average strength of interband optical transitions and remains constant within the band gap. The graph of $(n^2-1)^{-1}$ versus $(h\nu)^2$ presented in Figure 5.9 can be utilized to determine the values of E_d and E_0, as detailed in Table 5.1. The amount of V_2O_5 as a doping agent in the produced samples enhances the localized states in the energy gap, promoting low energy transitions and lowering the E_o value. There is a change in the material's structural order, which causes E_d values to increase as V_2O_5 concentration increases. Another important parameter is oscillator strength (f), which is calculated by using equation (5.7) [38,39].

$$f = E_o E_d \tag{5.7}$$

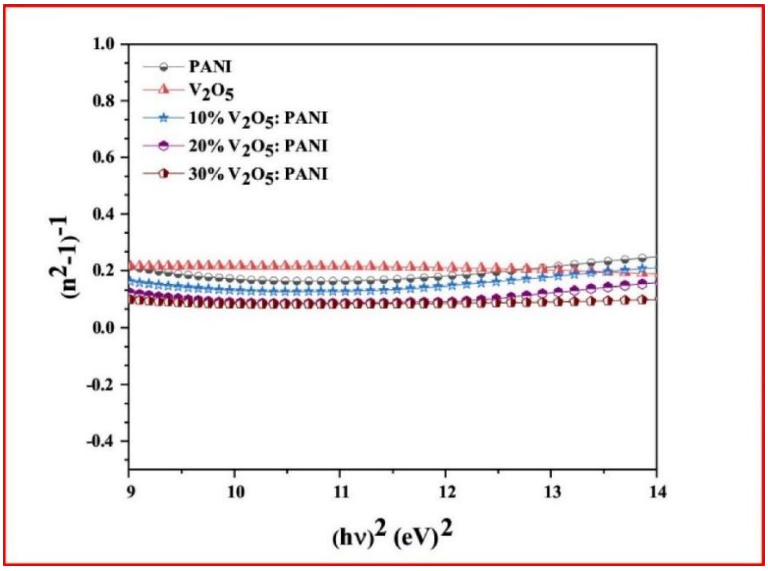

Figure 5.9. Variation of $(n^2-1)^{-1}$vs $(h\nu)^2$ for PANI, V_2O_5, and V_2O_5: PANI nanocomposites.

Table 5.1. Optical parameters of pure V_2O_5, PANI, and V_2O_5: PANI nanocomposites.

Samples	E_g (B)^{opti} (eV)	E_g(Q)^{opti} (eV)	E_d (eV)	E_o (eV)	ε_1	$(e^2/\pi c^2)$ (N/m*) (10^{-7}) (nm^{-2})
PANI	3.40	2.59	7.80	5.32	3.21	9.08
V_2O_5	-----	-----	47.35	10.55	5.62	56.2
10% V_2O_5: PANI	3.30	2.50	11.95	4.96	4.53	18.6
20% V_2O_5: PANI	3.21	2.47	17.96	4.69	4.61	22.58
30% V_2O_5: PANI	2.78	2.25	18.97	4.48	4.67	22.66

Table 5.2. Other important optical parameters of pure V_2O_5, PANI, and V_2O_5: PANI nanocomposites.

Samples	f (eV)^2	$S_1\times10^{12}$ (m^{-2})	λ_1 (nm)	n_1
PANI	41.49	24	315.86	1.56
V_2O_5	499.5	70	355.0	2.34
10% V_2O_5: PANI	59.27	30	291.40	1.84
20% V_2O_5: PANI	84.23	41	280.7	1.95
30% V_2O_5: PANI	84.98	59	271.06	2.28

The values of average oscillator strength (S_1) and average oscillator wavelength (λ_{1}) can be calculated for V_2O_5: PANI nanocomposites by using (5.8), (5.9) and (5.10) equations [40,41].

$$\frac{n_1^2 - 1}{n^2 - 1} = 1 - \left(\frac{\lambda_1}{\lambda}\right)^2 \tag{5.8}$$

Equation (5.8) can be written in the following form:

$$n^2 - 1 = \frac{S_1 \lambda_1^2}{1 - \left(\frac{\lambda_1}{\lambda}\right)^2} \tag{5.9}$$

The average oscillator strength (S_1) can be calculated as

$$S_1 = \frac{(n_1 - 1)}{\lambda_1^2} \tag{5.10}$$

Where n_1 denotes the refractive index at zero photon energy and can be calculated using equation (5.11).

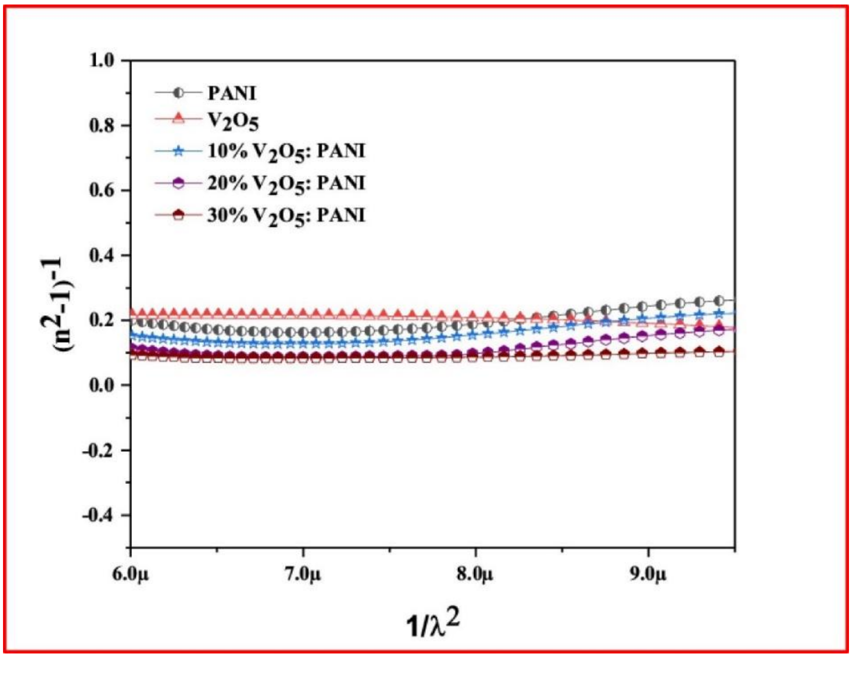

Figure 5.10. Variation of $(n^2-1)^{-1}$vs $(\lambda)^{-2}$ for PANI, V_2O_5, and V_2O_5: PANI nanocomposites.

$$n_1 = \left(1 + \frac{E_d}{E_0}\right)^{\frac{1}{2}} \tag{5.11}$$

The values of λ_1 and S_1 were obtained from the slope and intercepts of $((n^2 - 1)^{-1}$vs $(\lambda)^{-2})$ (see Figure 5.10). Table 5.2 demonstrates that the oscillator parameters increased with the concentration of V_2O_5 in PANI. Table 5.2 also includes the computed values of oscillator strength and refractive index at zero photon energy for pure PANI, V_2O_5, and V_2O_5 nanocomposites. Additionally, nonlinear parameters such as the nonlinear refractive index, first-order susceptibility, and third-order susceptibility were computed using equations (5.12), (5.13), and (5.14) [41].

$$\chi^{(1)}(esu) = \frac{E_d}{4\pi E_0} \tag{5.12}$$

$$\chi^{(3)}(esu) = 6.82\times10^{-15}\left(\frac{E_d}{E_0}\right)^4 \tag{5.13}$$

$$n^{(2)}(esu) = 12\pi\frac{\chi^{(3)}}{n_1} \tag{5.14}$$

where the nonlinear refractive index, first and third orders of susceptibilities are $n^{(2)}$, $\chi^{(1)}$ and $\chi^{(3)}$ respectively. It has been found that as the V_2O_5 concentration in the PANI matrix increases, the values of $n^{(2)}$, $\chi^{(3)}$, and $\chi^{(1)}$ also increase (see Table 5.3). For each concentration, the values of $n^{(2)}$ and $\chi^{(3)}$ are higher than for pure PANI. As a result, the as-synthesized samples have improved nonlinear parameters that could be used in nonlinear optical applications.

The dielectric constant of lattice (ε_1) and the carrier concentration in terms of electron effective mass $(e^2/\pi c^2)$ (N/m^*) were calculated from the intercepts and slope of $((n^2)$ vs $(\lambda)^2)$ respectively (see Figure 5.11) [42].

$$n^2 = \varepsilon_1 - \left(\frac{e^2}{\pi c^2}\right)\left(\frac{N}{m^*}\right)\lambda^2 \tag{5.15}$$

The values of $(e^2/\pi c^2)$ (N/m^*) increase as the concentration of V_2O_5 increases (see Table 5.1).

This indicates that adding V_2O_5 as a doping agent enhances the concentration of charge carriers inside the PANI matrix. The energy loss of the materials is represented by the energy absorption produced by individual electron transitions or the cumulative effects created inside the solid. The surface energy (SELF) and volume energy (VELF) loss functions are used to represent this energy loss. The probability that fast electrons will lose energy while moving through the bulk or surface of the material is represented by these two functions (VELF and SELF), respectively.

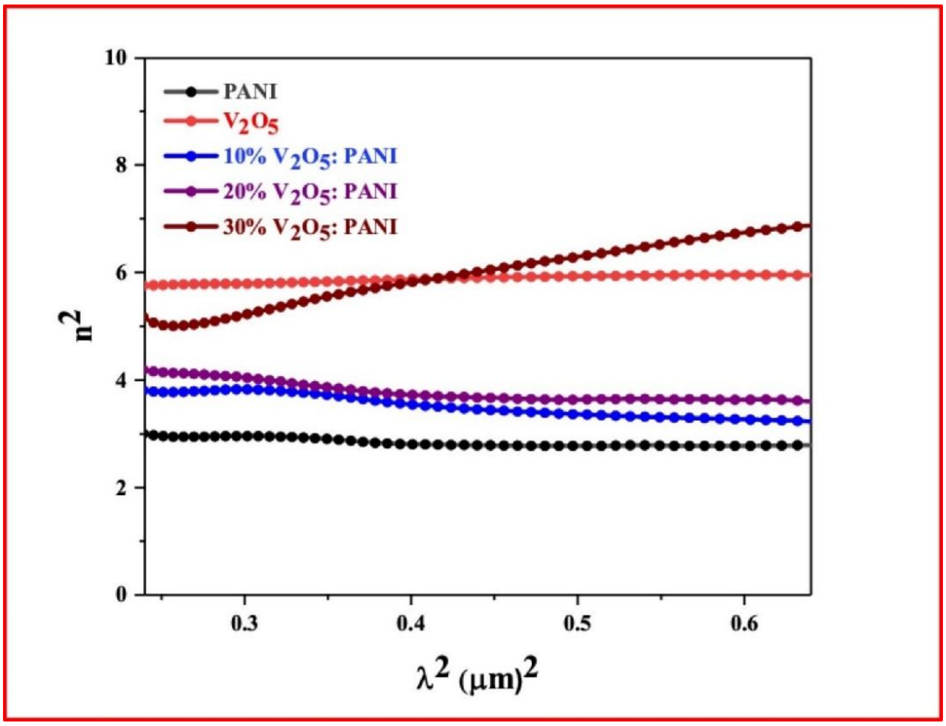

Figure 5.11. Variation of $(n)^2$vs $(\lambda)^2$ for PANI, V_2O_5, and V_2O_5: PANI nanocomposites.

Table 5.3. Non- linear optical parameters of pure V_2O_5, PANI and V_2O_5: PANI nanocomposites.

Samples	$\chi^{(1)}$ (esu)	$\chi^{(3)}$ (esu)	$n^{(2)}$ (esu)
PANI	0.10	0.03×10^{-12}	0.72×10^{-12}
V_2O_5	0.35	2.74×10^{-12}	4.4×10^{-11}
10% V_2O_5: PANI	0.2	0.22×10^{-12}	4.5×10^{-12}
20% V_2O_5: PANI	0.30	1.45×10^{-12}	2.8×10^{-11}
30% V_2O_5: PANI	0.33	2.18×10^{-12}	3.6×10^{-11}

According to the following equations, surface energy and volume energy are both linked to the real (ε_r) and imaginary components (ε_i) of the complex dielectric constant [43].

$$VELF = \frac{\varepsilon_i^2}{\left(\varepsilon_i^2 + \varepsilon_r^2\right)} \tag{5.16}$$

$$SELF = \frac{\varepsilon_i^2}{\varepsilon_i^2 + \left(\varepsilon_r + 1\right)^2} \tag{5.17}$$

Figure 5.12(a-b) illustrates how the volume and surface energy loss functions for V_2O_5: PANI nanoparticles depend on photon energy. It is clear from the Figures that both functions increase with the increase in V_2O_5 concentrations.

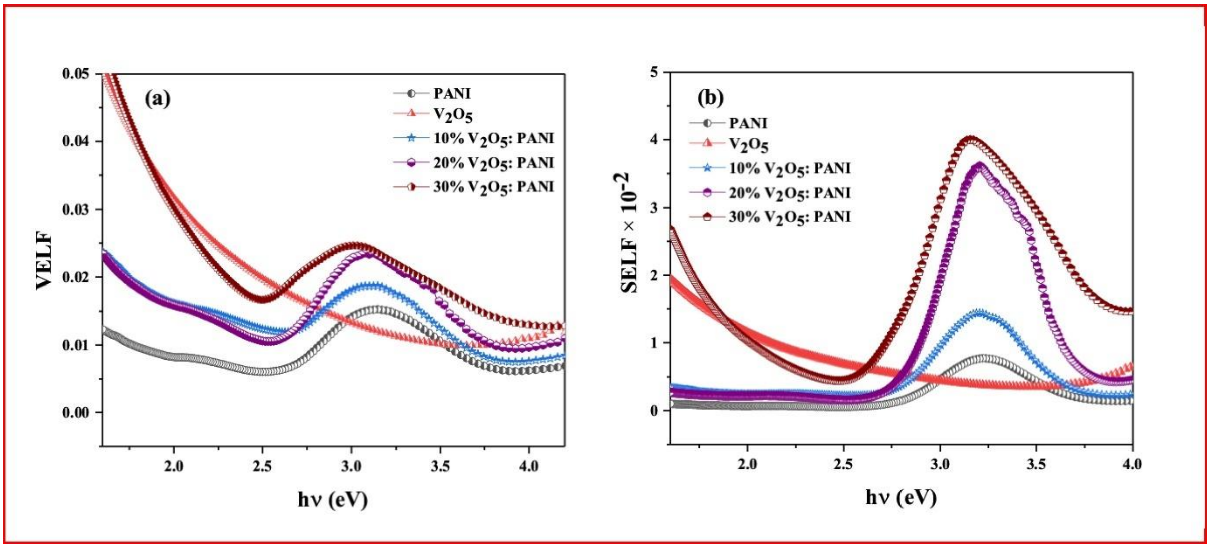

Figure 5.12. (a) Volume energy (b) surface energy loss function for PANI, V_2O_5, and V_2O_5: PANI nanocomposites.

Optical conductivity can be calculated and used to investigate the electronic states of materials [44].

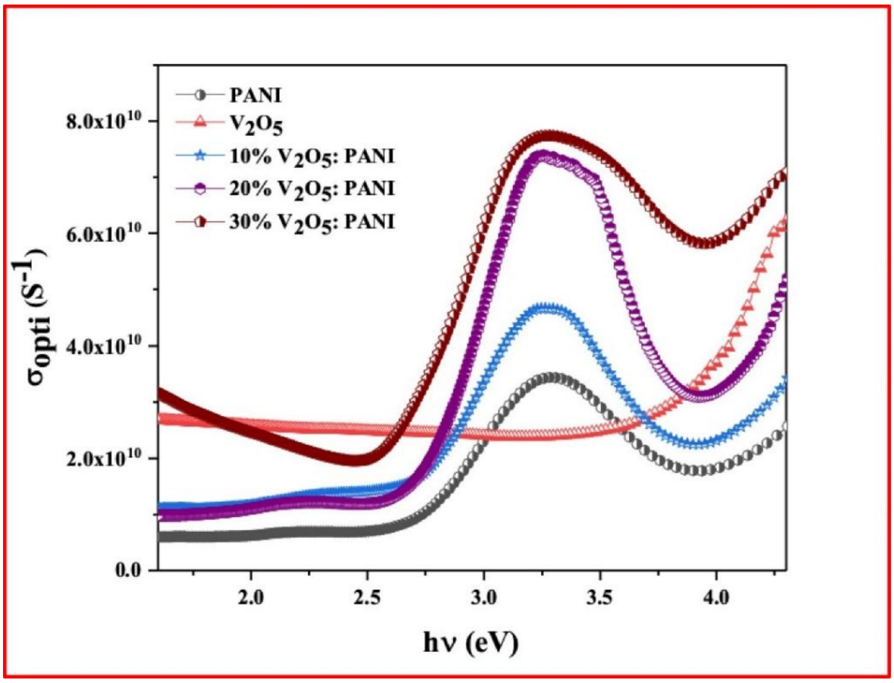

Figure 5.13. Optical conductivity of PANI, V_2O_5, and V_2O_5: PANI nanocomposites.

The following formula can be used to calculate the optical conductivity (σ_{opti}) of PANI, V_2O_5, and V_2O_5: PANI nanocomposites [45].

$$\sigma_{opti} = \frac{\alpha n c}{4\pi} \tag{5.18}$$

Here c, α, and n are the speed of light in a vacuum, absorption coefficient, and refractive index respectively. According to Figure 5.13, there is a noticeable increase in optical conductivity as photon energy rises. This increase in optical conductivity in nanocomposites correlates with higher concentrations of V_2O_5. This phenomenon occurs because V_2O_5, acting as a dopant, modifies the defects and density of localized states within the PANI matrix [44].

5.2.2.3. Optical study analysis

To investigate the interaction of the vanadium nanoparticle in the polymer matrix as well as access the applicability of prepared nanocomposites, a complete analysis of their optical properties were performed through optical measurements. Collective view of the obtained spectrums indicates that absorption spectrum is not a single absorption but having different absorption peaks due to different coordination between oxygen and V^{5+} ions [46]. Further absorption found to be strong in the UV region along with weakly extended tail in the visible region. Starting from as prepared V_2O_5, which shows major absorption band at peak position ~282 nm and broad absorption band in the range 425 to 549 nm (see Figure 5.2). The observed absorption bands attributes to the electronic transition from the O-2p valance band to the empty V-3d orbitals and d-d charge transitions of V_2O_5 [47]. In case of PANI two major absorption peaks at ~ 266 nm, ~ 361 nm along with one broad peak at ~ 515 nm has been observed. The origin of absorption band in the UV region is the characteristic of the aromatic nuclichain and assigned to π-π* transition in the benzeoid rings. The broad peak observed in the visible region is due to the excitation of an electron from the highest occupied molecular orbital (HOMO) to the lowest unoccupied molecular orbital (LUMO) [48]. Further for the case of prepared V_2O_5: PANI nanocomposites absorption band appears in wavelength range from ~ 250 to 650 nm. Furthermore, the absorption band in case of nanocomposite found to be red shifted with increase in filler concentrations. The observed red shift corresponds to the $\pi - \pi^*$ transition of benzenoid rings into quinoid rings. This means that the interactions between V_2O_5 and PANI results in narrowing of the band gap, which causes hassle fee transition of the electrons [49]. This is in good agreement with obtained decrease in the optical bandgap from 3.4 to 2.7 eV (see Figure 5.4). Added to this absorption found to be increased in the UV region, facilitated by the excitations of the donor level electrons to the conduction band. Collectively all observed findings indicates the doping of V_2O_5 on the quinoid ring of PANI facilitates electron delocalization among the composites and leads to form a conductive V_2O_5: PANI composite. V_2O_5 shows 82% transparency in the visible region whereas PANI shows 92% transparency in the visible region (see Figure 5.3). Pure PANI was transparent more in the visible region (480-800 nm) and shows 92% of transmittance. Most of or more properly we can say that UV part has been absorbed by PANI. However, if we take the case of V_2O_5 the obtained result reveals 82% of transmittance along with nearly 10% part of the UV region. Further, the analysis of nanocomposites with concentration (10, 20, and 30 wt.%) indicates that the percentage of transparency remains nearly comparable to that of PANI with a small increment in absorbance (up to 10%). Additionally, data reveals that with an increase in the vanadium oxide content transparency decreased showing a red shift.

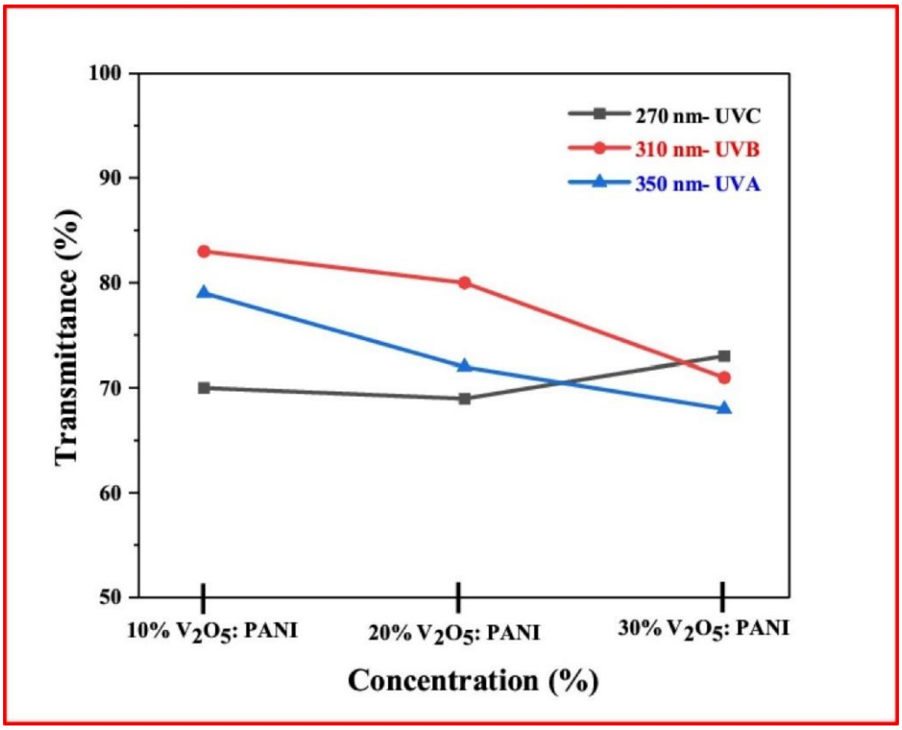

Figure 5.14. Transmittance of V_2O_5: PANI nanocomposites at specific wavelengths (UVA, UVB, and UVC).

To quantify the performance of PANI with the addition of different concentration of V_2O_5 in case of absorbance to have its applicability in UV shielding, we investigated the transmittance data for the different UV regions. In Figure 5.14, transmittance (%) of different (10, 20, and 30 wt.%) V_2O_5: PANI nanocomposites in UVA, UVB and UVC regions represented by blue, red, and black lines, respectively. It has been observed that 10% V_2O_5: PANI nanocomposite shows maximum transmittance of 83% for UVB region, however with increase in V_2O_5 concentration up to 30 wt.% in PANI, transmittance reduced to 71%. Consequently 10% V_2O_5: PANI nanocomposite shows maximum transmittance of 79% for UVA and minimum transmittance of 68% for 30% V_2O_5: PANI nanocomposite. But transmittance showed differing trend for UVC and observed maximum value of 73% transmittance for 30% V_2O_5: PANI and minimum value of 69% transmittance for 20% V_2O_5: PANI. The observed data clearly indicates that the addition of V_2O_5 in proportion influenced the transmittance of UVB and UVA regions which are more harmful to the human being. To have further insight of the UV shielding capability of nanocomposites and the contribution of filler, we investigate the UV shielding effect shown by V_2O_5 nanoparticles in PANI matrix (see Figure 5.15).

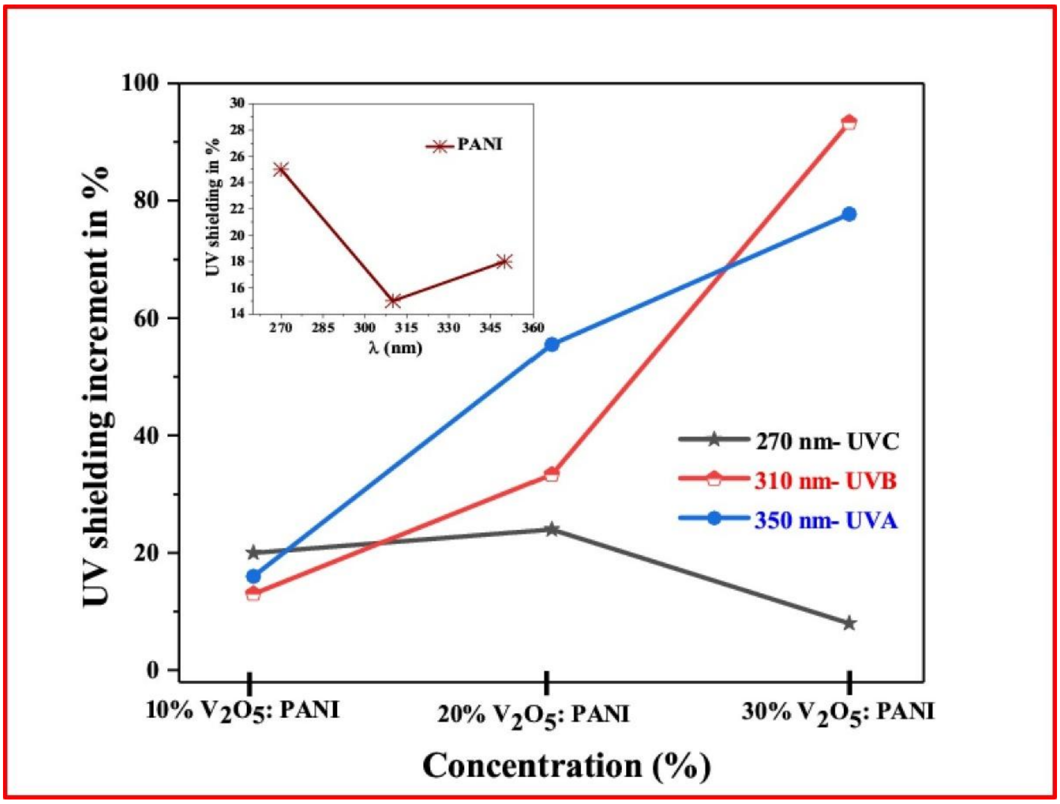

Figure 5.15. UV shielding increment of V_2O_5: PANI nanocomposites at specific wavelengths (UVA, UVB, and UVC).

It reflects that the proposed nanocomposite shows good shielding of UV light at 350 nm (UVA), 310 nm (UVB), and 270 nm (UVC) as compared to pure PANI. Pure PANI shows shielding as follows 25% for UVC, 15% for UVB, and 18% for UVA (see inset of Figure 5.15), whereas the percentage was found to be increased with an increase in doping concentration. For instance, 30 wt.% of V_2O_5 doped PANI shows an increment in UV shielding with respect to PANI of the order of 8% of UVC, 93% of UVB, and 77% of UVA. Therefore, results reveal that incorporation of V_2O_5 can be in favour of shielding of UV light and result in a novel transparent material with excellent UV shielding, especially in the UVB region.

Looking again on to the obtained result it is observed that there is an abrupt increase in the UV shielding response beyond 10 wt.% doping i.e., for 20 and 30 wt.% of V_2O_5. Moreover, the prepared nanocomposites found to be more suitable for shielding UVB part of the UV spectrum up to 93% with respect to PANI (see Figure 5.15). Better polarizability of the V_2O_5 than PANI could be one of the reasons behind such behaviour. Decrease in the band gap with an increase in concentration could be another probable reason, which supports by the increase in dielectric constant as well as carrier concentration. Added to this increased refractive index as well as dissipation factor points toward the roughness of the surface due to an increase in localization state have resulted in increased absorbance. Also, the observed trend of the graph reveals an overlapping situation for higher doping concentration. Therefore, in this study, it is clear that doping of V_2O_5 plays a vital role in the modification of the calculated optical parameters which indicates an improvement in the UV shielding efficiency of the nanocomposites in the area of interest. In other words, we could state that the solid solution of V_2O_5 in PANI should not be completely excluded and its range should be found to be less than 30 wt.% of V_2O_5 doping.

5.3. Conclusions

In situ polymerization technique successfully employed to synthesize V_2O_5:PANI nanocomposites. The prepared nanocomposites showed high purity without the presence of any impurity peaks defining the good harmony between V_2O_5 and PANI investigated through XRD scans. Additionally, the XRD peak intensities of prepared nanocomposites increases with doping concentration of V_2O_5, which signifies excellent dispersion in the prepared nanocomposites. Therefore, the modulation of different optical properties of V_2O_5:PANI nanocomposites were mediated by the excellent dispersion of V_2O_5 in polymer matrix. Furthermore, we also investigated the UV shielding performance and visible light transmission of fabricated nanocomposites. It is observed that 30 wt.% V_2O_5:PANI nanocomposite displayed a 93% enhancement in UV shielding performance with respect to PANI in the UVB range. Conclusively the prepared nanocomposites could deliver important insight for the design and advancement of novel outstanding UV-protecting materials.

References

[1] Dai Y, Tang Q, Zhang Z, Yu C, Li H, Xu L, Zhang S, Zou Z. Enhanced mechanical, thermal, and UV-shielding properties of poly (vinyl alcohol)/metal–organic framework nanocomposites. RSC advances. 2018;8(67):38681-8.

[2] Amrollahi S, Ramezanzadeh B, Yari H, Ramezanzadeh M, Mahdavian M. Synthesis of polyaniline-modified graphene oxide for obtaining a high performance epoxy nanocomposite film with excellent UV blocking/anti-oxidant/anti-corrosion capabilities. Composites Part B: Engineering. 2019;173:106804.

[3] Roy HS, Mollah MY, Islam MM, Susan MA. Poly (vinyl alcohol)–MnO_2 nanocomposite films as UV-shielding materials. Polymer Bulletin. 2018;75(12):5629-43.

[4] Islam S, Lakshmi GB, Siddiqui AM, Husain M, Zulfequar M. Synthesis, electrical conductivity, and dielectric behavior of polyaniline/V 2 O 5 composites. International Journal of Polymer Science. 2013;2013.

[5] Marcovici I, Coricovac D, Pinzaru I, Macasoi IG, Popescu R, Chioibas R, Zupko I, Dehelean CA. Melanin and melanin-functionalized nanoparticles as promising tools in cancer research—A review. Cancers. 2022;14(7):1838.

[6] Li Q, Liao G, Tian J, Xu Z. Preparation of novel fluorinated copolyimide/amine-functionalized sepia eumelanin nanocomposites with enhanced mechanical, thermal, and UV-shielding properties. Macromolecular Materials and Engineering. 2018;303(2):1700407.

[7] Zhang Y, Zhuang S, Xu X, Hu J. Transparent and UV-shielding ZnO@ PMMA nanocomposite films. Optical materials. 2013;36(2):169-72.

[8] Wang C, Sheng X, Xie D, Zhang X, Zhang H. High-performance TiO2/polyacrylate nanocomposites with enhanced thermal and excellent UV-shielding properties. Progress in Organic Coatings. 2016;101:597-603.

[9] Doddapaneni V, Zhao Y, Ye F, Gati R, Edin H, Toprak MS. Improving Uv radiation absorption by copper oxide NPs/PMMA nanocomposites for electrical switching applications. Powder metallurgy and metal ceramics. 2015;54:397-401.

[10] Namsheer K, Rout CS. Conducting polymers: a comprehensive review on recent advances in synthesis, properties and applications. RSC advances. 2021;11(10):5659-97.

[11] Baker AG. The study of optical energy gap, refractive index, and dielectric constant of pure and doped polyaniline with HCl and H2SO4 acids. ARO-The Scientific Journal of Koya University. 2019;7(1):47-52.

[12] Niranjana M, Yesappa L, Ashokkumar SP, Vijeth H, Chapi S, Raghu S, Devendrappa H. Optical and electrical studies of vanadium pentoxide doped polyaniline composite. InAIP Conference Proceedings 2017 (Vol. 1832, No. 1). AIP Publishing.

[13] Babel V, Hiran BL. A review on polyaniline composites: Synthesis, characterization, and applications. Polymer Composites. 2021;42(7):3142-57.

[14] Chen CY, Wei TC, Hsiao PH, Hung CH. Vanadium oxide as transparent carrier-selective layer in silicon hybrid solar cells promoting photovoltaic performances. ACS Applied Energy Materials. 2019;2(7):4873-81.

[15] Huotari J, Lappalainen J. Nanostructured vanadium pentoxide gas sensors for SCR process control. Journal of Materials Science. 2017;52:2241-53.

[16] Lin TC, Jheng BJ, Huang WC. Electrochromic properties of the vanadium pentoxide doped with nickel as an ionic storage layer. Energies. 2021;14(8):2065.

[17] Rasheed RT, Mansoor HS, Abdullah TA, Juzsakova T, Al-Jammal N, Salman AD, Al-Shaikhly RR, Le PC, Domokos E, Abdulla TA. Synthesis, characterization of V_2O_5 nanoparticles and determination of catalase mimetic activity by new colorimetric method. Journal of Thermal Analysis and Calorimetry. 2021;145:297-307.

[18] Molli M, Bhat Kademane A, Pradhan P, Sai Muthukumar V. Study of nonlinear optical absorption properties of V_2O_5 nanoparticles in the femtosecond excitation regime. Applied physics A. 2016;122:1-4.

[19] Hou TF, Johar MA, Boppella R, Hassan MA, Patil SJ, Ryu SW, Lee DW. Vertically aligned one-dimensional ZnO/V_2O_5 core–shell hetero-nanostructure for photoelectrochemical water splitting. Journal of Energy Chemistry. 2020;49:262-74.

[20] Maruthi N, Faisal M, Raghavendra N, Prasanna BP, Nandan KR, Kumar KY, Prasad SB. Polyaniline/V_2O_5 composites for anticorrosion and electromagnetic interference shielding. Materials Chemistry and Physics. 2021;259:124059.

[21] Putrolaynen VV, Velichko AA, Pergament AL, Cheremisin AB, Grishin AM. UV patterning of vanadium pentoxide films for device applications. Journal of Physics D: Applied Physics. 2007;40(17):5283.

[22] Sharma S, Acharya AD, Thakur YS, Bhawna. Controlled synthesis of hierarchical BiOCl nanostructure with exposed {010} facets to yield enhanced photocatalytic performance for PMMA deterioration. Journal of Polymer Research. 2022;29(11):466.

[23] Ghosh A. Diffuse transmission dominant smart and advanced windows for less energy-hungry building: A review. Journal of Building Engineering. 2023;64:105604.

[23] Webster S, Czerw R, Nesper R, DiMaio J, Xu JF, Ballato J, Carroll DL. Optical properties of vanadium oxide nanotubes. Journal of Nanoscience and Nanotechnology. 2004;4(3):260-4.

[24] Saraswat VK, Kishore V, Deepika KS, Saxena NS, Sharma TP. Band gap studies on Se-Te-Sn ternary glassy films. Chalcogenide Lett. 2007;4(5):61-4.

[25] Mammad MH, Gülfen M, Olgun U, Özdemir A. Synthesis, spectroscopy, band gap energy and electrical conductivity of poly (dopamine–co–aniline) copolymer. Spectrochimica Acta Part A: Molecular and Biomolecular Spectroscopy. 2024;308:123712.

[26] Soliman TS, Zaki MF, Hessien MM, Elkalashy SI. The structure and optical properties of PVA-$BaTiO_3$ nanocomposite films. Optical Materials. 2021;111:110648.

[27] Basavaraj B, G. Metri P, Shweta GC, Sannakki B. Complex optical studies on conducting polypyrrole doped with ZnO nanoparticles. InMacromolecular Symposia 2020 Oct (Vol. 393, No. 1, p. 2000096).

[28] Yahia IS, Farag AA, Cavas M, Yakuphanoglu F. Effects of stabilizer ratio on the optical constants and optical dispersion parameters of ZnO nano-fiber thin films. Superlattices and Microstructures. 2013;53:63-75.

[29] Jafar MM. Comprehensive formulations for the total normal-incidence optical reflectance and transmittance of thin films laid on thick substrates. Eur. Int. J. Sci. Technol. 2013;2:274.

[30] Tsai CM, Hsu SH, Ho CC, Tu YC, Tsai HC, Wang CA, Su WF. High refractive index transparent nanocomposites prepared by in situ polymerization. Journal of Materials Chemistry C. 2014;2(12):2251-8.

[31] Kurt A. Influence of $AlCl_3$ on the optical properties of new synthesized 3-armed poly (methyl methacrylate) films. Turkish Journal of Chemistry. 2010;34(1):67-80.

[32] Hamad TK. Refractive index dispersion and analysis of the optical parameters of (PMMA/PVA) Thin film. Al-Nahrain Journal of Science. 2013;16(3):164-70.

[33] Sharma P, Katyal SC. Determination of optical parameters of a-(As2Se3) 90Ge10 thin film. Journal of Physics D: Applied Physics. 2007;40(7):2115.

[34] Atyia HE, Hegab NA. Optical spectroscopy and dispersion parameters of Ge15Se60X25 (X= As or Sn) amorphous thin films. The European Physical Journal-Applied Physics. 2013;63(1):10301.

[35] DrDomenico Jr M, Wemple SH. Oxygen-octahedra ferroelectrics. I. Theory of electro-optical and nonlinear optical effects. Journal of Applied Physics. 1969;40(2):720-34.

[36] Wemple SH, DiDomenico Jr M. Behavior of the electronic dielectric constant in covalent and ionic materials. Physical Review B. 1971;3(4):1338.

[37] Wemple SH. Refractive-index behavior of amorphous semiconductors and glasses. Physical Review B. 1973;7(8):3767.

[38] Mansour AF, Mansour SF, Abdo MA. Improvement structural and optical properties of ZnO/PVA nanocomposites. IOSR J Appl Phys. 2015;7(2):60-9.

[39] El-Nahass MM, Sallam MM, Afifi MA, Zedan IT. Structural and optical properties of polycrystalline $CdSexTe_{1-x}$ ($0\leq x\leq 0.4$) thin films. Materials research bulletin. 2007;42(2):371-84.

[40] I. Saini, J. Rozra, N. Chandak, S. Aggarwal, P. K. Sharma, and A. Sharma, Tailoring of electrical, optical and structural properties of PVA by addition of Ag nanoparticles, Mater Chem Phys, 139 (2013) 802–810.

[41] Flytzanis C, Hache F, Klein MC, Ricard D, Roussignol P. V Nonlinear Optics in Composite Materials: 1. Semiconductor and Metal Crystallites in Dielectrics: 1. Semiconductor and Metal Crystallites in Dielectrics. InProgress in optics 1991(Vol. 29, pp. 321-411). Elsevier.

[42] Chahal RP, Mahendia S, Tomar AK, Kumar S. γ-Irradiated PVA/Ag nanocomposite films: Materials for optical applications. Journal of Alloys and Compounds. 2012;538:212-9.

[43] Atyia HE, Hegab NA. Influence of thermal treatment on the optical aspects for $Ge_{20}In_5Se_{75}$ films. Optik. 2016;127(8):3888-94.

[44] Salem AM, Dahy TM, El-Gendy YA. Thickness dependence of optical parameters for ZnTe thin films deposited by electron beam gun evaporation technique. Physica B: Condensed Matter. 2008;403(18):3027-33.

[45] Taha TA, Saleh A. Dynamic mechanical and optical characterization of PVC/fGO polymer nanocomposites. Applied Physics A. 2018;124(9):600.

[46] Jayaraj SK, Sadishkumar V, Arun T, Thangadurai P. Enhanced photocatalytic activity of V_2O_5 nanorods for the photodegradation of organic dyes: a detailed understanding of the mechanism and their antibacterial activity. Materials Science in Semiconductor Processing. 2018;85:122-33.

[47] Ali H, Ismail AM. Honeycomb-like V_2O_5 based films: Synthesis, structural, thermal, and optical properties for environmental applications. Journal of Inorganic and Organometallic Polymers and Materials. 2022;32(8):3012-29.

[48] Hu F, Li W, Zhang J, Meng W. Effect of graphene oxide as a dopant on the electrochemical performance of graphene oxide/polyaniline composite. Journal of Materials Science & Technology. 2014;30(4):321-7.

[49] Kundu S, Satpati B, Kar T, Pradhan SK. Microstructure characterization of hydrothermally synthesized PANI/$V_2O_5 \cdot nH_2O$ heterojunction photocatalyst for visible light induced photodegradation of organic pollutants and non-absorbing colorless molecules. Journal of hazardous materials. 2017;339:161-73.

Chapter 6

Role of Different Solvents in Improving the Electrochemical Performance of BiOCl Battery-type Electrode Material for the Supercapacitor Devices

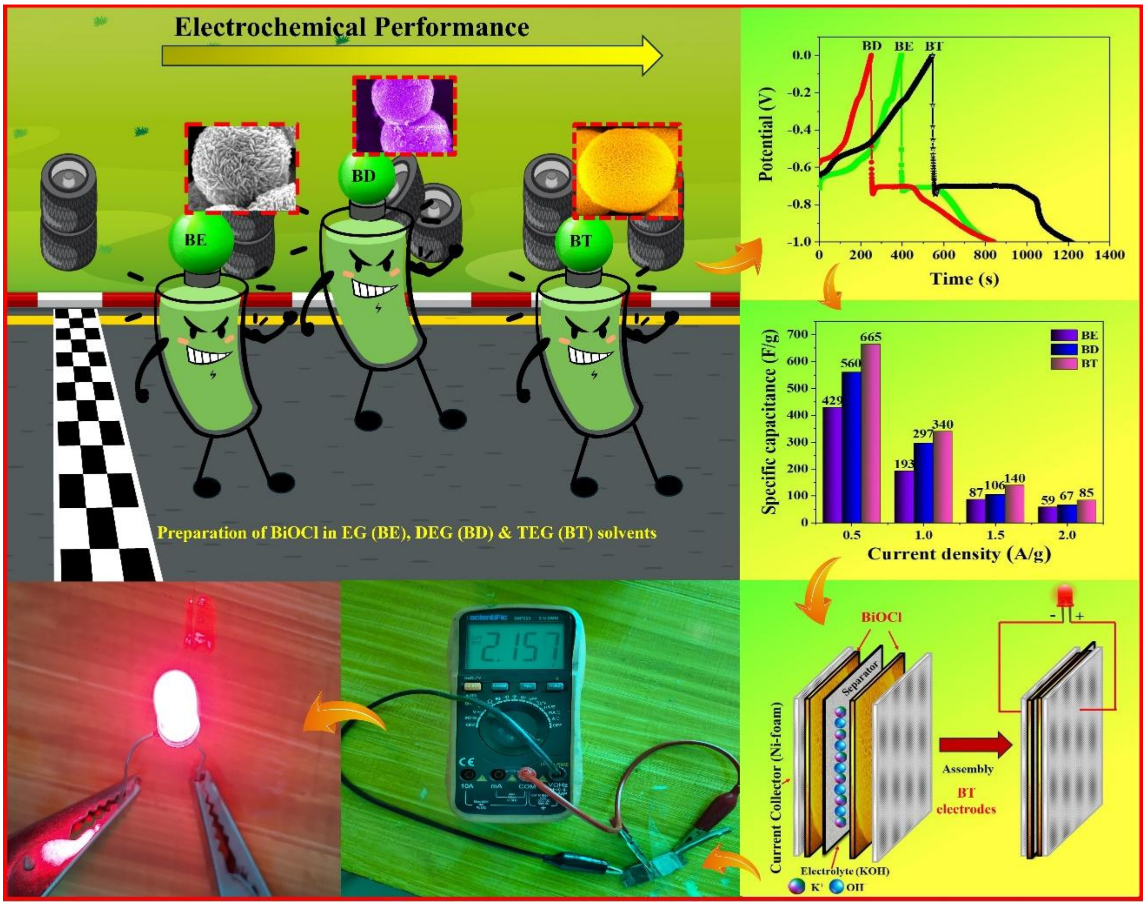

This investigation examines the effects of different solvents for BiOCl synthesis by solvothermal method to study its electrochemical and physical characteristics. Herein, ethylene glycol (EG), diethylene glycol (DEG), and triethylene glycol (TEG) are used to prepare different 3D hierarchical BiOCl nanostructures. Among all three prepared samples, BiOCl synthesized using TEG as the solvent (BT), exhibits a marigold flower-like morphology with an extended surface area. However, BT electrode exhibits the peak specific capacity owing to its elevated electrical conductivity and expanded surface area, leading to a diminished potential drop in the galvanometric charge-discharge study. The prepared BT electrode material was utilized as the working electrode material in the supercapacitor. In three electrode configurations, an extreme specific capacity of 665 F/g at 0.5 A/g was observed in 6 M KOH aqueous electrolyte solution with 93.8% cyclic reliability after 2000 cycles. For the two electrodes system, a symmetric cell was fabricated with a BT//BT configuration and demonstrates a extreme energy density (ED) of 15.6 Wh/kg at 838 W/kg power density (PD). Notably, the practical viability of the constructed symmetric cell was validated through the illumination of a red LED and supported the application of BT electrode for energy storage technology.

6.1. Introduction

To enhance the electrochemical performance of supercapacitors using metal oxides with pseudocapacitive properties has proven highly effective strategy. The electrochemical functioning of supercapacitors is significantly altered by the electron transport attributes of the electrode materials [1,2]. In this context, bismuth oxides and bismuth oxyhalides exhibit attractive properties to accelerate the multi-electron transfer processes during electrochemical reactions and make them highly favorable candidates for supercapacitor applications. Various nanostructures of bismuth oxides, including nanosheets and nano belts, have been explored for their potential application in supercapacitors [3]. These nanostructures have shown good specific capacitances ranging from 98 to 996 F/g. The use of electroplated Bi_2O_3 films on copper substrates as supercapacitor electrodes was earliest introduced by Gujar and his co-workers [4]. Ma et al. introduced an asymmetric cell by employing MnO_2 as the cathode and β-Bi_2O_3 as an anode electrode, which rose in an impressive ED of 32.4 Wh/kg [5]. Bismuth oxychloride (BiOCl), a close relative of the same group, exhibits a tetragonal lamellar arrangement. This structure involves stacking [Cl–Bi–O–Bi–Cl] sheets through van der Waals forces, particularly via the Cl atoms, along the c-axis [6]. The fabrication of various BiOCl morphologies has been described in the literature using a variety of synthesis techniques. BiOCl with different nanostructures has a potential future in photocatalysis, optics, electronics, and biomedicine due to its excellent crystalline structure, geometric anisotropy, amazing photostability, favorable electrical properties, and non-toxic nature [7]. So far, a wide array of micro and nanostructures of BiOCl has been successfully synthesized, including nanocrystals, nanowires, nanofibers, nanobelts, nanosheets, nanoplates, thin films, intricate flower-like hierarchies, hollow microspheres, and porous nanospheres [8]. Up to now, numerous capable reports of BiOCl have arisen such as Dutta and his co-workers fabricated BiOCl doped multi-walled carbon nanotubes-based nanocomposites electrode, achieving a maximum specific capacitance of 421 F/g at 5 mV/s scan rate and demonstrates outstanding longevity, retaining an impressive capacitance ~94% even afterward undergoing 2000 cycles [9]. Recently, Shankar et al. utilized BiOCl and FeOCl/BiOCl nanomaterial as anode electrodes and studied their electrochemical attributes. Prepared pure BiOCl and FeOCl/BiOCl nanocomposites attain largest capacitance of 228 F/g and 424 F/g respectively at 1 A/g current density (CD) [10].

Characteristically, BiOCl materials have a tendency to adopt 2-dimensional (2D) nanosheet morphologies due to their intrinsic layered crystalline structure. Nevertheless, a suitable template agent can be used to organize 2D material nanosheets into 3-dimensional

(3D) hierarchical microspheres of BiOCl. In comparison to 2D nanosheets, 3D hierarchical structures exhibit significant potential for practical applications due to their essential properties. This includes rapid interfacial charge transfer and a multitude of reactive sites, these combined benefits substantially enhance electrochemical as well as photocatalytic activity, making them highly promising materials for practical applications [11,12]. In this regard, our research group recently reported a 3D hierarchical BiOCl flower nanostructure with exposed {010} facets to provide improved PMMA photocatalytic functions [13]. Consequently, significant attempts have been made to synthesize 3D hierarchical structures but the studies are limited to checking their photocatalytic activity only. According to the aforementioned literature survey, BiOCl shows its potential in supercapacitor applications as electrode material. Therefore, detailed research is needed to synthesize 3D hierarchical nanostructures containing multiple active sites, which can achieve excellent electrochemical performance.

The hydro/solvothermal method is the most popular synthetic approach in experiments because it makes it possible to fabricate BiOCl nanostructures with outstanding efficiency and accuracy [14]. Particularly, it has the capability to create intricate self-assembled three-dimensional (3D) architectures of BiOCl using the hydro/solvothermal method. BiOCl 3D microspheres were successfully synthesized by Zhang et al. under the influence of ethylene glycol, resulting in good photocatalytic activity [15]. Wang et al. exposed the (001) facet by hydrothermally synthesizing porous BiOCl micro flowers while using glycerol as a structure-directing agent [16]. These investigations show the solvents used in the hydro/solvothermal process have a substantial impact on the shape and surface structure of the nanomaterial. The solvent used in synthesis serves as a template agent and structure-directing agent [17]. In general, the solvent can effectively regulate the crystal growth, self-assembly, and nucleation processes. Consequently, new structures with diverse forms and surface characteristics can be attained through innovative architectures. However, there is a need for a systematic investigation into the correlation between various solvents and the morphologies/surface properties of BiOCl. This will provide directions for creating a straightforward and efficient method for producing controllable BiOCl hierarchical nanostructures, along with improved electrochemical properties.

This work presents a novel and highly effective solvothermal strategy employing different glycols as mediating agents. This method enables the precise fabrication of BiOCl nanostructures, allowing us to investigate the impact of different glycol solvents (specifically ethylene glycol, diethylene glycol, and triethylene glycol) on the resulting structure, morphology, and electrochemical behavior of the BiOCl material. The fabricated BiOCl in triethylene glycol solvent with marigold-like flower nanostructure responded electrochemically more efficiently than other nanostructures. Furthermore, the symmetric supercapacitor device constructed from BiOCl material with a marigold flower-like morphology showcases remarkable electrochemical performance. Notably, the practical feasibility of this device is demonstrated by a glowing red LED, which signifies its suitability in energy storage systems.

6.2. Experimental Procedures

6.2.1. Synthesis of BiOCl 3D hierarchical nanostructures

A one-step solvothermal method was used to synthesize different BiOCl 3D morphologies via various synthesis solvents such as ethylene glycol (EG), diethylene glycol (DEG), and triethylene glycol (TEG). In the synthesis method 1.458 g of $Bi(NO_3)_3.5H_2O$ dissolved in 75 ml of EG, DEG, and TEG solvents individually and ultrasonicated solution for 20 min. After the ultrasonication process, 0.318 g of $NaClO_3$ was mixed into the solution and again ultrasonicated for 20 min. Subsequently, the resulting solution was exiled into a 100 ml autoclave and heated for 3 h at 150 ^{0}C in a hot air oven.

Table 6.1. Synthesis of BiOCl 3D hierarchical nanostructures under experimental conditions.

Sample name	Precursor name	Reagent	Solvent used	Morphology
BE	Bismuth Nitrate Pentahydrate	Sodium Chlorate	Ethylene Glycol	Rice like
BD	Bismuth Nitrate Pentahydrate	Sodium Chlorate	Diethylene Glycol	Allium flower-like
BT	Bismuth Nitrate Pentahydrate	Sodium Chlorate	Triethylene Glycol	Marigold flower-like

Once the mix solution cooled down to normal temperature, centrifugation was used to collect the produced precipitates. These collected precipitates were afterward subjected to seven washes with deionized water to eliminate any impurities in the solution. Finally, the material endured drying in an oven at 60°C for 12 h. Table 6.1 shows the synthesis process of 3D hierarchical nanostructures of BiOCl under specified experimental conditions.

6.2.2. Fabrication of supercapacitor electrode

To fabricate the working electrode for the supercapacitor in a three-electrode system, BiOCl active material, carbon black, and PVDF binder were mixed in NMP solvent with an 80:10:10 wt.% ratio. In the next step, 1h ultrasonication was required to form a uniform ink. This ink was then applied with a micropipette to a 1 x 1 cm^2 nickel foam surface. Subsequently, the electrode was heated at 70°C for 13 h. The mass loaded on nickel foam was 4 mg and acted as the working electrode in a 6 M KOH electrolyte solution. Platinum wire was utilized as the counter electrode, while Ag/AgCl was employed as the reference electrode in a three-electrode system.

6.3. Results and discussion

6.3.1. Structural Elucidation and Surface Morphology

X-ray diffraction (XRD) analysis was utilized to investigate the crystal structures of BiOCl nanoparticles. Figure 6.1 depicts the XRD patterns of the BiOCl samples fabricated through 3 h of solvothermal treatment using bismuth nitrate pentahydrate as a precursor and sodium chlorate as an oxidizing agent in different solvents, namely EG, diethylene glycol DEG and TEG. All the diffraction peaks in XRD data closely match (see Figure 6.1) with tetragonal phase of BiOCl (Reference code. 96-901-1783).

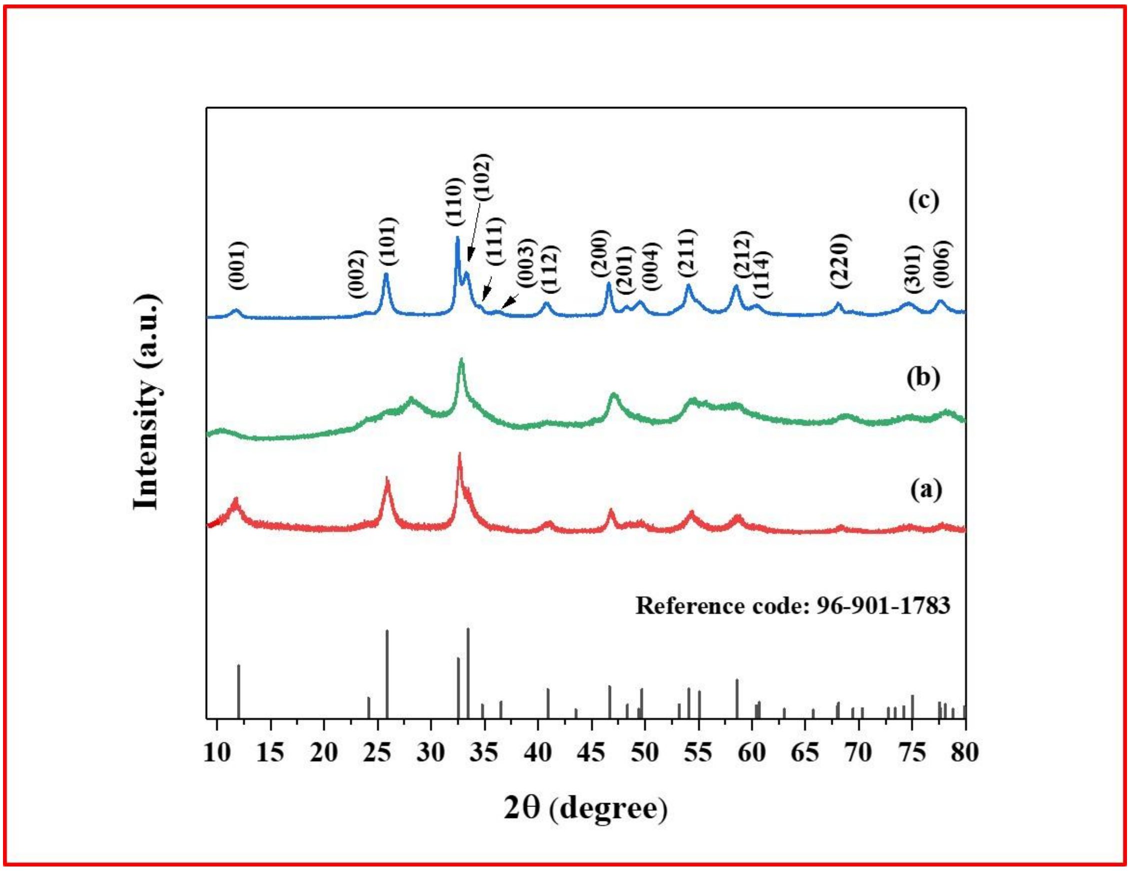

Figure 6.1. illustrates the XRD patterns of the BiOCl products synthesized using various solvents: (a) BE (b) BD, and (c) BT samples.

The pronounced and well-defined diffraction peaks of XRD indicate that the BiOCl nanoparticles exhibit a high degree of crystallinity. The observed peaks correspond to the crystal planes (001), (002), (101), (110), (102), (111), (003), (112), (200), (201), (004), (211), (212), (114), (220), (301) and (006) of tetragonal BiOCl, with 2θ values of 11.7^0, 23.8^0, 25.9^0, 32.6^0, 33.63^0, 34.5^0, 36.2^0, 40.9^0, 46.7^0, 48.2^0, 49.4^0, 53.9^0, 58.5^0, 60.47^0, 68.1^0, 74.6^0 and 77.5^0, respectively. The Debye-Scherrer formula was employed to determine the crystallite size, which was derived from the full width at half maximum (FWHM) observed in the various diffraction peaks [18].

$$D = \frac{k\lambda}{\beta Cos\theta} \tag{6.1}$$

where, "D" represents the average crystallite size, "λ" denotes the X-ray wavelength,"k" stands for Scherrer constant, "β" represents the FWHM of the diffraction and "θ" is the Bragg diffraction angle. The typical crystallite sizes for BE, BD, and BT samples are around 19 nm, 17 nm, and 14 nm, respectively.

Experimental findings suggest that the size of crystallites is responsive to the specific glycol solvent employed during the solvothermal treatment. Therefore, to achieve smaller crystallites, it is preferable to use glycol solvents with a higher number of oxygen atoms (TEG). Conversely, to obtain larger crystallites, glycol solvents with fewer oxygen atoms are more suitable (EG). This change in crystalline size could be also attributed to the varied polar characteristics of these solvents [19].

The morphologies of the prepared BiOCl samples (BE, BD, and BT) were studied through FESEM images. Figure 6.2(a-i) depicts FESEM images of BiOCl samples at high and low magnification, which were synthesized using different solvents. To prepare a variety of uniform hierarchical nanostructures with various morphologies (see Figure 6.2(a-c)) BiOCl was prepared using EG, DEG, and TEG solvents. The obtained 3D hierarchical nanostructures of BiOCl using EG, DEG and TEG solvents exhibited sizes ranging from ~1-6 µm (calculated using ImageJ software).

The high magnification FESEM images (Figure 6.2(d-f)) clearly show rice-like (BE), allium flower-like (BD), and marigold flower-like (BT) morphology of BiOCl respectively. Each of the hierarchical nanostructures was made up of multiple radially growing nanorices for BE, nanoflakes for BD, and nanosheets for BT samples, which provides a noteworthy surface-to-volume ratio leading to the establishment of a porous structure. The characteristic thickness of these nanoflakes or nanosheets was found to be ~9-21 nm. The rice-like BiOCl grains (BE) were self-assembled and formed a highly close-packed hierarchical nanostructure.

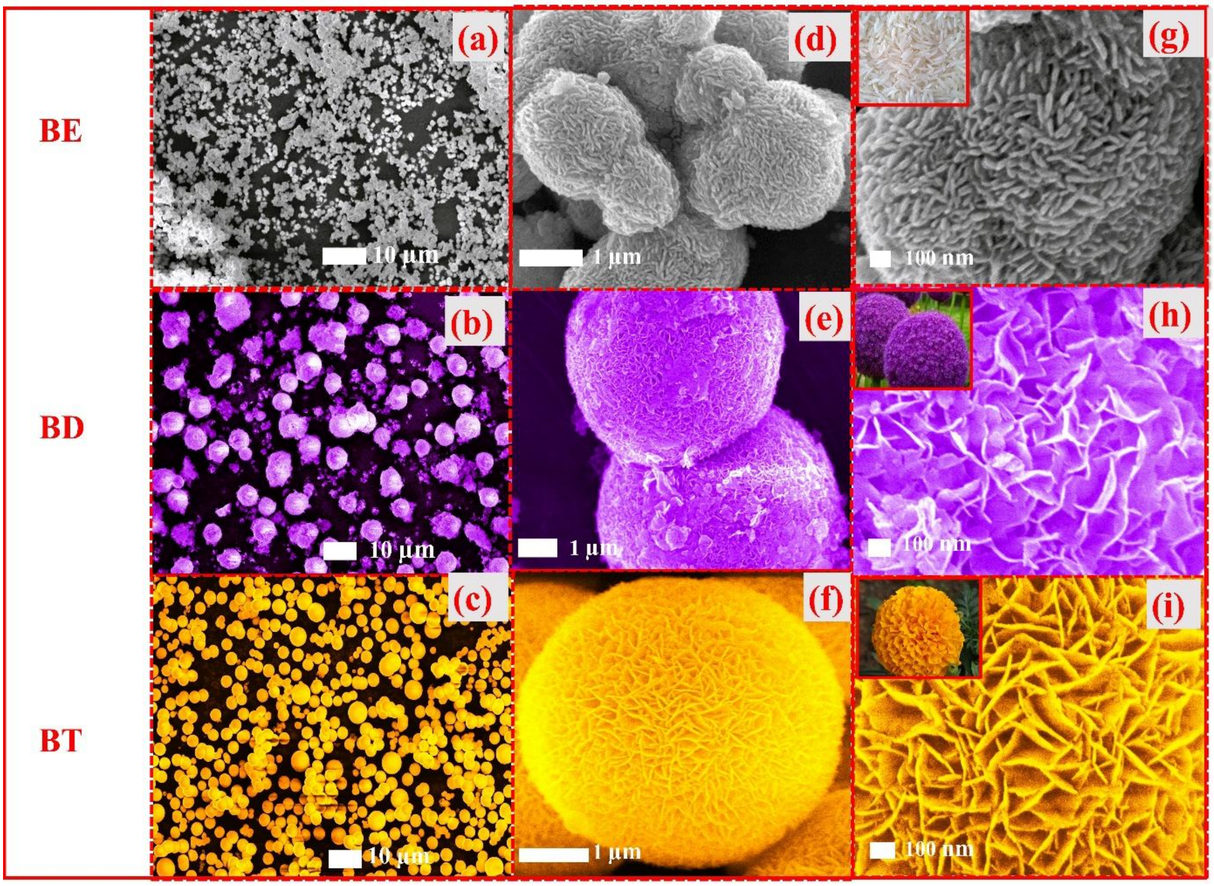

Figure 6.2. (a-i) FESEM images of 3D hierarchical nanostructures of BE, BD, and BT samples.

Furthermore, in BD and BT samples nanosheets or nanoflakes were uniform self-assembled, and formed loosely packed nanostructures. The sequence of a loosely arranged uniform configuration was BT>BD>BE. This sequence indicates that the BT sample demonstrates a significant surface-to-volume ratio, resulting in the establishment of a porous nanostructure with amplified surface area, which makes BT samples a potential candidate to offer superior electrochemical performance.

The chemical composition of the BE, BD, and BT samples has been confirmed through EDX spectra (see Figure 6.3(a-c)). Figure 6.3(a-c) unveils the existence of carbon (C), oxygen (O), bismuth (Bi), and chlorine (Cl) atoms in the prepared sample. The presence of bismuth, oxygen, and chlorine in the BiOCl sample is attributed to the chemical composition, while the carbon signature originates from the carbon tape used for sample fixation. EDX analysis reveals a higher intensity peak of bismuth and chlorine for the BT sample (see Figure 6.3(c)). This indicates a larger concentration of these elements in BT. The substantial presence of bismuth and chlorine can influence a material's electrochemical behavior. For example, bismuth can enhance conductivity, while chlorine might modify the material's stability or act as a dopant, potentially improving its electrochemical function.

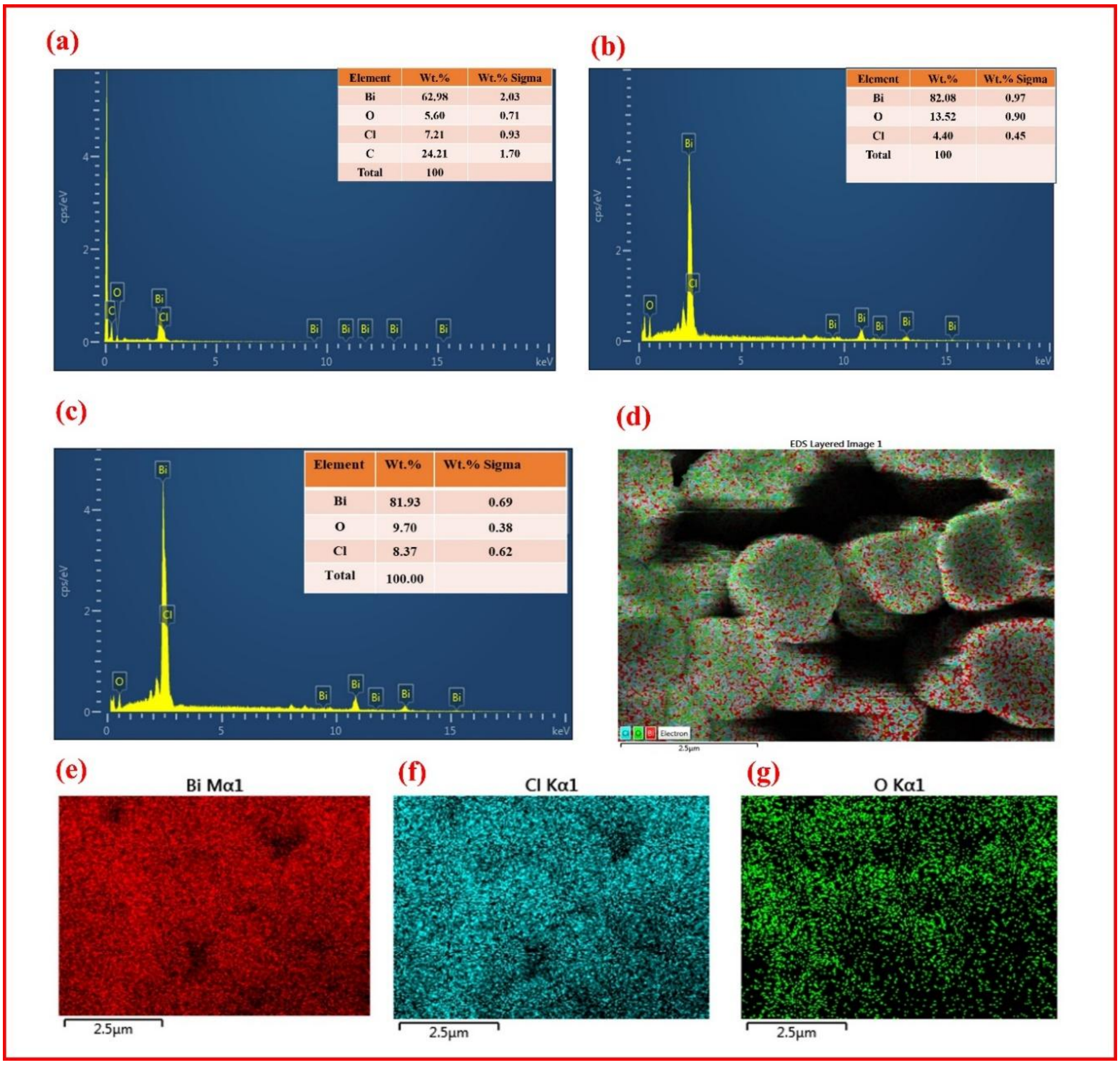

Figure 6.3. EDX spectra of (a) BE (b) BD, and (c) BT samples (d-g) Elemental distribution mapping of BT sample.

Figure 6.3(d) shows the structural hierarchy of the BT sample, representing the nanostructural arrangement and elemental distribution. For a more comprehensive visualization, the elemental mappings of Bi, O, and Cl are individually illustrated in Figure 6.3(e–g). Notably, these mappings emphasize the regular distribution of the significant constituents Bi, O, and Cl throughout the surface of the sample. Furthermore, BET analysis was used to examine the sample's pore size distribution and surface area, as shown in Figure 6.4(a-c). As observed from Figure 6.4(a-c), the adsorption-desorption curves exhibit characteristics consistent with a type-IV isotherm with an H_3 hysteresis loop, confirming the mesoporous nature of the samples [20]. However, the BJH (Barrett-Joyner-Halenda) pore size distribution of all samples further confirmed the mesoporous structure (see Figure 6.4(a-c) inset).

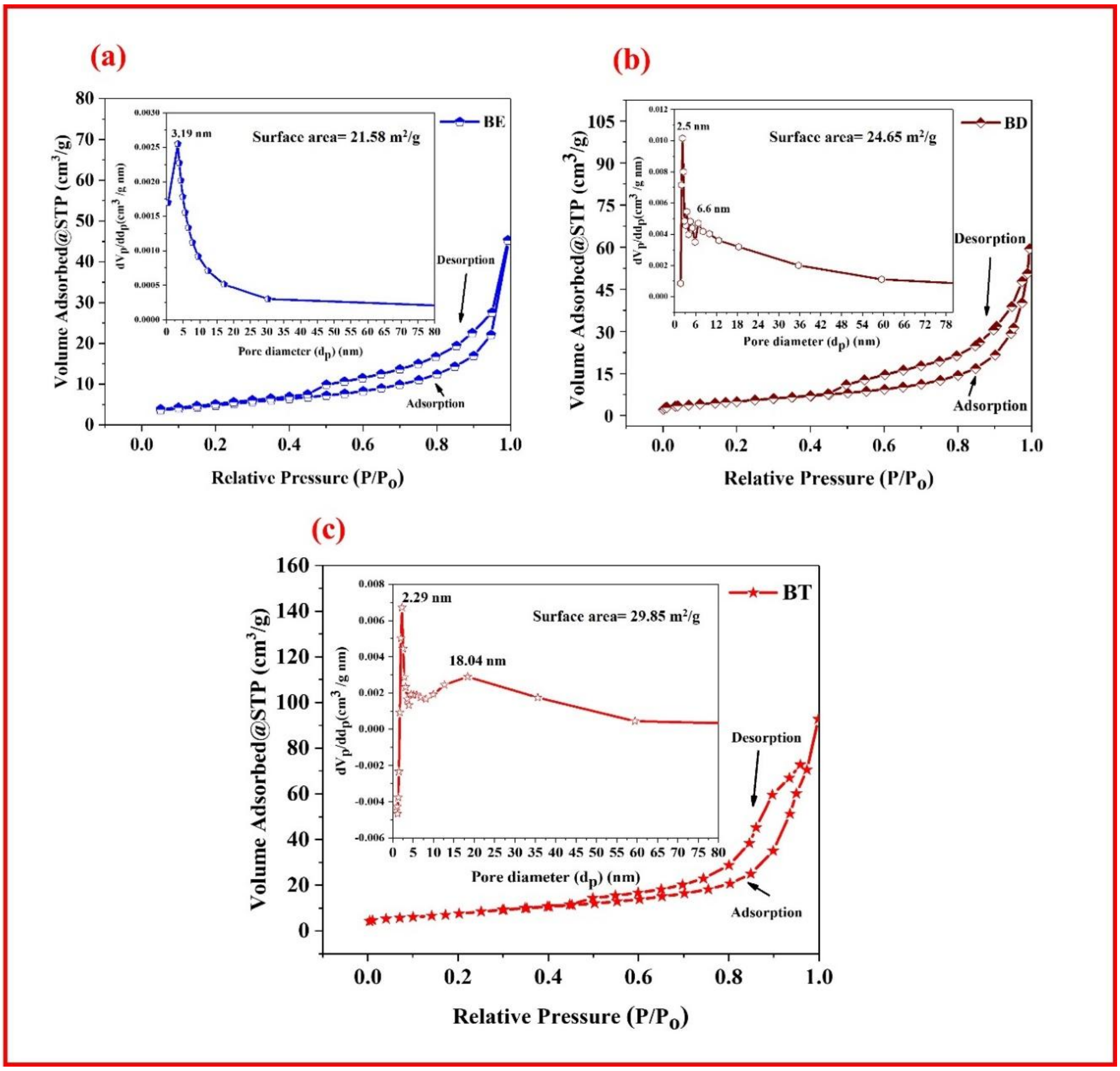

Figure 6.4. N_2 adsorption-desorption isotherm of (a) BE (b) BD (c) BT samples and the inset of the figures shows the BJH pore size distribution of corresponding samples.

The pore size distribution for the prepared samples primarily falls around 3.19 nm for BE, 2.5-6.6 nm for BD, and 2.29-18.04 nm for BT. Additionally, BE, BD, and BT samples were found to have surface areas of 21.58, 24.65, and 29.85 m^2/g, respectively. As a result, it is expected that the mesoporous structure of the BT sample could be particularly favorable for supercapacitor applications which is later discussed. The BT sample reveals a notably elevated surface area in contrast to earlier reported works [21,22]. This suggests that the synthesized nanoparticles possess potential not only for supercapacitors but also for a broad range of photocatalytic applications with less duration time preparation method i.e. 3 h solvothermal treatment.

FTIR spectroscopy was employed to further elucidate the chemical assemblies found within the synthesized BiOCl samples (see Figure 6.5(a)). In all samples, the bands observed at 1281 and 1051.8 cm^{-1} can be attributed to the asymmetric and symmetric stretching vibration peaks respectively of the Bi-Cl bond within the BiOCl structure [23]. The absorption peaks observed at 1610 cm^{-1} signify the flexural vibrations associated with the hydroxyl groups [24].

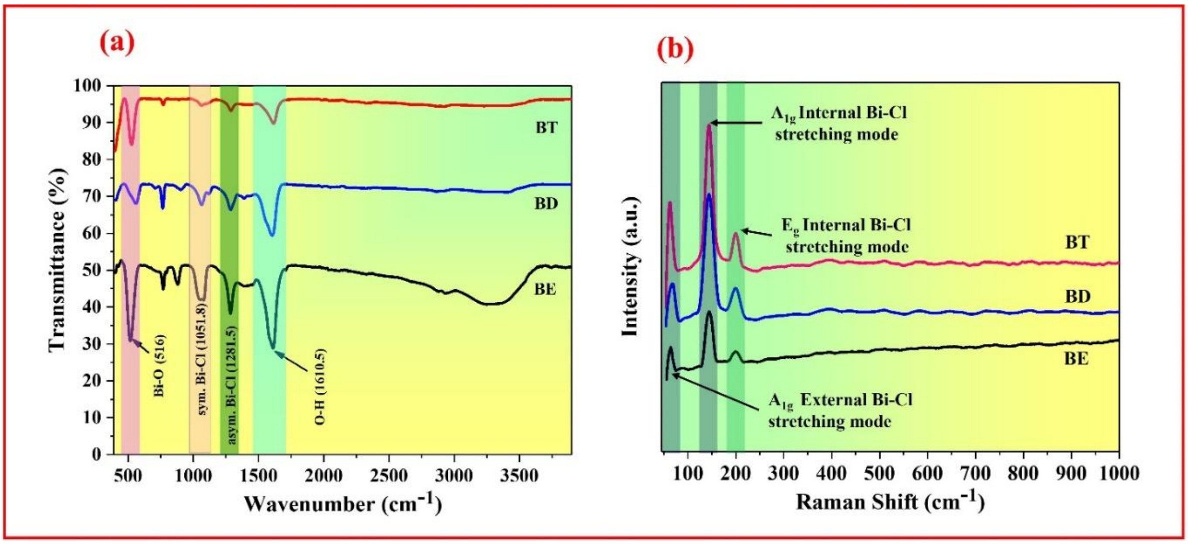

Figure 6.5. (a) FTIR (b) Raman spectra of prepared BE, BD, and BT samples.

The peaks observed around ~516 cm^{-1} in the FTIR spectra (see Figure 6.5(a)) correspond to the valent symmetrical A_{2u} mode vibrations of the Bi-O stretching mode [23]. The Raman spectra were used to confirm the purity of the prepared samples (see Figure 6.5(b)) illustrating one prominent band with two weaker bands. The band mentioned at 144.7 cm^{-1} is designated as the A_{1g} type internal Bi-Cl stretching [25]. The less intense bands observed at 200.6 cm^{-1} are attributed to the E_g type internal Bi-Cl stretching. Additionally, the band at 62.6 cm^{-1} is assigned to the A_{1g} external Bi-Cl stretching mode [26]. These wavenumbers are reliable with values reported in the literature, indicating the high purity of prepared BiOCl samples.

6.3.1.1. Possible mechanism of hierarchical nanostructures with different morphology

Due to implementations of the identical conditions in fabrications of the samples, contribution of the parameters such as pH as well as temperature in the growth of the distinct morphologies would be considered negligible. So, the solvent is the only factor capable of influencing material morphologies. This underscores the significant role of solvents in determining the varied range of morphological outcomes. The present study emphasizes the profound significance of the solvent in variations within morphological outcomes. As a first thought, we proposed that the formation mechanism of 3D BiOCl nanostructures included initial nucleation of amorphous prime particles (Solvent, Precursor, Capping agent), succeeded by the subsequent cluster and crystallization of these prime particles. This hypothesis points towards the anisotropic growth characteristics of BiOCl crystals and is well understood from the results of our experiments as follows. Bismuth alkoxide was formed by dissolving $Bi(NO_3)_3.5H_2O$ in various polyol solvents, as illustrated in Figure 6.6 [27–30]. After that when a solution is subjected to solvothermal treatment, the bismuth alkoxide weakens, leading to the gradual formation of BiO^+. Simultaneously, Cl^- ions were produced through the reduction of $NaClO_3$ through polyols. BiOCl nuclei were established in the next step and rapidly expanded into primary particles. Subsequently, with time, these BiOCl nuclei came together to form 3D microspheres exhibiting crystallographic orientation. This alignment was controlled via the objective of reducing the overall energy of the whole system as the growing mechanism extended [31]. It persisted in its growth by merging with the remaining primary particles, ultimately giving growth to hierarchical nanostructures through the phenomenon referred to as Ostwald ripening [29-31]. Unique characteristics of solvents namely viscosity, chelation capacity, basicity, vapor pressure, and hydrogen bonding exert diverse influences on the eventual buildings and geomorphologies of developed micro-nanostructures [32]. The polyol used in this work has the ability to construct long chain-like or crosslinked network structures through hydrogen bonding with interactions between its multiple hydroxyl groups [33].

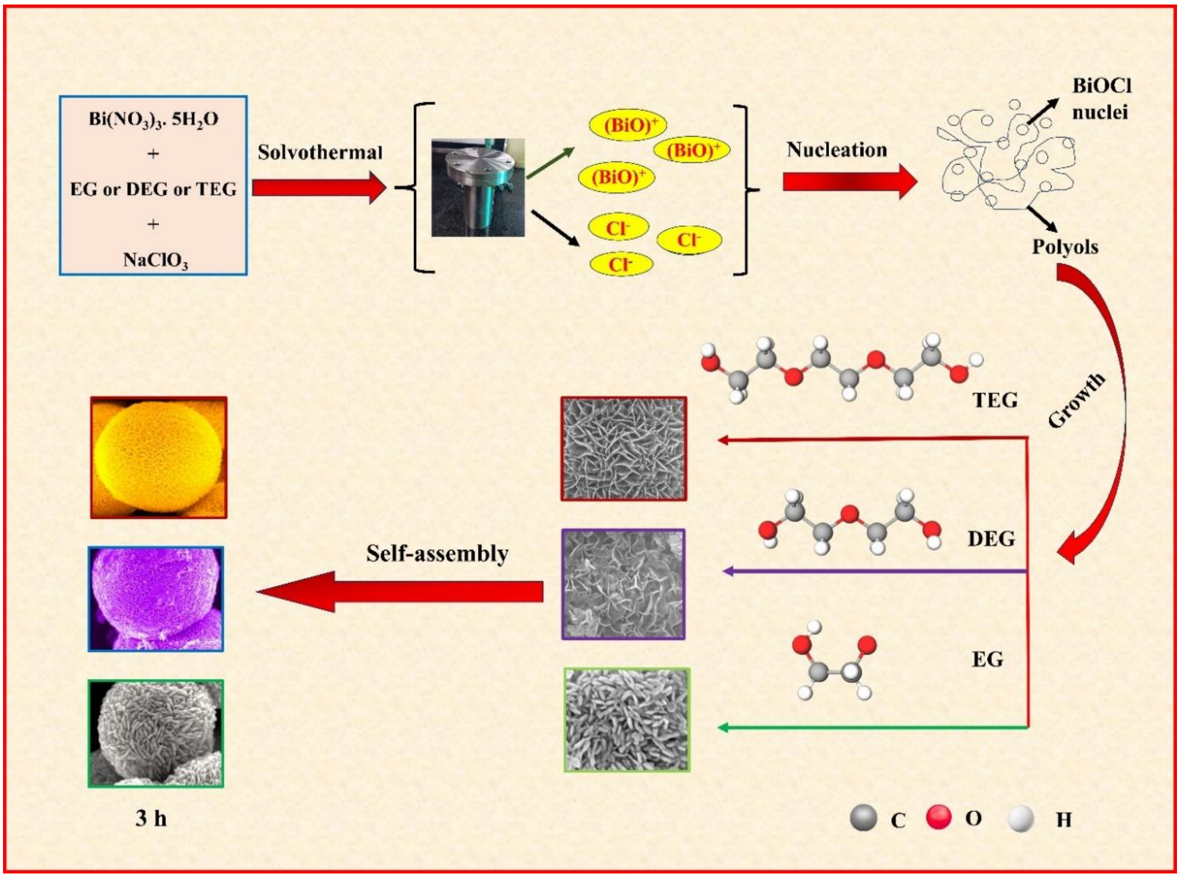

Figure 6.6. 3D hierarchical nanostructures of BiOCl possible growth mechanism.

It was proposed that the aggregated nanoplates could act as a template, controlling the directed assembly and development of the nanoparticles, which results in the creation of BiOCl structures [34]. The varying viscosities of the polyols could be considered another possible reason for the variation in formed hierarchical nanostructures.

It is to be noted that TEG has comparatively higher viscosity than DEG and EG which prevented BiOCl nuclei from diffusion and led to the development of highly loosely packed uniform hierarchical nanostructures [35]. Furthermore, the fluctuating polarity of solvents could also be contributed to the observed differences in morphologies and it is important to note that TEG exhibits higher level of polarity compared to DEG and EG. This increased polarity of TEG facilitates the adsorption of Cl^- anions onto specific crystal facets through robust hydrogen bonding interactions between the protic solvent and bismuth molecules. Consequently, this helps in the growth of a higher symmetry compared to DEG and EG microstructure in BiOCl as shown in Figure 6.6. This experimental finding deduces that polyols play a valuable job in the synthesis of BiOCl as reducing and morphology-directing agents. Their multiple roles make polyols a crucial component in producing BiOCl 3D-hierarchical nanostructures with the desired properties.

6.3.2. Supercapcitive study and charge storage mechanism

To evaluate the supercapacitive properties of synthesized BiOCl nanoparticles the CV and GCD measurements were used. CV characteristics of BE, BD, and BT are represented in Figure 6.7(a), showing the redox behavior of the samples under a 5 mV/s scanning rate within a voltage selection of -1 V- 0 V. Notably, all samples exhibited distinct redox peaks, indicative of faradaic-type behavior. These peaks, encompassing two oxidation and one reduction peaks, correspond to different states ($Bi^{(+3)}$, $Bi^{(0)}$, and Bi(metal)) of BiOCl in the 6 M potassium hydroxide liquid electrolyte [36,37]. The probable redox reactions of the prepared BiOCl are displayed in the inset of Figure 6.7(a). The redox process produced two oxidation peaks (O_1 and O_2), suggesting that $Bi^{(0)}$ is oxidized to Bi(metal) and then oxidized again to $Bi^{(+3)}$. The emergence of peaks at positions O_1 and O_2 (see Figure 6.7(a)) are associated with the existence of a limited quantity of bismuth (Bi) metal located at the junction between the bismuth metal and the KOH electrolyte [38]. The occurrence of peak (O_2) in conjunction with the plateau indicates the transition from the state of Bi(metal) to $Bi^{(+3).}$ In addition, a notable reduction peak, distinguished by its high intensity, indicates the fall of $Bi^{(+3)}$ to $Bi^{(0)}$ state for BiOCl. The CV curves (see Figure 6.7(a)) illustrate that the BT sample demonstrates superior supercapacitive behavior, as indicated by its extreme current response and larger area under the curvature. This enhancement can be attributed to several factors.

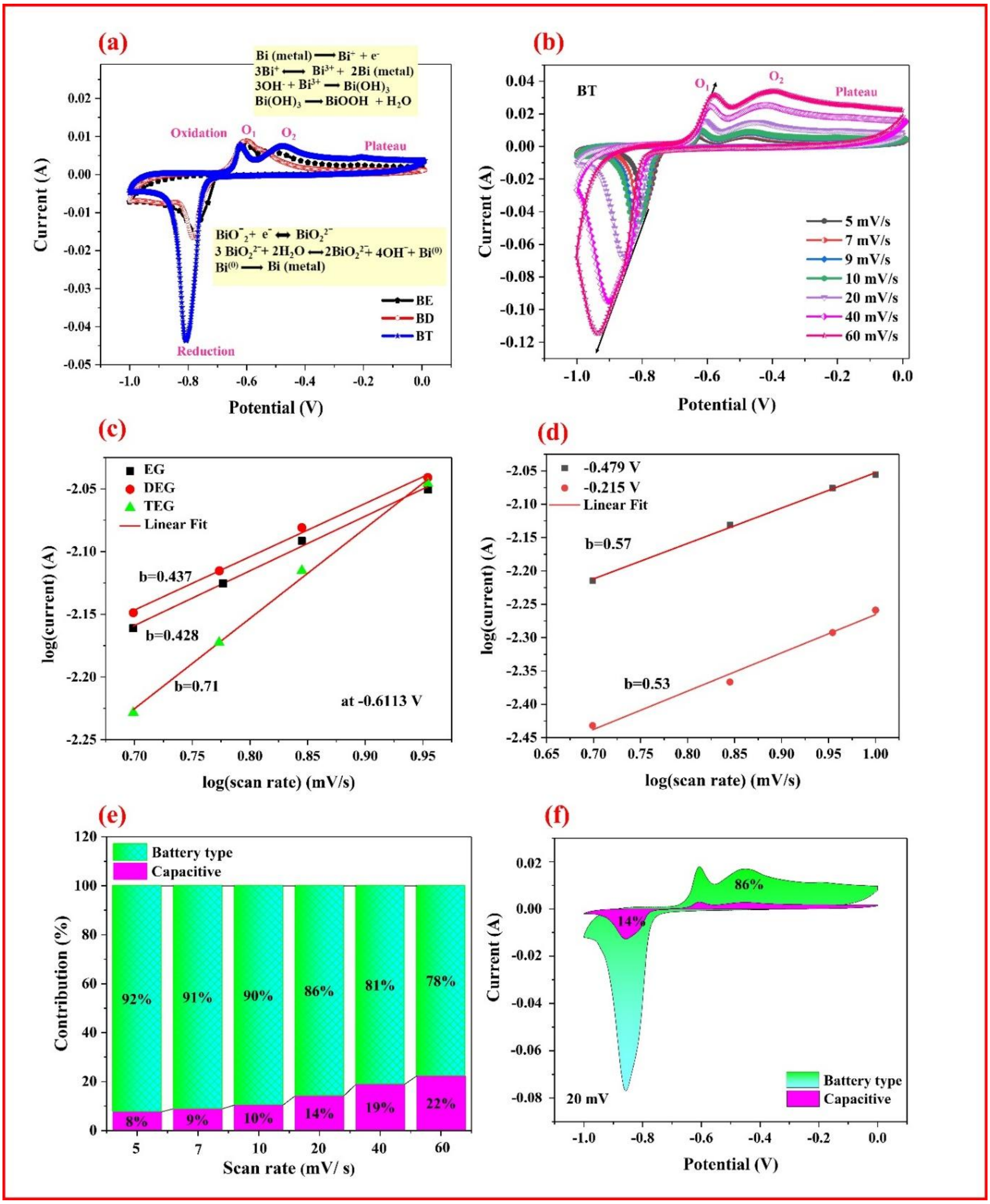

Figure 6.7. (a) CV curvatures of BE, BD, and BT samples at 5 mV/s scanning rate. (b) CV curvature of BT electrode at altered scanning rates. (c) Linear fit of BE, BD, and BT electrodes using log(current) vs log(scan rate) plot. (d) Linear fit of BT electrode at -0.479 and -0.215 V constant potential. (e) Separation of capacitive and battery type behavior of BT electrode at different scanning rates. (f) Battery type and capacitive behavior visualization in CV curve at 20 mV/s scan rate.

Firstly, BiOCl prepared in TEG solvent (BT) exhibits improved crystallinity and a well-organized morphology, leading to a higher surface area, as confirmed by XRD, FESEM, and BET analyses. These characteristics facilitate better accessibility of electrolyte ions to a larger portion of the crystal structure, thereby increasing the involvement of active sites in faradaic reactions and enhancing supercapacitive behavior. Additionally, to evaluate the influence of scan rate on the BT sample's performance, CV studies were conducted at various rates (ranging from 5 to 60 mV/s) while maintaining a constant potential range (see Figure 6.7(b)). Interestingly, the peak current and area under the curve in CV demonstrate a linear increase with the scanning rate. This observation underscores the high-power ability and reversibility of the BT material throughout the testing process. Additionally, we also examine the energy storage mechanism in our study to figure out various factors, which are responsible for the outstanding rate performance of BT sample. The CV profiles of the BT electrode are the backbone of this investigation. CV curves demonstrate a consistent shape with the redox peaks steadily shifting toward the opposite direction as the scan rate increases (see Figure 6.7(b)). The primary factor responsible for this shifting phenomenon was a change in the crystallite IR-drop component, which becomes predominant when current values are higher [39]. Moreover, we employ a power law fitting approach to distinguish and describe the charge storage process of prepared samples. The correlation between the ($\log(i)$) and ($\log(v)$) at constant potential explains the charge storage mechanism in prepared BiOCl electrodes. The power law fit can be expressed in equations (6.2) and (6.3), where 'i' represents peak current, 'v' denotes scan rate, and 'b' is a variable (calculated from the slope of equation (6.3)) that varies dynamically. The 'b' equal to 0.5 corresponds to diffusion or battery type behavior predominance, while 'b' equal to 1.0 signifies the dominance of capacitive behavior [40]. Besides, the area where b values fall between 0.5 and 1.0 is considered to represent the boundary between materials that behave capacitively and those that exhibit behavior like battery-type materials [41].

$$i = av^b \tag{6.2}$$

$$\log(i) = \log(a) + b\log(v) \tag{6.3}$$

Based on the calculations presented in Figure 6.7(c), it can be concluded that at a consistent voltage of -0.6113 V, the 'b'-values for BE, BD, and BT electrodes are determined to be 0.428, 0.437, and 0.71, respectively. These results reveal that the storage mechanisms are mainly controlled by battery type for BE and BD electrodes. The obtained 'b' value of 0.71 signifies that the storage process in the BT electrode is a combination of battery type and capacitive processes, suggesting a coupled mechanism. Moreover, at -0.479 and -0.215 V potential BT electrode displays 'b' values equal to 0.57 and 0.53 (see Figure 6.7(d)) respectively, signifying that the energy storage mechanism is diffusion or battery type controlled.

The relative contributions of capacitance and diffusion to the overall current are further investigated through equations (6.4) and (6.5) [42].

$$i_{total} = i_{capacitive} + i_{diffusion} = k_1 v + k_2 v^{1/2} \tag{6.4}$$

To address investigative needs, equation (6.4) can be written as

$$i / v^{1/2} = k_1 v^{1/2} + k_2 \tag{6.5}$$

where, i, $k_1 v^{1/2}$ and k_2 signifies overall current, quantities of capacitive, and diffusive ions (battery-type) respectively at a constant potential. In order to get the values of k_1 and k_2, we plot $i / v^{1/2}$ versus $v^{1/2}$ graph and perform a straight-line fitting. Through this analysis, the values of k_1 and k_2 can be obtained at each potential. This study makes it possible to show clearly how different battery types and capacitive contributions affect the overall current. Figure 6.7(e) illustrates the distribution of battery type and capacitive contributions for the BT electrode. In Figure 6.7(e) the battery type mechanism contribution current at a potential of -0.215 V is shown by the green-cyan area. While the pink shaded area indicates the charge storage is centered on the capacitive mechanism. The fraction of battery type and capacitive current at 20 mV/s scan rate (see Figure 6.7(f)) noticeably indicates that the battery type mechanism is responsible for the majority of the capacitance, rather than the capacitive mechanism.

Figure 6.8(a) illustrates the GCD profiles of the BE, BD, and BT electrodes at a lower current density (CD) of 0.5 A/g within a -1.0 to 0.0 V potential range. The non-symmetrical nature of the GCD profiles indicates that BiOCl has battery-type properties with an internal resistance. The initial portion of each GCD curve exhibits a sharp decline in voltage, a consequence of the internal resistance (IR drop) present in the system. To reduce the large IR drop demonstrated by BiOCl we are currently working on it and exploring methods. Some promising methods include using different solvents during synthesis, creating nanocomposites with polyaniline and polypyrrole conductive polymers, and incorporating reduced graphene oxide [43]. Furthermore, the second region is characterized by an extended voltage plateau, signifying the contribution of faradaic processes in BiOCl [44]. Interestingly, increasing the current density leads to an opposite shift with a shortening of this plateau. This rapid change in the plateau region suggests fast reaction rates (kinetics) associated with the electrochemical conversion (redox reaction) occurring within the BiOCl electrodes [44,45].

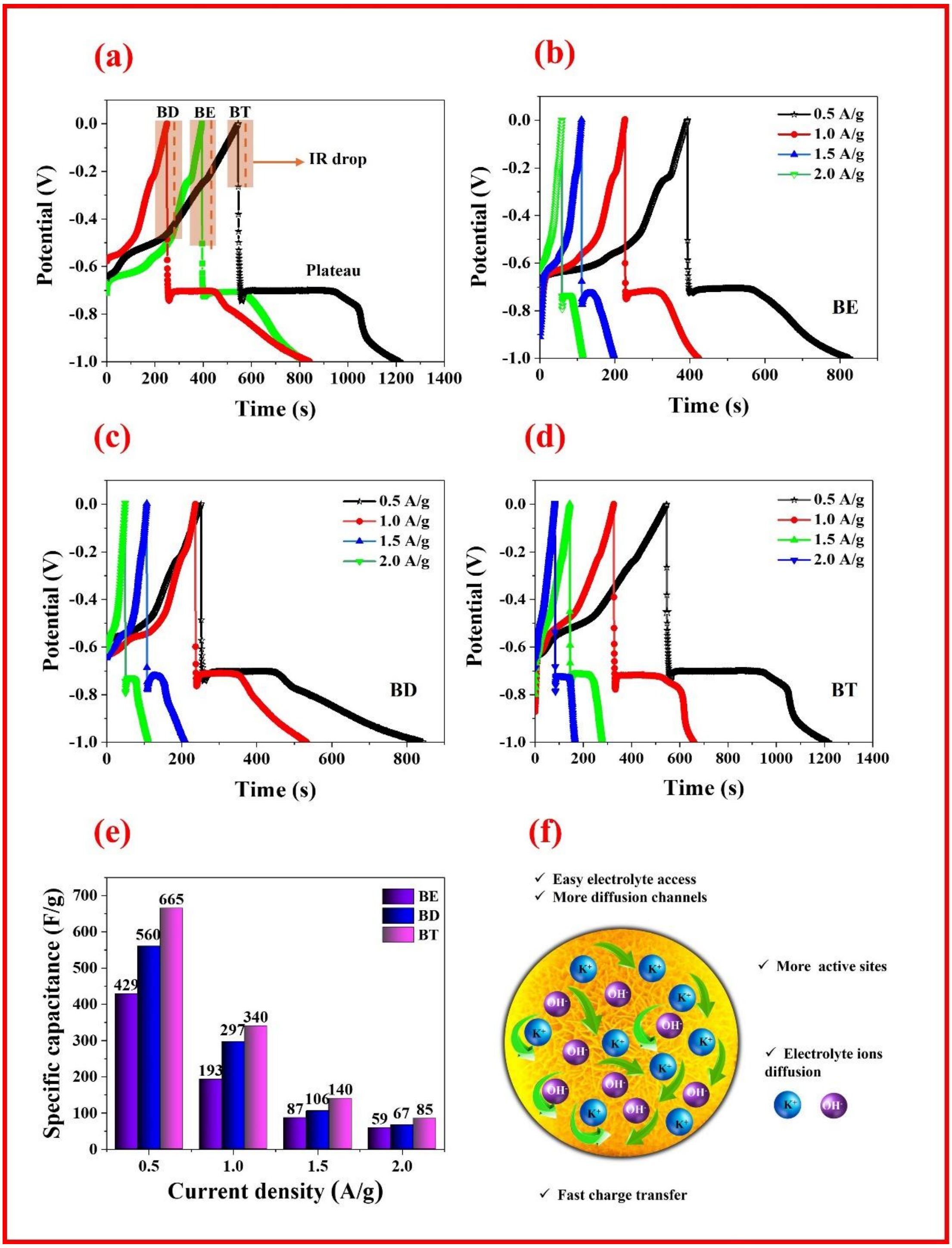

Figure 6.8(a) GCD of BE, BD, and BT electrodes at 0.5 A/g current density. (b-d) GCD of BE, BD, and BT electrodes at altered CDs. (e) Specific capacitance values of BE, BD, and BT electrodes. (f) Supportive properties of BT electrodes in KOH electrolyte.

From Figure 6.8(a), it is observed that (i) IR drop in the BE electrode is notably large, indicating a need for substantial efforts to address this issue in order to enhance overall performance. (ii) In contrast, the BT electrode exhibits a considerably lower IR drop and an extended charging/discharging duration compared to both the BE and BD electrodes. This lower IR drop of the BT electrode is supported by its favorable conductivity and improved ion mobility. These features facilitate efficient charge transfer and rapid ion diffusion, thus improving the electrode's efficacy in energy storage. The specific capacitance values of 429, 560, and 665 F/g were calculated using equation (6.6) at a lower CD of 0.5 A/g for the BE, BD, and BT electrodes, respectively [46].

$$C_{sp} = \frac{it}{mV} \tag{6.6}$$

Where, C_{sp}, t, V, m and i symbols denote the specific capacitance (F/g), discharging time, potential window, mass loaded on the electrode, and response current respectively of different electrodes.

Figure 6.8(b-d) demonstrates the GCD curve at altered CDs. The GCD curves reveal a rise in IR drop with increasing CDs. This behavior aligns with Ohm's law, where voltage is directly proportional to current. Consequently, a higher CD translates to a greater voltage drop due to the inherent resistance within the electrode material. Moreover, Figure 6.8(e) shows the computed specific capacitance for prepared electrodes at various CDs. The specific capacitance of the prepared electrodes exhibits an inverse relationship with increasing current densities. This reduction in electrochemical performance can be ascribed to constraints on ion diffusion within the electrode material when charging rates increase rapidly. The Marigold flower-like BiOCl nanostructure (see Figure 6.8(f)) displays several features that are ideal for electrochemical energy storage. Its wide-open nanosheets provide open access for electrolytes, while the numerous diffusion channels facilitate ion movement throughout the material. Additionally, the abundant active sites promote rapid electron transfer, further enhancing the electrode's performance.

Nyquist plots of BE, BD, and BT samples (see Figure 6.9(a)) can serve as a beneficial tool for assessing electrode conductivity and kinetics. Insight into various electrochemical system parameters can be gleaned from different features of the impedance plot. For instance, at high frequencies, the semicircle diameter offers an estimate of the charge transfer resistance (Rct), while the x-axis intercept aids in determining the series resistance (Ro) of the system (see Figure 6.9(a)) [47]. Additionally, analyzing the slope at low frequencies assists in identifying diffusion resistance. Through this analysis, the Ro for BE, BD, and BT electrodes was calculated to be 0.82, 0.73, and 0.65 Ω, respectively. Similarly, the Rct for BE, BD, and BT electrodes was determined as 1.5, 0.8, and 0.4 Ω, respectively.

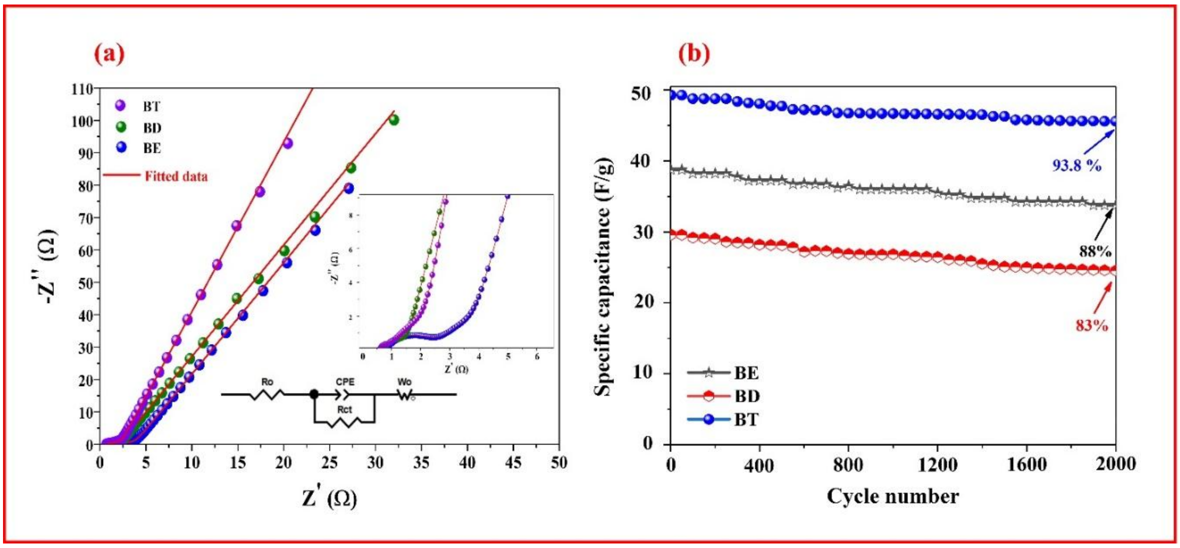

Figure 6.9. (a) Nyquist plot. (b) Stability test for BE, BD, and BT electrodes.

The comparatively lower values of Ro and Rct for BT electrodes, as opposed to BD and BE electrodes, underscore a higher conductivity in the BT electrodes. This characterization further confirms the superior performance of BT electrodes in terms of conductivity and reduced diffusion limitations. In analyzing the practical efficiency of supercapacitor electrodes, cyclic stability is extremely important. The cyclic stability was evaluated via GCD analysis during 2000 cycles under 3 A/g current density. According to Figure 6.9(b), the electrodes BE, BD, and BT have 83%, 88%, and 93.8% retention of their original capacity at the finishing point of the 2000 cycles. Therefore, the overall three-electrode study reveals that BT electrode is a highly beneficial and efficient candidate for supercapacitors in terms of specific capacity, rate competence, and cyclic stability.

6.3.2.1. Fabrication of symmetrical supercapacitor device

To assess the realistic suitability of the BT electrode, we fabricate a symmetric supercapacitor device. In this configuration, the BT electrode acts as both positive and negative electrode, while a Whatman filter paper soaked in 6 M KOH solution serves as a separator. The schematic diagram of the assembled symmetric cell is displayed in Figure 6.10(a). Notably, the CV curve of the BT//BT symmetrical device (see Figure 6.10(b)) shows a larger area under the curve with higher intensity oxidation-reduction peaks as the scan rate was increased from 5 to 60 mV/s. The CV curves maintain their shape without significant distortion as the scan rate increases. This indicates that the charge and ionic transfer are favorable due to the structural and microstructural characteristics of the BT//BT symmetrical device.

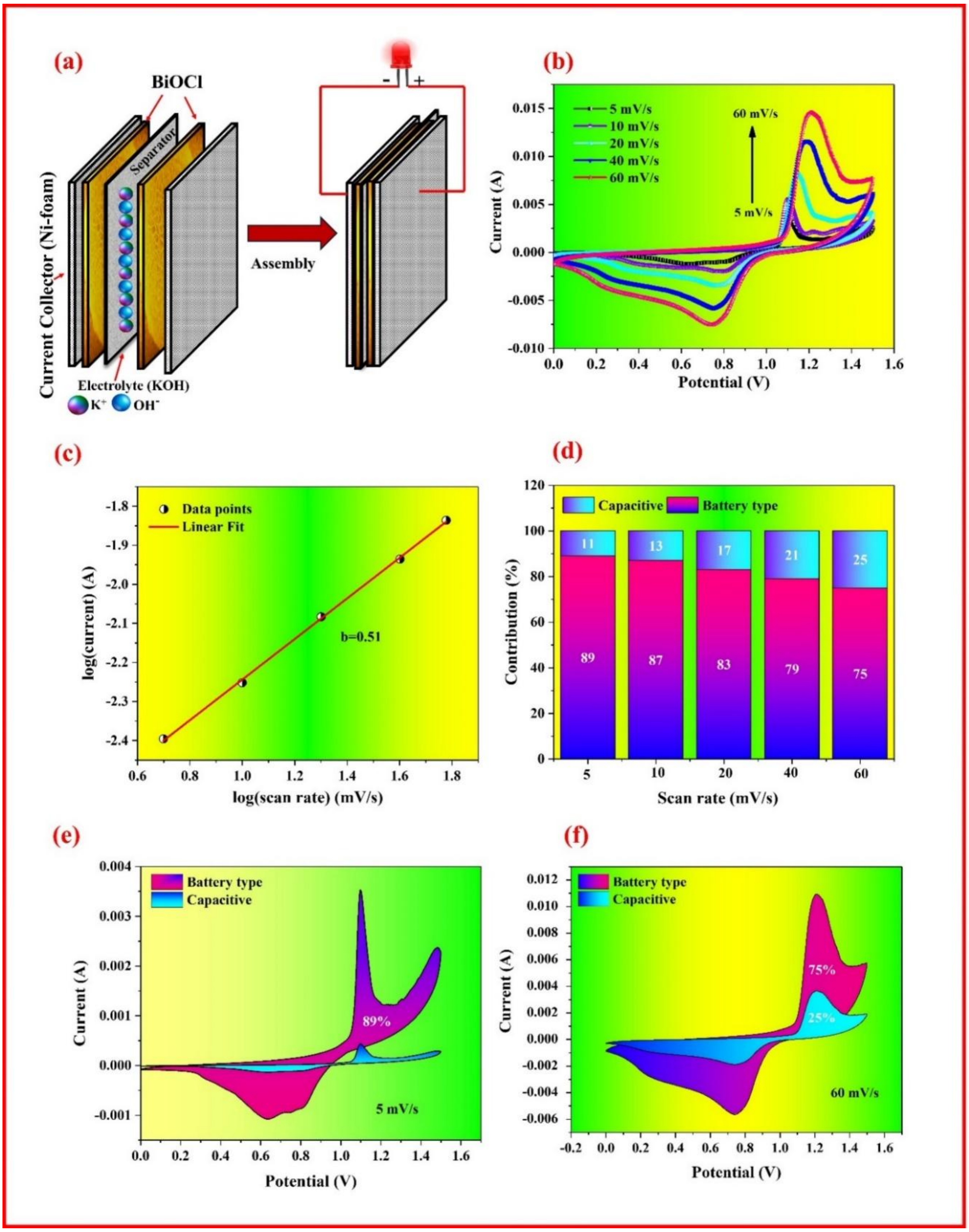

Figure 6.10. (a) Schematic diagram of the assembled symmetric cell (b) CV curves (c) log(peak current vs log(scan rate) (d) Relative contribution of battery type and capacitive behavior (e-f) Separation of battery type (pink-blue color) and capacitive (cyan-blue color) behavior at 5 and 60 mV/s of BT symmetrical device.

The higher oxidation-reduction peaks (see Figure 6.10) of the symmetrical device illustrate the battery-type characteristics of the BiOCl [48]. Furthermore, battery type attributes of the device are also verified by 'b' parameter value and found to be 0.51 (see

Figure 6.10(c)). The pattern of battery type and capacitive contribution at numerous scan rates are shown in Figure 6.10(d). It is noticed that battery type contributes more than capacitive contribution at both scan rates. Figure 6.10 (e-f) displays the partition of battery type (pink-blue color) and capacitive (cyan-blue color) at (e) 5 mV/s, and (f) 60 mV/s. Based on the findings mentioned above, it is evident that in a symmetrical device, a battery type mechanism predominantly contributes at low scan rates, while a smaller amount of capacitive behavior is seen at high scan rates. At low scan rates, the KOH electrolyte ions have ample opportunities to interact with the active electrochemical sites of the electrode, leading to significant charge storage through battery-like processes. Conversely, at high scan rates, limited charge storage occurs primarily through non-faradic or electric double-layer capacitor (EDLC) processes.

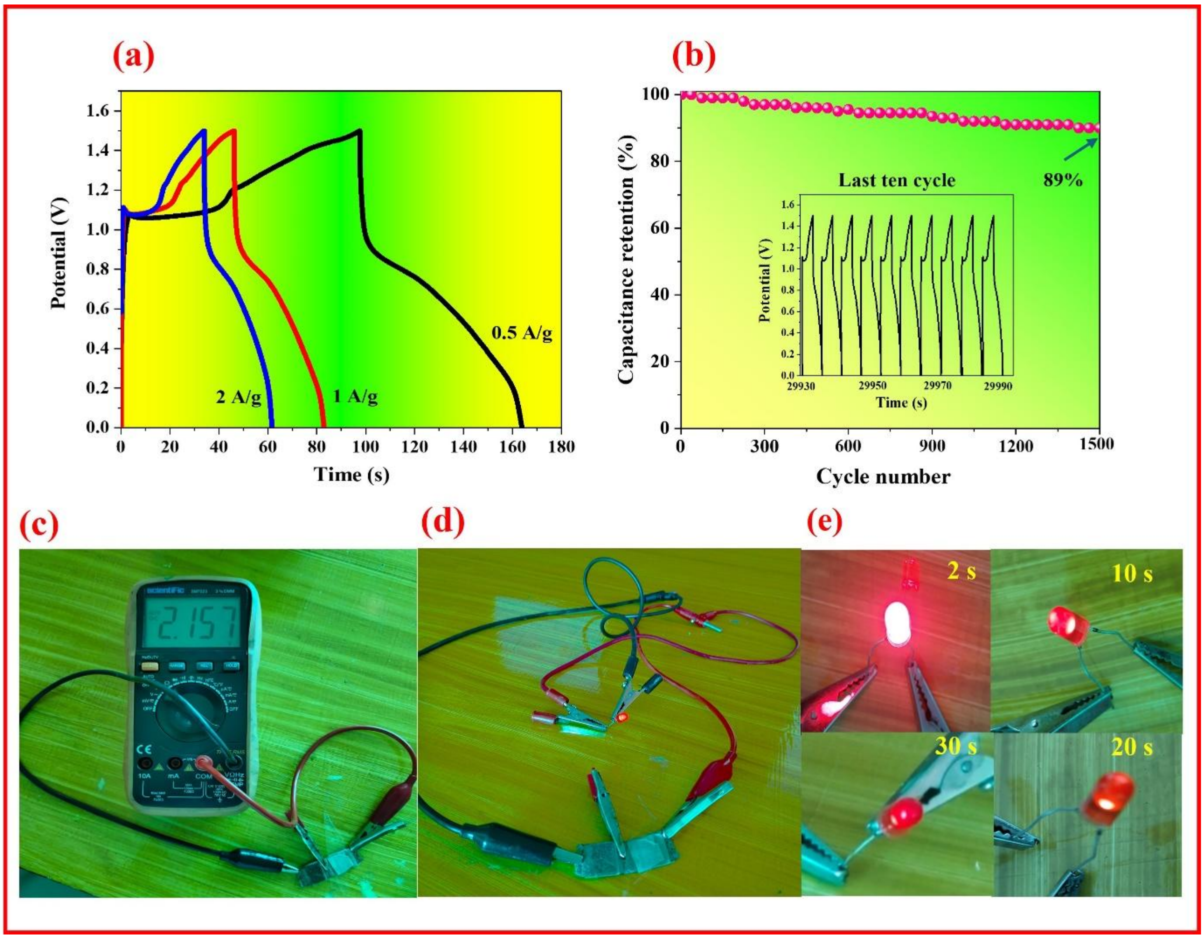

Figure 6.11 (a) GCD curves (b) Cyclic stability test of symmetrical BT//BT fabricated cell (c) After charging of 3V symmetrical supercapacitor cell stable output voltage reading (d-e) Discharging of the symmetrical cell via glowing of a red LED.

The GCD profile of the constructed symmetrical supercapacitor device (see Figure 6.11(a)) displays asymmetric charge and discharge curves, further validating its battery type characteristics. The specific capacitance (C_{cell}) of the complete cell is observed to be 50 F/g at 0.5 A/g. Furthermore, the key factors deciding the efficacy of energy storage devices are *ED* and *PD*. The *ED* and *PD* for the cell can be computed using the (6.7) and (6.8) equations [49-50].

$$ED = \frac{C_{cell} \times \Delta V^2}{7.2}(Wh / kg) \tag{6.7}$$

$$PD = \frac{ED \times 3600}{\Delta t}(W / \mathrm{kg}) \tag{6.8}$$

Where Δt, and ΔV represents discharging time (s) and potential window 1.5 V of the complete cell respectively.

Table 6.2. Comparison of device configuration electrochemical results from previously reported studies.

Electrode material	**Morphology**	**Device configuration**	**Specific capacitance** (F/g)	**ED (Wh/kg)**	**PD (W/kg)**	**References**
Bi_2O_3	Flower-like	Bi_2O_3//graphite	37	11	720	[54]
Bi_2O_3	Flower-like	Bi_2O_3//AC	29	35.4	497.4	[55]
Bi_2O_3	Flower-like	Bi_2O_3//MnO_2	25.2	11.3	3370	[56]
ECNF@Bi_2O_3	Core shell	ECNF@Bi_2O_3//CF@$NiCo_2O_4$	50	25.1	786.2	[57]
BiOCl	Camellia-	BiOCl//AC	124	17.2	250.9	[50]
BiOCl	like	BiOCl//BiOCl	36	12	1125	[58]
BiOCl	Nanoplates	BiOCl / MWCNT// BiOCl /	-----	14.62	947.5	[9]
/MWCNT	Nanoplates	MWCNT				
BiOCl	**Marigold flower-like**	**BT//BT**	**50**	**15.6**	**838**	**Present Work**

The highest ED value for the assembled symmetric device is 15.6 Wh/kg at 838 W/kg of PD. Table 6.2 displays that these results are equivalent, higher, or have lower values than those previously reported for Bi-based and BiOCl supercapacitor devices. The stability of the BT//BT symmetric device was tested through GCD operations. The device exhibits moderate chemical stability (see Figure 6.11(b)) and mechanical strength, as demonstrated by the cycling lifespan test (~89% capacitance retention) after undergoing 1500 cycles at a current density of 3 A/g. Furthermore, two cells were connected in series to confirm the fabricated BT//BT symmetrical supercapacitor device's feasibility. After that, they were charged for 15 s at 3.0 V using a DC battery supply. The device was linked to a multimeter (see Figure 6.11(c)) to confirm a steady output voltage i.e. 2.17 V. It concluded that this voltage was sufficient to light up a red LED (1.5 V). Subsequently, the device was connected to a red LED and discharged through a red LED for around 30 s (see Figure 6.11(d-e)) demonstrating the future potential of marigold flower-like BiOCl in energy storage systems.

6.3.2.2. Proposed charged storage mechanism for symmetrical supercapacitor cell

The observed results and the real demonstration of the device for energy storage application, allow us to propose a mechanism for charge storage. This mechanism can offer a clear understanding of the assembled symmetric cell working based on our consideration. The schematic diagram of the charged storage mechanism for a symmetric supercapacitor cell is illustrated in Figure 6.12.

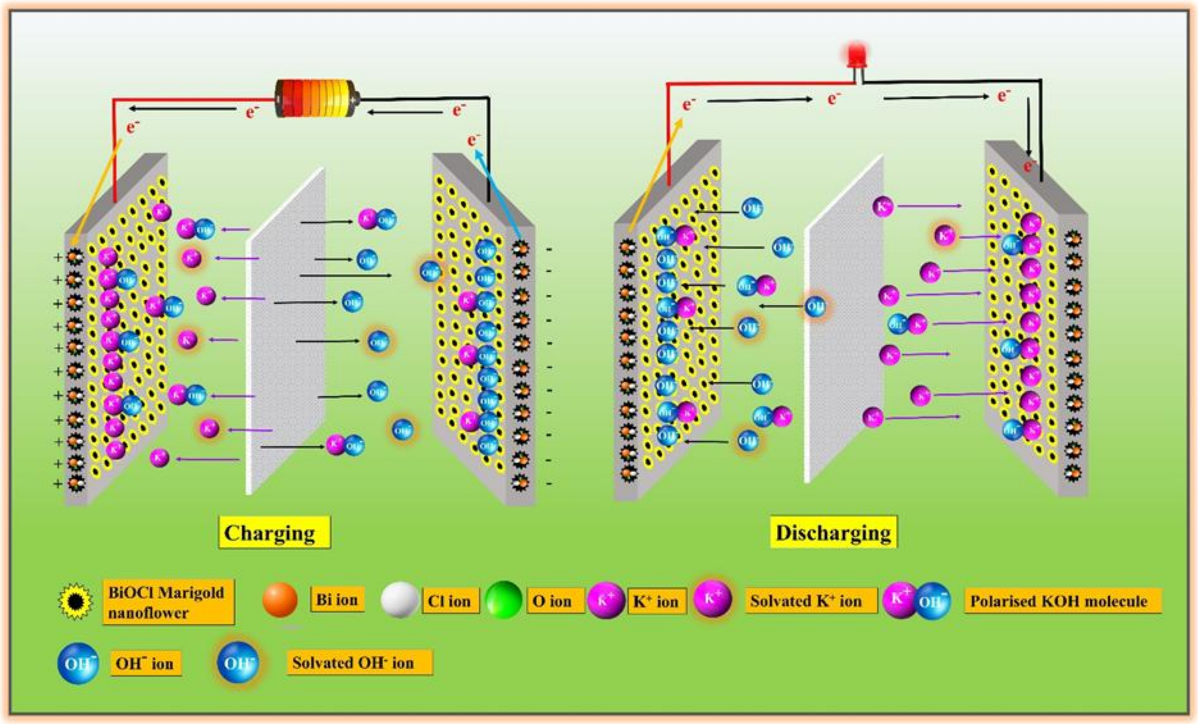

Figure 6.12. Proposed energy storage mechanism of BT//BT symmetrical supercapacitor device.

The electrochemical process while charging and discharging is shown in Figure 6.12. BiOCl mesoporous material is used as the electrode material in the creation of a symmetric device. The material used is a combination of double layer and faradaic redox processes to facilitate charge storage for the symmetric cell. Surface activity of the used material is linked with its capacitive storage nature, whereas internal reactions contribute to its faradic energy storage features [51]. Upon charging, KOH electrolyte undergoes dissociation into potassium (K^+) and hydroxide (OH^-) ions and these ions subsequently migrate to the positive and negative terminals, respectively. At the electrode-electrolyte junction, potassium and hydroxide ions form layers (see Figure 6.12), while some ions diffuse into the BT material to engage in charge storage processes. The reactions occurring at the anode and cathode during the cell's charging cycle are outlined below [52].

At anode:

$$BiOCl + K^{+} + e^{-} \rightarrow BiOClK^{+} \tag{6.9}$$

$$(BiOCl)_{surface} + K^{+} + e^{-} \rightarrow (BiOCl^{-}K^{+})_{surface} \tag{6.10}$$

At cathode:

$$BiOCl + OH^{-} \rightarrow BiOClOH^{-} + e^{-} \tag{6.11}$$

$$(BiOCl)_{surface} + OH^{-} \rightarrow (BiOCl^{+}OH^{-})_{surface} + e^{-} \tag{6.12}$$

In addition to the potassium and hydroxide ions, the region between the oppositely polarised electrodes contains solvated potassium and hydroxide ions, along with polarised potassium hydroxide molecules. This arrangement helps to speed up the charging process. When the cell discharges, it produces a voltage that causes an electric current to flow through an external circuit. This current flow can be seen by connecting a red LED. Discharging is essentially the opposite of charging a cell. In the discharging phase, complete reactions and the motion of entirely dissociated and solvated ions are converse from the charging cycle [53].

6.4. Conclusions

In conclusion, we have synthesized various 3D hierarchical BiOCl nanostructures by using different solvents (EG, DEG, and TEG) in solvothermal methods. The produced 3D hierarchical nanostructure's physical, morphological, electrochemical, and other characteristics were meticulously studied using a range of spectral and analytical techniques. Among all prepared samples, the BT electrode shows a unique marigold flower-like morphology and demonstrates a notable specific capacity of 665 F/g at 0.5 A/g current density. This admirable specific capacitance is ascribed to the high specific surface area of 29.85 m^2/g and the substantial available active site. However, the appearance of surface-active sites, uniform growth, and stable integration of active materials on nickel foam, resulted in low charge transfer resistance and excellent electrical conductivity. These factors also contribute to the lower potential drop examined in GCD, facilitating rapid ion and electron transfer leading to enhanced electrochemical performance of BT electrode. Moreover, the fabricated BT//BT symmetrical device delivers a maximum ED of 15.6 Wh/kg at 838 W/kg PD and shows good cyclic lifespan of ~80% after 1500 cycles. Finally, the device glows up a red LED after charging which indicates that the BT//BT device has elevated capability in practical application. In addition to the fabricated symmetric supercapacitor device, an appropriate charge storage mechanism is proposed. Overall, present work outcomes signify that the TEG solvent could be considered as the better choice for solvothermal synthesis of BiOCl instead of EG and DEG solvents for enhanced electrochemical performance.

References

[1] Sharma K, Arora A, Tripathi SK. Review of supercapacitors: Materials and devices. Journal of Energy Storage. 2019;21:801-25.

[2] Akir S, Fomekong RL, Chacko L, Děkanovský L, Mazánek V, Sturala J, Koňáková D, Sofer Z. Nanoengineering bismuth-modified vanadium carbide MXene for enhanced electrochemical performance in neutral electrolyte: A pathway toward high-performance supercapacitors. Journal of Energy Storage. 2024;85:110962.

[3] Danamah HM, Shaikh ZA, Al-Hejri TM, Siddiqui TA, Jadhav VV, Mane RS. Conversion of the Bi_2O_3 to Bi_2S_3: An ion exchange strategy for tailoring the surface morphology with accrued energy storage performance. Journal of Energy Storage. 2024;78:109820.

[4] Gujar TP, Shinde VR, Lokhande CD, Han SH. Electrosynthesis of Bi_2O_3 thin films and their use in electrochemical supercapacitors. Journal of power sources. 2006;161(2):1479-85.

[5] Ma XJ, Zhang WB, Kong LB, Luo YC, Kang L. β-Bi_2O_3: an underlying negative electrode material obeyed electrode potential over electrochemical energy storage device. Electrochimica Acta. 2016;192:45-51.

[6] Zhang Y, Xu Z, Wang Q, Hao W, Zhai X, Fei X, Huang X, Bi Y. Unveiling the activity origin of ultrathin BiOCl nanosheets for photocatalytic CO_2 reduction. Applied Catalysis B: Environmental. 2021;299:120679.

[7] Yang Z, Wang D, Zhang Y, Feng Z, Liu L, Wang W. Photoreductive BiOCl ultrathin nanosheets for highly efficient photocatalytic color switching. ACS applied materials & interfaces. 2020;12(7):8604-13.

[8] Liu WW, Peng RF. Recent advances of bismuth oxychloride photocatalytic material: Property, preparation and performance enhancement. Journal of Electronic Science and Technology. 2020;18(2):100020.

[9] Dutta S, Pal S, Sikder D, De S. Light-weight flexible solid-state supercapacitor based on highly crystalline 2D BiOCl nanoplates/MWCNT nanocomposites. Journal of Alloys and Compounds. 2020;820:153115.

[10] Shankar VU, Kumar PS, Govindarajan D, Vinoth Kumar P, Suganya P, Rangasamy G. Design and Construction of rGO/$NiMoO_4$ and FeOCl/BiOCl Utilised as a Positive and Negative Electrode for Asymmetric Capacitance. Journal of Inorganic and Organometallic Polymers and Materials. 2023;33(11):3551-64.

[11] Gao X, Guo Q, Tang G, Zhu W, Luo Y. Controllable synthesis of solar-light-driven BiOCl nanostructures for highly efficient photocatalytic degradation of carbamazepine. Journal of Solid State Chemistry. 2019;277:133-8.

[12] Zhu LP, Liao GH, Bing NC, Wang LL, Yang Y, Xie HY. Self-assembled 3D BiOCl hierarchitectures: tunable synthesis and characterization. CrystEngComm. 2010;12(11):3791-6.

[13] Sharma S, Acharya AD, Thakur YS, Bhawna. Controlled synthesis of hierarchical BiOCl nanostructure with exposed {010} facets to yield enhanced photocatalytic performance for PMMA deterioration. Journal of Polymer Research. 2022;29(11):466.

[14] Wei X, Akbar MU, Raza A, Li G. A review on bismuth oxyhalide based materials for photocatalysis. Nanoscale Advances. 2021;3(12):3353-72.

[15] Zhang X, Ai Z, Jia F, Zhang L. Generalized one-pot synthesis, characterization, and photocatalytic activity of hierarchical BiOX (X= Cl, Br, I) nanoplate microspheres. The Journal of Physical Chemistry C. 2008;112(3):747-53.

[16] Wang DH, Gao GQ, Zhang YW, Zhou LS, Xu AW, Chen W. Nanosheet-constructed porous BiOCl with dominant {001} facets for superior photosensitized degradation. Nanoscale. 2012;4(24):7780-5.

[17] Datta S, Mahin J, Liberti E, Manasi I, Edler KJ, Torrente-Murciano L. Role of the Deep Eutectic Solvent Reline in the Synthesis of Gold Nanoparticles. ACS Sustainable Chemistry & Engineering. 2023;11(28):10242-51.

[18] Yadav MS. Synthesis and characterization of $Mn_2O_3-Mn_3O_4$ nanoparticles and activated charcoal based nanocomposite for supercapacitor electrode application. Journal of Energy Storage. 2020;27:101079.

[19] Rosbottom I, Ma CY, Turner TD, O'connell RA, Loughrey J, Sadiq G, Davey RJ, Roberts KJ. Influence of solvent composition on the crystal morphology and structure of p-aminobenzoic acid crystallized from mixed ethanol and nitromethane solutions. Crystal Growth & Design. 2017;17(8):4151-61.

[20] Chen H, Ma X, Shen PK. $NiCo_2S_4$ nanocores in-situ encapsulated in graphene sheets as anode materials for lithium-ion batteries. Chemical Engineering Journal. 2019;364:167-76.

[21] Gao X, Peng W, Tang G, Guo Q, Luo Y. Highly efficient and visible-light-driven BiOCl for photocatalytic degradation of carbamazepine. Journal of Alloys and Compounds. 2018 15;757:455-65.

[22] Zou Z, Xu H, Li D, Sun J, Xia D. Facile preparation and photocatalytic activity of oxygen vacancy rich BiOCl with {0 0 1} exposed reactive facets. Applied Surface Science. 2019;463:1011-8.

[23] Song JM, Mao CJ, Niu HL, Shen YH, Zhang SY. Hierarchical structured bismuth oxychlorides: self-assembly from nanoplates to nanoflowers via a solvothermal route and their photocatalytic properties. CrystEngComm. 2010;12(11):3875-81.

[24] Dong W, Xie T, Wu Z, Peng H, Ren H, Meng F, Lin H. Oxygen-vacancy-rich BiOCl materials with ultrahigh photocatalytic efficiency by etching bismuth glass. RSC advances. 2021;11(61):38894-906.

[25] Samreen Naz GS, Soundarya TL, Nagaraju G, RajaNaika H. Facile synthesis of BiOCl NPs for methylene blue removal, antibacterial with novel antifungal properties against Fusarium oxysporum, and enhanced germination of Solanum lycopersicum L. seeds. Environment, Development and Sustainability. 2024:1-23.

[26] Wu Z, Li Z, Wu M, Shen J, Feng W, Li X, Xu D, Zhang S, Ma N. Defective BiO_2-x/BiOCl porous ultrathin nanosheets for efficient solar-light-driven photoreduction of Cr (VI). Materials Science in Semiconductor Processing. 2021;128:105781.

[27] Liu Z, Peng S, Xie Q, Hu Z, Yang Y, Zhang S, Qian Y. Large-Scale Synthesis of Ultralong Bi_2S_3 Nanoribbons via a Solvothermal Process. Advanced Materials. 2003;15(11):936-40.

[28] Liu Z, Liang J, Li S, Peng S, Qian Y. Synthesis and growth mechanism of Bi_2S_3 nanoribbons. Chemistry–A European Journal. 2004;10(3):634-40.

[29] Wang Y, Jiang X, Xia Y. A solution-phase, precursor route to polycrystalline SnO_2 nanowires that can be used for gas sensing under ambient conditions. Journal of the American Chemical Society. 2003;125(52):16176-7.

[30] Cao AM, Hu JS, Liang HP, Wan LJ. Self-assembled vanadium pentoxide (V_2O_5) hollow microspheres from nanorods and their application in lithium-Ion batteries. Angewandte Chemie International Edition. 2005;44(28):4391-5.

[31] Zhong LS, Hu JS, Liang HP, Cao AM, Song WG, Wan LJ. Self-Assembled 3D flowerlike iron oxide nanostructures and their application in water treatment. Advanced materials. 2006;18(18):2426-31.

[32] Duan F, Zheng Y, Liu L, Chen M, Xie Y. Synthesis and photocatalytic behaviour of 3D flowerlike bismuth oxide formate architectures. Materials letters. 2010;64(14):1566-9.

[33] Ma D, Huang S, Chen W, Hu S, Shi F, Fan K. Self-assembled three-dimensional hierarchical umbilicate Bi_2WO_6 microspheres from nanoplates: controlled synthesis, photocatalytic activities, and wettability. The Journal of Physical Chemistry C. 2009;113(11):4369-74.

[34] Zhou YX, Yao HB, Zhang Q, Gong JY, Liu SJ, Yu SH. Hierarchical $FeWO_4$ microcrystals: solvothermal synthesis and their photocatalytic and magnetic properties. Inorganic Chemistry. 2009;48(3):1082-90.

[35] Xiong J, Cheng G, Lu Z, Tang J, Yu X, Chen R. BiOCOOH hierarchical nanostructures: Shape-controlled solvothermal synthesis and photocatalytic degradation performances. CrystEngComm. 2011;13(7):2381-90.

[36] Vivier V, Régis A, Sagon G, Nedelec JY, Yu LT, Cachet-Vivier C. Cyclic voltammetry study of bismuth oxide Bi_2O_3 powder by means of a cavity microelectrode coupled with Raman microspectrometry. Electrochimica Acta. 2001;46(6):907-14.

[37] Samdani KJ, Park JH, Joh DW, Lee KT. Self-assembled Bi_2MoO_6 nanopetal array on carbon spheres toward enhanced supercapacitor performance. ACS sustainable chemistry & engineering. 2018;6(12):16702-12.

[38] Senthilkumar B, Selvan RK, Vasylechko L, Minakshi M. Synthesis, crystal structure and pseudocapacitor electrode properties of γ-Bi_2MoO_6 nanoplates. Solid state sciences. 2014;35:18-27.

[39] Shameem A, Devendran P, Siva V, Murugan A, Sasikumar S, Nallamuthu N, Hussain S, Bahadur SA. Robust one-step synthesis of bismuth molybdate nanocomposites: A promising negative electrode for high end ultracapacitors. Solid State Sciences. 2020;106:106303.

[40] Wang X, Li H, Li H, Lin S, Bai J, Dai J, Liang C, Zhu X, Sun Y, Dou S. Heterostructures of Ni–Co–Al layered double hydroxide assembled on V_4C_3 MXene for high-energy hybrid supercapacitors. Journal of materials chemistry A. 2019;7(5):2291-300.

[41] Wang S, Shao Y, Liu W, Wu Y, Hao X. Elastic sandwich-type GaN/MnO 2/MnON composites for flexible supercapacitors with high energy density. Journal of Materials Chemistry A. 2018;6(27):13215-24.

[42] Javed MS, Najam T, Sajjad M, Shah SS, Hussain I, Idrees M, Imran M, Assiri MA, Siyal SH. Design and fabrication of highly porous 2D bimetallic sulfide ZnS/FeS composite nanosheets as an advanced negative electrode material for supercapacitors. Energy & Fuels. 2021;35(18):15185-91.

[43] Mohd Tarmizi EZ, Baqiah H, Talib ZA. Facile synthesis and characterizations of polypyrrole/BiOCl hybrid composites. Journal of Solid State Electrochemistry. 2017;21:3247-55.

[44] Shinde NM, Xia QX, Yun JM, Mane RS, Kim KH. Polycrystalline and mesoporous 3-D Bi_2O_3 nanostructured negatrodes for high-energy and power-asymmetric supercapacitors: superfast room-temperature direct wet chemical growth. ACS applied materials & interfaces. 2018 Feb 27;10(13):11037-47.

[45] Shinde PV, Shinde NM, Yun JM, Mane RS, Kim KH. Facile chemical synthesis and potential supercapattery energy storage application of hydrangea-type Bi2MoO6. ACS omega. 2019;4(6):11093-102.

[46] Thakur YS, Acharya AD, Sharma S, Bisoyi S. Enhanced electrochemical performance of in situ polymerized V_2O_5-PANI nanocomposites and its practical application confirmation by assembling ionic liquid as well as solid state-based supercapacitor device. Results in Chemistry. 2024;7:101259.

[47] Ning J, Xia M, Wang D, Feng X, Zhou H, Zhang J, Hao Y. Superior pseudocapacitive storage of a novel Ni_3Si_2/NiOOH/graphene nanostructure for an all-solid-state supercapacitor. Nano-Micro Letters. 2021;13:1-4.

[48] Thakur YS, Acharya AD, Sharma S, Bisoyi S, Manhas SS. Synthesis of 3D rice-like BiOCl battery-type electrode material and evaluation of their electrochemical performance in a symmetrical supercapacitor device configuration. Materials Science in Semiconductor Processing. 2024;177:108376.

[49] Deng H, Huang J, Hu Z, Chen X, Huang D, Jin T. Fabrication of a three-dimensionally networked MoO_3/PPy/rGO composite for a high-performance symmetric supercapacitor. ACS omega. 2021 ;6(14):9426-32.

[50] Hong W, Wang L, Liu K, Han X, Zhou Y, Gao P, Ding R, Liu E. Asymmetric supercapacitor constructed by self-assembled camellia-like BiOCl and activated carbon microspheres derived from sweet potato starch. Journal of Alloys and Compounds. 2018;746:292-300.

[51] Arya A, Iqbal M, Tanwar S, Sharma A, Sharma AL, Kumar V. Mesoporous carbon/titanium dioxide composite as an electrode for symmetric/asymmetric solid-state supercapacitors. Materials Science and Engineering: B. 2022;285:115972.

[52] Shen B, Guo R, Lang J, Liu L, Liu L, Yan X. A high-temperature flexible supercapacitor based on pseudocapacitive behavior of FeOOH in an ionic liquid electrolyte. Journal of materials chemistry A. 2016; 4(21):8316-27.

[53] Tanwar S, Singh N, Sharma AL. High-performance different shape carbon decorated asteroidea-like cobalt diselenide electrode for energy storage device. Fuel. 2022;330:125602.

[54] Shinde NM, Xia QX, Yun JM, Singh S, Mane RS, Kim KH. A binder-free wet chemical synthesis approach to decorate nanoflowers of bismuth oxide on Ni-foam for fabricating laboratory scale potential pencil-type asymmetric supercapacitor device. Dalton Transactions. 2017;46(20):6601-11.

[55] Senthilkumar ST, Selvan RK, Ulaganathan M, Melo JS. Fabrication of Bi_2O_3|| AC asymmetric supercapacitor with redox additive aqueous electrolyte and its improved electrochemical performances. Electrochimica Acta. 2014;115:518-24.

[56] Xu H, Hu X, Yang H, Sun Y, Hu C, Huang Y. Flexible asymmetric micro-supercapacitors based on Bi_2O_3 and MnO_2 nanoflowers: larger areal mass promises higher energy density. Advanced Energy Materials. 2015;5(6):1401882.

[57] Li L, Zhang X, Zhang Z, Zhang M, Cong L, Pan Y, Lin S. A bismuth oxide nanosheet-coated electrospun carbon nanofiber film: a free-standing negative electrode for flexible asymmetric supercapacitors. Journal of materials chemistry A. 2016;4(42):16635-44.

[58] Shinde NM, Ghule BG, Raut SD, Narwade SH, Pak JJ, Mane RS. Hopping electrochemical supercapacitor performance of ultrathin BiOCl petals grown by a room-temperature soft-chemical process. Energy & Fuels. 2021;35(8):6892-7.

Chapter 7

Doubling up the Electrochemical Performance of 3D Hierarchical BiOCl Electrode through Optimized Polypyrrole Doping for Supercapacitors Application

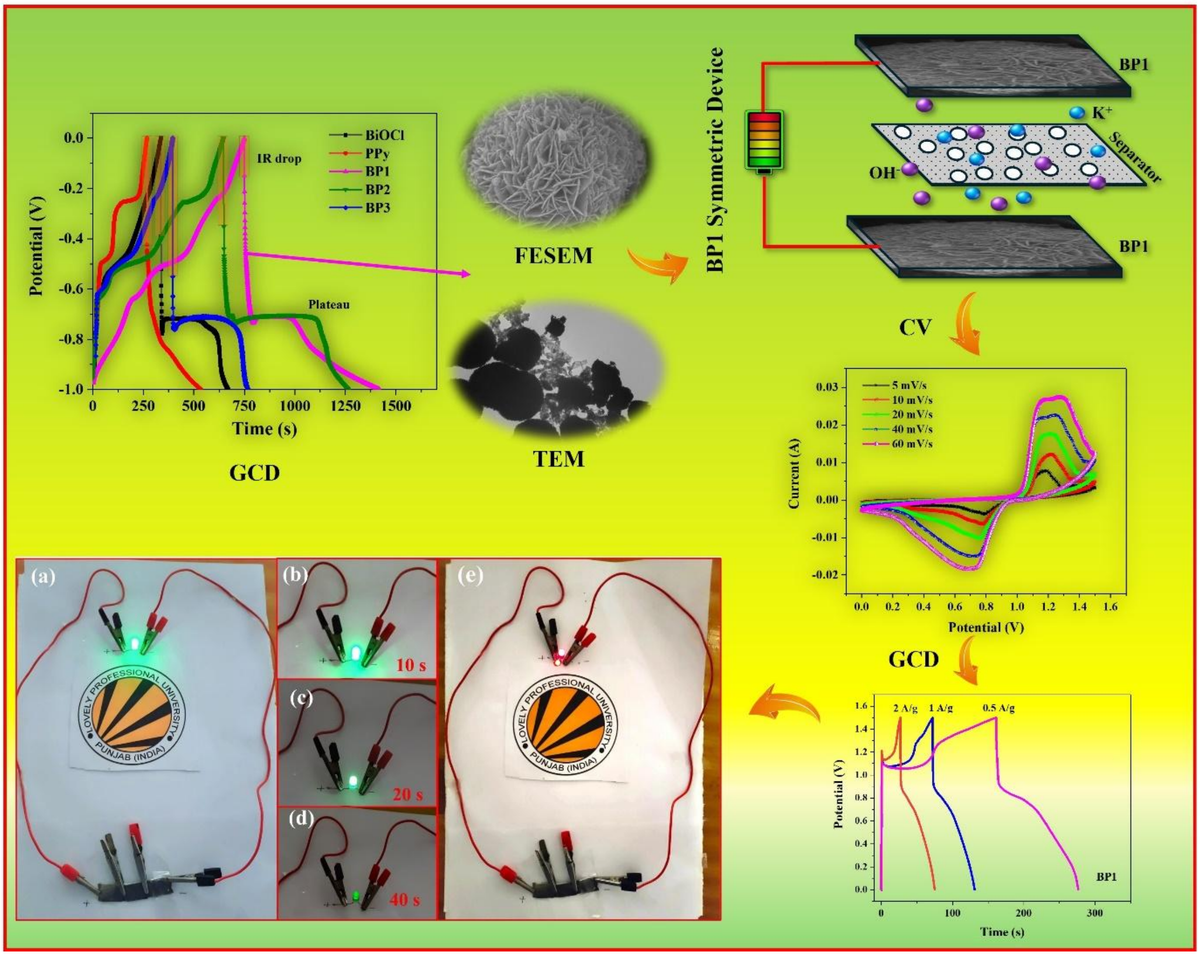

In this chapter, 3D porous PPy-BiOCl (wt.% of PPy 5,7, and 9) nanocomposites were prepared via a physical blending technique that serves as electrode material for supercapacitor technology. The prepared BP1 (5 wt.%) nanocomposite supported on nickel foam textile exhibits high oxidation reduction peaks suggesting the battery-type charge storage ability of nanocomposite in 6 M potassium hydroxide aqueous electrolyte solution. The dominance of the battery-type charge storage mechanism of the BP1 electrode was confirmed through the cyclic voltammetry study. Furthermore, the galvanometric charge-discharge study revealed a good specific capacity of 659 F/g at 1.0 A/g current density. In the presence of a 6 M potassium hydroxide electrolyte, a symmetric cell was constructed with two similar 3D porous BP1 electrodes. This configuration unveiled an impressive energy density (ED) of 24.0 Wh/kg at 750.0 W/kg power density (PD). To illustrate its practical viability, two BP1//BP1 symmetric devices were connected in series, successfully powering a green and red LED for approximately 50 s with good light intensity. This underscores the practical potential of the BP1 electrode in energy storage systems.

7.1. Introduction

The sustained rise in energy demand has led to an increased load on the utilization of common energy resources such as fossil fuels and coal. However, this escalating demand has also stimulated the growth of renewable energy resources. Therefore, among different energy storage devices, supercapacitor stands out as an encouraging energy storage device, primarily owing to its extensive array of applications. It offers several desirable advantages, including large PD, high ED, excellent rate stability, and less expensive [1–4]. Generally, supercapacitors are characterized into two main types known as pseudocapacitors and electric double-layer capacitors (EDLCs) depending on their distinct charge storage process [5]. For fabrication of a supercapacitor, the main factor influencing its performance is the electrode material [6], which relies significantly on both positive and negative electrode materials (potential window >0 vs saturated calomel electrode (SCE) for positive and <-0.1 vs SCE for negative electrode), as each plays a key function in the process [7]. Therefore, there has been extensive research on synthesizing electrode materials using facile and economical techniques. In recent years, research efforts have primarily focused on pinpointing high-performance positive electrode materials for supercapacitors. Notably, researchers have identified efficient contenders for positive electrodes such as spinel oxides ($CuCo_2O_4$ and $MnCo_2O_4$) and metal sulfides (SnS_2 and MoS_2) [8–13]. However, there has been a lack of importance given to negative electrode materials despite their significant role in enhancing the performance of supercapacitors [14]. So far, only a limited number of materials have been utilized for the negative electrodes namely carbon/graphene, vanadium oxides (V_2O_5 and VO_2), bimetallic sulfides (ZnS/FeS), iron oxides (Fe_2O_3 and Fe_3O_4) and bismuth-based material (Bi_2O_3, Bi_2S_3, Bi_2MoO_6) [15–19]. Among various negative electrodes, bismuth-based materials are known for their natural inclination towards forming 2D nanosheet structures, owing to their layered crystalline arrangement. However, with the aid of suitable surfactants, these materials can be orchestrated into 3D hierarchical microspheres. Contrasting 2D nanosheets, these 3D nanostructures offer promising avenues for practical utilization. This is attributed to their inherent characteristics such as large surface area, strong interface connection between electrolytes and electrodes, and shortened diffusion paths for electrolyte ions. These features are crucial for attaining superior energy and power storage capabilities [20]. Wang et al. utilized a solvothermal technique to synthesize a composite of graphene and Bi_2O_3, demonstrating remarkable rate capability, reversibility, and a capacitance of 757 F/g [21]. Shinde et al. synthesized a 3D nanostructured Bi_2O_3 material and utilized it as the negative electrode in an asymmetrical supercapacitor, resulting in a large ED of 51 Wh/kg at a PD of 1500 W/kg [22].

Among the family of bismuth-based oxides, BiOCl shows its influence due to its tetragonal lamellar layered structure. This structure consists of stacked [Cl–Bi–O–Bi–Cl] sheets, held closely via van der Waals interactions, specifically through chlorine (Cl) atoms across the c-axis which provides multi-electron transfer capabilities during electrochemical reactions with wide negative potential window [23,24]. Shinde et al. successfully fabricated ultrathin petal-type BiOCl electrode material and investigated its electrochemical performance in a potassium hydroxide electrolyte. In a three-electrode configuration, the BiOCl petal-type electrode exhibited a notable capacitance of 379 F/g at a current density (CD) of 1.25 A/g. This impressive performance was accredited to the material's good conduction and minimized diffusion length [23]. Chen et al. utilized BiOCl as an anode material in an aqueous rechargeable battery, while utilizing silver as the cathode in a NaCl electrolyte solution. Their investigation revealed a consistent and stable energy storage capability in this configuration [24]. To enhance the future potential of BiOCl, efforts could be directed towards addressing the challenge of potential drop. This could involve developing nanocomposites of BiOCl integrated with conductive material to improve its overall performance. In this regard, polypyrrole (PPy) would be a better choice as a dopant material for supercapacitors because of its excellent electrical conduction and larger specific capacitance [25]. Feng et al. synthesized nickel dicobalt tetrasulfide nanoneedles on nickel foam using a two-step hydrothermal approach. They then applied a layer of polypyrrole onto these nanoneedles through in-situ polymerization. The resulting nickel dicobalt tetrasulfide composite was tested for its supercapacitor performance, showing a huge specific capacitance of 1842.8 F/g at 1 A/g of CD. When used in an asymmetric supercapacitor device with activated carbon as the negative electrode and nickel dicobalt tetrasulfide -polypyrrole as the positive electrode, it achieved an ED of 41.2 Wh/kg at a PD of 402.2 W/kg and maintained admirable cycling lifespan, with 92.8% of its initial capacitance after 5000 charge-discharge cycles [4]. By integrating polypyrrole into BiOCl, the resulting material can effectively mitigate the challenge of potential drop, thereby enhancing the complete performance of BiOCl-based supercapacitors.

In the current research work, PPy-BiOCl was fabricated by the physical blending technique. The supercapacitive characteristics of the fabricated PPy-BiOCl nanocomposites were studied in a 6 M KOH electrolyte after being deposited onto a nickel foam substrate. To the best of our knowledge, this is the first report studying the supercapacitive performance of PPy-BiOCl nanocomposites as electrode material for energy storage applications. Optimal morphological and supercapacitive performances of electrodes have been also achieved by varying the wt.% of PPy in the BiOCl. Furthermore, the symmetric supercapacitor device constructed from PPy-BiOCl material showcases remarkable electrochemical performance. Notably, the practical feasibility of this device is demonstrated by glowing a green and red LED, which signifies its suitability in energy storage systems.

7.2. Experimental Procedures

7.2.1. Synthesis of BiOCl nanoparticles

A one-step solvothermal method was used to synthesize BiOCl 3D hierarchical nanostructure via triethylene glycol (TEG) solvent. In the synthesis method 1.458 g of $Bi(NO_3)_3.5H_2O$ dissolved in 75 ml of TEG solvent and ultrasonicated solution for 20 min. After the ultrasonication process, 0.318 g of $NaClO_3$ was combined into the solution and again ultrasonicated for 20 min. Subsequently, the resulting solution was poured into a 100 ml autoclave and heated for 3 h at 150 °C in a hot air oven. Once the solution cooled to normal temperature, centrifugation was employed to collect the produced precipitates. These collected precipitates were subjected to seven washes with distilled water afterward to eliminate any impurities in solution. Finally, the material endured drying in an oven at 60°C for 12 h.

7.2.2. Synthesis of PPy and PPy-BiOCl nanocomposites

Polypyrrole (PPy) is synthesized through the polymerization of pyrrole monomers. The chemical oxidative polymerization technique is employed to fabricate PPy polymer. This method involves the oxidative polymerization of pyrrole monomers employing $FeCl_3$ as an oxidizing agent. In this study, 0.2 g of methyl orange is dissolved in 200 ml of deionized water in a beaker. Subsequently, 0.70 ml of pyrrole monomer is added to create mixture “A”. Separately, 2.6 g of ferric chloride hexahydrate is mixed in 25 ml of distilled water to prepare an oxidant solution, termed solution “B”. Solution “B” is then added dropwise to mixture “A” in a 300 ml beaker. The polymerization process occurred at room temperature, specifically 25°C. Afterward, the resultant products are gathered through filtration and underwent washing using a centrifugation machine. Water and ethanol are employed as medium for washing, to eliminate the oxidant, methyl orange, and oligomers.

PPy-BiOCl nanocomposites are fabricated via a physical blending method. The weight ratios of PPy in BiOCl are 5% (BP1), 7% (BP2), and 9% (BP3). The nanocomposite components undergo thorough mixing using a mortar and pestle to achieve a homogeneous blend.

7.2.3. Fabrication of electrode

A mixture of PPy-BiOCl, acetylene black, and PVDF binder was used to develop electrodes with weight ratio of 80:10:10. Firstly, the mixture was properly grinded and an adequate amount of NMP was added to form the ink, which is further ultrasonicated for 20 minutes. Afterward, nickel foam dipped in a dilute solution of HCl and ultrasonicated for 25 minutes to remove any oxide layer or impurities. Later, the nickel foam was rinsed with distilled water to eliminate any remaining acid. Thereafter for the removal of any impurities, nickel foam was immersed in ethanol for couple of minutes and finally rinsed in the deionized water. Finally, the nickel foam was dried in a vacuum oven. The previously formed ink was drop cast onto nickel foam and subjected to vacuum conditions at 60 °C for 12 hours to dry. Similar methodology is adopted for the preparation of pure PPy and pure BiOCl electrodes.

7.3. Results and discussion

7.3.1. Structural elucidation and surface morphology

The X-ray diffraction (XRD) analysis confirmed both the structural and purity phase of the BiOCl.

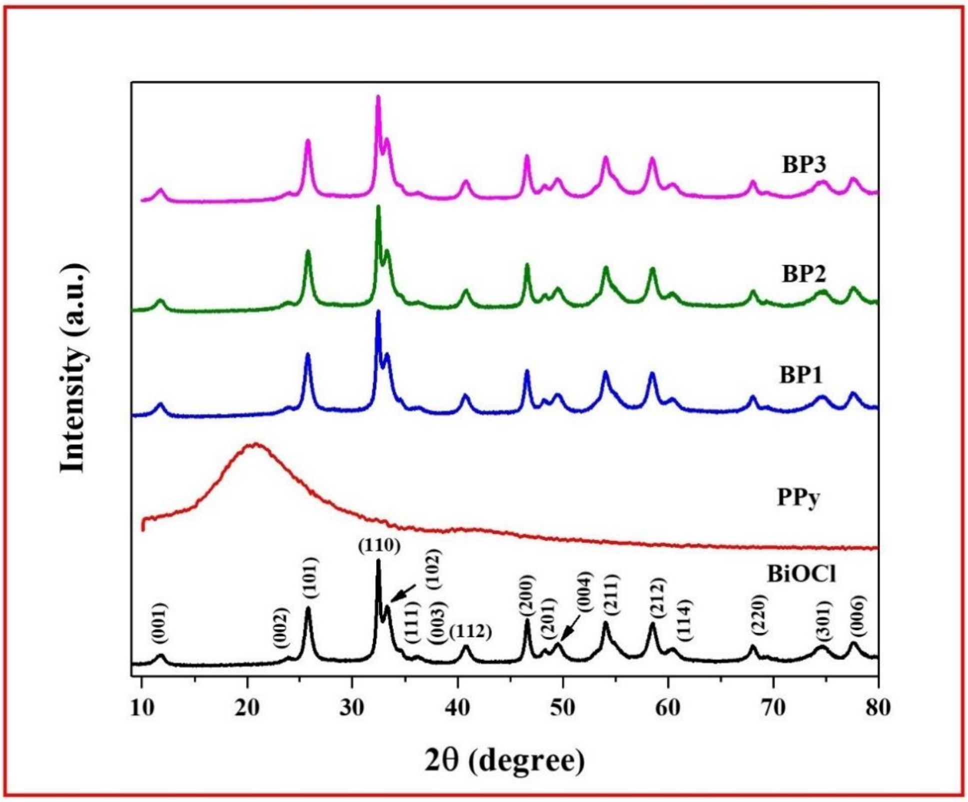

Figure 7.1. XRD of pure BiOCl, PPy, BP1, BP2, and BP3 nanocomposites.

Figure 7.1 displays well-indexed diffraction peaks (011), (002), (101), (110), (112), (200), (113), (211), (212), (220), (214), and (302) which match with standard data for BiOCl (Reference code. 96-901-1783) signifying the formation of tetragonal BiOCl. Figure 7.1 also depicts XRD patterns for pure PPy and its nanocomposites. The XRD pattern of pure PPy shows an amorphous nature with a broad peak at around $2\theta{\sim}23^0$. In contrast, the XRD patterns of BP1, BP2, and BP3 nanocomposites closely resemble pure BiOCl, suggesting that PPy retains its amorphous state when incorporated into BiOCl. This resemblance confirms the successful integration of amorphous PPy into the BiOCl structure. To obtain information about morphology, FESEM images are obtained at different magnifications. It has been noted that pure BiOCl shows marigold flower-like morphology (see Figure 7.2(a-c)). As depicted in Figure 7.2(c), BiOCl displays a structure of nanosheets, distributed uniformly within the material. The FESEM image of pure PPy displays the earthworm-like morphology with randomly oriented grains as exposed in Figure 7.2(d-f). Figure 7.3(a-f) shows the FESEM images for BP1, BP2 and BP3 nanocomposites. In Figure 7.3(a-b) it has been observed that the PPy earthworm-like nanoparticles are randomly oriented in BiOCl (see Figure 7.3(b)) with porous morphology. This unique porous morphology can synergistically enhances the supercapacitive properties, offering more active sites for electrochemical reactions.

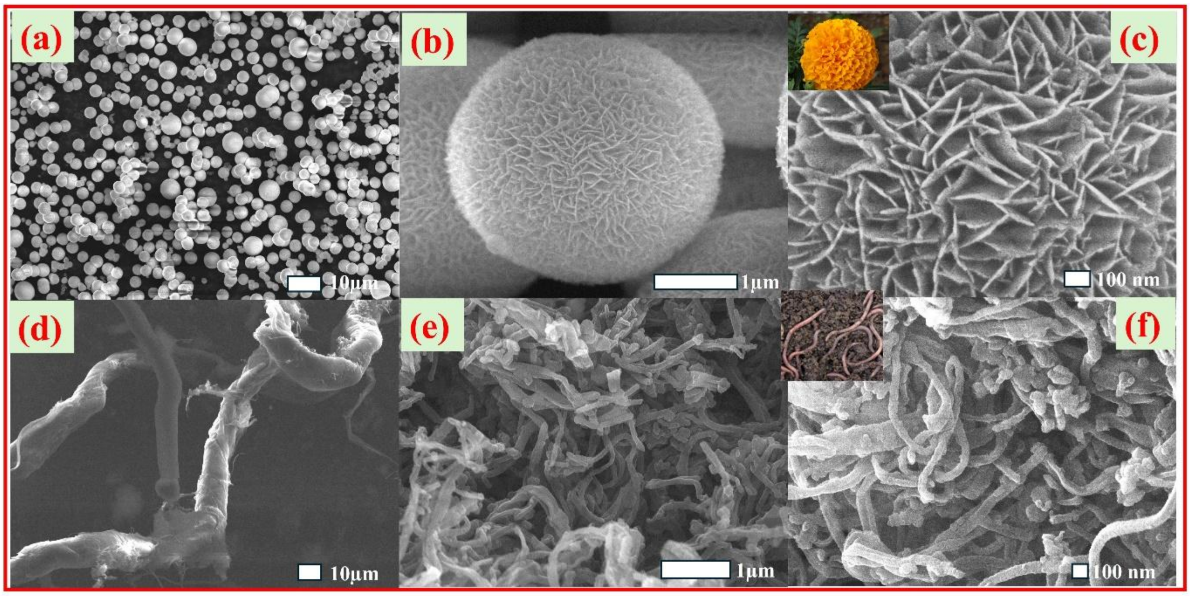

Figure 7.2. Recorded FESEM images of pure BiOCl (a-c) and PPy (d-f).

Furthermore, the increased concentration in the BP2 nanocomposite leads to reduced porosity, while the BP3 nanocomposite exhibits an aggregated morphology (see Figure 7.3(c-f)). This can be attributed to poor dispersion and the development of high stress within the BiOCl nanoparticles [26]. Therefore, it is noted that the incorporation of PPy nanoparticles up to 5 wt.% is sufficient to prevent aggregation for promoting superior nanocomposite properties.

Consequently, the polymer's ability to uniformly grow with high porosity on BiOCl nanoparticles is hindered at concentrations above 5 wt.%, as illustrated in Figure 7.3(c-f).

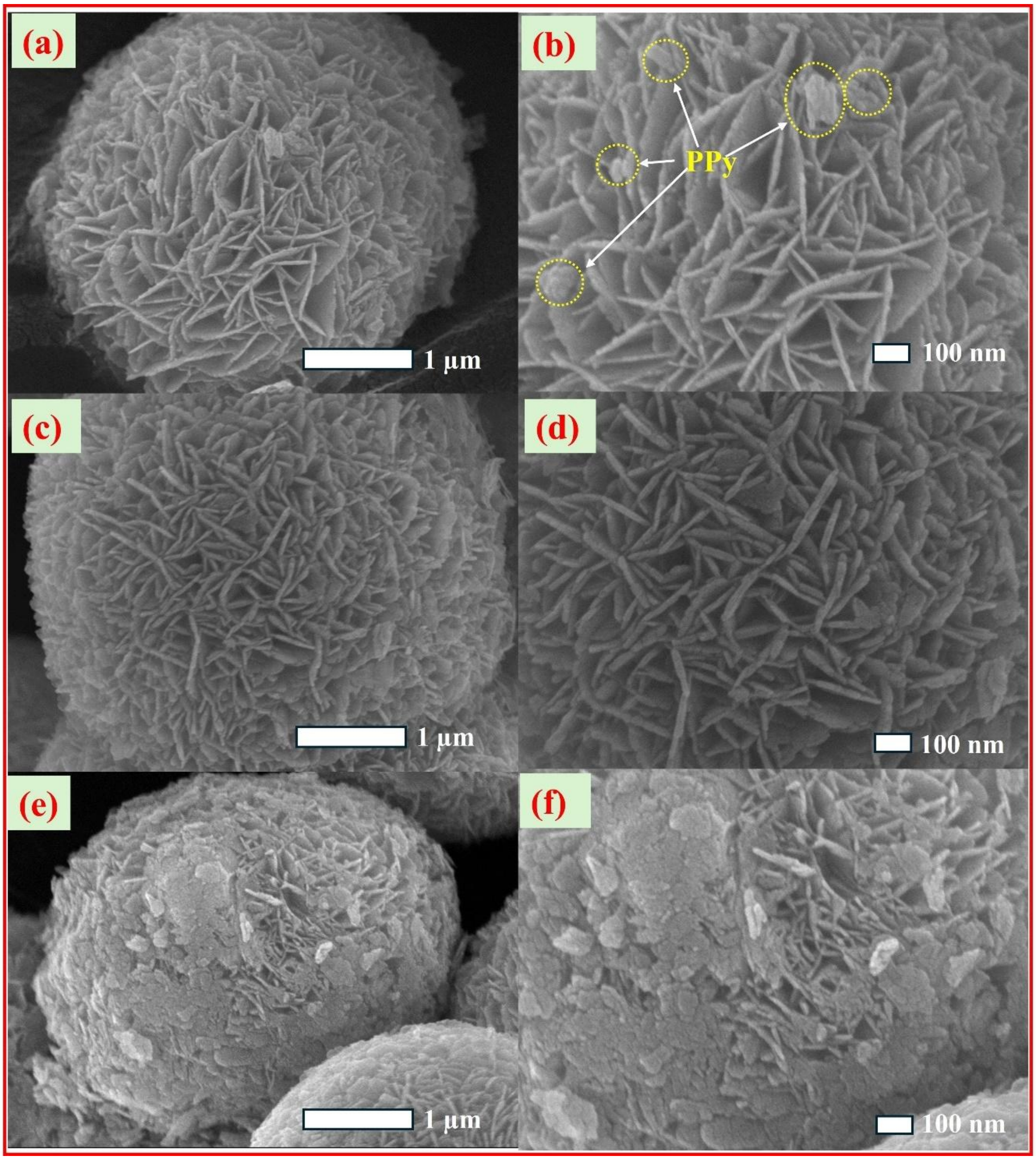

Figure 7.3. Recorded FESEM images of nanocomposites (a-b) BP1, (c-d) BP2, and (e-f) BP3.

Therefore, it is concluded that the ideal concentration of PPy in BiOCl should not exceed 5 wt.% to achieve an ordered and porous morphology. In addition, TEM analysis was conducted to examine the interior structure of the BiOCl sample. The low-magnification TEM image (Figure 7.4(a)) revealed a marigold flower-like morphology and the high-magnification TEM image (Figure 7.4(b)) showed nanosheets within the BiOCl sample. Figure 7.4(c-d) presents TEM images of PPy at lower and higher magnifications, revealing a porous internal nanostructure. In addition, Figure 7.4(e) displays the selected area diffraction pattern (SAED) of PPy, showing a diffraction ring without a bright spot, indicating the amorphous nature of PPy and these findings are consistent with the XRD data of PPy (see Figure 7.1) [27].

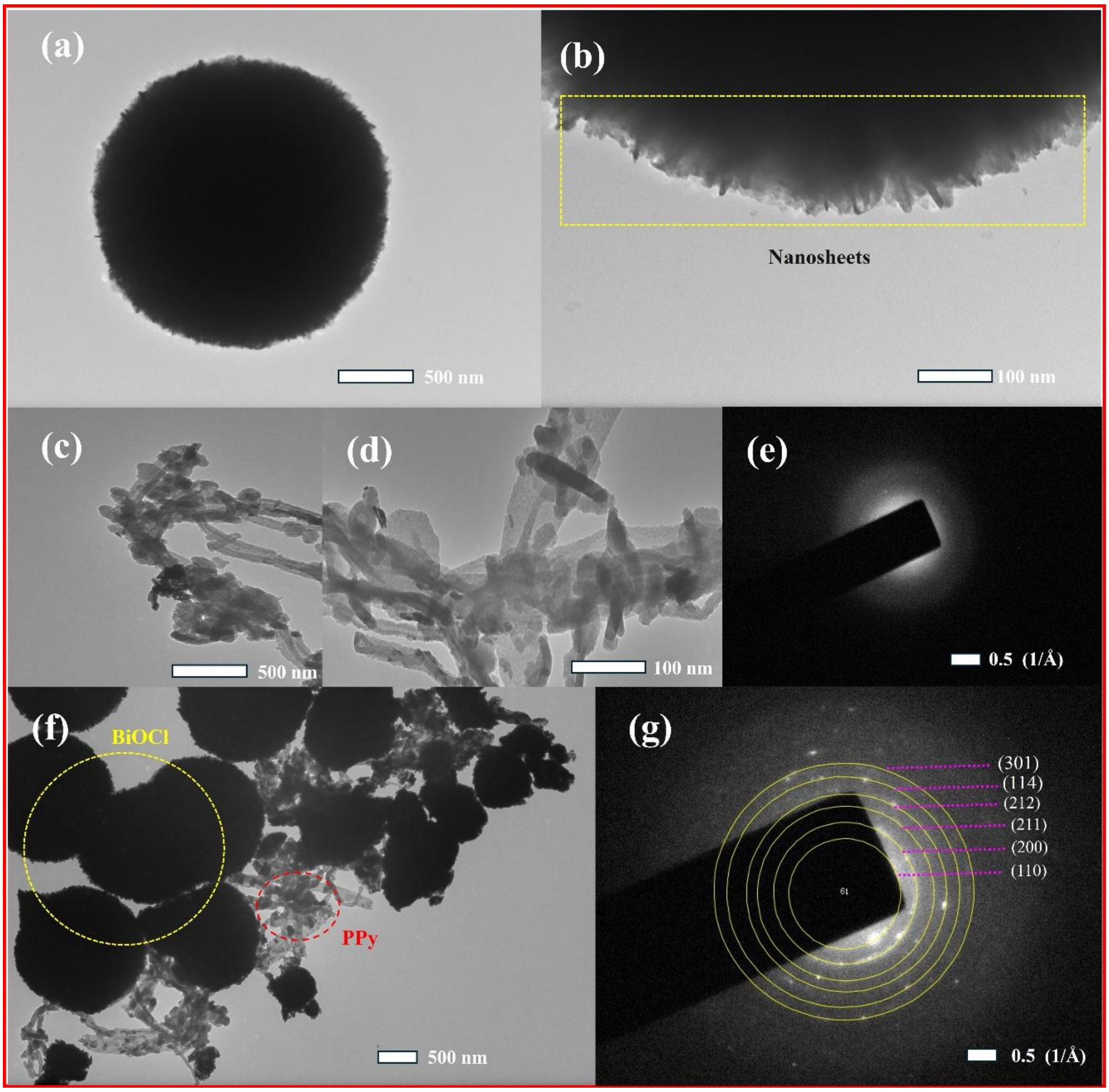

Figure 7.4. Recorded TEM images of (a-b) BiOCl, (c-d) PPy, (f) BP1 nanocomposite, and SAED patterns of PPy (e) and BP1 (g) nanocomposite.

Figure 7.4(f) depicts the TEM image of BP1 nanocomposites, revealing PPy nanoparticles interconnected with BiOCl. The presence of PPy facilitates electron passage throughout the charge storage process. The crystal structure of the BP1 nanocomposites was further analyzed using the SAED pattern. Figure 7.4(g) shows the SAED pattern of BP1 nanocomposites. The presence of six distinct diffraction rings with white intense dots corresponds to the (110), (200), (211), (212), (114), and (301) sets of lattice planes, highlighting the polycrystalline nature of the BP1 nanocomposite [28]. These observations align with the planes identified in the XRD data (see Figure 7.1). The BET surface area of the pure BiOCl and BP1 nanocomposite is determined through the analysis of gas absorption-desorption isotherms, as illustrated in Figure

7.5(a-b). As observed from Figure 7.5(a-b), the adsorption-desorption curves exhibit characteristics consistent with a type-IV isotherm along the H_3 hysteresis loop, confirming the mesoporous nature of the samples [29].

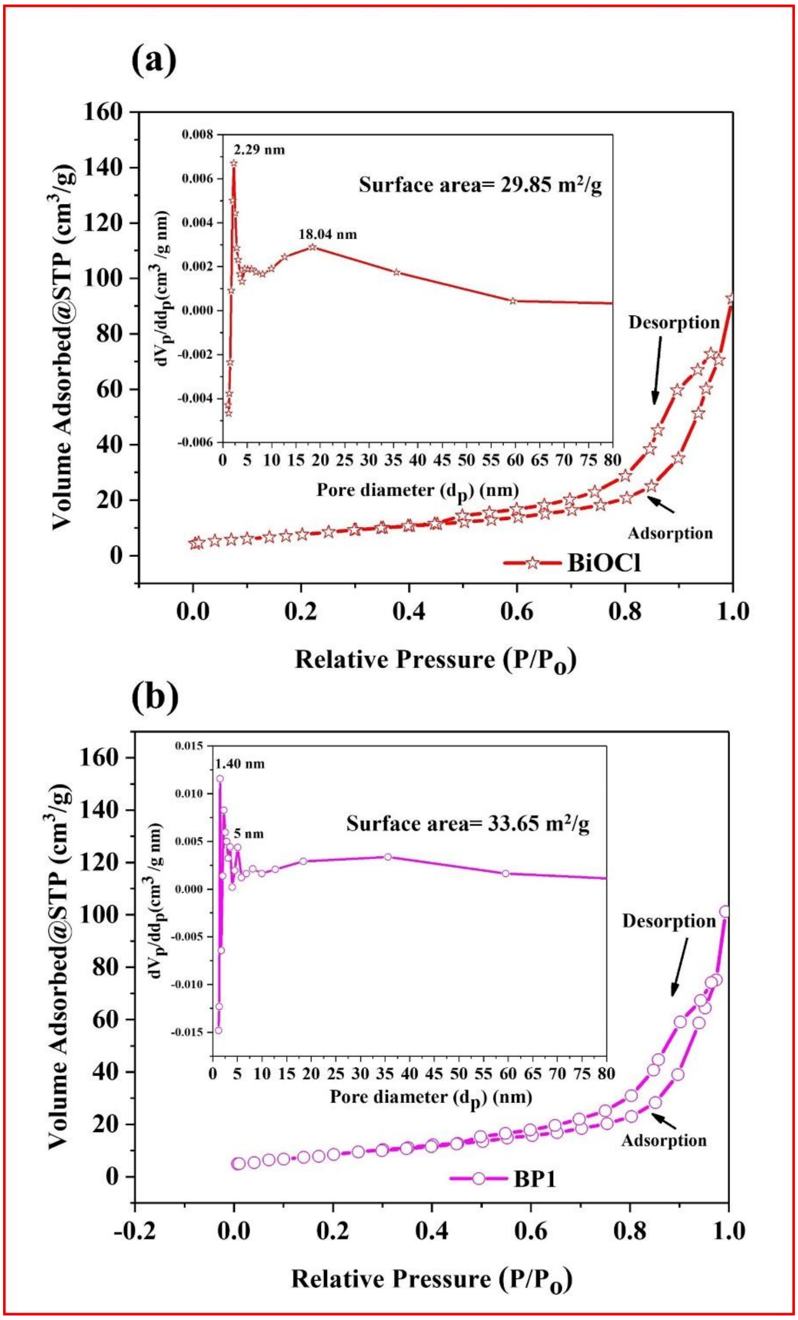

Figure 7.5. BET of (a) BiOCl, (b) BP1 nanocomposite.

However, the BJH (Barrett-Joyner-Halenda) pore size distribution of all samples further confirmed the mesoporous structure (see Figure 7.5(a-b) inset). The pore size distribution for the prepared samples primarily falls around 2.29-18.04 nm and 1.40-5 nm for pure BiOCl and BP1 nanocomposite respectively. Additionally, it was observed that the surface area of BiOCl, and BP1 nanocomposite were 29.85 and 33.65 m^2/g respectively. As a result, it is expected that the mesoporous structure of the BP1 nanocomposite with a large surface area could be particularly favorable for supercapacitor applications which is later discussed. The XPS analysis of the BiOCl and BP1 nanocomposites (refer to Figure 7.6(a)) confirmed the presence of distinct elements.

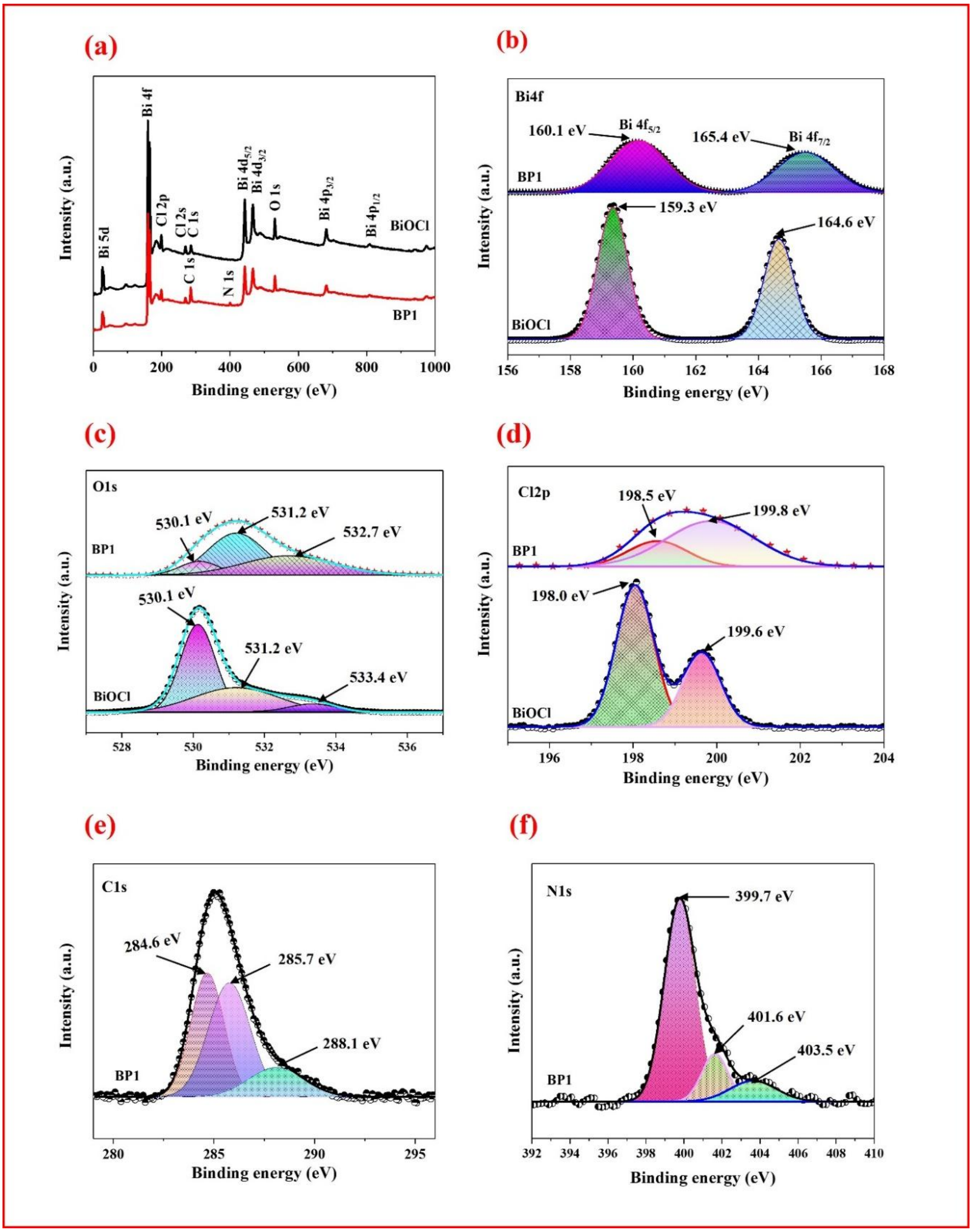

Figure 7.6. (a) XPS survey of prepared samples (b) Bi 4f region (c) O 1s region (d) Cl 2p region of BiOCl and BP1 (e) C 1s region (f) N 1s region of BP1 nanocomposites.

The high-resolution XPS spectrum (see Figure 7.6(b)) shows major spikes at 160.1 and 165.4 eV for the BP1 sample, and at 159.3 and 164.6 eV for BiOCl. The two prominent peaks observed in Bi 4f correspond to the Bi 4f 5/2 and Bi 4f 7/2 states, confirming the presence of Bi^{3+} ions in the prepared samples [30]. Furthermore, no photoelectron signals were detected for Bi^{2+}, Bi^{4+}, and Bi^{5+} in BP1 and BiOCl samples, demonstrating the sample's high reliability. The XPS spectrum (see Figure 7.6(c)) within the O 1s range revealed three peaks, indicating the presence of Bi–O bond in the BP1 and BiOCl samples [31]. Additionally, the peaks observed at 198.5 and 199.8 eV for BP1 (see Figure 7.6(d)) and 198.0 and 199.6 eV for BiOCl corresponded to the Cl $2p_{3/2}$ and Cl $2p_{1/2}$ peaks respectively, indicating the presence of Cl ions derived from BiOCl [32]. The XPS spectrum within C 1s is shown in Figure 7.6(e) for the BP1 sample. The BP1 nanocomposite displays three peaks in its high spectrum: 284.6 eV corresponding to C–C bonds, 285.7 eV associated with C–OH and C–N groups, and 288.1 eV indicative of C=O bonds [33]. Figure 7.6(f) depicts the high-resolution XPS spectrum for the N 1s region. The spectrum reveals a prominent peak at 399.7 eV, attributed to pyrrolic-N, and confirms the presence of a PPy ring within the BiOCl nanocomposite. Furthermore, two peaks at 401.6 and 403.5 eV corresponded to quaternary-N and oxidative-N respectively [34]. These findings contribute to a comprehensive understanding of the chemical composition and purity of the BiOCl and BP1 samples.

7.3.2. Supercapcitive study and charge storage mechanism

The cyclic voltammetry (CV) curves corresponding to BiOCl, PPy, BP1, BP2, and BP3 were recorded within the voltage window of -1.0 V–0.0 V at 10 mV/s scanning rate. Figure 7.7(a) illustrates the oxidation-reduction spikes associated with the faradaic reactions of different electrodes. The obtained geometry of CV curve for all samples is found to be different from that of rectangular-shaped ideal electric double-layer behaviour of CV curve. This indicates the growth of the redox reaction and pseudocapacitive behavior of electroactive materials. The CV curve (see Figure 7.7(a)) of the BiOCl, PPy, BP1, BP2, and BP3 electrodes at a scan rate of 10 mV/s precisely illustrates a large unified area under the curve for BP1, suggesting that the BP2 as well as BP3 electrodes have poor electrochemical activity due to the low charge diffusion rate. The electrode with a more contact area (BP1) provides a more appropriate alleyway for ion diffusion in the electrode peak and shows excellent faradic behavior. The study of PPy and BP1 exhibits a constant shape in the CV curve (see Figure 7.7(b-c)) as the scan rate rises from 7 to 60 mV/s, indicating that the materials offer remarkable capability at high scan rates. The escalation in scan rate induces a change of the oxidation spikes towards a higher potential range and the reduction spikes towards a reduce potential range in the CV curve, indicating the influence of internal electrode resistance [35].

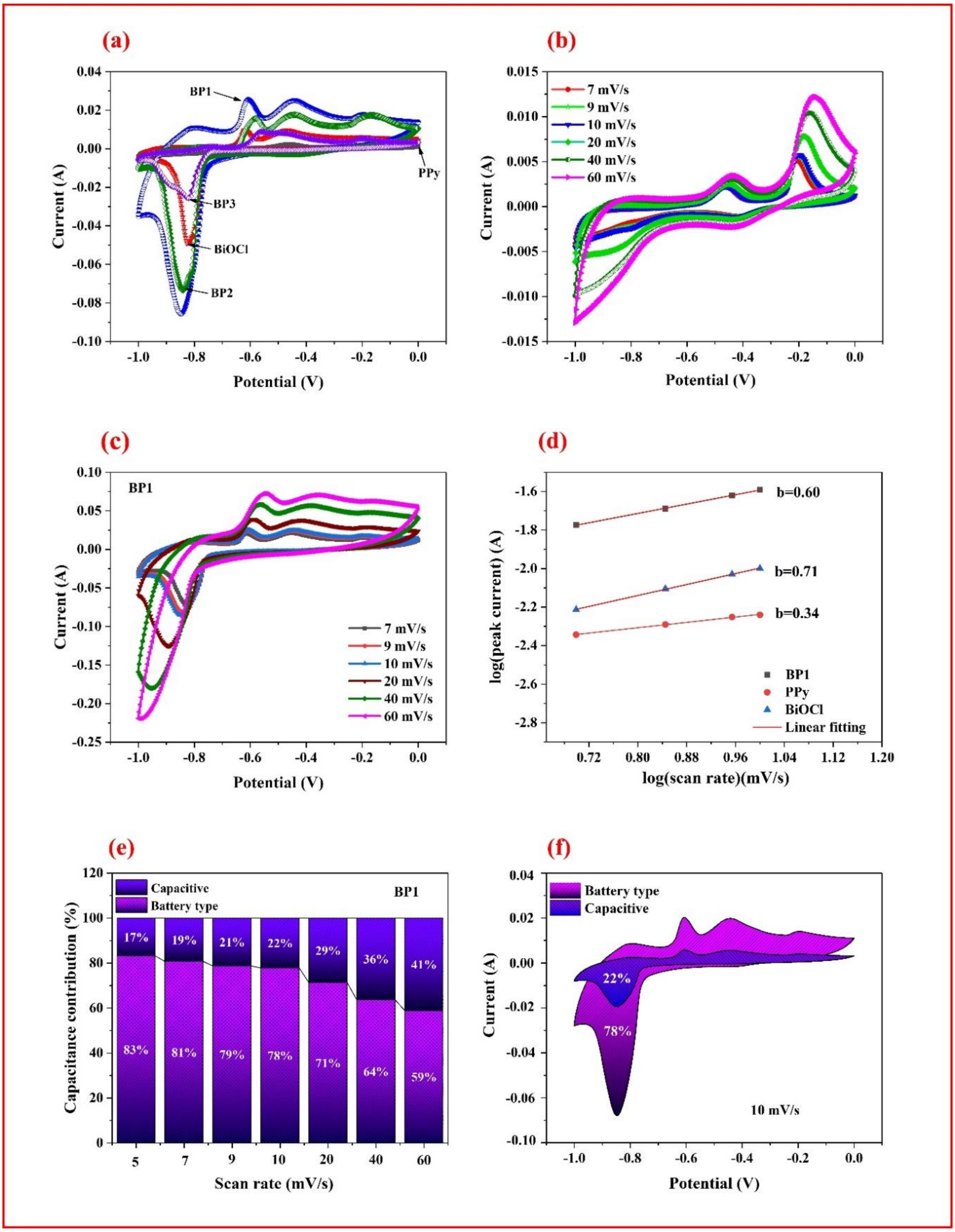

Figure 7.7. (a) CV curvatures of BiOCl, PPy, BP1, BP2, and BP3 at 10 mV/s (b-c) CV curvatures of PPy and BP1 at diverse scanning rates (d) log(current) vs log(scan rate) of the prepared BiOCl, PPy and BP1 electrodes (e) relative contribution percentages of the battery-type and capacitive charge storage (f) separation of battery-type and the capacitive current at 10 mV/s.

The elevation in the scanning rate causes a slight decrease in the supercapacitive performance of the assembled electrode. This is because, at higher scan rates, the active pores within the electrode struggle to facilitate whole redox transitions, and the transportation of charge experiences inhibition in diffusion [36]. Therefore, it can be stated that the electrode material achieves its maximum utilization when the electrode is subjected to lower scan rates. As we progress towards higher scan rates see Figure 7.7(b-c) (>20 mV/s), minimal variations in electrochemical parameters are observed, due to the restriction of ion movement to the surfaces of the electrode. Conversely, at lower scan rates (<10 mV/s), the majority of active sites are engaged by ions for charge storage. Moreover, equations (7.1) and (7.2) have been used to systematically differentiate the comparative contributions of capacitive and battery (diffusion) type processes to the overall charge stored in the electrodes [37]:

$$I = Av^b \tag{7.1}$$

$$\log(\mathrm{I}) = \log(\mathrm{A}) + b\log(v) \tag{7.2}$$

where, ‘ I ’, ‘ v ’represents the current, scan rate (mV/s) and ‘ A ’, ‘ b ’are alterable parameters.

By measuring the slope of log(scan rate) plotted with respect to log(peak current) under constant voltage (V), the value of ‘ b ’ is determined. When ‘ b ’is less or near to 0.5, it indicates that the current follows the battery-type or diffusion mechanism and when ‘ b ’ is larger or near to 1, it suggests that the active material operates under a capacitive process [38]. Figure 7.7(d) illustrates a graphical representation of log(peak current) and log(scan rate) and the value of ‘ b ’is found to be 0.34, 0.71, and 0.60 for PPy, BiOCl, and BP1 respectively. The observed values for these samples indicate diffusion (battery) type mechanisms are dominated. For the BP1 electrode ‘ b ’ value is 0.60 indicating a combination of both capacitive and diffusion-controlled processes. Further quantification of the capacitive and diffusion contribution to the total current is analyzed using equations (7.3) and (7.4) [39].

$$I_{total} = I_{capacitive} + I_{diffusion} = k_1 v + k_2 v^{1/2} \tag{7.3}$$

Equation (7.3) can be expressed as follows.

$$I_{total} / v^{1/2} = k_1 v^{1/2} + k_2 \tag{7.4}$$

where, $\mathrm{I}_{total}(V)$, $k_1 v^{1/2}$ and k_2 represents total current, amount of capacitive and diffusive ions respectively. The values of k_1 and k_2 can be determined by performing a linear fit of the plot between $I_{total} / v^{1/2}$ and $v^{1/2}$. By analyzing the values of k_1 and k_2 at each potential, we can easily visualize the respective contributions of capacitive and battery type processes to the overall current. Figure 7.7(e) presents a summary of the calculated capacitive and battery type current using (7.3) and (7.4) equations. The current governed by diffusion (battery type) is more pronounced at shorter scan rates, attributed to the enhanced capability of KOH ions to penetrate the BP1 electrode material more profoundly. Conversely, at higher scan rates, a notable rise in capacitive current occurred. The proportion of diffusion and capacitive current at 10 mV/s scan rate is also displayed in Figure 7.7(f). This analysis supports the conclusion that the energy storage process in the BP1 electrode is mainly dominated by a battery-type mechanism.

Figure 7.8 displays the galvanostatic charge-discharge (GCD) curvatures of pure BiOCl, PPy, BP1, BP2, and BP3 at 1 A/g of CD. These curves were obtained at various current densities within a wide potential window of -1.0 to 0.0 V. All GCD curvatures exhibit a non-symmetrical behavior with a step voltage drop, which is primarily attributed to the battery type characteristics of BiOCl, PPy, BP1, BP2, and BP3. The GCD curvatures of pure BiOCl can be divided into two distinct sections. The first section is characterized by a potential drop, which is ascribed to internal resistance. It could arise from the semiconducting properties of BiOCl, featuring a band gap of approximately 3.3 eV [40]. Although BiOCl facilitates charge transfer but less efficient than metals. Within BiOCl, grain boundaries serve as traps for moving charge carriers due to defects or impurities. When charge carriers are trapped at these grain boundaries, they accumulate, forming a localized charge buildup. This accumulation creates a potential barrier hindering the movement of charge carriers, thereby obstructing conductivity [41]. Consequently, the flow of charge through the material decreases, leading to a large potential drop in BiOCl (see Figure 7.8 (a)). This drop is transient, typically lasting a few seconds until trapped charge carriers are released from the grain boundaries. Therefore, in the present work, PPy is used as a dopant material to address this issue. Figure 7.8(a) demonstrates that the potential drop is small for the BP1 sample which indicates that the sample shows superior supercapacitive behavior. The discharge time of BP2 is found to be widely extended signifying the higher charge storage capacity of the electrode. The specific capacitance (C) of fabricated electrodes can be computed by using equation (7.5) [42].

$$C = \frac{I_d \times \Delta t}{\Delta V} \tag{7.5}$$

where, 'I_d' is current density, 'Δt' is discharging time and 'ΔV' is a potential window used in the GCD curve. The calculated values of specific capacitance for BiOCl, PPy, BP1, BP2, and BP3 electrodes at 1 A/g of CD are 340, 264, 659, 622, and 373 F/g respectively, and are in accordance with the CV study.

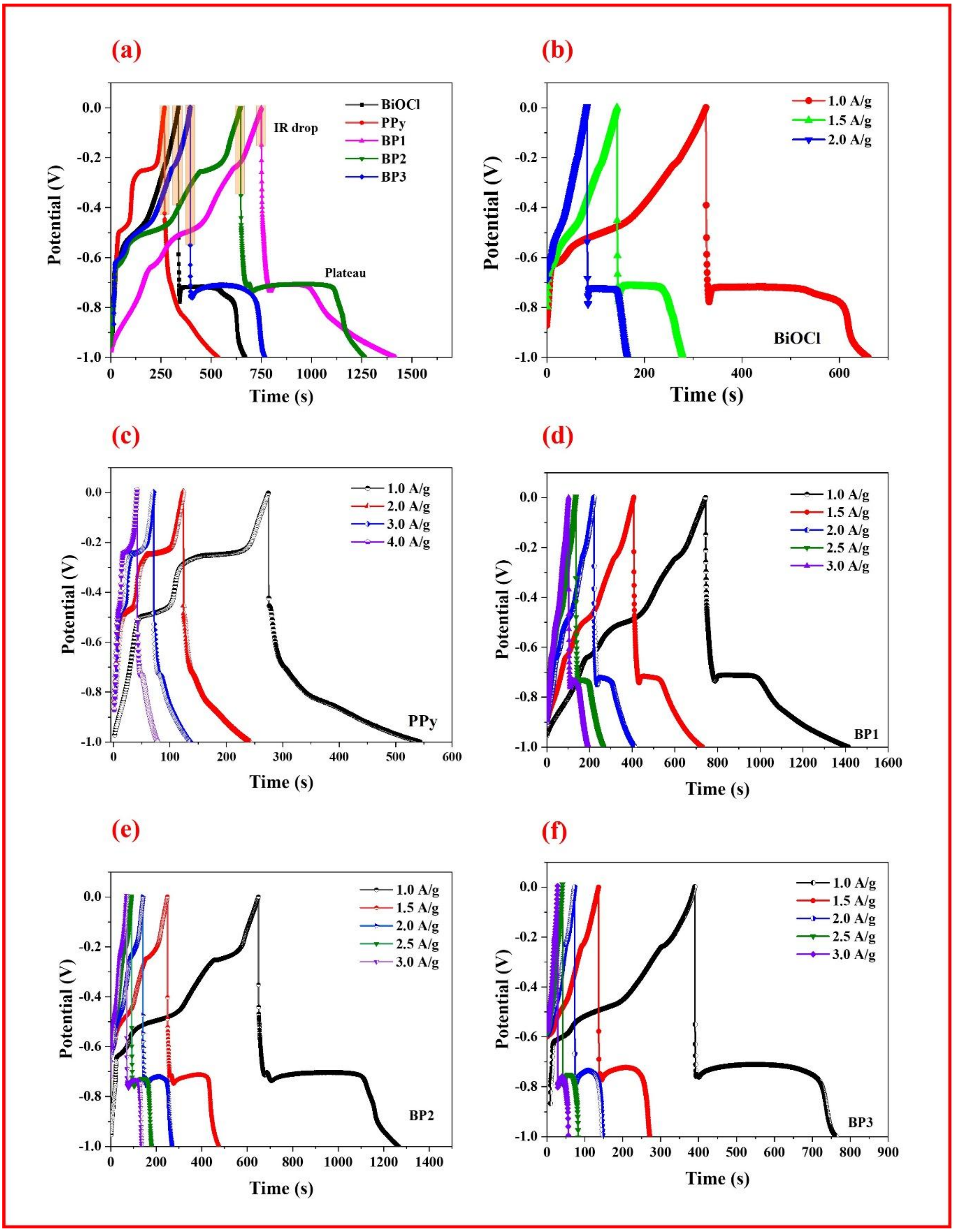

Figure 7.8. (a) GCD curvatures of BiOCl, PPy, BP1, BP2, and BP3 at 1A/g current density (b) GCD curvatures at various current densities for (b) BiOCl (c) PPy (d) BP1 (e) BP2 and (f) BP3.

Furthermore, the GCD curvatures of BiOCl, PPy, BP1, BP2, and BP3 were examined at various current densities (see Figure 7.8(b-f)) and the specific capacitance values were estimated using equation (7.5) and plotted in Figure 7.9. From the plot (see Figure 7.9) it is evident that the BP1 electrode shows higher specific capacitance values as compared to pure

BiOCl and pure PPy, which further confirms the establishment of a porous structure to expand the electrochemical activity of the electrode. Moreover, the obtained trend of the graph clearly depicts the gradual decrement of specific capacitance with an increment in CD, which is in good agreement with earlier reports [43–45].

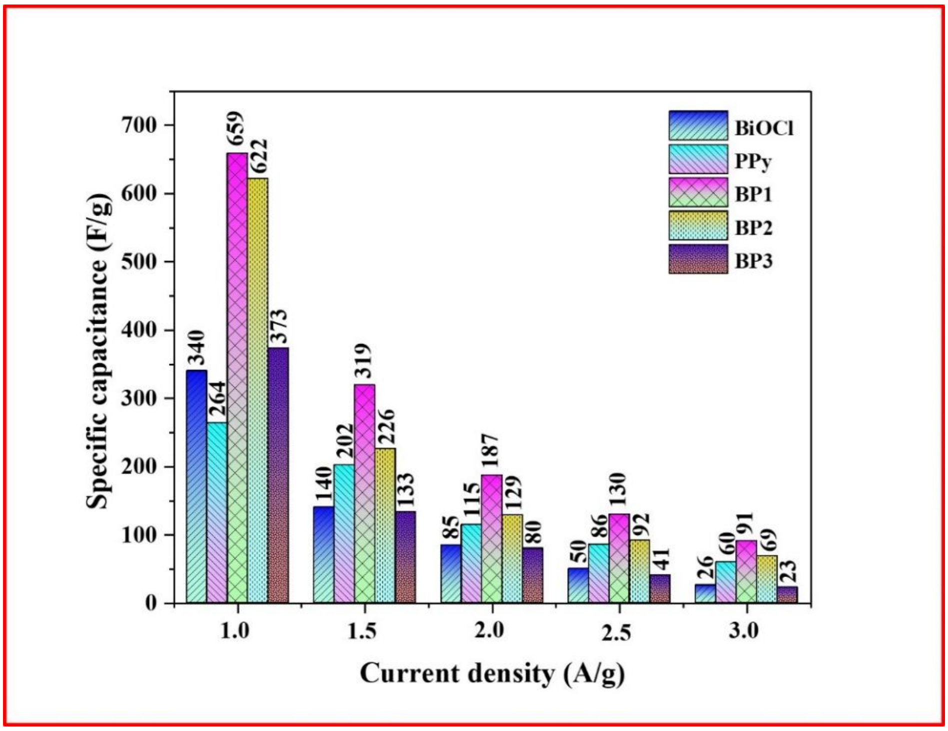

Figure 7.9. Alteration of specific capacitance at several CDs.

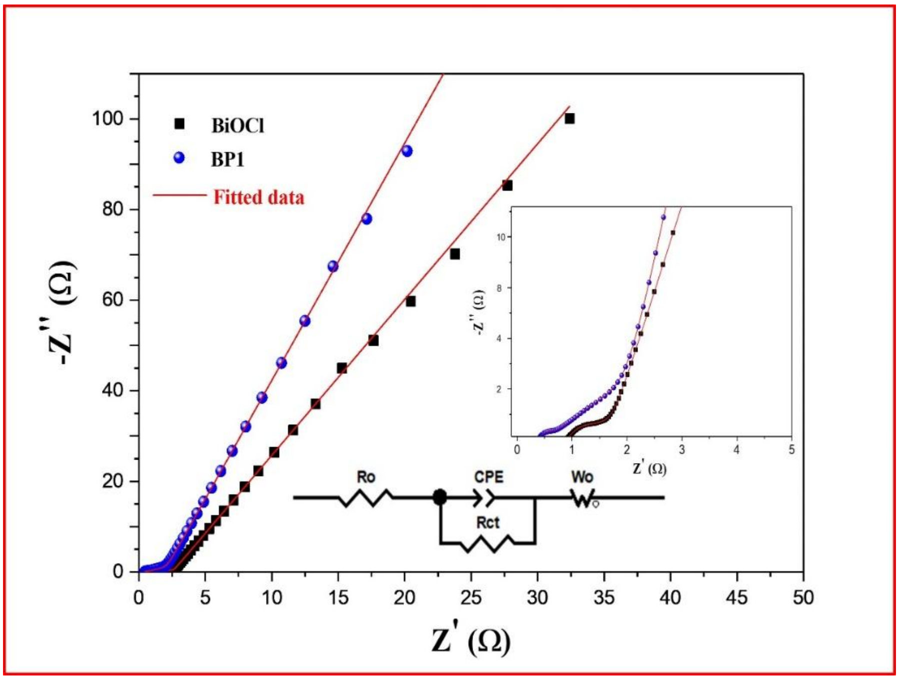

Figure 7.10. EIS plot of BiOCl and BP1 electrodes.

Electrochemical Impedance Spectroscopy (EIS) stands out as a paramount tool for scrutinizing the supercapacitive behavior of electrode materials. As displayed in Figure 7.10, the EIS plot exhibited a vertical orientation in both high and low-frequency regions, indicating the existence of both capacitive and battery-type processes. The semi-circular feature with a diameter of 0.6 Ω for BiOCl and 0.25 Ω for BP1 observed at higher frequencies (see inset of Figure 7.10) corresponds to the charge-transfer resistance, and the relatively small size of the semi-circle for BP1 suggests electrolyte ions are transported via an effective bridging of the electrolyte/electrode interface [46]. Additionally, the series resistance of the BiOCl and BP1 electrode, was measured at 0.9 and 0.4 Ω ((see inset of Figure 7.10), which signifies a favorable ionic response, confirming the BP1 electrode's good performance.

7.3.2.1. Fabrication of symmetrical supercapacitor device

The supercapacitor device with a configuration of a cathode and anode was assembled, using identical BP1 electrodes with an active area of 1×1 cm^2. The electrolyte employed was a wet 6 M KOH Whatman filter with a separator (see Figure 7.11(a)). Significantly, the CV curves displayed an increased area under the curve with higher intensity oxidation-reduction peaks (see Figure 7.11(b)) as the scan rate increased, demonstrating the battery-type behavior of BP1.

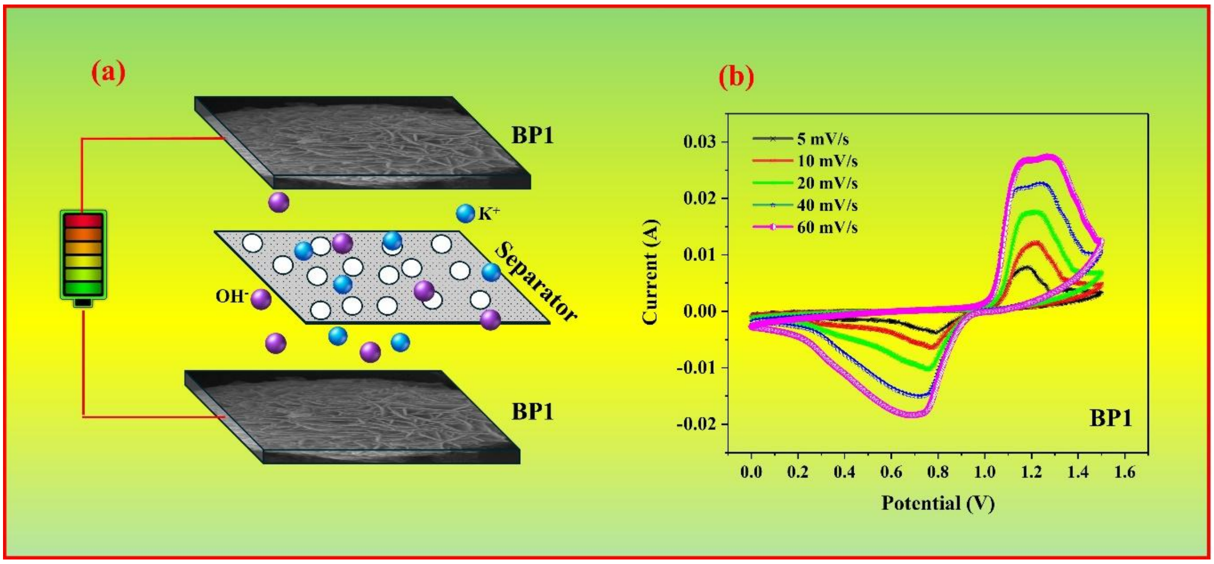

Figure 7.11. (a) BP1//BP1 symmetrical assembled supercapacitor device (b) CV curve of the fabricated device.

Figure 7.12(a) demonstrates that incorporating 5 wt.% PPy into BiOCl results in a twofold increase in current for BP1 compared to pure BiOCl, effectively doubling its electrochemical performance. The GCD curves of the BP1//BP1 device exhibit asymmetrical charge and discharge profiles, as depicted in Figure 7.12(b). These patterns align with the characteristics observed in the corresponding CV curve, indicating a battery-type behavior. Figure 7.12(c) presents the comparative GCD curves of BiOCl and BP1-based symmetrical devices at 1 A/g of CD. The data reveal that the discharge time of the BP1 device is twice as long as that of the pure BiOCl device, confirming BP1's enhanced supercapacitive performance as evidenced by both CV and GCD analyses. The specific capacitance of the BP1 device has been estimated and found to be 76.8 F/g at 0.5 A/g CD, suggesting a practical potential of BP1 in a symmetrical device system. Furthermore, ED and PD can be calculated using (7.6) and (7.7) equations [47-49].

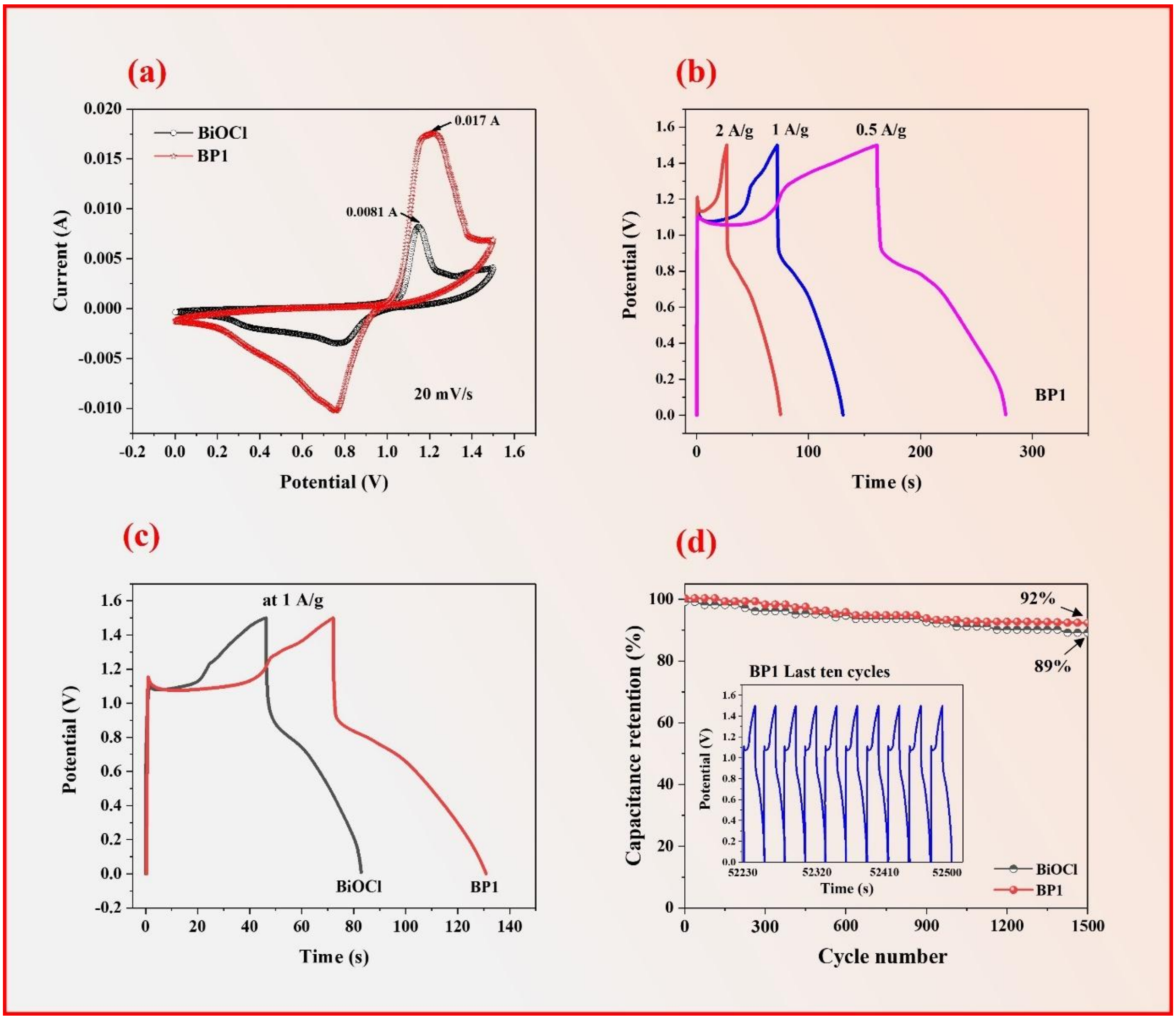

Figure 7.12. (a) Comparative CV of pure BiOCl and BP1 nanocomposite device (b) GCD curves of BP1 device (c) Comparative GCD of BiOCl and BP1 (d) Cyclic stability test.

$$ED = \frac{0.5 C_s \Delta V^2}{3.6}\left(Wh/kg\right) \tag{7.6}$$

$$PD = \frac{ED \times 3600}{t}\left(W/kg\right) \tag{7.7}$$

where 'C_s' represents the specific capacitance of the BP1//BP1 device, 'ΔV' denotes the potential window in volts (V), and 't' signifies the discharging time.

Table 7.1. Comparative Electrochemical Performance of Previously Reported Bi-Based Energy Storage Devices.

Electrode material	Device configuration	Specific capacitance (F/g)	ED (Wh/kg)	PD (W/kg)	References
Bi_2O_3	Bi_2O_3//graphite	37	11	720	[49]
Bi_2O_3	Bi_2O_3//AC	29	35.4	497.4	[50]
Bi_2O_3	Bi_2O_3//MnO_2	25.2	11.3	3370	[51]
ECNF@Bi_2O_3	ECNF@Bi_2O_3//CF@$NiCo_2O_4$	50	25.1	786.2	[52]
BiOCl	BiOCl//AC	124	17.2	250.9	[48]
BiOCl	BiOCl//BiOCl	36	12	1125	[23]
BiOCl/rGO	BiOCl/rGO// BiOCl/rGO	----	21.2	1370	[53]
BiOCl/CNT	BiOCl/CNT// BiOCl/CNT	----	14.6	997.5	[54]
BP1	**BP1**	**76.8**	**24.0**	**750.0**	**Present Work**

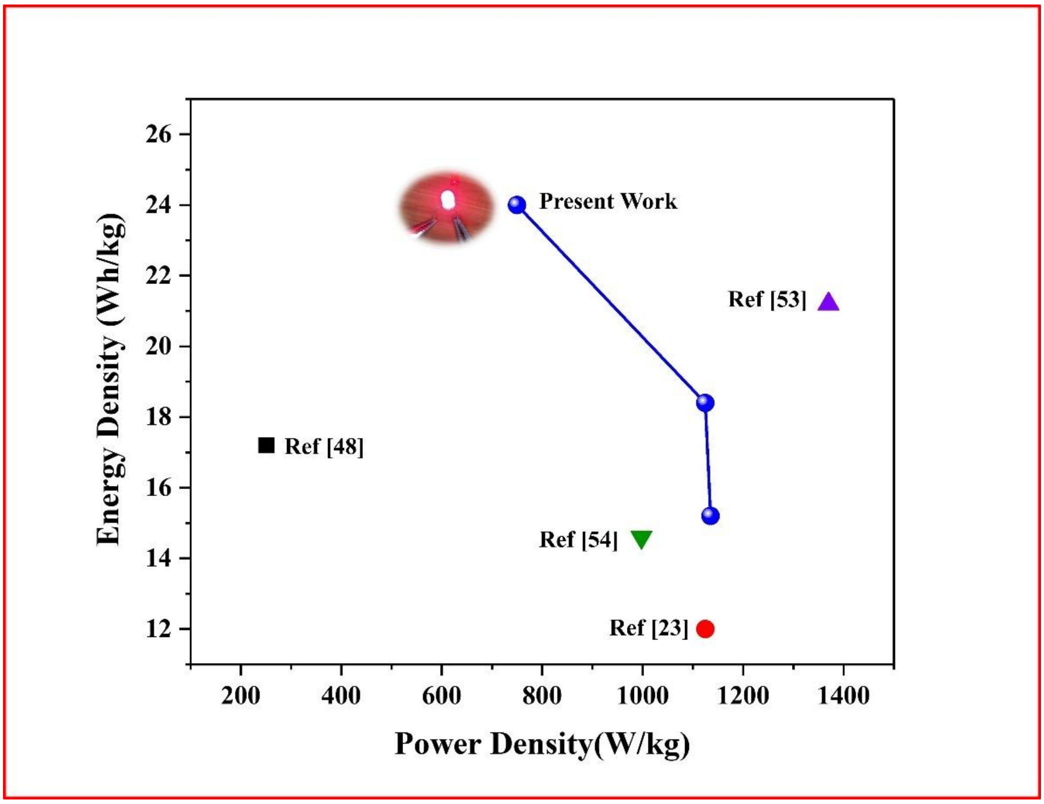

Figure 7.13. Ragone plot of BiOCl based supercapacitor cell.

The symmetric device BP1//BP1 electrode configuration (see Figure 7.11(a)) demonstrated an ED of 24.0, 18.4, 15.2 Wh/kg at 750.0, 1124.6, 1135.3 W/kg of PD. These results not only showcased compatibility or superiority but also unveiled acceptability when compared to previously reported outcomes for both symmetrical and asymmetrical supercapacitor devices using Bismuth (Bi) material. These earlier findings are elaborated in Table 7.1 and the corresponding Ragone plot for BiOCl based materials present in Figure 7.13, covering specific capacitance, ED, and PD. The present work findings underscore the significant potential of the BP1 electrode material in the context of energy storage systems. The BP1 device exhibits excellent cyclic stability ~92% (see Figure 7.12(d)) compared to BiOCl ~89% after undergoing 1500 cycles at a CD of 3 A/g.

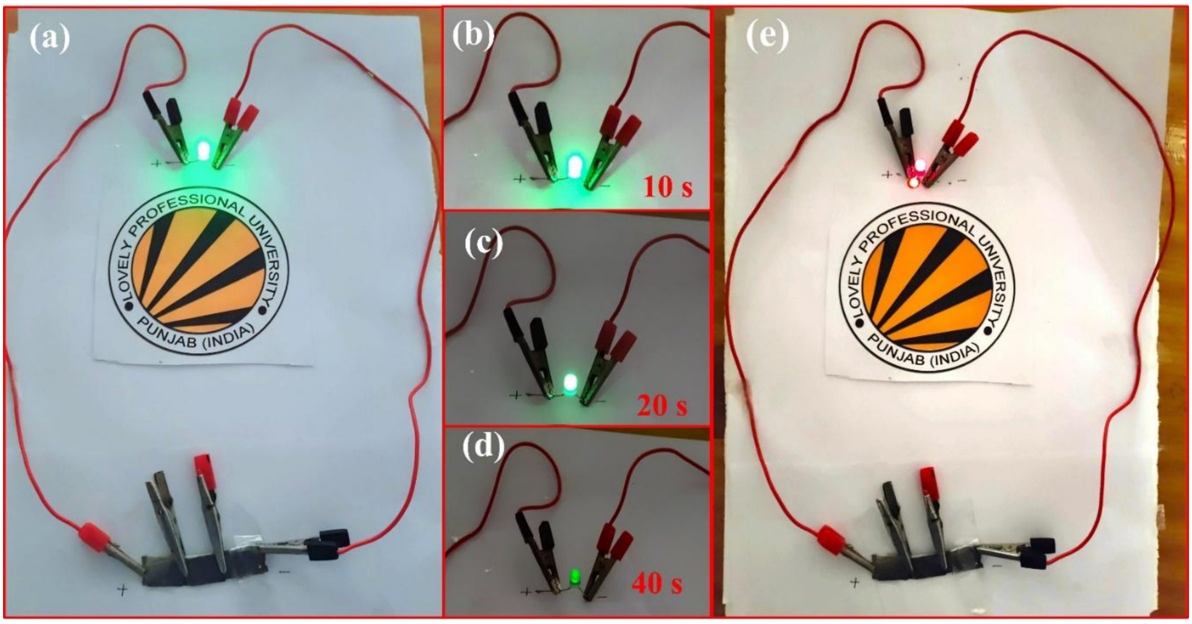

Figure 7.14(a-e) Green and red LED are powered by a pair of symmetric supercapacitor cells linked in sequence.

To assess the commercial potential of the newly developed BP1 electrode material, a pair of supercapacitors utilizing 6 M KOH electrolyte were linked in series. The charging phase involved applying a direct current of 3V for 30 s, followed by discharging through the activation of green ~50 s and two red ~30 s LED (see Figure 7.14(a-e)) which demonstrates that the BP1 electrode has practical application in the energy storage system.

7.4. Conclusions

In summary, BP1 nanocomposite with a unified specific surface area of 33.65 m^2/g was successfully fabricated by the physical blending method. These optimized properties of BP1 support to improve overall performance, electrode surface utilization, and the range of ion transport from the exterior electrolyte to the inner surfaces. In electrochemical investigations, the BP1 electrode demonstrated a battery- type behavior with a specific capacitance of 659 F/g at 1.0 A/g of CD. Furthermore, a symmetric supercapacitor device of BP1 attained a specific capacitance value of 76.8 F/g with an ED of 24.0 Wh/kg and a PD of 750.0 W/kg. Finally, the fabricated symmetric supercapacitor device has effectively powered green and red LED, demonstrating its potential in energy storage systems. Furthermore, considering the favorable specific capacitance of BP1 within the negative potential window in a three-electrode system, it holds potential as negative electrode material in asymmetrical supercapacitors as well as batteries, aiming to further enhance their energy density.

References

[1] Meng F, Ding Y. Sub-micrometer-thick all-solid-state supercapacitors with high power and energy densities. Advanced Materials. 2011;35(23):4098-102.

[2] Wu Q, Xu Y, Yao Z, Liu A, Shi G. Supercapacitors based on flexible graphene/polyaniline nanofiber composite films. ACS nano. 2010;4(4):1963-70.

[3] Weng Z, Su Y, Wang DW, Li F, Du J, Cheng HM. Graphene–cellulose paper flexible supercapacitors. Advanced Energy Materials. 2011;1(5):917-22.

[4] Li J, Zou Y, Li B, Xu F, Chu H, Qiu S, Zhang J, Sun L, Xiang C. Polypyrrole-wrapped $NiCo_2S_4$ nanoneedles as an electrode material for supercapacitor applications. Ceramics International. 2021;47(12):16562-9.

[5] Hwang JY, Kim HM, Shin S, Sun YK. Designing a high-performance lithium–sulfur batteries based on layered double hydroxides–carbon nanotubes composite cathode and a dual-functional graphene–polypropylene–Al_2O_3 separator. Advanced Functional Materials. 2018;28(3):1704294.

[6] Liu H, Zhao D, Liu Y, Hu P, Wu X, Xia H. Boosting energy storage and electrocatalytic performances by synergizing $CoMoO_4$@ $MoZn_{22}$ core-shell structures. Chemical Engineering Journal. 2019;373:485-92.

[7] Javed MS, Mateen A, Hussain I, Ali S, Asim S, Ahmad A, tag Eldin E, Bajaber MA, Najam T, Han W. The quest for negative electrode materials for Supercapacitors: 2D materials as a promising family. Chemical Engineering Journal. 2023;452:139455.

[8] Sun J, Xu C, Chen H. A review on the synthesis of $CuCo_2O_4$-based electrode materials and their applications in supercapacitors. Journal of Materiomics. 2021;7(1):98-126.

[9] Bao E, Ren X, Wu R, Liu X, Chen H, Li Y, Xu C. Porous $MgCo_2O_4$ nanoflakes serve as electrode materials for hybrid supercapacitors with excellent performance. Journal of Colloid and Interface Science. 2022;625:925-35.

[10] Liu Y, Du X, Li Y, Bao E, Ren X, Chen H, Tian X, Xu C. Nanosheet-assembled porous $MnCo_2O_{4.5}$ microflowers as electrode material for hybrid supercapacitors and lithium-ion batteries. Journal of colloid and interface science. 2022;627:815-26.

[11] Wu R, Sun J, Xu C, Chen H. $MgCo_2O_4$-based electrode materials for electrochemical energy storage and conversion: a comprehensive review. Sustainable Energy & Fuels. 2021;5(19):4807-29.

[12] Bao E, Sun J, Liu Y, Ren X, Liu X, Xu C, Chen H. Facile preparation of SnS_2 nanoflowers and nanoplates for the application of high-performance hybrid supercapacitors. International Journal of Hydrogen Energy. 2022;47(92):39204-14.

[13] Du X, Ren X, Xu C, Chen H. Recent advances on the manganese cobalt oxides as electrode materials for supercapacitor applications: a comprehensive review. Journal of Energy Storage. 2023;68:107672.

[14] Han Y, Ge Y, Chao Y, Wang C, Wallace GG. Recent progress in 2D materials for flexible supercapacitors. Journal of energy chemistry. 2018;27(1):57-72.

[15] Shinde PV, Shinde NM, Yun JM, Mane RS, Kim KH. Facile chemical synthesis and potential supercapattery energy storage application of hydrangea-type Bi_2MoO_6. ACS omega. 2019;4(6):11093-102.

[16] Sun C, Pan W, Zheng D, Guo G, Zheng Y, Zhu J, Liu C. Advanced asymmetric supercapacitors with a squirrel cage structure Fe_3O_4@carbon nanocomposite as a negative electrode. RSC advances. 2021;11(62):39399-411.

[17] Yang P, Ding Y, Lin Z, Chen Z, Li Y, Qiang P, Ebrahimi M, Mai W, Wong CP, Wang ZL. Low-cost high-performance solid-state asymmetric supercapacitors based on MnO_2 nanowires and Fe_2O_3 nanotubes. Nano letters. 2014;14(2):731-6.

[18] Sun C, Pan W, Zheng D, Zheng Y, Zhu J, Liu C. Low-crystalline FeOOH nanoflower assembled mesoporous film anchored on MWCNTs for high-performance supercapacitor electrodes. ACS omega. 2020;5(9):4532-41.

[19] Lu X, Li G, Tong Y. A review of negative electrode materials for electrochemical supercapacitors. Science China Technological Sciences. 2015;58:1799-808.

[20] Mu J, Chen B, Guo Z, Zhang M, Zhang Z, Zhang P, Shao C, Liu Y. Highly dispersed Fe_3O_4 nanosheets on one-dimensional carbon nanofibers: synthesis, formation mechanism, and electrochemical performance as supercapacitor electrode materials. Nanoscale. 2011;3(12):5034-40.

[21] Wang HW, Hu ZA, Chang YQ, Chen YL, Lei ZQ, Zhang ZY, Yang YY. Facile solvothermal synthesis of a graphene nanosheet–bismuth oxide composite and its electrochemical characteristics. Electrochimica Acta. 2010;55(28):8974-80.

[22] Shinde NM, Xia QX, Yun JM, Mane RS, Kim KH. Polycrystalline and mesoporous 3-D Bi_2O_3 nanostructured negatrodes for high-energy and power-asymmetric supercapacitors: superfast room-temperature direct wet chemical growth. ACS applied materials & interfaces. 2018;10(13):11037-47.

[23] Shinde NM, Ghule BG, Raut SD, Narwade SH, Pak JJ, Mane RS. Hopping electrochemical supercapacitor performance of ultrathin BiOCl petals grown by a room-temperature soft-chemical process. Energy & Fuels. 2021;35(8):6892-7.

[24] Chen F, Leong ZY, Yang HY. An aqueous rechargeable chloride ion battery. Energy Storage Materials. 2017;7:189-94.

[25] Namsheer K, Rout CS. Conducting polymers: a comprehensive review on recent advances in synthesis, properties and applications. RSC advances. 2021;11(10):5659-97.

[26] Chen LY, Xu JQ, Choi H, Pozuelo M, Ma X, Bhowmick S, Yang JM, Mathaudhu S, Li XC. Processing and properties of magnesium containing a dense uniform dispersion of nanoparticles. Nature. 2015;528(7583):539-43.

[27] Majumder M, Choudhary RB, Thakur AK, Karbhal I. Impact of rare-earth metal oxide (Eu_2O_3) on the electrochemical properties of a polypyrrole/CuO polymeric composite for supercapacitor applications. RSC advances. 2017;7(32):20037-48.

[28] Mayimele N, Otieno F, Naidoo SR, Wamwangi D, Quandt A. Efficiency enhancement of organic solar cell using surface plasmon resonance effects of Ag nanoparticles. Optical and Quantum Electronics. 2021;53:1-4.

[29] Chen H, Ma X, Shen PK. $NiCo_2S_4$ nanocores in-situ encapsulated in graphene sheets as anode materials for lithium-ion batteries. Chemical Engineering Journal. 2019;364:167-76.

[30] Dong W, Xie T, Wu Z, Peng H, Ren H, Meng F, Lin H. Oxygen-vacancy-rich BiOCl materials with ultrahigh photocatalytic efficiency by etching bismuth glass. RSC advances. 2021;11(61):38894-906.

[31] Kang S, Pawar RC, Pyo Y, Khare V, Lee CS. Size-controlled BiOCl–RGO composites having enhanced photodegradative properties. Journal of Experimental Nanoscience. 2016;11(4):259-75.

[32] Qi R, Liu J, Yuan H, Yu Y. Sulfur-doped BiOCl with enhanced light absorption and photocatalytic water oxidation activity. Nanomaterials. 2021;11(9):2221.

[33] Cao J, Wang Y, Chen J, Li X, Walsh FC, Ouyang JH, Jia D, Zhou Y. Three-dimensional graphene oxide/polypyrrole composite electrodes fabricated by one-step electrodeposition for high performance supercapacitors. Journal of Materials Chemistry A. 2015;3(27):14445-57.

[34] Yuan X, Li L, Ma Z, Yu X, Wen X, Ma ZF, Zhang L, Wilkinson DP, Zhang J. Novel nanowire-structured polypyrrole-cobalt composite as efficient catalyst for oxygen reduction reaction. Scientific reports. 2016;6(1):20005.

[35] Gujar TP, Shinde VR, Lokhande CD, Han SH. Electrosynthesis of Bi_2O_3 thin films and their use in electrochemical supercapacitors. Journal of power sources. 2006;161(2):1479-85.

[36] Yao F, Pham DT, Lee YH. Carbon-based materials for lithium-ion batteries, electrochemical capacitors, and their hybrid devices. ChemSusChem. 2015;8(14):2284-311.

[37] Wang X, Li H, Li H, Lin S, Bai J, Dai J, Liang C, Zhu X, Sun Y, Dou S. Heterostructures of Ni–Co–Al layered double hydroxide assembled on V_4C_3 MXene for high-energy hybrid supercapacitors. Journal of Materials Chemistry A. 2019;7(5):2291-300.

[38] Thakur YS, Acharya AD, Sharma S, Bisoyi S, Manhas SS. Synthesis of 3D rice-like BiOCl battery-type electrode material and evaluation of their electrochemical performance in a symmetrical supercapacitor device configuration. Materials Science in Semiconductor Processing. 2024;177:108376.

[39] Shameem A, Devendran P, Siva V, Murugan A, Sasikumar S, Nallamuthu N, Hussain S, Bahadur SA. Robust one-step synthesis of bismuth molybdate nanocomposites: A promising negative electrode for high end ultracapacitors. Solid State Sciences. 2020;106:106303.

[40] Saddique Z, Imran M, Javaid A, Latif S, Hussain N, Kowal P, Boczkaj G. Band engineering of BiOBr based materials for photocatalytic wastewater treatment via advanced oxidation processes (AOPs)–A review. Water Resources and Industry. 2023;29:100211.

[41] Xin R, Han X, He J. Atomic-Scale Insights into the Activation of Near-Infrared-Responsive Photoactivity in BiOCl Grain Boundaries. The Journal of Physical Chemistry C. 2023;127(28):13759-66.

[42] Iqbal M, Saykar NG, Arya A, Banerjee I, Alegaonkar PS, Mahapatra SK. High-performance supercapacitor based on MoS_2@ TiO_2 composite for wide range temperature application. Journal of Alloys and Compounds. 2021;883:160705.

[43] Boukhalfa S, Evanoff K, Yushin G. Atomic layer deposition of vanadium oxide on carbon nanotubes for high-power supercapacitor electrodes. Energy & Environmental Science. 2012;5(5):6872-9.

[44] Ramesh S, Karuppasamy K, Msolli S, Kim HS, Kim HS, Kim JH. A nanocrystalline structured NiO/MnO_2@ nitrogen-doped graphene oxide hybrid nanocomposite for high performance supercapacitors. New Journal of Chemistry. 2017;41(24):15517-27.

[45] Nithya VD, Hanitha B, Surendran S, Kalpana D, Selvan RK. Effect of pH on the sonochemical synthesis of $BiPO_4$ nanostructures and its electrochemical properties for pseudocapacitors. Ultrasonics sonochemistry. 2015;22:300-10.

[46] Thakur YS, Acharya AD, Sharma S, Bisoyi S. Enhanced electrochemical performance of in situ polymerized V_2O_5-PANI nanocomposites and its practical application confirmation by assembling ionic liquid as well as solid state-based supercapacitor device. Results in Chemistry. 2024;7:101259.

[47] Deng H, Huang J, Hu Z, Chen X, Huang D, Jin T. Fabrication of a three-dimensionally networked MoO_3/PPy/rGO composite for a high-performance symmetric supercapacitor. ACS omega. 2021;6(14):9426-32.

[48] Hong W, Wang L, Liu K, Han X, Zhou Y, Gao P, Ding R, Liu E. Asymmetric supercapacitor constructed by self-assembled camellia-like BiOCl and activated carbon microspheres derived from sweet potato starch. Journal of Alloys and Compounds. 2018;746:292-300.

[49] Shinde NM, Xia QX, Yun JM, Singh S, Mane RS, Kim KH. A binder-free wet chemical synthesis approach to decorate nanoflowers of bismuth oxide on Ni-foam for fabricating laboratory scale potential pencil-type asymmetric supercapacitor device. Dalton Transactions. 2017;46(20):6601-11.

[50] Senthilkumar ST, Selvan RK, Ulaganathan M, Melo JS. Fabrication of Bi2O3|| AC asymmetric supercapacitor with redox additive aqueous electrolyte and its improved electrochemical performances. Electrochimica Acta. 2014;115:518-24.

[51] Xu H, Hu X, Yang H, Sun Y, Hu C, Huang Y. Flexible asymmetric micro-supercapacitors based on Bi_2O_3 and MnO_2 nanoflowers: larger areal mass promises higher energy density. Advanced Energy Materials. 2015;5(6):1401882.

[52] Li L, Zhang X, Zhang Z, Zhang M, Cong L, Pan Y, Lin S. A bismuth oxide nanosheet-coated electrospun carbon nanofiber film: a free-standing negative electrode for flexible asymmetric supercapacitors. Journal of Materials Chemistry A. 2016;4(42):16635-44.

[53] Dutta S, Pal S, Ahammed N, Sahoo S, Chatterjee S, De S. Enhanced Electrochemical Performance of BiOCl Nanoflower-RGO Based Supercapacitor in the Presence of Redox Additive Electrolyte. ECS Journal of Solid State Science and Technology. 2023;12(9):091002.

[54] Dutta S, Pal S, Sikder D, De S. Light-weight flexible solid-state supercapacitor based on highly crystalline 2D BiOCl nanoplates/MWCNT nanocomposites. Journal of Alloys and Compounds. 2020;820:153115.

Chapter 8

Conclusions and Future Scope

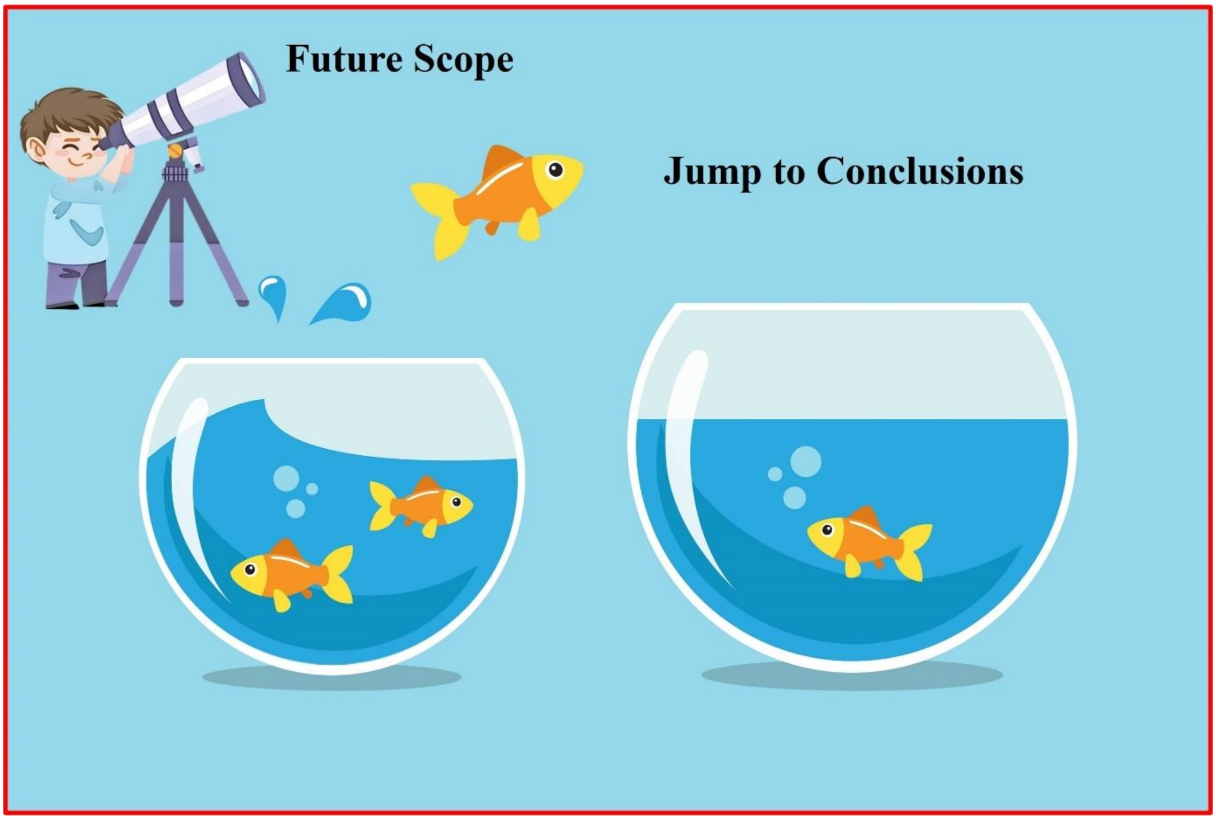

This chapter provides a summary of the research work conducted in this thesis, highlighting key findings related to materials, cell configurations, and their corresponding performance. Additionally, it offers a concise overview of potential possibilities for future research.

8.1. Conclusions

With the rapid evolution in consumer electronics and electric vehicles, electrochemical energy storage systems must also advance swiftly. These systems need to handle significant amounts of energy in seconds or minutes, particularly for transportation and grid storage applications. Although conductive polymer materials meet the power density requirements, but unfortunately their limited cycle stability and specific capacitance restrict their use. In this context, metal oxides exhibiting pseudocapacitance are highly promising. Pseudocapacitance arises from reversible redox reactions at the electrode surface, enhancing performance. This thesis work shows that fabrication of nanocomposites such as V_2O_5-PANI and PPy-BiOCl can produce electrode architectures with high specific capacitance, substantial power and energy densities, a wide voltage range, and improved cycle life. **Chapter 3** details the experimental techniques and methodologies employed for preparing and characterizing conducting polymer nanocomposites for renewable energy applications. The summary and key outcomes of the thesis are presented as follows.

- In **Chapter 4**, we investigate the electrochemical performance, as well as the structural, morphological, and thermal properties of the V_2O_5-PANI nanocomposite. V_2O_5 nanoparticles were successfully synthesized using the sol-gel method and doped in a PANI matrix with different wt.% using the in situ polymerization method. The prepared nanoparticles were characterized through XRD to determine the electron density, microstrain, and crystallite size via Rietveld refinement and Williamson-Hall calculations. Uniform dispersion of V_2O_5 inside the PANI matrix was confirmed through FESEM, showing the alignment of non-uniform grains to uniform grains giving a porous morphology for 20 wt.% V_2O_5-PANI nanocomposite which is valuable for good electrochemical activity. FTIR and Raman spectra of the V_2O_5-PANI nanocomposites show shifts in peaks, providing evidence of the effective intercalation of V_2O_5 into the PANI matrix. In the electrochemical studies, among all electrodes 20 wt.% V_2O_5-PANI electrode exhibited a high specific capacitance of 820.5 F/g at a current density of 1 A/g and demonstrated decent cyclic stability with a capacity retention rate of 88% after 1000 cycles. Additionally, the 20 wt.% V_2O_5-PANI electrode also delivered a good energy and power density of 4.6 Wh/kg and 80.7 W/kg respectively. Finally, the successful illumination of a red LED by the symmetric device strongly suggests that the 20 wt.% V_2O_5-PANI electrode is a promising candidate for next-generation energy storage devices.

- In **Chapter 5**, In situ polymerization technique successfully employed to synthesize V_2O_5:PANI nanocomposites. The prepared nanocomposites showed high purity without the presence of any impurity peaks defining the good harmony between V_2O_5 and PANI investigated through XRD scans. Additionally, the XRD peak intensities of prepared nanocomposites increases with doping concentration of V_2O_5, which signifies excellent dispersion in the prepared nanocomposites. Therefore, the modulation of different optical properties of V_2O_5:PANI nanocomposites were mediated by the excellent dispersion of V_2O_5 in polymer matrix. Furthermore, we also investigated the UV shielding performance and visible light transmission of V_2O_5:PANI nanocomposites. It is observed that 30 wt.% V_2O_5:PANI nanocomposite displayed a 93% enhancement in UV shielding performance with respect to PANI in the UVB range. Conclusively the prepared nanocomposites could provide important insight for the design and development of novel outstanding UV shielding materials.
- In **Chapter 6**, we have synthesized various 3D hierarchical BiOCl nanostructures by using different solvents (EG, DEG, and TEG) in solvothermal methods. The produced 3D hierarchical nanostructure's physical, morphological, electrochemical, and other characteristics were meticulously studied using a range of spectral and analytical techniques. Among all prepared samples, the BT electrode (BiOCl prepared in TEG solvent) shows a unique marigold flower-like morphology and demonstrates a notable specific capacitance of 665 F/g at 0.5 A/g current density. This admirable specific capacitance is attributed to the high specific surface area of 29.85 m^2/g and the substantial available active site. However, the presence of surface-active sites, uniform growth, and stable integration of active materials on nickel foam, resulted in low charge transfer resistance and excellent electrical conductivity. These factors also contribute to the lower potential drop examined in GCD, facilitating rapid ion and electron transfer leading to enhanced electrochemical performance of BT electrode. Moreover, the fabricated BT//BT symmetrical device delivers a maximum energy density of 15.6 Wh/kg at 838 W/kg power density and shows good cyclic stability of ~80% after 1500 cycles. Finally, the device glows up a red LED after charging which indicates that the BT//BT device has elevated capability in practical application. In addition to the fabricated symmetric supercapacitor device, an appropriate charge storage mechanism is proposed. Overall, present work outcomes signify that the TEG solvent might be the better choice for solvothermal synthesis of BiOCl instead of EG and DEG solvents for enhanced electrochemical performance.

- In **Chapter 7**, we enhance the electrochemical performance of pure marigold flower-like morphology BiOCl by incorporating polypyrrole, as a dopant. BP1 nanocomposite (5 wt.% of PPy in BiOCl) with a specific surface area of 33.65 m^2/g was successfully synthesized by the physical blending method. These optimized properties of BP1 support to improve overall performance, electrode surface utilization, and the range of ion transport from the exterior electrolyte to the inner surfaces. In electrochemical investigations, the BP1 electrode demonstrated a battery-type behavior with a specific capacitance of 659 F/g at 1.0 A/g current density. Furthermore, a symmetric supercapacitor device of BP1 achieved a specific capacitance value of 76.8 F/g with an energy density of 24.0 Wh/kg and a power density of 750.0 W/kg. Finally, the fabricated symmetric supercapacitor device has effectively powered green and red LED, demonstrating its potential in energy storage systems.

8.2. Future Scope

Although the present research work investigated innovative methods for developing supercapacitors using conducting polymer nanocomposites with metal oxides, which resulted in good cycle life and high specific capacitance, several challenges still persist in enhancing supercapacitor performance. A primary concern is improving their energy density without compromising power density or safety. The following approaches have been identified as potential solutions to address these challenges in future research.

- Conducting polymers with spinel oxide nanocomposites: Future research could focus on exploring the use of conducting polymers combined with spinel oxide nanocomposites as electrode materials for supercapacitors. Spinel oxides, known for their excellent electrical conductivity, structural stability, and high specific capacitance, could significantly enhance the performance characteristics of supercapacitors. This approach has the potential to improve energy density while keeping or even boosting power density and cycle life, by capitalizing the strengths of both conducting polymers and spinel oxides.
- Binder-free conducting polymer-based nanocomposite electrode material: The development of binder-free conducting polymer-based nanocomposites for supercapacitor electrodes represents a promising area for future research. The aim of this approach is to eliminate the need for traditional binders, which often diminish energy and power density. By directly synthesizing conducting polymer nanocomposites into electrodes, it could be possible to enhance electrical conductivity

and electrochemical performance. This binder-free strategy might potentially result in supercapacitors with improved energy density, higher power density, and extended cycle life by boosting mechanical stability, maximizing active material utilization, and overall performance.

- Fabrication of asymmetrical supercapacitor devices based on conducting polymer-based nanocomposites for the cathode or anode of asymmetrical supercapacitors can be studied. This method could improve overall supercapacitor performance by providing a large potential window with enhanced specific capacitance, energy density, and power density.
- Design supercapacitors that can bend and flex without breaking using a flexible substrate with organic gel electrolytes: In future research, the focus should shift towards designing supercapacitors that can bend and flex without damage by using flexible substrates combined with organic gel electrolytes. Emphasis will be placed on selecting a stretchable polymer film or fabric as the substrate to ensure both structural and electrical integrity under mechanical stress. Organic gel electrolytes will be explored for their ability to conform to the flexible substrate, prevent leakage, and enhance durability. Additionally, the investigation will include flexible and conductive electrode materials, such as conducting polymers or carbon-based substances, which can maintain their performance despite bending and stretching. The research will also aim to optimize the integration process to achieve an even distribution of the gel electrolyte and effective adhesion to the substrate. This approach is intended to develop supercapacitors suitable for applications in flexible electronics and wearable devices, with enhanced reliability and performance under dynamic conditions.

List of publications, conferences and workshops

List of publications

1. **Yugesh Singh Thakur**, Aman Deep Acharya, Sakshi Sharma, Muzahir Iqbal, Sagar Bisoyi, Amisha, and Bhawna. “Optimizing solvent mixtures to boost the electrochemical performance of BiOCl for supercapacitor applications”. Materials Research Bulletin, 184 (2025), 113259.
2. **Yugesh Singh Thakur**, Aman Deep Acharya, Sakshi Sharma, Amisha, Sagar Bisoyi, Bhawna and Sandeep Singh Manhas. “Synthesis of 3D rice-like BiOCl battery-type electrode material and evaluation of their electrochemical performance in a symmetrical supercapacitor device configuration”. *Materials Science in Semiconductor Processing*, 177 (2024), 108376.
3. **Yugesh Singh Thakur**, Aman Deep Acharya, Sakshi Sharma, Sagar Bisoyi and Bhawna. “Enhanced electrochemical performance of in situ polymerized V_2O_5-PANI nanocomposites and its practical application confirmation by assembling ionic liquid as well as solid state-based supercapacitor device”. *Results in Chemistry*, 7 (2024), 101259.
4. **Yugesh Singh Thakur**, Aman Deep Acharya, Sakshi Sharma and Bhawna. “Reinforcement of V_2O_5 nanoparticle in polyaniline to improve the optical and UV-shielding properties”. *Results in Optics*, 11 (2023), 100400.
5. **Yugesh Singh Thakur**, Aman Deep Acharya, Bhawna and Bhavana Singh. “Preparation and characterization of vanadium oxide (V_2O_5) sheet like nanostructure”. *AIP Conference Proceedings*, 2800 (2023).
6. **Yugesh Singh Thakur**, Aman Deep Acharya, Sakshi Sharma, Bhawna and Sandeep Singh Manhas. “Synthesis and characterization of PANI doped V_2O_5 nanocomposites for supercapacitor application”. *Materials Today: Proceedings*.
7. Sakshi Sharma, Aman Deep Acharya, **Yugesh Singh Thakur** and Bhawna. “Solvothermal synthesized mesoporous BiOCl nano-ellipsoids with oxygen vacancies for photocatalytic degradation of low density polyethylene (LDPE) plastic”. *Materials Research Bulletin.* 183 (2025), 11321.
8. Sakshi Sharma, Aman Deep Acharya, **Yugesh Singh Thakur** and Bhawna. “Harnessing BiOCl nanoparticles for advanced optical and UV shielding properties in LDPE”. *Materials Today Communications*. 42 (2025), 111471.

9. Sakshi Sharma, Aman Deep Acharya, **Yugesh Singh Thakur**, Bhawna. "Effective Photocatalytic Degradation of Non-Biodegradable Polymer using BiOCl Nanostructure". *AIP Conference Proceedings*.

10. Sakshi Sharma, Aman Deep Acharya, Bhawna, **Yugesh Singh Thakur** and Sagar Bisoyi. "Optimizing BiOCl concentration for enhanced LDPE performance: Investigation of structure, thermal stability, and optical characteristics". *Journal of Molecular Structure,* 1294 (2023), 136382.
11. Sakshi Sharma, Aman Deep Acharya, Bhawna and **Yugesh Singh Thakur**. "Experimental studies of BiOCl nanostructures synthesized by sol-gel and solvothermal routes for photocatalytic application". *Materials Today: Proceedings.*
12. Sakshi Sharma, Aman Deep Acharya, **Yugesh Singh Thakur** and Bhawna. "Controlled synthesis of hierarchical BiOCl nanostructure with exposed {010} facets to yield enhanced photocatalytic performance for PMMA deterioration". *Journal of Polymer* Research, 29 (2022), 46.
13. Amisha, Aman Deep Acharya, and **Yugesh Singh Thakur** "Tuning Electrochemical Performance of Polyaniline-Based Supercapacitors by Inclusion of Protonic Acid and Electrolyte Concentration"**.** *Journal of the Indian Chemical Society*, 102 (2025) 101836.

3. *Intellectual Property Rights (IPR)*

1. Copy right granted, Class and description of the work: Dramatic work the graphical abstract present “BiOCl Nanoparticle Assisted photocatalytic Degradation of Nonbiodegradable Polymers”, Registration Number. L-129407/2023,Diary Number: 10610/2023-CO/L.

2. Published Indian patent, Title of the invention: “OPTIMIZED POLYPYRROLE DOPING” This invention is a polypyrrole/bismuth oxychloride super capacitance cell and belong to electrochemical energy storage. The method is an optimized doping of polypyrrole in bismuth oxychloride incorporation of 5 wt.% PPy-BiOCl significantly enhances the electrochemical performance, Application No.202411000191 A, Publication Date : 09/02/2024.

Presentations in International/National Conferences

1. International Conference on “Recent Advancements in Nanotechnology for Sustainable Development (ICRANSD-22)” during 11- 12 November, 2022 organised by Maharaja Agrasen University, Baddi, India Presented a paper entitled “Synthesis and characterization of PANI doped V_2O_5 nanocomposites for supercapacitor application”.

2. International Conference on “ Materials for Emerging Technologies (ICMET-21)” during 18-19 February 2022 organised by Department of Research Impact and Outcome, Division of Research and Development, Lovely Professional University, Punjab, India Presented a paper entitled “ Preparation and characterization of vanadium oxide (V_2O_5) sheet like nanostructure”.

Workshops and Courses

1. Workshop on " Spectroscopic, Chromatographic, Bioanalytical and Imagining Techniques" (28th November- 04th December 2022) conducted by the Department of Science and Technology (DST) Government of India under Synergistic Training Utilizing Scientific and Technological Infrastructure (STUTI).

2. Completing "ACS Reviewer Lab online course" Date granted 21/07/2024.

3. Attended Summer Internship for Science Students on " Basic and Applications of X-ray Diffraction organized by Narayana Institute of Advanced Sciences (NIAS) under the aegis of International Society of Life Sciences (ISLS) from 1st-21st June 2021.

4. Participated in 9 day Online Hands-on Training on "Rietveld Refinement" during 25th January- 02 February 2023 conducted by SIAS Research Forum in collaboration with the Department of Physics, PSMO College, Tiruangadi, Kerala.

5. Successfully completed the Three-week Online Workshop on "Electrochemical Data Analysis" during 05-23 June 2023 jointly organized by the Department of Physics, Guru Nanak Dev University Amritsar, India and SIAS Research Forum.

6. Participated in the course on "Nanomaterials: By Design for Energy Applications" from 22-26 February 2022 organized by Global Initiative of Academic Networks (GIAN).

7. Participated in the "European Advanced Materials Congress" from 23-26 September 2023 Southampton, UK organized by the International Association of Advanced Materials, Sweden.

8. Participated e- workshop on " Materials and their characterization" from June 14-19 2021.

Invited talk

1. Delivered an invited talk entitled " Basic of Research and Research Methods in Energy Storage Devices" to M.Sc Physics Students on 6th June 2024 in the Lecture Theater-5 of MLSM College, Sundernagar Affiliated to Himachal Pradesh University Shimla.